PUMP-PROBE SPECTROSCOPY OF PHOTOVOLTAIC MATERIALS

A thesis submitted to The University of Manchester for the degree of PhD in the Faculty of Engineering and Physical Sciences

2011

BEN SPENCER

School of Physics and Astronomy, the Photon Science Institute and the Cockcroft Institute

Contents

List of Figures 4
List of Tables 8
Abstract 9
Declaration 10
Copyright statement 11
Publications 12
Acknowledgements 13

1 Introduction. 15

2 Theory. 20
2.1 Electrons in a crystal 20
2.2 Semiconductors 37
2.3 Excitons 42
2.4 Band bending at surfaces 44
2.5 Photovoltaics 47
2.6 Quantum confinement 48
2.7 Terahertz absorption and photoconductivity 55

3 Experimental. 60
3.1 Laser system 60
3.1.1 Mode-locking and pulse-picking 63
3.1.2 Waveplates and the Pockels effect 64
3.1.3 Frequency doubling and phase matching 66
3.1.4 Regenerative amplifier 67
3.1.5 Optical parametric amplifier 71
3.1.6 Laser beam radius measurement 77
3.2 Laser-pump synchrotron-probe experiments 78
3.2.1 X-ray photoelectron spectroscopy (XPS) 79
3.2.2 Synchronization of the laser system to the SRS 85
3.2.3 Pump-probe experiments at SOLEIL 88
3.3 Time-resolved THz spectrometer 90
3.3.1 Schematic layout 90
3.3.2 THz generation and detection 93
3.3.3 Lock-in amplifier 99
3.3.4 Water absorption 101
3.3.5 Etalon effect 102
3.3.6 Pump-probe experiments 105
3.3.7 Material parameter extraction 106

4 Time-resolved terahertz spectroscopy of photovoltaic materials 109
4.1 Commissioning the spectrometer . . . 109
4.1.1 Terahertz absorption of quartz . . . 109
4.1.2 Terahertz absorption of toluene and hexane . . . 112
4.1.3 Time-resolved terahertz spectroscopy of GaAs . . . 116
4.2 Time-resolved terahertz spectroscopy of InP . . . 120
4.2.1 Motivation . . . 120
4.2.2 Photoconductivity spectra . . . 123
4.2.3 Efficiency of bulk InP . . . 131
4.3 InP Quantum Dot measurements . . . 136
4.4 Conclusions . . . 141

5 Laser-pump synchrotron-probe experiments of bulk and nanoparticulate photovoltaic materials. 143
5.1 Surface photovoltage in *n*-type Si(111) . . . 143
5.1.1 Surface preparation . . . 144
5.1.2 Spectral analysis . . . 145
5.1.3 Surface photovoltage analysis . . . 150
5.2 PbS quantum dots attached to ZnO . . . 153
5.2.1 Sample preparation . . . 154
5.2.2 XPS measurements . . . 158
5.2.3 Surface photovoltage measurements . . . 163
5.3 Conclusions . . . 174

6 Conclusions and future work. 177

Bibliography 181

Word count: 51,929

List of Figures

1.1 The pump-probe technique 17

2.1 Splitting of atomic levels with interatomic separation 28
2.2 Kronnig-Penney potential representing a periodic lattice 29
2.3 The Kronig-Penney condition 31
2.4 Dispersion diagram for electrons in a periodic potential compared to the free electron model 32
2.5 Dispersion diagram for electrons in a periodic potential compared to the free electron model over the first Brillouin zone 33
2.6 Density of populated states 36
2.7 Dispersion diagram of an electron transition 38
2.8 Dispersion diagram of an electron transition in an indirect band gap semiconductor 39
2.9 The degenerate valence band 40
2.10 Donor and acceptor states 41
2.11 Dispersion diagram of the formation of a free exciton 43
2.12 Absorption spectrum for a bulk direct band gap semiconductor with free exciton states 43
2.13 Band bending at the surface of an n-type semiconductor 45
2.14 Surface photovoltage in an n-type semiconductor under photoexcitation 46
2.15 The p-n junction 48
2.16 The effect of quantum confinement on the density of states 50
2.17 The effect of quantum confinement on electronic energy levels . . . 51
2.18 Absorption spectra of a series of PbSe quantum dots 51
2.19 A model for a hybrid solar energy cell 52
2.20 The creation of multiple excitons from one high energy photon via Impact Ionization 53
2.21 The solar spectrum versus the quantum yield of bulk silicon 53

3.1 Schematic of the top tier of the laser system 61
3.2 Schematic of the bottom tier of the laser system 62
3.3 Photograph of the laser system on beamline 6.1 at the SRS 62
3.4 Schematic layout of regenerative amplifier 68
3.5 Optical parametric amplifier 75
3.6 TOPAS tuning range 76
3.7 Knife-edge beam radius measurement 78
3.8 Universal inelastic mean free path curve 80

3.9 The X-ray photoelectron spectroscopy (XPS) experiment 81
3.10 The Auger emission process 83
3.11 Laser-synchrotron synchronization electronics 86
3.12 Laser-pump synchrotron-probe experiment 87
3.13 Surface photovoltage measured with XPS 88
3.14 SOLEIL pump-probe electronics 89
3.15 Time-resolved terahertz spectrometer 91
3.16 Time-resolved terahertz spectrometer utilizing the OPA 92
3.17 Photograph of the time-resolved terahertz spectrometer 92
3.18 Electro-optic detection of terahertz pulses 95
3.19 Screen shot of the THz automation software written in LabView . . 95
3.20 Data acquisition in the THz spectrometer 96
3.21 Typical terahertz pulse 97
3.22 Terahertz power spectrum 97
3.23 Raw and unwrapped phase data 99
3.24 Circuit diagram of a lock-in amplifier 100
3.25 Characteristic absorptions in the infrared and terahertz regions . . . 102
3.26 Terahertz power spectra with and without purging with dry air . . . 103
3.27 Multiple reflections observed in the time domain 104
3.28 Multiple reflections observed in the frequency domain 104
3.29 Change in optical density spectra for varying pump beam sizes . . . 106

4.1 Time-domain THz data for a quartz cuvette compared to the air reference 110
4.2 Power spectra of THz pulses through a quartz cuvette compared to the air reference 110
4.3 Refractive index of quartz 111
4.4 Absorption coefficient of quartz 111
4.5 Time-domain THz pulses for toluene and hexane 113
4.6 Power spectra for toluene and hexane 113
4.7 Unwrapped Fourier transform phase spectra for toluene and hexane 114
4.8 Refractive indices of toluene and hexane 114
4.9 Absorption spectra for toluene and hexane 115
4.10 Two-dimensional plot of the photoexcitation of a GaAs wafer 116
4.11 Two-dimensional plot of the photoexcitation of a GaAs wafer, taken from the literature 117
4.12 Two-dimensional plot of the photoexcitation of a GaAs wafer 117
4.13 Rising edge of the change in the THz waveform for GaAs photoexcited with 400 and 800 nm laser pulses 118
4.14 Band structure of GaAs 119
4.15 Refractive index of InP 123
4.16 Absorption coefficient of InP 124
4.17 Time-domain traces of THz pulses through InP 125
4.18 Power spectrum of THz pulses in InP 125
4.19 Photoconductivity spectrum of InP upon photoexcitation with an 800 nm pump beam 126
4.20 Photoconductivity spectrum of InP upon photoexcitation with a 450 nm pump beam 126

4.21 Photoconductivity spectrum of InP upon photoexcitation with a 511 nm pump beam 127
4.22 Power dependence of plasma frequencies for InP photoexcited with a 511 nm pump beam 127
4.23 Pump scans for InP photoexcited with a 511 nm pump beam 129
4.24 Rising edges of pump scans for InP photoexcited with a variety of pump wavelengths 129
4.25 Band structure of InP 130
4.26 Complex photoconductivity spectrum for bulk PbS taken from the literature 131
4.27 Efficiency of bulk and nanoparticulate InP compared to an InP photovoltaic device 132
4.28 Quantum efficiency of bulk PbS 133
4.29 Quantum efficiency of GaAs 135
4.30 Band structure of PbS 135
4.31 Visible absorbance spectrum of 6 nm InP quantum dots 137
4.32 Time-domain traces of THz pulses through 6 nm InP quantum dots 137
4.33 Absorption spectrum of 6 nm InP quantum dot samples over THz frequencies 139
4.34 A change in the InP quantum dot sample upon photoexcitation is not detected 139
4.35 Carrier multiplication in InAs quantum dots measured with time-resolved THz spectroscopy 140

5.1 The Si(111) (7×7) surface 144
5.2 Photograph of the LEED pattern of Si(111) (7×7) 145
5.3 Fitting of Si 2p core level 146
5.4 Surface photovoltage in an n-type semiconductor studied with XPS. 147
5.5 The Si 2p core level 4 ns after photoexcitation 148
5.6 Fitting of Si 2p core level 4 ns after photoexcitation 148
5.7 Alternative fitting of the Si 2p core level 4 ns after photoexcitation . 149
5.8 Fitted surface photovoltage for Si(111) 151
5.9 Electronic structure at the silicon surface 152
5.10 Energy level line-up of PbS quantum dots on an n-type ZnO substrate 154
5.11 Photograph of the annealing of ZnO 155
5.12 Photograph of the LEED pattern of the ZnO (1×1) surface 156
5.13 The ZnO(10$\bar{1}$0) surface 156
5.14 3-mercaptopropionic acid linking a PbS quantum dot to the ZnO surface 157
5.15 Fitting of the sulfur 2p core level of PbS quantum dots attached to ZnO 159
5.16 Fitting of the lead 4f core level of PbS quantum dots attached to ZnO 160
5.17 Oxidized species of the S 2p core level 160
5.18 Change in the S 2p XPS spectrum upon exposure to the X-ray beam 161
5.19 Change in the Pb 4f XPS spectrum upon exposure to the X-ray beam 162
5.20 Valence band scans for clean ZnO and PbS quantum dots attached to ZnO 163
5.21 Fitting of the Zn 3d core level 164

5.22 The Zn 3*d* core level with and without laser illumination 164
5.23 SPV shift of the Zn 3*d* core level studied at the SRS 165
5.24 Power dependence of the surface photovoltage of ZnO 166
5.25 A typical scan of the Zn 3*d* core level taken at SOLEIL 167
5.26 The SPV shift of the Zn 3*d* core level for clean ZnO 168
5.27 The SPV shift of the Zn 3*d* core level repeated to show the laser on and off timing 169
5.28 Power dependence of the SPV shift in clean ZnO photoexcited with a CW laser 170
5.29 The rising edge of the SPV shift of the Zn 3*d* core level for clean ZnO 171
5.30 The SPV effect in ZnO caused by chemisorption and photodesorption of oxygen. 172
5.31 The SPV shift of the Zn 3*d* core level for clean ZnO compared to PbS quantum dots attached to ZnO 172
5.32 The decay of the SPV of the Zn 3*d* core level for PbS quantum dots attached to ZnO 173
5.33 The rise of the SPV of the Zn 3*d* core level for PbS quantum dots attached to ZnO 174

List of Tables

1.1 Solar cell efficiencies 16

3.1 Degeneracy of the s, p, d and f electronic orbitals 81
3.2 Electron configurations up to the $4f_{7/2}$ orbital 82
3.3 Water absorption lines in the THz spectral region 101

4.1 Conduction band parameters in GaAs and InP 120

5.1 Surface states of the Si $2p$ core level 146
5.2 FWHM of bulk and surface Si $2p$ states 149
5.3 Physical origins of the XPS components in the S $2p$ and Pb $4f$ spectra. 161
5.4 Fitting parameters for the SPV of the Zn $3d$ core level for clean ZnO and PbS quantum dots attached to ZnO 171

Abstract

The University of Manchester
Ben Spencer
Doctor of Philosophy
Pump-Probe Spectroscopy of Photovoltaic Materials
April 2011

The study of photovoltaic materials is important so as to develop new solar energy technologies: in particular, quantum-confined semiconductors could offer increased quantum efficiencies at a much lower manufacture cost. This thesis contains results from a number of pump-probe experiments designed to probe the carrier dynamics in bulk and quantum-confined photovoltaics.

A THz time-domain spectrometer was designed, built and commissioned. The THz refractive indices and absorption coefficients of toluene and hexane were determined, and the spectrometer was benchmarked using a photoexcited GaAs wafer. Results are presented of time-resolved THz spectroscopy of photoexcited bulk InP as a function of laser excitation wavelength. These data were used to extract the quantum efficiency of bulk InP in order to compare with recent results for InP quantum dots. The quantum efficiency in quantum dots increases when the incident photon energy is at least twice the band gap energy, whereas the efficiency of the bulk material is found to decrease. This is because of surface recombination, and these measurements therefore verify the potential superiority of quantum dot materials over bulk materials for use in solar energy applications. Initial measurements of quantum dots using THz spectroscopy highlighted the various experimental challenges involved and the upgrades required to study such samples in the future.

The time-dependence of the photoinduced surface photovoltage (SPV) in Si was studied on nanosecond timescales by synchronizing an ultrafast laser system to a synchrotron radiation source (the SRS at Daresbury, UK), and measuring the resulting shift in the photoelectron spectrum. The equilibrium band bending was determined, and the decay of the SPV was attributed to the recombination of charge carriers across the band gap.

Results are presented for the SPV in bulk ZnO and for PbS quantum dots chemically attached to ZnO. The fact that the PbS quantum dots were chemically attached to the surface without becoming oxidized was verified using X-ray photoelectron spectroscopy (XPS). The changes caused by photoexcitation occur on much longer timescales in ZnO than Si (sub-milliseconds rather than nanoseconds), and these timescales were conveniently accessed using the time-resolved XPS facility at the TEMPO beamline at Synchrotron SOLEIL (Paris, France). This is due to oxygen adsorption and desorption processes at the ZnO surface affecting the transfer of charge carriers. The addition of PbS quantum dots to the ZnO surface was found to increase the speed of this charge transfer due to injection of carriers directly from the PbS quantum dot to the bulk ZnO conduction band.

Declaration

No portion of the work referred to in this thesis has been submitted in support of an application for another degree or qualification of this or any other university or other institute of learning.

Copyright statement

i The author of this thesis (including any appendices and/or schedules to this thesis) owns certain copyright or related rights in it (the "Copyright") and s/he has given The University of Manchester certain rights to use such Copyright, including for administrative purposes.

ii Copies of this thesis, either in full or in extracts and whether in hard or electronic copy, may be made only in accordance with the Copyright, Designs and Patents Act 1988 (as amended) and regulations issued under it or, where appropriate, in accordance with licensing agreements which the University has from time to time. This page must form part of any such copies made.

iii The ownership of certain Copyright, patents, designs, trade marks and other intellectual property (the "Intellectual Property") and any reproductions of copyright works in the thesis, for example graphs and tables ("Reproductions"), which may be described in this thesis, may not be owned by the author and may be owned by third parties. Such Intellectual Property and Reproductions cannot and must not be made available for use without the prior written permission of the owner(s) of the relevant Intellectual Property and/or Reproductions.

iv Further information on the conditions under which disclosure, publication and commercialisation of this thesis, the Copyright and any Intellectual Property and/or Reproductions described in it may take place is available in the University IP Policy, in any relevant Thesis restriction declarations deposited in the University Library, The University Library's regulations and in The University's policy on Presentation of Theses.

Publications

Ben F. Spencer, Darren M. Graham, Samantha J. O. Hardman, Elaine A. Seddon, Fausto Sirotti, Mathieu Silly, Swapan Chattopadhyay and Wendy R. Flavell, "Surface photovoltage spectroscopy of the carrier dynamics in PbS quantum dots attached to ZnO", *(In preparation)*.

Samantha J. O. Hardman, Darren M. Graham, Stuart K. Stubbs, **Ben F. Spencer**, Elaine A. Seddon, Ho-Ting Fung, Sandra Gardonio, Fausto Sirotti, Mathieu G. Silly, Javeed Akhtar, Paul O'Brien, David J. Binks, Wendy R. Flavell, "Electronic and surface properties of PbS nanoparticles exhibiting efficient multiple exciton generation", *(In preparation)*.

B. F. Spencer, D. M. Graham, C. Lange, S. Chattopadhyay, and W. R. Flavell, "Developing InP-based solar cells: time-resolved terahertz measurements of photoconductivity and carrier multiplication efficiencies", *Proceedings of Infrared, Millimetre and Terahertz Waves*, IEEE, vol. 35 (2010). DOI: 10.1109/ICIMW.2010.5612377.

Stuart K. Stubbs, Samantha J. O. Hardman, Darren M. Graham, **Ben F. Spencer**, Wendy R. Flavell, Paul Glarvey, Ombretta Masala, Nigel L. Pickett, and David J. Binks, "Efficient carrier multiplication in InP nanoparticles", *Physical Review B*, vol. 81, p. 081303(R) (2010).

Javeed Akhtar, M. Azad Malik, Paul O'Brien, K. G. U. Wijayantha, R. Dharmadasa, Samantha J. O. Hardman, Darren M. Graham, **Ben F. Spencer**, Stuart K. Stubbs, Wendy R. Flavell, David J. Binks, Fausto Sirotti, Mario El Kazzi and Mathieu Silly, "A greener route to photoelectrochemically active PbS nanoparticles", *Journal of Materials Chemistry*, vol. 20, pp. 2336–2344 (2010).

Acknowledgements

To Dr. Darren Graham, Dr. Samantha Hardman, Dr. Ian Shinton, Dr. Jonathan Smith and Dr. Phillip Law for all their assistance and support; to my supervisors Prof. Wendy Flavell, Prof. Swapan Chattopadhyay and Dr. David Binks for giving me this research opportunity; to the Cockcroft Institute at Daresbury Laboratory for my funding; to the technicians at Daresbury, the Photon Science Institute, and SOLEIL for their assistance; and to all my other friends for everything else. This thesis is dedicated to my parents, who always had more faith in my abilities than I ever could.

New knowledge is the most valuable commodity on Earth. The more truth we have to work with, the richer we become.

Kurt Vonnegut, *Breakfast of Champions*

‘

Chapter 1

Introduction.

We are currently in a global energy crisis. The current consumption of energy worldwide per year is estimated to be 14 TW, and is set to double by the year 2050. As the amount of available fossil fuels dwindles, there is a large effort being made into the research and development of sustainable, clean energy sources. The amount of energy incident upon the Earth from solar radiation is approximately 120,000 TW per year; the amount of energy incident on the Earth in one hour is equivalent to the worldwide consumption in a year. Clearly solar power is a vastly underexploited source of renewable energy [1].

Absorption of a photon (photoexcitation) leads to the generation of charge carriers in semiconductors, namely electrons promoted into the conduction band and positively-charged holes in the valence band. An electron and hole can be bound as an exciton, which is analogous to a hydrogen atom. Solar energy cells traditionally contain a p-type material which is used for the extraction of holes at a cathode and an n-type material which is used for electron extraction at an anode. This allows for current to flow and thus electricity is generated. The efficiency of a solar cell is defined as the percentage of electrons collected compared to the number of photons absorbed.

Highly efficient, commercially available silicon solar energy cells are not a viable option for the mass production of solar power because of their cost (the silicon is grown to obtain an extremely high level of purity). Instead, a number of alternative approaches have been proposed [2]. These include thin film solar cells [3], photochemical dye sensitised solar cells [4], organic polymer, and multijunction devices [5, 6, 7]. The latter currently holds a world-record solar cell efficiency of 41.3 $\pm$ 2.5 %. The efficiencies of these different cells are listed in table (1.1) [8].

Crystalline solar cells are 1st-generation solar cells with good efficiencies at relatively high costs. 2nd-generation solar cells include thin-film and dye sensitised solar cells which have lower efficiencies than crystalline cells, but which also have

Material	Solar cell type	Efficiency (%)	Reference
Si	Crystalline	24.7 ± 0.5	[9]
GaAs	Crystalline	26.4 ± 0.8	[8]
InP	Crystalline	22.1 ± 0.7	[10]
CuInGaSe2	Thin film	19.9 ± 0.6	[11]
CdTe	Thin film	16.7 ± 0.5	[12]
	Dye sensitised	10.4 ± 0.3	[13]
	Organic polymer	3.0 ± 0.1	[8]
GaInP/GaAs	Multijunction	30.3	[5]
GaInP/GaInAs/Ge	Multijunction	35.8 ± 1.5	[6]
InGaP/GaAs/InGaAs	Multijunction	41.3 ± 2.5	[7]

Table 1.1: Solar cell efficiencies measured under the global AM1.5 solar spectrum at 25 °C, adapted from [8].

a greatly reduced fabrication cost. As such it is these types of solar cells that will probably have the largest market share of the domestic solar cell market in the near-future, especially because these thin-film solar cells can be engineered into 'rolls' of solar cell that can easily be attached to any surface. 3rd-generation solar cells are designed to achieve high efficiencies at low costs, and include organic polymer and multijunction cells as well as novel solar cells where the light-harvesting elements are semiconductor nanoparticles [14]. These nanoparticles are quantum-confined in three dimensions, and so are often referred to as quantum dots. The processes involved in manufacturing quantum dots can easily effect the size of the quantum dots which in turn affects the absorption energy. Therefore quantum dots can be specifically tailored to absorb the optimum wavelengths of the solar spectrum [14]. 3rd-generation solar cells are the focus of current solar cell research, which also includes novel hybrid solar cell models combining organic and inorganic components.

Nanoparticles may also benefit from an efficiency increase caused by the process of carrier multiplication, speculated to be enhanced by the quantum confinement of such structures [15]. Carrier multiplication occurs when a highly photoexcited carrier, created upon the absorption of a photon with energy greater than twice the band gap energy, generates another pair of charge carriers. The energy in excess of the band gap is transferred to promote another electron across the band gap, effectively multiplying the number of carriers generated by one photon. This excess energy is often lost as heat when carriers relax to the band edge non-radiatively. It is currently unclear whether or not quantum confinement enhances the amount of carrier multiplication, and thus it is important to compare the quantum efficiencies of bulk materials to quantum dot counterparts [16, 17].

Indium phosphide (InP) is currently a material of particular interest, because carrier multiplication has recently been shown to occur in InP quantum dots [18]. Moreover, InP is non-toxic compared to other commonly-used quantum dots that often include lead or cadmium. However, measurements of the carrier multiplication quantum yields in bulk InP have yet to be made, and so it is unclear whether the quantum yields observed in InP quantum dots are due to quantum confinement.

It is crucially important that the charge carrier dynamics in bulk and nanoparticulate photovoltaics is fully understood and characterised in order to optimise the design of solar cells based upon them. Carrier dynamics are measured using pump-probe techniques. A laser pump beam is used to photoexcite a sample by promoting electrons across the band gap and into the conduction band, analogous to solar radiation being absorbed by a solar cell. The properties of the sample are then measured after photoexcitation using a probe beam which does not alter the state of the sample. The evolution of the photoexcited sample over time is then measured by varying the delay time, τ, between the pump and probe beams as shown in figure (1.1).

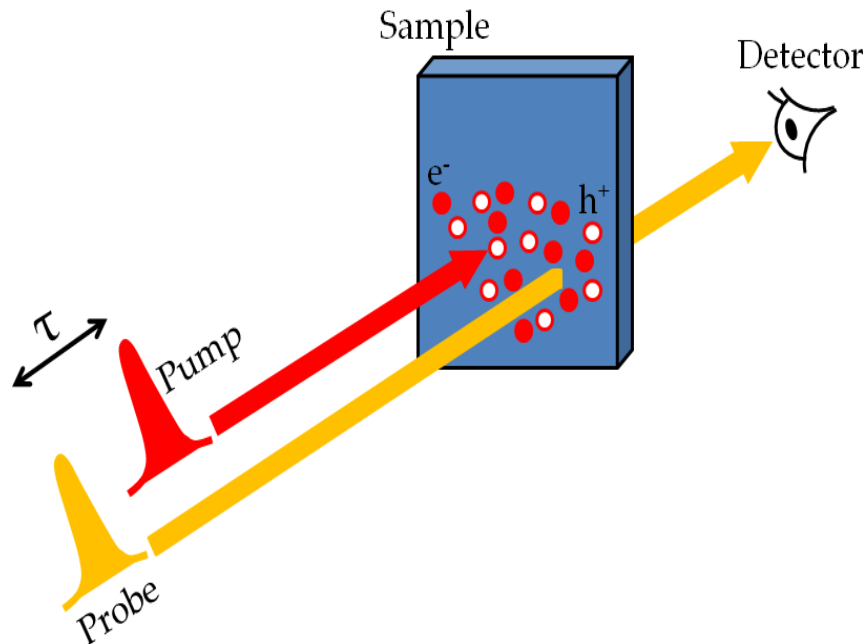

Figure 1.1: The pump-probe technique. A pump beam photoexcites the sample creating charge carriers (electrons, filled circles, and holes, empty circles), which are then probed at a delay time of τ. The probe beam does not alter the state of the system.

Two types of probe beam are used in the work presented in this thesis: a highly energetic X-ray probe beam frees electrons from the sample (the photoelectric effect). The detection technique is then X-Ray Photoelectron Spectroscopy (XPS) [19].

Another probe beam used is a terahertz (THz) beam generated and detected by optical rectification and electro-optic sampling in nonlinear optical crystals [20]. THz radiation is absorbed by a material depending on the concentration of free carriers, and the absorption of THz radiation can be used to extract the frequency-dependent, complex photoconductivity of a sample [16].

Time-resolved spectroscopy using THz radiation (the spectral region in between the infrared and microwave regions) is a relatively new spectroscopic technique. Historically there have been difficulties in both the generation and detection of THz radiation [21]. Time-resolved THz spectroscopy also requires ultrafast laser pulses that are another relatively new technological advance [22, 20]. Radiation over a frequency range of 0.1 - 2 THz have energies between approximately 0.4 and 8 meV, and are absorbed by phonon modes (lattice vibrations). When a semiconductor is photoexcited, a plasma of free carriers is created which also absorbs the THz radiation [23]. THz radiation is therefore an ideal probe of carrier dynamics in semiconductors.

Time-resolved THz spectroscopy can be used as a non-contact probe of the photoconductivity of a material over picosecond timescales. Previous measurements of photoconductivity have involved attaching electrodes to a sample, where measurements are perturbed by the large distances carriers travel before being detected [16]. THz spectroscopy instead allows an ultrafast measurement of photoconductivity, as well as a means of measuring photoconductivity in samples where attaching electrodes is impossible, such as in nanoparticles [24, 25, 26, 27]. THz spectroscopy has many other applications, including the use in security (it is non-ionizing and can detect metallic objects underneath clothing), spectroscopy of drug and explosive detection, and art conservation [28, 29, 30].

Another important aspect involved in the physics of photovoltaics is the charge carrier dynamics at the interfaces in a *p*-*n* junction (the interface between the *p* and *n*-type semiconductor materials) of a solar cell. These dynamics can be studied using laser-pump X-ray-probe spectroscopy, where the X-ray probe can be generated by a synchrotron. Ultrafast laser pulses are synchronized to an external synchrotron radiation source, where the pump-probe delay time can be controlled [31, 32, 33, 34, 35]. This allows the photoinduced change in the band bending at semiconductor interfaces, the surface photovoltage (SPV), to be investigated.

In chapter 2 of this thesis the free and nearly-free models of electrons in a crystal are described before the properties of bulk semiconductors and excitons within them are discussed. Banding bending at semiconductor surfaces is then introduced before a description of the *p*-*n* junction of a traditional solar cell. Finally, the effects of quantum confinement on the properties of semiconductors are introduced as well the use of THz radiation in photoconductivity measurements. The

experimental chapter firstly outlines the ultrafast laser system that was used both for laser-pump X-ray-probe measurements at Daresbury Laboratory (UK) as well as for time-resolved THz spectroscopy. The laser-pump X-ray-probe experiments are introduced, including a description of X-ray Photoelectron Spectroscopy (XPS). The synchronization of the laser system to the Synchrotron Radiation Source (SRS) at Daresbury Laboratory for these measurements, as well as the use of a continuous wave (CW) laser for pump-probe experiments at Synchrotron SOLEIL, Paris, France are described. The time-resolved THz spectrometer that has been designed, built and commissioned during this project is then described and the experimental challenges involved in this pump-probe technique are addressed.

Chapter 4 gives results obtained using the time-resolved THz spectrometer. Measurements of quartz, organic solvents and a GaAs wafer were made to benchmark the technique. Photoconductivity measurements of bulk InP are then described, and the quantum efficiency over a range of pump photon energies is extracted to compare to recent results from InP quantum dots. Finally, THz absorption measurements of colloidal InP quantum dots suspended in hexane are described. Chapter 5 details measurements of the photoinduced SPV in bulk Si, ZnO, and of PbS quantum dots chemically attached to ZnO. The PbS/ZnO system is studied because it forms the basis of a model for a 3rd-generation hybrid solar cell where PbS quantum dots are used for light harvesting and electrons are transferred to ZnO nanorods (holes are transported in a *p*-type organic conductor). Bulk Si and ZnO experiments were carried out at the SRS, and the photoinduced SPV in bulk ZnO was also measured at Synchrotron SOLEIL before PbS quantum dots were attached. Finally, a Conclusions chapter outlines the main findings of this thesis as well as providing suggestions for the next steps in the THz and SPV studies.

Chapter 2

Theory.

This chapter starts from a description of electrons in a crystal before expanding to the properties of bulk semiconductors and bound electron-hole pairs (excitons) within semiconductors. This leads on to a description of the physics involved in a photovoltaic cell; the changing properties of semiconductors as they are quantum confined with a view to their applications in novel photovoltaic cells; and finally to how terahertz (THz) radiation interacts with matter and to how it can be utilized to study such materials.

2.1 Electrons in a crystal

The classical properties of particles such as position and momentum become of little use on the atomic, quantum scale. Heisenberg explained this with the uncertainty principle:

$$\Delta x \Delta p \geq \frac{\hbar}{2}, \tag{2.1}$$

where x is position, p is momentum and $\hbar$ is the reduced Planck constant ($h/2\pi$). If the position of the particle is well known, its momentum cannot be as well known. To describe the particle on quantum scales this information is instead described by a wave function, Ψ, which describes the probability of the particle being in a certain state, α:

$$P_{\alpha}(x,y,z,t) = |\Psi_{\alpha}(x,y,z,t)|^2. \tag{2.2}$$

It is this probability function which connects the quantum and observable worlds. The wave function must therefore adhere to the normalization condition:

$$\int_{-\infty}^{+\infty} |\Psi(x,y,z,t)|^2 \, dxdydzdt = 1, \tag{2.3}$$

in that it must be in *some* state, and thus the trivial solution $\Psi = 0$ cannot represent a particle [36].

Newton's 2nd law of classical mechanics states

$$m\left(\frac{\partial^2 x}{\partial t^2} + \frac{\partial^2 y}{\partial t^2} + \frac{\partial^2 z}{\partial t^2}\right) = -\left(\frac{\partial V}{\partial x} + \frac{\partial V}{\partial y} + \frac{\partial V}{\partial z}\right), \tag{2.4}$$

where V is a potential energy function, and is here presumed to be independent of time. The analogous equation on the quantum scale is given by the Schrödinger equation for $\Psi(x, y, z, t)$:

$$-\frac{\hbar^2}{2m}\left[\frac{\partial^2}{\partial x^2} + \frac{\partial^2}{\partial y^2} + \frac{\partial^2}{\partial z^2}\right]\Psi + V\Psi = i\hbar\frac{\partial \Psi}{\partial t}. \tag{2.5}$$

Once the wave function is known, the expectation value of x, for example, can be found by

$$\langle x \rangle = \int_{-\infty}^{+\infty} x\,|\Psi|^2\,dx, \tag{2.6}$$

where the expectation value of a system is the average of the measurements taken on an ensemble of identically-prepared systems, as opposed to the average of repeated measurements on one system [36].

The potential, V, is independent of time for a central potential such as that of a hydrogen atom. The time independence in this case therefore leads to the derivation of a Schrödinger equation also independent of time. A separation of variables is performed on the Schrödinger equation:

$$\Psi(x, y, z, t) = \psi(x, y, z) f(t), \tag{2.7}$$

and thus the separable solutions are found:

$$\frac{\partial \Psi}{\partial t} = \psi\frac{\partial f}{\partial t}, \tag{2.8}$$

$$\frac{\partial^2 \Psi}{\partial x^2} = \frac{\partial^2 \psi}{\partial x^2} f. \tag{2.9}$$

Substituting into Eq. (2.5) becomes

$$-\frac{\hbar^2}{2m}\left(\frac{\partial^2 \psi}{\partial x^2} + \frac{\partial^2 \psi}{\partial y^2} + \frac{\partial^2 \psi}{\partial z^2}\right) f + V\psi f = i\hbar\psi\frac{\partial f}{\partial t}, \tag{2.10}$$

and dividing by ψf yields

$$-\frac{\hbar^2}{2m}\frac{1}{\psi}\left(\frac{\partial^2 \psi}{\partial x^2} + \frac{\partial^2 \psi}{\partial y^2} + \frac{\partial^2 \psi}{\partial z^2}\right) + V = i\hbar\frac{1}{f}\frac{\partial f}{\partial t}, \tag{2.11}$$

giving a LHS purely dependent on position (x, y, z) and a RHS purely dependent on time t.

In classical mechanics, the total energy of a system is given by the Hamiltonian:

$$H = T + V, \tag{2.12}$$

where T is kinetic energy given by

$$T = \frac{p^2}{2m}, \tag{2.13}$$

where p is momentum. On the quantum scale momentum is replaced by

$$p \rightarrow \frac{\hbar}{i}\left(\frac{\partial}{\partial x} + \frac{\partial}{\partial y} + \frac{\partial}{\partial z}\right), \tag{2.14}$$

which is a canonical substitution: momentum and spatial position are a canonical (or conjugate) pair of variables [36]. The Hamiltonian operator therefore becomes

$$\hat{H} = -\frac{\hbar^2}{2m}\left(\frac{\partial^2}{\partial x^2} + \frac{\partial^2}{\partial y^2} + \frac{\partial^2}{\partial z^2}\right) + V. \tag{2.15}$$

Substituting into Eq. (2.11) and multiplying by ψ gives

$$\hat{H}\psi = \left(i\hbar \frac{1}{f}\frac{\partial f}{\partial t}\right)\psi. \tag{2.16}$$

Because the Hamiltonian operator gives the total energy of the system:

$$E = i\hbar \frac{1}{f}\frac{\partial f}{\partial t} \tag{2.17}$$

and so

$$\hat{H}\psi = E\psi, \tag{2.18}$$

which yields the time independent Schrödinger equation:

$$-\frac{\hbar^2}{2m}\left[\frac{\partial^2}{\partial x^2} + \frac{\partial^2}{\partial y^2} + \frac{\partial^2}{\partial z^2}\right]\psi + V\psi = E\psi. \tag{2.19}$$

The time dependence $f(t)$ has been separated, and solving Eq. (2.17) gives

$$f(t) = e^{-iEt/\hbar}. \tag{2.20}$$

This time dependence does not affect the probability function (equation (2.2)), as

$$f^* f = e^{+iEt/\hbar} e^{-iEt/\hbar} = 1. \tag{2.21}$$

Energy and time are also a canonical pair of variables: time independence implies energy conservation [36].

The time-independent Schrödinger equation has other important consequences: firstly, there are allowed stationary states for the wave function Ψ. The wave function depends on time according to

$$\Psi(x, y, z, t) = \psi(x, y, z) e^{-iEt/\hbar}, \tag{2.22}$$

whereas the probability density from Eq. (2.2) does not:

$$|\Psi(x, y, z, t)|^2 = \Psi^* \Psi = \psi^* e^{+iEt/\hbar} \psi e^{-iEt/\hbar} = \psi^* \psi. \tag{2.23}$$

thus the expectation value for position (Eq. (2.6)) is constant (and so $\langle p \rangle = 0$) meaning nothing will happen in a stationary state. Secondly, it implies that there are allowed states of definite total energy.

To solve Eq. (2.19) for a free electron in a crystal (or rather, a box with sides $L_x = L_y = L_z = L$), the crystal will be described by an infinite potential square well of length L in x, y and z so that

$$V = \begin{cases} 0 & \text{for } 0 \leq x, y, z \leq L, \text{ and} \\ \infty & \text{elsewhere.} \end{cases} \tag{2.24}$$

Outside the well $\psi = 0$, and for the case inside the well Eq. (2.19) becomes

$$-\frac{\hbar^2}{2m} \left[\frac{d^2}{dx^2} + \frac{d^2}{dy^2} + \frac{d^2}{dz^2} \right] \psi = E\psi \tag{2.25}$$

and so

$$\left[\frac{d^2}{dx^2} + \frac{d^2}{dy^2} + \frac{d^2}{dz^2} \right] \psi = -(k_x^2 + k_y^2 + k_z^2)\psi, \tag{2.26}$$

where

$$\sqrt{(k_x^2 + k_y^2 + k_z^2)} = k = \frac{\sqrt{2mE}}{\hbar}. \tag{2.27}$$

Here k is the wave vector. Eq. (2.26) represents a 3-dimensional simple harmonic oscillator; the solutions of the wavefunction are standing waves within the box. The general solution is thus

$$\psi = A\sin(k_x x)\sin(k_y y)\sin(k_z z) + B\cos(k_x x)\cos(k_y y)\cos(k_z z). \tag{2.28}$$

However, the continuity of $\psi(x,y,z)$ such that $\psi(0,0,0) = \psi(L,L,L)$ means that $B = 0$. This also means that $\sin kL = 0$ gives solutions for the wave vector to be

$$k_x^2 + k_y^2 + k_z^2 = k^2 = \frac{\pi^2 n^2}{L^2}, \tag{2.29}$$

where $n^2 = n_x^2 + n_y^2 + n_z^2$ are integers. Hence the solutions for energy are found to be

$$E = \frac{\hbar^2 k^2}{2m} = \frac{\pi^2 n^2 \hbar^2}{2mL^2}. \tag{2.30}$$

This is known as the *dispersion relation*. Using the normalization condition of Eq. (2.3) allows A to be determined as $A = \sqrt{8/L_x L_y L_z}$ and so the solutions are

$$\psi_n(x,y,z) = \sqrt{\frac{8}{L^3}}\sin\left(\frac{n_x\pi}{L}x\right)\sin\left(\frac{n_y\pi}{L}y\right)\sin\left(\frac{n_z\pi}{L}z\right). \tag{2.31}$$

The time-independent Schrödinger equation yields an infinite number of solutions, one for each integer n. The general solution for the wave function Ψ is therefore the sum of all these solutions:

$$\Psi(x,y,z,t) = \sum_{n=1}^{\infty} C_n \psi_n(x,y,z) e^{-iE_n t/\hbar}. \tag{2.32}$$

This generalized wave function only describes one electron: the next step is to consider two non-interacting electrons in the 'box' which behave completely independently. Let electron 1 be in a state $\psi_a(r)$ with $r^2 = x^2 + y^2 + z^2$, with electron 2 in a state $\psi_b(r)$. These wavefunctions are then combined in product because the probability distributions of each electron are independent (the probability of finding one electron in a given state and another electron in another state is the product of the two individual probabilities). $\psi(r_1, r_2)$ is therefore:

$$\psi(r_1, r_2) = \psi_a(r_1)\psi_b(r_2). \tag{2.33}$$

However, this assumes that it is known which electron is which. Electrons are identical, and so the wavefunctions must be combined in a way that does not require knowledge of which electron is in which state, so that the probability $|\psi(r_1, r_2)|^2$ remains unchanged upon exchanging electrons. The possible wavefunctions are therefore:

$$\psi_{\pm}(r_1, r_2) = A\left[\psi_a(r_1)\psi_b(r_2) \pm \psi_b(r_1)\psi_a(r_2)\right], \tag{2.34}$$

where ψ_+ is the symmetric state and ψ_- is the antisymmetric state (because upon exchange of electrons ($r_1 \leftrightarrow r_2$) the antisymmetric wavefunction changes sign:

$$\begin{aligned} \psi_+(r_1, r_2) &= \psi_+(r_2, r_1) \\ \psi_-(r_1, r_2) &= -\psi_-(r_2, r_1)). \end{aligned} \tag{2.35}$$

But this is not the complete picture: ψ is the orbital, or spatial, wavefunction, and electrons also have intrinsic angular momentum known as spin. The total wavfunction, Ψ_T, is obtained by multiplying the spatial wavefunction by the spin wavefunction, χ:

$$\Psi_T = \psi\chi. \tag{2.36}$$

Electrons have a spin $s = \frac{1}{2}$, so that the resultant spin, S, for two electrons becomes

$$S = s_1 \pm s_2 = 0, 1. \tag{2.37}$$

For $S = 1$ the spins of the two electrons are parallel, and for $S = 0$ the spins are antiparallel. The spin state of the electron can therefore be described by the spin angular momentum number, m_S, with $m_S = +\frac{1}{2}$ for the spin up state $\chi_\uparrow$, and $m_S = -\frac{1}{2}$ for the spin down state $\chi_\downarrow$.

There are therefore four possible spin states for the two electron system: $\uparrow\uparrow$, $\downarrow\downarrow$, $\uparrow\downarrow$ and $\downarrow\uparrow$. These states either give a resultant spin $S = 0$ or $S = 1$. The symmetrised spin wavefunction for the $S = 0$ state is antisymmetric upon the exchange of electrons and a singlet in that the spin wavefunction, χ_-, is

$$\chi_-(1, 2) = \frac{1}{\sqrt{2}}[\chi_\uparrow(1)\chi_\downarrow(2) - \chi_\uparrow(2)\chi_\downarrow(1)]. \tag{2.38}$$

The spin wavefunction for the state with resultant spin $S = 1$, χ_+, is symmetric and a triplet state. This is because for $S = 1$ there are three possible values for the total spin angular momentum number, M_S, of +1, 0 or -1:

$$\chi_+ = \begin{cases} \chi_\uparrow(1)\chi_\uparrow(2) & M_S = +1 \\ \frac{1}{\sqrt{2}}[\chi_\uparrow(1)\chi_\downarrow(2) + \chi_\uparrow(2)\chi_\downarrow(1)] & M_S = 0 \\ \chi_\downarrow(1)\chi_\downarrow(2) & M_S = -1 \end{cases}, \tag{2.39}$$

where the two electrons can either be both spin up or spin down, or one can be

spin up and one spin down.

The complete wavefunction combining spatial and spin wavefunctions (eq. (2.36)) for a many-particle state is antisymmetric under the exchange of any pair of identical fermions (electrons, protons and neutrons) and symmetric under the exchange of any pair of identical bosons (mesons, photons *etc.*) [37]. Therefore, for fermions, antisymmetric orbital wavefunctions combine with symmetric spin wavefunctions and *vice versa* so that the total wavefunction, Ψ_T^-, becomes:

$$\Psi_T^- = \psi_\pm \chi_\mp, \tag{2.40}$$

and for bosons:

$$\Psi_T^+ = \psi_\pm \chi_\pm. \tag{2.41}$$

In the case where two electrons have the same spin such that the spin wavefunction is symmetric (χ_+) and thus the orbital wavefunction is antisymmetric (ψ_-), the two electrons are forbidden from occupying the same state, because the two-electron wavefunction vanishes if $\psi_a = \psi_b$:

$$\psi_-(r_1, r_2) = A\left[\psi_a(r_1)\psi_a(r_2) - \psi_a(r_1)\psi_a(r_2)\right] = 0. \tag{2.42}$$

This is one form of the *Pauli Exclusion Principle*. However, for the symmetric spin wavefunction the two electrons can occupy the same energy eigenstate if one has spin down and the other spin up. In the case where two electrons have opposite spins and the spin wavefunction is antisymmetric (χ_-), the orbital wavefunction is symmetric (ψ_+) and so the electrons are allowed to occupy the same space at the same time.

In the case of an antisymmetric orbital wavefunction for the system, the Pauli Exclusion Principle states that there is a zero probability of two electrons occupying the same space at the same time. The repulsion between the electrons is therefore less than the ψ_+ state, and so ψ_- is a more stable state. This is a purely quantum mechanical phenomenon with no classical counterpart. The ψ_- energy eigenstate will therefore be reduced by a small stabilising *exchange term*, E_{12}^{ex}. For two electrons this is given by the integral

$$E_{12}^{ex} = \int\int dV_1 dV_2 \psi_a^*(r_1)\psi_b(r_1)\frac{e^2}{4\pi\epsilon_0 r_{12}}\psi_b^*(r_2)\psi_a(r_2), \tag{2.43}$$

where ϵ_0 is the permittivity of free space and e is the elementary electron charge. In the case of a symmetric orbital wavefunction, on the other hand, this exchange term is positive and destabilises the state. The energy eigenstate for two electrons

in a helium atom, for example, is therefore

$$E = E_a + E_b + E_{12}^c \pm E_{12}^{ex}, \tag{2.44}$$

where E_a and E_b are the energy eigenstates of the individual electrons, E_{12}^c is the classical Coulomb repulsion term between the two electrons, and E_{12}^{ex} is the exchange energy, positive for ψ_+ and negative for ψ_-. The exchange term leads to macroscopic effects including ferromagnetism, where atoms with partially-filled electron shells containing unpaired electrons have a magnetic dipole moment. When these unpaired electrons align with the same spin, the electrostatic field between atoms is reduced by the exchange energy as they move further apart. This spin alignment leads to the addition of the atomic dipole moments that creates a macroscopic magnetic field.

A useful quantity that links the description of elementary particles, with mass and momentum, with their wave properties is the de Broglie wavelength:

$$\lambda_B = h/p, \tag{2.45}$$

where h is the Planck constant. For an isolated hydrogen atom with one electron, the electron can only interact with (and is bound to) the positive nucleus under a Coulomb attraction with the potential

$$V(r) = -\frac{1}{4\pi\epsilon_0}\frac{e^2}{r}. \tag{2.46}$$

In a crystal, however, with N atoms, electrons will also interact with other nuclei and electrons because the interatomic separation, r, is less than the de Broglie wavelength of the electron, and thus the wavefunctions of the electrons overlap. The relatively straightforward potential for the hydrogen atom in Eq. (2.46) will thus become complex and periodic. This leads to the formation of a band of energy levels whose spacing is as low as $\approx 10^{-19}$ eV which are considered continuous [38]. This is illustrated in figure (2.1), the dependence of the energy levels on interatomic separation being governed by the Coulomb potential.

A crystal structure can be described by a periodic potential with periods at the lattice constants in three dimensions, a, b and c. To begin with a one-dimensional system with an array of N atoms along the x-direction, the potential does not change between a point x and a point $x + na$ separated by an integer multiple of the lattice constant:

$$V(x + na) = V(x) \quad (n = 0, 1, 2, 3, \ldots). \tag{2.47}$$

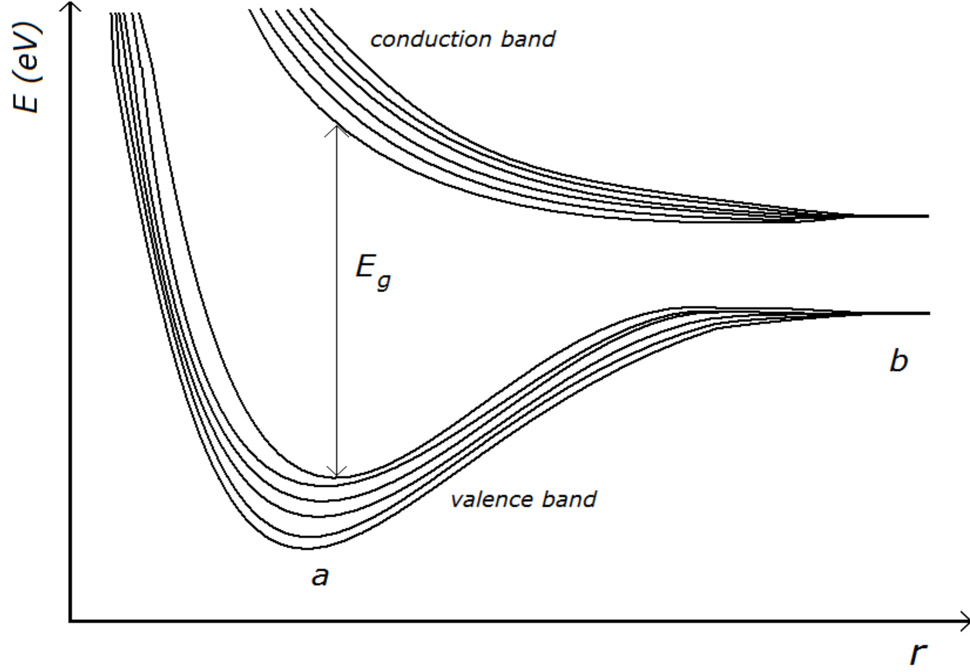

Figure 2.1: Splitting of atomic levels with interatomic separation (r), adapted from [39]. Label a illustrates the interatomic separation in a crystal, whereas b shows where the interatomic separation has become large enough for the electrons in each nucleus to cease interacting with other nuclei (the interatomic separation is larger than the de Broglie wavelength of the electron). The minimum of the valence band occurs at the equilibrium lattice spacing of the crystal.

The Hamiltonian for an electron in this periodic potential is also invariant under $x \rightarrow x + na$ [37]:

$$\hat{H} = -\frac{\hbar^2}{2m}\frac{d^2}{dx^2} + V(x) = -\frac{\hbar^2}{2m}\frac{d^2}{d(x+na)^2} + V(x+na). \tag{2.48}$$

The periodicity and translational symmetry of the Hamiltonian means that the probability distribution, $|\psi(x)|^2$, for an electron in an energy eigenstate should also have this symmetry:

$$|\psi(x+na)|^2 = |\psi(x)|^2 \quad (n = 0, 1, 2, 3, \ldots). \tag{2.49}$$

Therefore the eigenfunction itself must be periodic. Bloch's theorem states that a simultaneous eigenfunction must be of the form

$$\psi_k(x) = e^{ikx}u_k(x), \quad \text{where} \quad u_k(x+a) = u_k(x), \tag{2.50}$$

where $u_k(x)$ again has the same periodicity of the crystal lattice and

$$k = \frac{2\pi n}{Na}, \tag{2.51}$$

where $n = 0, \pm 1, \pm 2, \ldots, \pm\frac{1}{2}N$ for an even number of units cells N (atoms). The important change that has occurred from the free electron model to electrons occupying a periodic potential is that the Bloch electron wavefunctions are now travelling, as opposed to standing, wavefunctions. The fact that these travelling wavefunctions allow propagation of electrons through the lattice means that this model is known as the *nearly free* electron model. Eq. (2.51) also shows that values of k are continuous because $\frac{n}{N} \ll 1$ due to N being large. Energy eigenfunctions for the system are therefore continuous over the range $-\frac{\pi}{a} \leq k \leq \frac{\pi}{a}$ for $n = \pm\frac{1}{2}N$, known as the first Brillouin zone.

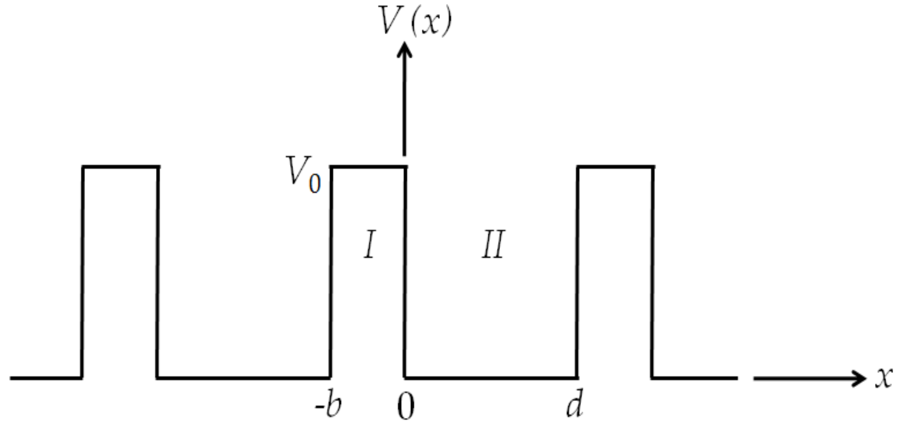

Figure 2.2: The Kronnig-Penney potential for a periodic potential present in a one-dimensional array of atoms. Labelled are two regions, I and II.

Solving the Schrödinger equation for Bloch wavefunctions in a periodic potential is not straightforward. Kronig and Penney solved the problem using an approximation whereby the potential $V(x)$ is a periodic square-well potential of width b and height V_0 repeated at each lattice constant a as shown in figure (2.2). The potential is thus V_0 for the region $-b < x < 0$ (I) and 0 for the region $0 < x < d$ (II), where V_0 is much larger than the energy of the electrons and the lattice constant is $a = b + d$. The Schrödinger equations for these two regions therefore become [40]:

$$\frac{d^2\psi_I(x)}{dx^2} + \frac{2m}{\hbar^2}(E - V_0)\psi_I(x) = 0 \quad \text{for} \quad -b < x < 0, \quad \text{and} \tag{2.52a}$$

$$\frac{d^2\psi_{II}(x)}{dx^2} + \frac{2m}{\hbar^2}E\psi_{II}(x) = 0 \quad \text{for} \quad 0 < x < d. \tag{2.52b}$$

To simplify the mathematics two quantities, α and β, are defined as

$$\alpha^2 = \frac{2mE}{\hbar^2}, \quad \text{and} \quad \beta^2 = \frac{2m(V_0 - E)}{\hbar^2}. \tag{2.53}$$

Assuming that the solutions for the Schrödinger equations in eq. (2.52) are Bloch functions such that $\psi_I(x) = e^{ikx}u_I(x)$ *etc.* gives

$$\frac{d^2u_I(x)}{dx^2} + 2ik\frac{du_I(x)}{dx} + (\beta^2 + k^2)u_I(x) = 0, \quad \text{and} \tag{2.54a}$$

$$\frac{d^2u_{II}(x)}{dx^2} + 2ik\frac{du_{II}(x)}{dx} + (\alpha^2 - k^2)u_{II}(x) = 0. \tag{2.54b}$$

The solutions of these equations are

$$u_I(x) = Ae^{(\beta - ik)x} + Be^{-(\beta + ik)x}, \quad \text{and} \tag{2.55a}$$

$$u_{II}(x) = Ce^{i(\alpha - k)x} + De^{-i(\alpha + k)x}, \tag{2.55b}$$

where A, B, C and D are constants. Boundary conditions are now applied in that $u_I(x)$, $u_{II}(x)$ and the first derivatives of $u_I(x)$ and $u_{II}(x)$ must be continuous at the discontinuity of the potential, *i.e.* at $x = 0$:

$$u_I(0) = u_{II}(0), \quad \text{and} \quad \left.\frac{du_I(x)}{dx}\right|_{x=0} = \left.\frac{du_{II}(x)}{dx}\right|_{x=0}. \tag{2.56}$$

Applying these conditions to equations (2.55) gives

$$A + B = C + D, \quad \text{and} \tag{2.57a}$$

$$\beta A - \beta B = i\alpha C - i\alpha D. \tag{2.57b}$$

Because Bloch's theorem states $u(x) = u(x + a)$, the solutions of equations (2.55) and the derivatives of equations (2.55) must be periodic in that

$$u_I(-b) = u_{II}(d) \quad \text{and} \quad \left.\frac{du_I(x)}{dx}\right|_{x=-b} = \left.\frac{du_{II}(x)}{dx}\right|_{x=d}. \tag{2.58}$$

Applying these conditions to equations (2.55) now gives

$$Ae^{-(\beta - ik)b} + Be^{(\beta + ik)b} = Ce^{i(\alpha - k)d} + De^{-i(\alpha + k)d}, \quad \text{and} \tag{2.59a}$$

$$\begin{aligned}(\beta - ik)Ae^{-(\beta - ik)b} &- (\beta + ik)Be^{(\beta + ik)b} \\ &= i(\alpha - k)Ce^{i(\alpha - k)d} - i(\alpha + k)De^{-i(\alpha + k)d}.\end{aligned} \tag{2.59b}$$

In order for there to be nontrivial solutions to the equations (2.57) and (2.59) for A, B, C and D, the determinant of the coefficients of these equations must equal zero. It can be shown that [41]:

$$\frac{\beta^2 - \alpha^2}{2\alpha\beta}\sinh(\beta b)\sin(\alpha d) + \cosh(\beta b)\cos(\alpha d) = \cos k(d + b). \tag{2.60}$$

A simplification of this condition is obtained by considering the case of the potential barriers being delta functions, so that $V_0 \to \infty$ and $b \to 0$ (and so $d \to a$, the lattice constant) but $V_0 b$ remains finite. This gives [42]:

$$\cos ka = P\frac{\sin \alpha a}{\alpha a} + \cos \alpha a, \tag{2.61}$$

with

$$\alpha = \frac{\sqrt{2mE}}{\hbar} \quad \text{and} \quad P = \frac{mV_0 ba}{\hbar^2}. \tag{2.62}$$

Equation (2.61) gives an approximate dependence of energy (R.H.S.) on momentum (L.H.S.). Values for the R.H.S. expression for the case of $P = 2\pi$ are shown in figure (2.3). The figure also contains shaded regions where the R.H.S. yields values between 1 and -1, which are the only values accepted by the cosine at the L.H.S.. This means that there are regions of allowed and forbidden αa, or regions of allowed and forbidden energies. Thus the periodicity of the lattice potential has led to bands of allowed energies as well as energy band gaps for electrons travelling through the lattice.

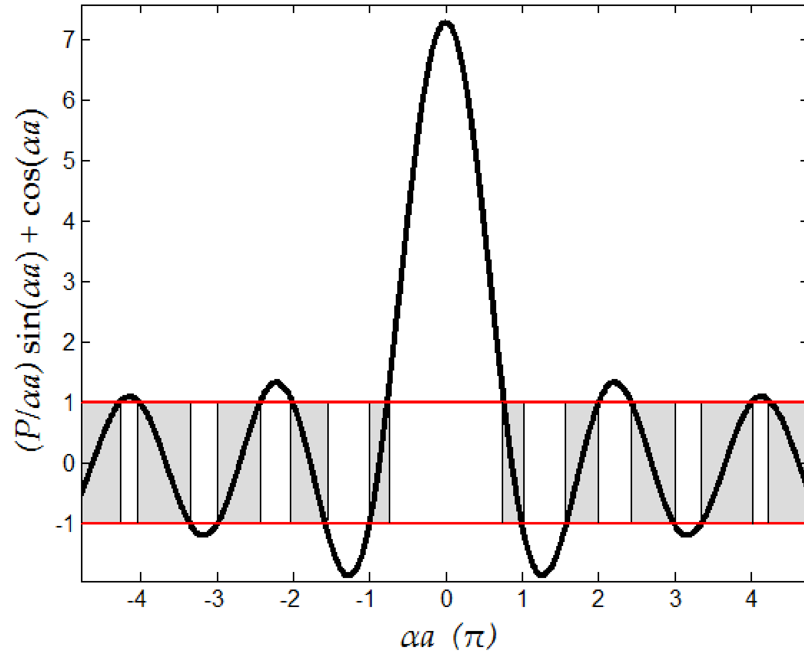

Figure 2.3: The Kronig-Penney condition of eq. (2.61) for $P = 2\pi$. The y-axis is the R.H.S. of the equation. The condition is only valid for the case when the R.H.S. yields values between 1 and -1 so as to equal the L.H.S. ($\cos ka$), as illustrated by the shaded regions. These represent the allowed energy bands, whereas the unshaded regions represent energy band gaps.

The Kronig-Penney solution shows that the width of the allowed energy bands increases with energy (αa) due to the $(P/\alpha a)$ term in eq. (2.61). The width of the allowed energy bands decreases with increasing P, which is a measure of how

tightly bound electrons are to a particular potential well. For higher values of P, the probability of electrons crossing the potential well (tunneling) reduces. Should $P \rightarrow \infty$ the allowed regions are reduced to line spectra (infinitely narrow). Solutions are now only valid if $\sin(\alpha a) = 0$, or $\alpha a = \pm n\pi \quad (n = 1, 2, 3, \ldots)$. Substitution into eq. (2.62) thus yields the energy levels of the free electron contained in a box as expected in this limit.

Figure (2.3) also shows that the ends of an allowed energy band occur at $\alpha a = n\pi$, *i.e.* at $k = n\pi/a$, or at each Brillouin zone boundary, in the dispersion $(E - k)$ diagram. The dispersion diagram for the solution of the Kronig-Penney condition compared to the free electron model is shown in figure (2.4). At each Brillouin zone boundary, illustrated by dashed vertical lines, a gap in energy occurs. Figure (2.5) shows how this is plotted in the reduced-zone diagram, in that all energy dispersions are plotted in the first Brillouin zone between $-\frac{\pi}{a} < k < +\frac{\pi}{a}$. There is no difference in the physical information contained in these figures since there is no physical significance in the choice of Brillouin zone [37].

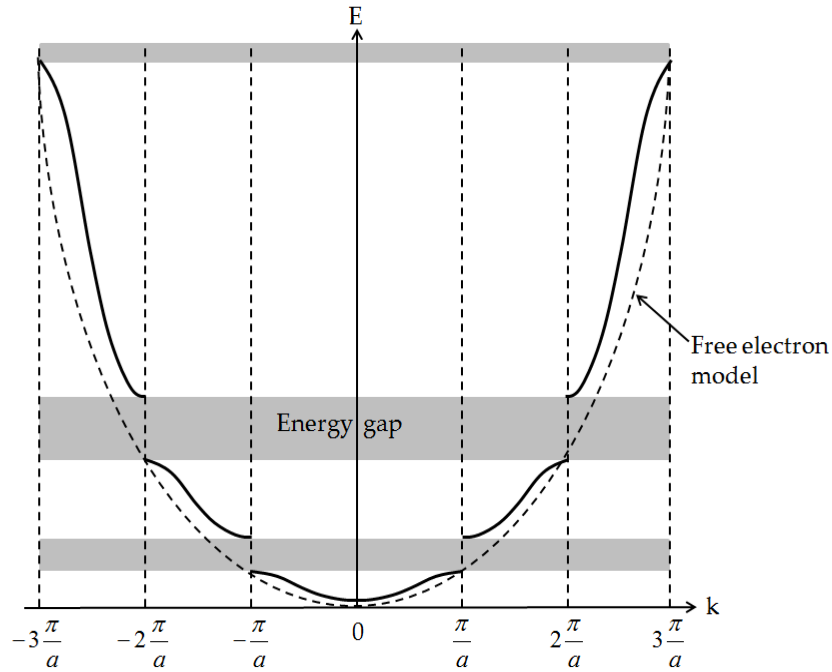

Figure 2.4: Dispersion diagram for electrons in a periodic potential compared to the free electron model (dashed curve). The periodic potential of the lattice leads to regions of forbidden energy at the Brillouin zone edges, or band gaps, illustrated with shaded regions.

The creation of the band gap can also be understood in terms of Bragg diffraction occurring at the Brillouin zone edges [42]. The periodicity of the lattice potential means that the wavefunctions of electrons are standing waves at $k = n\pi/a$, with the incident and reflected wavefunctions either being in or out of phase with each other. For a one-dimensional periodic potential, $V(x)$, with a periodicity of

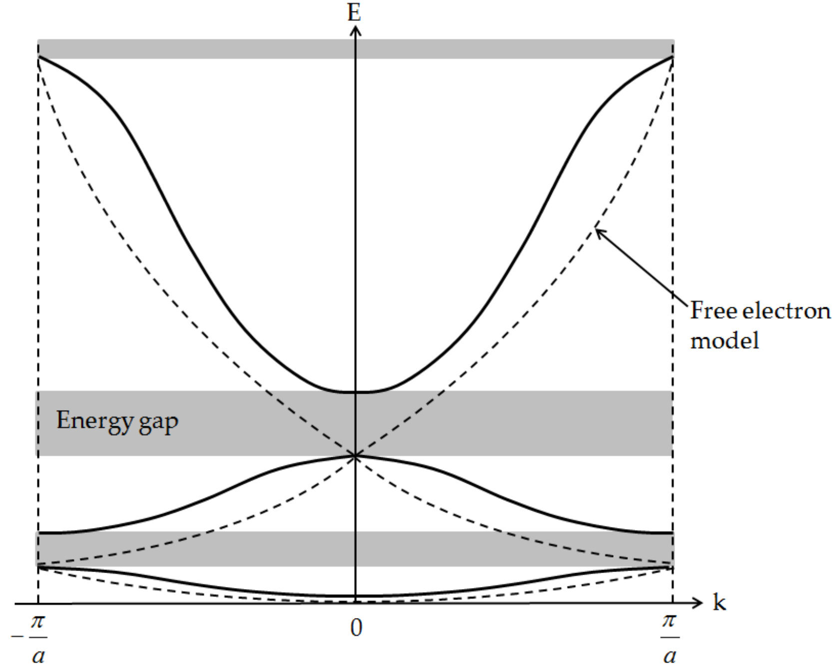

Figure 2.5: Dispersion diagram for electrons in a periodic potential compared to the free electron model of figure (2.4) over the reduced Brillouin zone.

the lattice constant a, the combined wavefunction for in-phase incident and reflected wavefunction, ψ_{in}, is

$$\psi_{in} = e^{ikx} + e^{-ikx} = 2\cos\frac{\pi x}{a}, \tag{2.63}$$

whereas the out-of-phase case, ψ_{out}, is

$$\psi_{out} = e^{ikx} - e^{-ikx} = -2i\sin\frac{\pi x}{a}. \tag{2.64}$$

ψ_{in} and ψ_{out} therefore have different probability density functions with different energy eigenvalues. Two possible energies are thus possible at $k = n\pi/a$, the difference between which is the band gap, and is due to the difference in potential energies of the two wavefunctions. The potential energy for the in-phase state, V_{in}, for $n = 1$ is given by

$$V_{in} = \int_0^a \frac{\cos(2\pi x/a)V(x)}{a}dx, \tag{2.65}$$

and the out of the phase state potential is $V_{out} = -V_{in}$, and so the band gap energy is $E_g = 2V_{in}$.

The occupancy of electrons in the available energy bands of a material, as well as the size of the band gaps, dramatically change the external, or macroscopic, properties of the material. Electron pairs (one spin up, one spin down) fill the available energy levels according to the Pauli Exclusion Principle from the lowest

energy upwards. For the case when the highest occupied energy band (the valence band) is almost completely filled, and the energy gap between this energy band and the lowest unoccupied energy band (the conduction band) is large, the material is an insulator. Little conductivity will occur in the presence of an electric field because there are very few unoccupied energy levels available in the valence band, and electrons cannot be promoted across the band gap thermally (*i.e.* at room temperature). If the band gap energy between an almost completely filled valence band and the conduction band is relatively small (typically a few eV), electrons can be promoted across the band gap for $T > 0$ K and can thus conduct in the presence of an electric field: in this case the material is an intrinsic semiconductor [43]. When the highest energy band is partially filled, the material is a metal in that there are many energy states available for electronic conduction in the presence of an electric field. The highest occupied and lowest unoccupied energy bands may also overlap to the same end.

The energy of the highest occupied quantum state for fermions at $T = 0$ K is called the Fermi energy. For a system of N electrons in a box with sides $L_x = L_y = L_z = L$, described by the quantum numbers n_x, n_y and n_z, the energy eigenvalues are described by the dispersion relation of eq. (2.30). The number of states with energy less than the Fermi energy, N, is therefore the number of states that lie within a sphere of radius $n_F = (n_x, n_y, n_z)$ in the region where n_x, n_y and n_z are positive:

$$N = 2 \times \frac{1}{8} \times \frac{4}{3}\pi n_F^3, \tag{2.66}$$

where the factor of 2 is due to two spin states (spin up and spin down) occupying one energy state, and the factor of an eighth is due to one eighth of the sphere having all positive values of n. The Fermi energy is therefore given by

$$E_F = \frac{\hbar^2\pi^2}{2mL^2}n_F^2 = \frac{\hbar^2\pi^2}{2mL^2}\left(\frac{3N}{\pi}\right)^{\frac{2}{3}}, \tag{2.67}$$

which leads to a definition of the Fermi energy in terms of the number of particles per volume V by substitution of L^2 with $V^{2/3}$:

$$E_F = \frac{\hbar^2}{2m}\left(\frac{3\pi^2 N}{V}\right)^{\frac{2}{3}}. \tag{2.68}$$

The total energy within the Fermi sphere is

$$E_{tot} = \int_0^N E_F dN = \frac{3}{5}NE_F. \tag{2.69}$$

It turns out that the approximation of eq. (2.68) is very good for electrons in a

metal.

To understand how electronic states within a solid are distributed, the density of states function, $Z(E)$, must be derived. The volume of a single quantum state in k-space can be obtained from Eq. (2.29):

$$k = \frac{2\pi}{L}, \tag{2.70}$$

which is the unit wave vector for $n = 1$ and thus

$$V_k = k^3 = \left(\frac{2\pi}{L}\right)^3 \tag{2.71}$$

is the unit volume in k-space. A differential density of quantum states, $g(k)dk$, can now be calculated using a differential volume in k-space (the volume of an annulus between k and $k + dk$, $4\pi k^2 dk$):

$$g(k)dk = 2\frac{4\pi k^2 dk}{V_k} = \frac{k^2 L^3}{\pi^2}dk. \tag{2.72}$$

Here, a factor of 2 is introduced due to the two allowed spin states for each energy state ($m_S = \pm 1/2$). The dispersion relation in Eq. (2.30) allows the differential dk to be obtained:

$$dk = \frac{1}{\hbar}\sqrt{\frac{m}{2E}}dE. \tag{2.73}$$

Substituting this, and an expression for k^2 also from Eq. (2.30), into Eq. (2.72) allows the density of quantum states per unit energy per unit volume to be determined:

$$g(E)dE = \frac{2mE}{\hbar^2}\frac{L^3}{\pi^2}\frac{1}{\hbar}\sqrt{\frac{m}{2E}}dE, \quad \text{giving} \tag{2.74}$$

$$Z(E) = \frac{g(E)}{L^3} = \frac{4\pi(2m^*)^{\frac{3}{2}}}{\hbar^3}\sqrt{E}. \tag{2.75}$$

Here, m^* is the *effective mass* of the electron. This differs from the rest mass of the electron, m_e, due to the interaction of the electron with the periodic potential of the atoms, and will vary from material to material, depending on crystal geometry and atomic composition. The use of an effective mass (for example, $m^* = 0.067m_e$ in GaAs [44]) allows the quantum mechanics of a free electron to still be utilized (*i.e.* it is assumed that the motion of the electron is unperturbed by the lattice). The effective mass of an electron therefore depends on the dispersion relation for

a particular material, using (eq. (2.30)), as:

$$m^* = \hbar^2 \left(\frac{d^2E}{dk^2}\right)^{-1}, \tag{2.76}$$

and thus the effective mass is inversely proportional to the curvature of the $E - k$ dispersion curve.

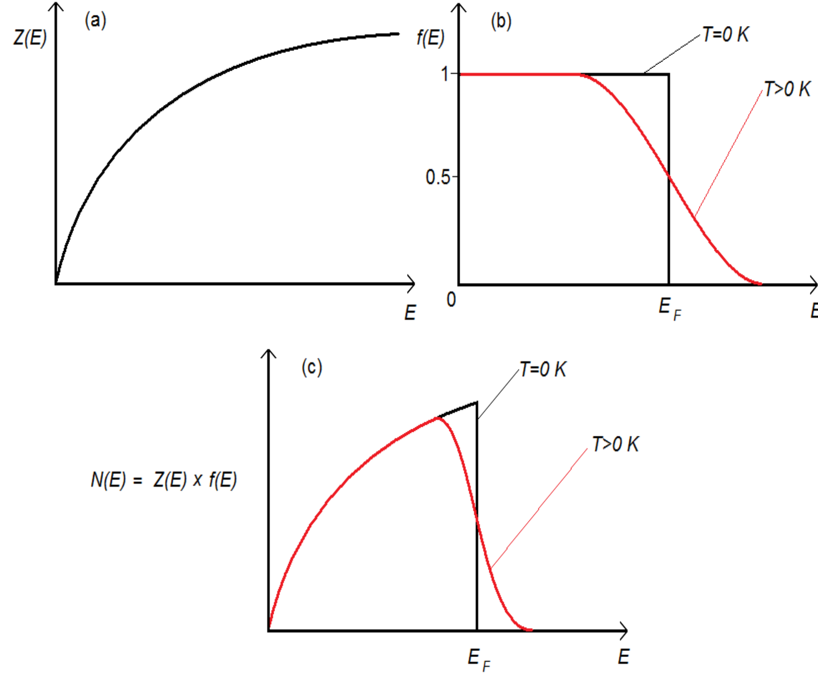

Figure 2.6: Obtaining the density of populated states, (c), from the density of states, (a), and Fermi-Dirac function, (b), adapted from [45]. The fact that the Fermi energy does not occur at the highest energy state for $T > 0K$ gives rise to conduction.

The density of quantum states can be used to determine the density of electrons within a crystal. Once the density of states is known, the probability of an electron being in such a quantum state is also required, and is described by the Fermi-Dirac function:

$$f(E) = \frac{1}{\exp\frac{(E-E_F)}{k_B T} + 1}, \tag{2.77}$$

where E_F is the Fermi energy, k_B the Boltzmann constant, and T the temperature. The probability of an electron occupying a state with energy E_F is 0.5, and the function is symmetrical about E_F [45].

Finally, to calculate the density of occupied electron states, $N(E)$, the density of states is multiplied by the probability of these states being occupied:

$$N(E) = Z(E)f(E), \tag{2.78}$$

and the total number of electrons is given by

$$N = \int_0^\infty Z(E)f(E)dE. \tag{2.79}$$

These functions are illustrated in figure (2.6). The fact that highest energy state is at a higher energy than the Fermi energy for $T > 0K$ allows for conduction in a metal because states with energies close to E_F are partially occupied.

2.2 Semiconductors

The interaction of electrons with a periodic lattice has been shown to create allowed bands of energy and energy band gaps, as shown by the Kronig-Penney model for a one-dimensional array of atoms. In reality, for a 3-dimensional solid, the dispersion diagram or band structure (typically plotted over the reduced Brillouin zone) of a material is complex.

A simple dispersion diagram for a semiconductor is shown in figure (2.7), where the highest occupied energy band (the valence band) and the lowest unoccupied energy band (the conduction band) are shown separated by the band gap energy, E_g. The fact that the maximum of the valence band and the minimum of the conduction band occur at the same position in momentum space makes the semiconductor illustrated in figure (2.7) a direct band gap semiconductor. This means electrons in the valence band can make a direct transition to the conduction band with the absorption of a photon whose energy is greater than or equal to the band gap:

$$h\nu \geq E_g. \tag{2.80}$$

Transitions purely involving the absorption of a photon can occur as long as the photon has sufficient energy. The transition for $h\nu = E_g$ can only occur at $k = 0$. When an electron is excited into the conduction band, the fact that the valence band is otherwise full with negatively charged electrons means that a positively charged quasi-particle called a *hole* is produced in place of the electron, with a charge of $+e$. An electron and hole are bound in an analogy of the hydrogen atom with Coulomb attraction, and this electron-hole pair is called an *exciton*.

The different curvatures (d^2E/dk^2) of the valence and conduction bands in figure (2.7) reflect the differences in the effective masses of the charge carriers in the valence and conduction bands according to equation (2.76), as well as how the effective masses can therefore vary within a particular energy band. The gradient

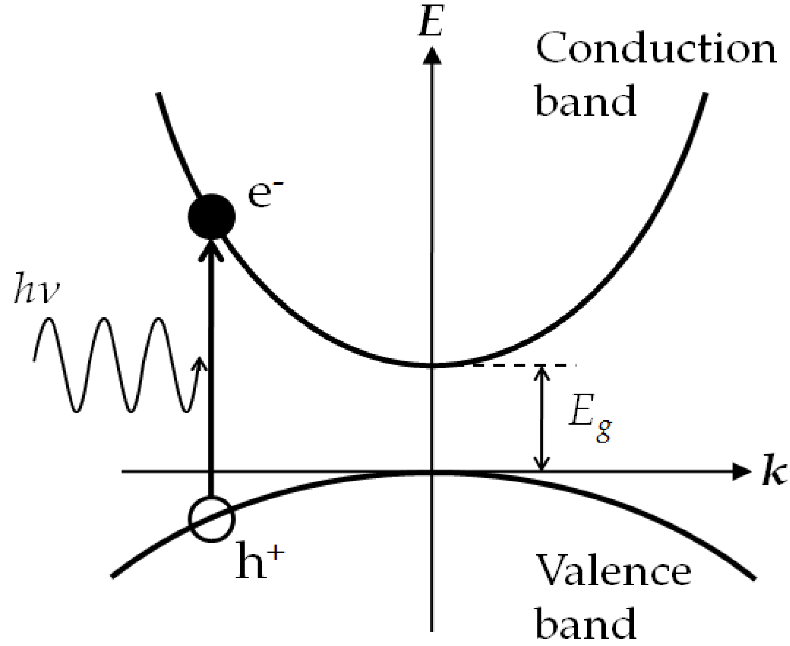

Figure 2.7: Dispersion diagram illustrating the transition of an electron from the valence band to the conduction band after the absorption of a photon whose energy $h\nu \geq E_g$. The transition is vertical in momentum space.

of the $E - k$ curve gives the group velocity of the electrons:

$$v_g = \frac{1}{\hbar}\frac{dE}{dk} = \frac{d\omega}{dk} \tag{2.81}$$

due to $E = \hbar\omega$, and so the electrons in the valence band shown in figure (2.7) are more closely bound to the atomic lattice [43]. This is intuitive since it is the partially unoccupied conduction band that allows for the transport of charge carriers.

Some semiconductors have an indirect band gap: due to many factors including the variation of interatomic separation in different directions and cumulative interactions with neighbouring atoms, the minimum energy of the conduction band, and likewise the maximum energy of the valence band, may not occur at $k_x = k_y = k_z = 0$. Moreover, conduction bands (or the shape of a constant energy surface) may have several minima, and valence bands may have several maxima. This means that some semiconductors can have both a direct and an indirect band gap.

In order for an electron to become excited into the conduction band in an indirect band gap semiconductor, excitation cannot occur by the absorption of photons alone. In this case, transfer of momentum occurs due to *phonons*, which are quantized vibrational modes of a crystal lattice, as shown in figure (2.8). At non-zero temperatures, phonon modes are significantly populated and are a cause of heat conduction. The absorption of a phonon simultaneously with electronic excitation

leads to a change in momentum which will then allow for an electronic transition to occur [38].

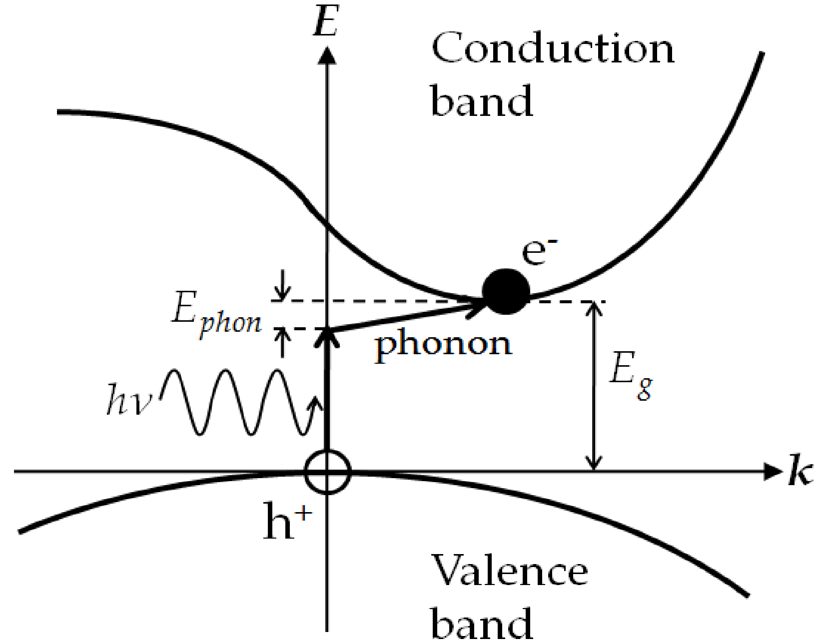

Figure 2.8: Excitation across an indirect band gap occurs with the absorption of both a photon and a phonon, a quantized vibrational mode of the lattice, which transfers momentum, k, to the electron. Phonons have a small amount of energy, E_{phon}, typically 10 to 100 meV.

Electrons possess both spin (or intrinsic) angular momentum and orbital angular momentum. Orbital angular momentum is described by the quantum number l which can have integer values as well as $l = 0$. Each orbital angular momentum state gives rise to different electron orbitals (or *shells*) around the nucleus: $l = 0$ is for the s-orbital; $l = 1$ the p-orbital and so on. The interaction of orbital angular momentum and spin angular momentum leads to the splitting of the valence band. The total angular momentum is given by

$$\vec{J} = \vec{L} + \vec{S} \tag{2.82}$$

and thus the interaction of the orbital and spin angular momenta becomes:

$$\vec{L}.\vec{S} = \frac{1}{2}(\vec{J}^2 - \vec{L}^2 - \vec{S}^2). \tag{2.83}$$

The valence band orbitals are typically p-orbitals with $l = 1$, and so a hole in this band can have total angular momentum of $J = 1/2$ and $J = 3/2$ for spin down and spin up respectively. Other effects including lattice crystal field splitting and the anisotropic nature of p-orbitals gives rise to two $J = 3/2$ states that are

degenerate at $k = 0$, as shown in figure (2.9). These two states are named the heavy-hole and light-hole bands, because of the difference in the effective masses (and hence different curvatures because $d^2E/dk^2 \propto 1/m^*$ in eq. (2.76)) of holes in these bands [43]. The holes in these bands also have different group velocities due to eq. (2.81).

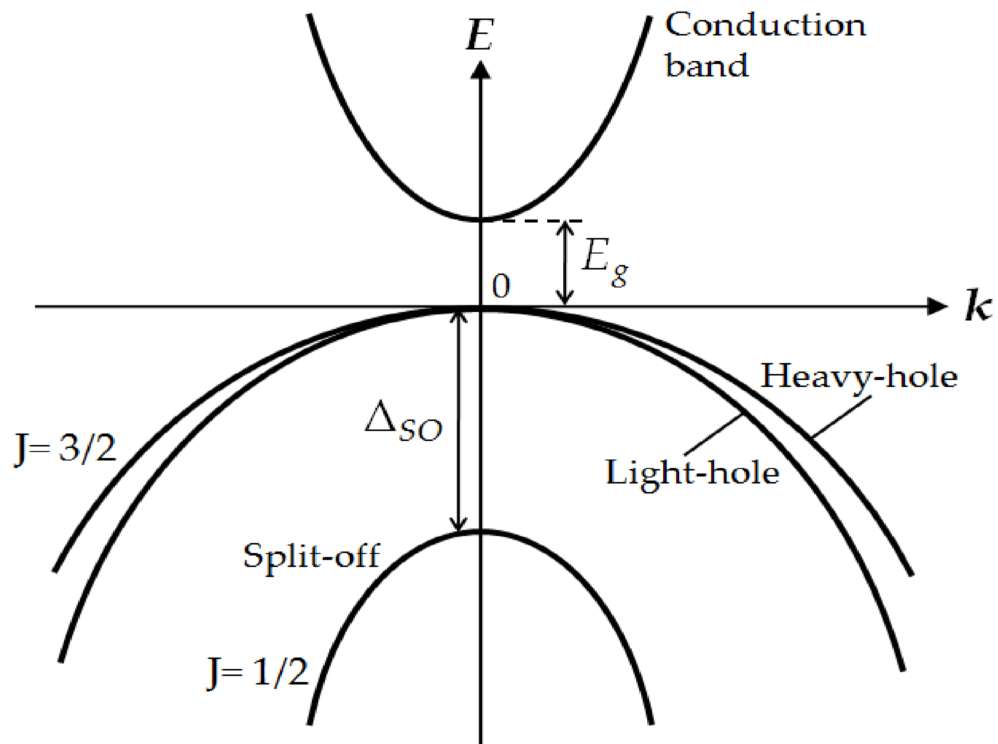

Figure 2.9: The degenerate valence band: spin orbit coupling causes a split-off band an energy Δ_{SO} below the main valence band, and the anisotropic nature of the valence band p-orbitals creates bands with different curvatures, and thus different effective masses, called the heavy-hole and light-hole bands.

The properties of a semiconductor, such as its electrical conductivity, can be controlled by the introduction of impurity states, or *doping*, into the crystal. Donor and acceptor states (just below the conduction band, and just above the valence band, respectively) can be created by adding impurities with extra, or too few, valence electrons. Donor states occur when an impurity with "spare" valence electrons is introduced into the crystal. These spare electron(s) are free to move in the Coulomb field of the impurity atom. Therefore the extra electron has a relatively small ionization energy (usually much less than an electron-volt), and the dopant is therefore said to 'donate' electrons to the conduction band. An acceptor impurity has too few valence electrons, and thus 'accepts' an electron from the valence band in order to bond successfully in the crystal lattice. It therefore leaves a hole in the otherwise filled valence band as illustrated in figure (2.10). The shift

in the Fermi energy towards to the conduction band minumum in the presence of donor states leads to a partially filled conduction band for $T > 0$ K, such that $k_BT \gg E_D$, where E_D is the donor ionization energy (the difference in energy between the donor energy state and the conduction band minimum). The shift in the Fermi energy towards the valence band in the presence of acceptor states leads to a partially filled valence band for $T > O$ K [46].

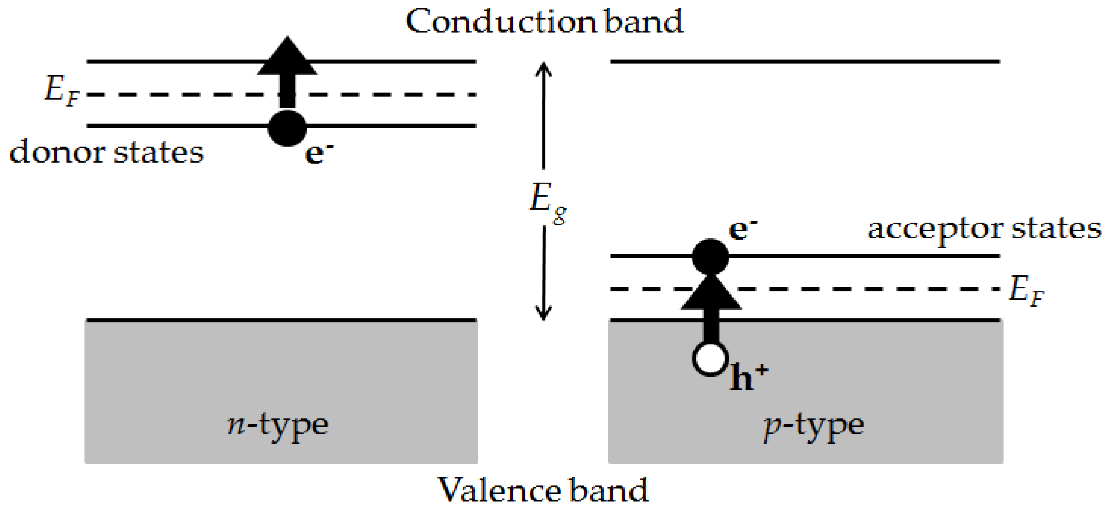

Figure 2.10: Impurities causing donor and acceptor states in an intrinsic semiconductor, adapted from [39]. Donors can donate an electron to the conduction band; acceptors can accept an electron from the valence band and hence create a positively charged hole in the valence band. Acceptor and donor states increase the probability of electrons occupying states closer to the valence and conduction bands respectively, and so the Fermi level E_F, illustrated with a dashed line, shifts from the middle of the band gap.

The ionization energy of a donor state is dependent on the effective mass of the electron and the relative permittivity, ϵ_r, of the semiconductor:

$$E_D = 13.6\frac{m^*}{m_e}\left(\frac{1}{\epsilon_r^2}\right). \tag{2.84}$$

Typical donor ionization energies are of the order of several meV. Semiconductors with donor states present are n-type, and those with acceptor levels are p-type semiconductors. This is because in an n-type semiconductor the majority charge carrier is negatively charged (*i.e.* electrons) whereas for p-type semiconductors the majority carrier is positively charged (*i.e.* holes). A typical photovoltaic is constructed using an n-type and a p-type semiconductor together so as to transport electrons to an anode through an n-type material and to transport holes to a cathode through a p-type material. Therefore a current is generated, as will be discussed in §2.5.

2.3 Excitons

Absorption of a photon with energy greater than, or equal to, the band gap energy, $h\nu \geq E_g$, will photoexcite an electron across the band gap into the conduction band, creating a positively charged hole in the valence band. A bound electron-hole pair, analogous to the hydrogen atom, is called an exciton. Free excitons have a binding energy given by

$$E_B = \frac{\mu e^4}{2n^2 \left(4\pi\epsilon_r\epsilon_0\hbar\right)^2}, \tag{2.85}$$

where $n = 1$ for the ground state of the exciton, μ is the reduced mass of the exciton ($1/\mu = 1/m_e^* + 1/m_h^*$), ϵ_r the relative permittivity of the semiconductor, ϵ_0 the permittivity of free space, and e the elementary electron charge. Due to the effective masses of the electron and hole, m_e^* and m_h^*, being significantly less than their respective rest masses, and the difference between the permittivity of the semiconductor compared to that of vacuum, the exciton binding energy is significantly less than the Rydberg energy of atomic hydrogen. Instead of 13.6 eV, the excitonic Rydberg energy is typically a few to one hundred meV [47]. This energy range falls in the terahertz region of the electromagnetic spectrum.

The excitonic binding energy reduces the required energy of a photon, $h\nu$, to create an exciton:

$$h\nu = E_g - E_B. \tag{2.86}$$

This energy is further reduced should the electron be bound to a donor state (or, likewise, a hole bound to an acceptor state) so that $h\nu = E_g - E_B - E_D$, where E_D is the donor state binding energy for an n-type semiconductor. In a p-type semiconductor the exciton binding energy will be reduced by the acceptor state binding energy E_A.

The dispersion curve for an exciton is given by:

$$E_{ex} = \frac{n\hbar^2}{2\mu}K^2, \tag{2.87}$$

where K is the exciton wavevector, $K = k_e + k_h$, and $n = 1, 2, 3\cdot$ because excited states ($n > 1$) are also present. The dispersion diagram is shown in figure (2.11), where a transition can only occur from $K = 0$, due to conservation of energy and momentum. Likewise, recombination of the exciton can only occur at $K = 0$.

Measuring the spectrum of absorption (α) in semiconductors can determine the exciton binding energies: the spectrum will essentially give the joint density of states for free electrons and holes, as the semiconductor is excited with

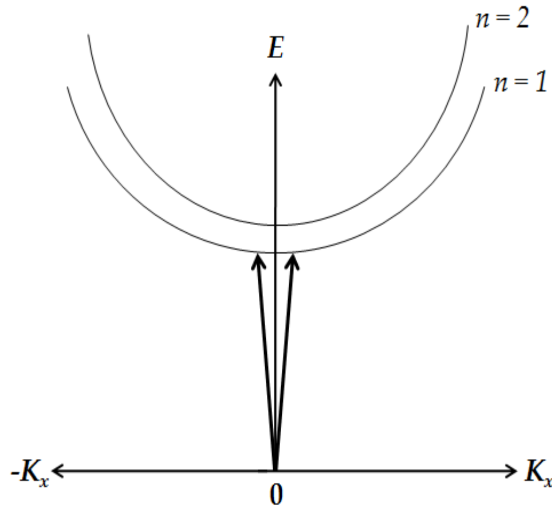

Figure 2.11: Dispersion diagram of free exciton states according to eq. (2.87). Conservation of energy and momentum means that the transition can only occur at $K = 0$, where the slight diagonal of the transitions is due to photons possessing a small amount of momentum.

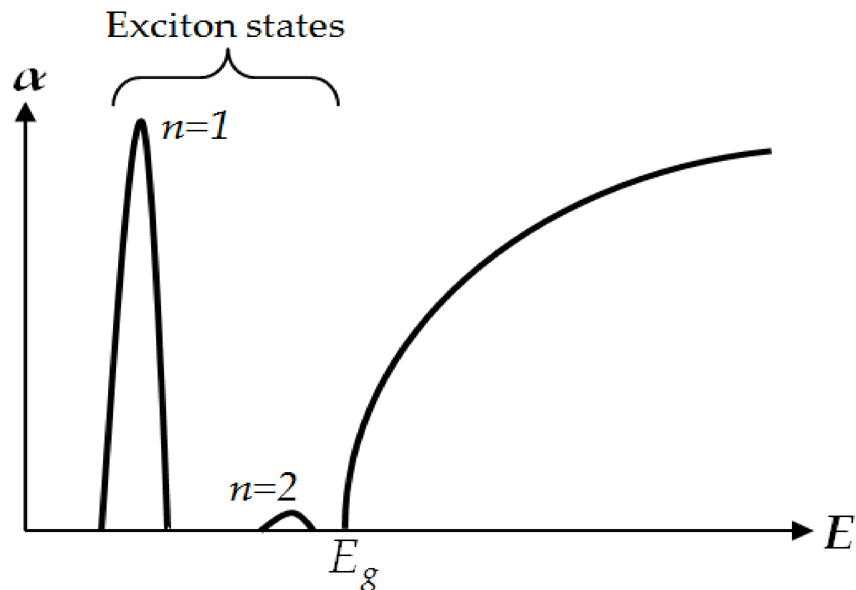

Figure 2.12: Absorption spectrum for a bulk direct band gap semiconductor, with free exciton states at energies $h\nu < E_g$. The excited states of the exciton can also be observed. The absorption above the band-gap energy illustrates the dependence of the density of states on $E^{1/2}$ for a bulk crystal. This form of spectroscopy is a powerful tool in understanding the formation of excitons in semiconductors [45].

photons with an energy greater than the band-gap. However, exciton states will be observed at energies below the band-gap energy: moreover, the energy band structure of excitons can be observed, as excited states ($n > 1$) are also present.

The spatial separation between electron and hole is given by the Bohr exciton

radius, α_0:

$$\alpha_0 = \frac{m_e}{\mu}\epsilon_r a_0, \tag{2.88}$$

where a_0 is the Bohr radius (the most likely distance of the lowest energy orbital from the nucleus in the hydrogen atom):

$$a_0 = \frac{4\pi\epsilon_0\hbar^2}{m_e e^2}. \tag{2.89}$$

For example, the Bohr exciton radius in bulk silicon is 49 Å(with a relative permittivity $\epsilon_r = 11.68$). The Bohr exciton radius also becomes especially important when semiconductors are quantum confined, as discussed in §2.6.

The lifetime of an exciton is short, typically 10^{-8} s [39], due to the strong correlation between electron and hole. However, if the recombination process involves the emission of a photon (an exciton interacting with a photon is known as a polariton) with sufficient energy to create a new exciton, the lifetime is lengthened by subsequential generation of new excitons. This effect has led to the apparent lifetime of the exciton being several orders of magnitude greater than the expected value: in bulk CdS the decay time of the polariton emission was measured to be 9 µs after excitation [48].

2.4 Band bending at surfaces

The surface of a semiconductor is often affected by localized defect states or surface reconstruction, for example, so that the structure of the surface often differs greatly from the bulk crystal structure. This alters the electronic structure of the material, and surface states are present which often occupy the band gap. Other surface states that lie within the conduction or valence bands are resonant surface states. In an n-type semiconductor, for the case where there are surface states within the band gap at lower energies than the donor states, the electrons can lower their energy by occupying these surface states. This leads to a net surface charge Q_S (charge per unit area) which is negative in this case. To maintain charge neutrality, a depletion layer forms over a width z_D where a lack of electrons, and thus an excess of holes, creates a positively charged region with a total charge $-Q_S$. Likewise, for the case where holes occupy the surface states leading to a positively charged surface, an accumulation layer forms where an excess of electrons is present to maintain charge neutrality.

The depth of the depletion or accumulation layer, z_D, depends on the dopant density N_D in that a higher density of dopants in the material will lead to a higher

surface charge. It can be shown that the potential $V(z)$ over the depletion region $0 < z < z_D$ is [49]:

$$\frac{d^2V}{dz^2} = -\frac{-e^2N_D}{\epsilon_0\epsilon_r} \Longrightarrow V(z) = \frac{e^2N_D}{2\epsilon_0\epsilon_r}(z - z_D)^2, \tag{2.90}$$

where $V = 0$ for $z \geq z_D$ and ϵ_r is the relative permittivity of the material. The energy bands therefore bend quadratically over the depletion region as shown in figure (2.13). The total, or equilibrium, band bending at the surface, V_0, is $-e^2N_Dz_D^2/(2\epsilon_0\epsilon_r)$. The population of charge carriers at surface states within the band gap leads to the pinning of the Fermi level to the average energy of the surface states, E_S.

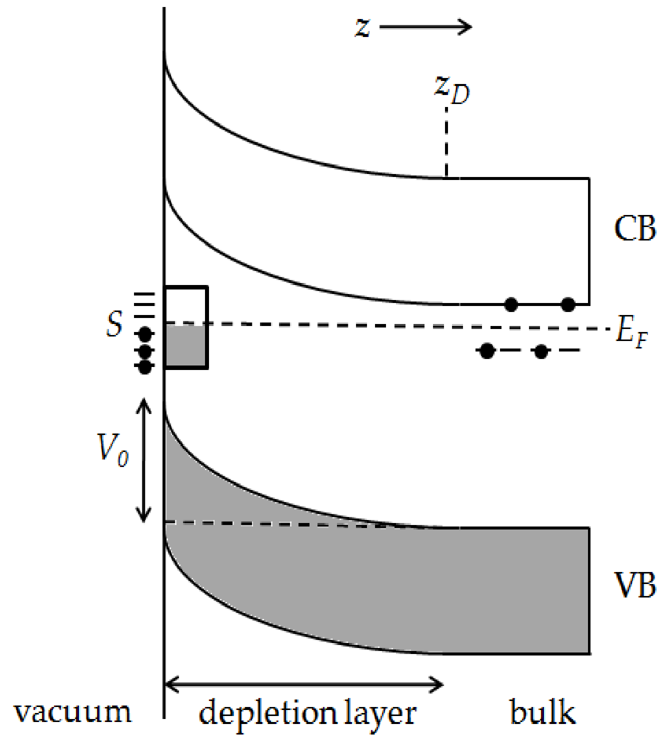

Figure 2.13: Band bending at the surface of an n-type semiconductor, where a few electrons (filled circles) will occupy the conduction band (CB) in the bulk at normal temperatures. The shaded valence band (VB) illustrates that it is fully occupied. The Fermi level is pinned to the partially filled (shaded) surface states (S). The occupation of electrons in the surface states leads to a depletion layer, lacking electrons, of width z_D containing ionized donors so that charge neutrality is maintained. This leads to the creation of an electric field across the surface. The difference in the electronic structure at the surface leads to the bands bending at the vacuum interface with a total band bending of V_0.

The amount of band bending will change under photoexcitation, as illustrated by figure (2.14): as the electron and hole created by photoexcitation separate (in the case of the n-type semiconductor in figure (2.14), the holes towards the surface

and the electrons into the bulk) the band bending changes, inducing a change in the surface potential [50]. Photoexcitation effectively re-injects carriers into the depletion layer, reducing the electric field across the interface. This is called the *surface photovoltage* effect (SPV), where the change in the surface potential, ΔV, is described by [51]:

$$\frac{\Delta V}{k_B T} \exp\left(\frac{\Delta V}{k_B T}\right) = \frac{n_P}{n_0} \exp\left(\frac{V_0}{k_B T}\right), \tag{2.91}$$

where n_0 is the doping carrier concentration, n_P is the photoexcited carrier concentration and V_0 is the equilibrium band bending. The surface photovoltage also affects the photoexcited carrier lifetime τ [52]:

$$\tau = \tau_\infty \exp\left(\frac{\Delta V}{\alpha k_B T}\right), \tag{2.92}$$

where α is a material parameter. It is important to understand this effect at surfaces and interfaces: the surface photovoltage in semiconductors may be studied with laser-pump synchrotron-probe spectroscopy, whereby laser radiation photoexcites the sample (promoting valence band electrons into the conduction band) and synchrotron radiation is used to probe the resulting surface photovoltage [53, 54, 55, 56, 57, 58].

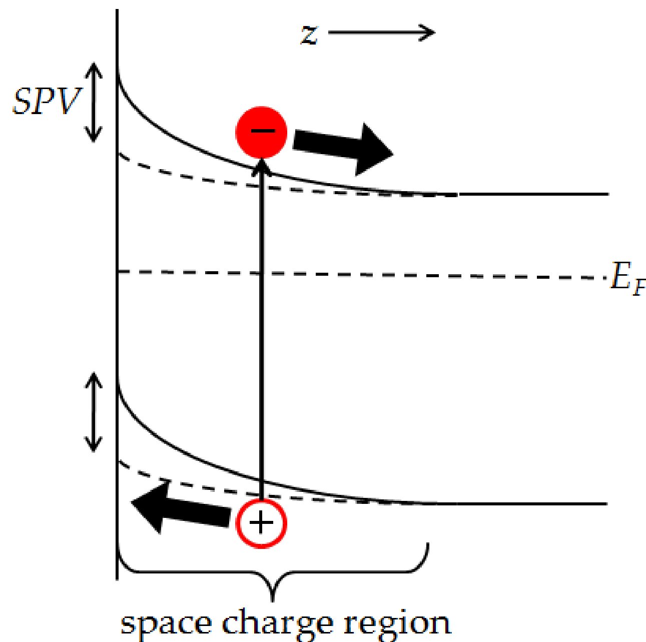

Figure 2.14: Surface photovoltage (SPV) effect in an *n*-type semiconductor under photoexcitation. The SPV is the illumination-induced change in the surface potential.

2.5 Photovoltaics

The purpose of a photovoltaic is to absorb radiation and convert this electromagnetic energy into current and voltage (the opposite of a light emitting diode, or LED). The greatest source of renewable energy available is from the Sun: 120,000 TW of energy from the Sun hits the Earth each year [1]. Considering the global consumption is currently $\approx$ 14 TW (although set to double by the year 2050), it is clear that more efficient (or alternatively cheaper) photovoltaics need to be manufactured.

The traditional solar energy cell is made from a *p-n junction*, that is a semiconductor that is one half p-type and one half n-type, where the dopant is altered across the crystal. The p-type material is used for the collection of holes and the n-type material for the electrons by connecting a cathode and an anode. The p-n junction is shown in figure (2.15), and shows that the band edges for the p-type (with acceptor states) and n-type (with donor states) semiconductors must bend at the interface because the Fermi level E_F is fixed when at equilibrium. The region in which this occurs is called the *space charge layer* because it is a region that is depleted of charge carriers, analogous to the semiconductor-vacuum interface discussed in §2.4. Photoexcited electrons migrate away from the interface to the conduction band minimum in the n-type material and the holes migrate to the valence band maximum in the p-type material. This depletion layer therefore creates an electric field across the junction.

Shockley and Queisser formulated the ultimate efficiency, e_u, that a solar energy cell is capable of under illumination from sunlight (a black body with temperature $T_{Sun} \approx$ 6000 K), now known as the Shockley-Queisser limit [59]:

$$e_u = E_g \frac{Q_s}{P_s} = \frac{x_g \int_{x_g}^{\infty} \left(x^2 dx/(e^x - 1)\right)}{\int_0^{\infty} \left(x^3 dx/(e^x - 1)\right)}, \tag{2.93}$$

where Q_s is the number of quanta of energy $E \geq E_g$ reaching the solar cell per unit area per unit time and P_s is the total energy density falling on unit area in unit time. The function turns out to purely be a function of x_g where

$$x_g = \frac{E_g}{k_B T_{Sun}} \quad . \tag{2.94}$$

For a silicon solar energy cell the Shockley-Queisser limit for its ultimate efficiency is 33%, whereas the current laboratory record is 24.7% [60]. The main factors affecting this ultimate efficiency are the fact that photons with energies below the band gap energy cannot create an electron-hole pair, preventing the utilization of the entire solar spectrum. Likewise, energy in excess of the band gap will

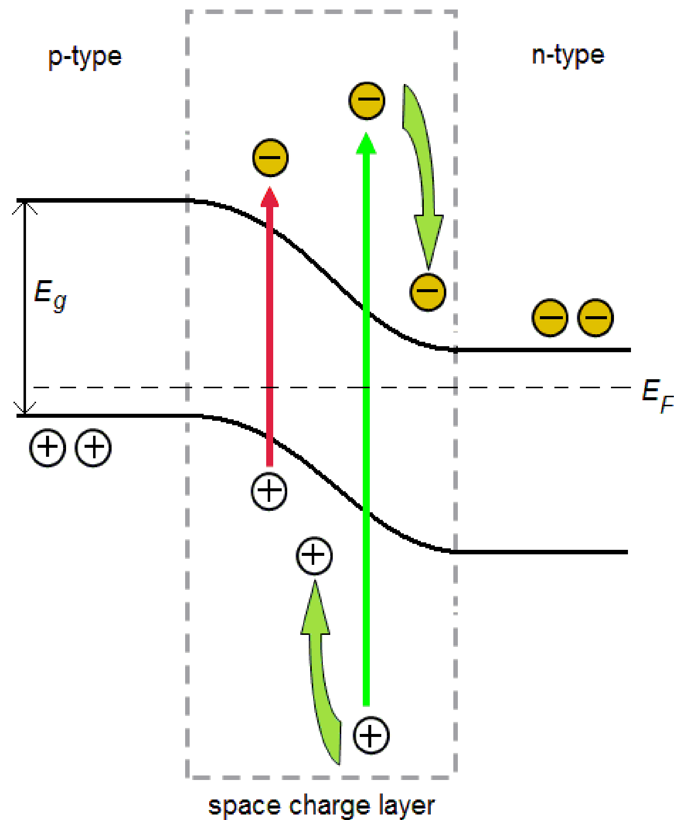

Figure 2.15: The p-n junction. The Fermi level E_F is fixed at equilibrium, and the region between the *p*-type and *n*-type semiconductors where the bands bend is called the space charge layer. The curved arrows show that the electrons and holes relax to the band edge when excited by a photon of energy $h\nu > E_g$ by phonon emission (the excess energy is lost as heat), migrating away from the space charge layer.

usually be lost as heat by phonon absorption. It is also important to note that the reflectance of a solar cell material across the solar spectrum will inhibit efficiency greatly (for silicon, 49% of 400 nm light will be reflected at the surface). Another key factor in solar cell efficiency is the recombination of electrons and holes before the charge carriers are transported to the anode and cathode. The main commercial problem with solar cells manufactured from silicon is that the silicon has to be grown to ensure it has high purity ($> 99.999\%$), leading to a high cost that makes these solar cells unviable for the mass production of electricity. The push to exploit solar power is therefore focused on reducing manufacturing cost as well as the optimization of efficiency.

2.6 Quantum confinement

One important advance in semiconductor technology is the manufacture of nanostructured semiconductors where charge carriers can be ‘quantum confined’. Con-

fining one dimension of a semiconductor to quantum scales (of the order of nm or less) produces thin films of semiconductors; quantum confinement in two dimensions produces nanowires, and three dimensional quantum confinement produces quantum dots (QDs). Isolating atoms on these scales means that electrons will no longer interact with the potentials of other atoms in one or more dimension, as the structures are separated by distances greater than the de Broglie wavelength of the electron (Eq. (2.45)).

Quantum confinement in one dimension leads to the formation of quantum wells, but because carriers are free to move in the remaining dimensions, continuous bands of energy still occur in these directions. The density of states for quantum confinement in one dimension (*i.e.* a two dimensional system) now becomes:

$$Z_{2D}(E) = \frac{m^*}{\pi\hbar^2}\sum_n \sigma(E - E_n), \tag{2.95}$$

where $\sigma(E - E_n)$ denotes a function of $(E - E_n)$. The density of states (and thus the absorption spectrum) is now a constant for each state, and so a step function $\sigma(E - E_n)$ for each quantized energy state with energy E_n is formed as shown in figure (2.16). The density of states of a one dimensional system (such as a nanowire) becomes

$$Z_{1D}(E) = \frac{1}{\pi\hbar}\sum_n \sqrt{\frac{m^*}{2(E - E_n)}}\sigma(E - E_n), \tag{2.96}$$

and for a zero dimensional system with quantum confinement in all three dimensions, *i.e.* a quantum dot, the density of states is reduced to a series of delta functions at each allowed energy state E_n:

$$Z_{0D}(E) = \sum_n 2\delta(E - E_n) \tag{2.97}$$

where the dispersion relation (Eq. (2.30)) no longer holds true and there is no dependence of energy on momentum. Energy levels are once again discrete and quantized, acting according to the 'particle-in-a-box' approximation, as shown in figure (2.17).

Quantum confinement in three dimensions causes the properties of the semiconductor to change. The effective band gap, E_g, changes depending on the size of the dots ($E \propto 1/L^2$) as illustrated in figure (2.18). As the size of a quantum dot decreases, the energy gap between the lowest confined states increases and so the absorption spectrum is blue-shifted in wavelength. The absorption spectra in figure (2.18) also show the first and second excited states in the quantum dot.

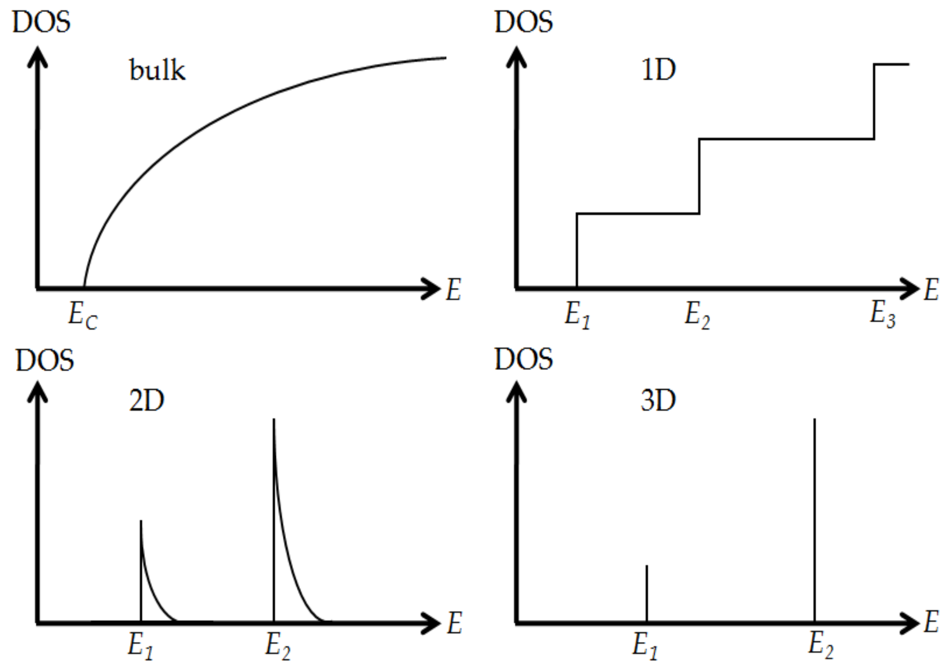

Figure 2.16: The density of states (DOS) as quantum confinement is achieved in 1D, 2D and 3D, as compared to a bulk semiconductor, adapted from [43]. The 1D and 2D plots show the DOS along the direction(s) of quantum confinement. Whereas the density of states (and thus absorption) for a bulk crystal is related to $E^{1/2}$, a quantum dot (confined in three dimensions) only absorbs at discrete energies: the density of states is reduced to a set of delta functions. The energy of the E_1 level increases as the number of quantum-confined dimensions increases, compared to the conduction band edge E_C in a bulk material.

The broad absorption features are due to the size dispersion of the quantum dots (typically 10%). Moreover, the spatial confinement causes the Coulomb interaction between electron and hole to be enhanced and so the exciton binding energy E_B is enhanced compared to bulk material [61, 62]. This enhanced Coulomb interaction in quantum confined structures was first proposed by Greene *et al.* in 1984 [63], and measured by Dawson *et al.* in 1986 [64].

The fact that the optical properties of semiconductor quantum dots can be so dramatically affected by their size and composition (properties that are easily modified in the manufacturing process) has potentially large implications for novel photovoltaic devices. Quantum dots that have been tailor-made to absorb the solar spectrum could be as efficient as traditional silicon solar cells, and much less costly to manufacture. A potential model of a solar cell utilizing quantum-confined semiconductors is shown in figure (2.19). The cell utilizes QDs for the harvesting of light as well as metal oxide nanorods (confined in two dimensions) for electron transportation after photoexcitation. The properties of the nanorods and of the hole-transporting material, such as their photoconductivity, are very

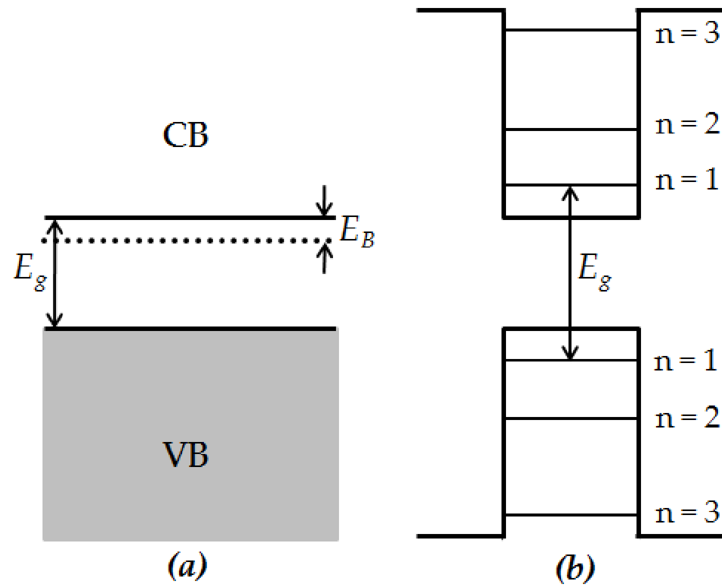

Figure 2.17: Energy bands in *(a)* bulk material, and *(b)* strongly quantum-confined structures, adapted from [43]. Quantum confinement causes the energy levels to become discrete and the effective band gap energy, E_g, increases. The dotted line shows the first exciton state with a binding energy E_B, which is also enhanced by quantum confinement.

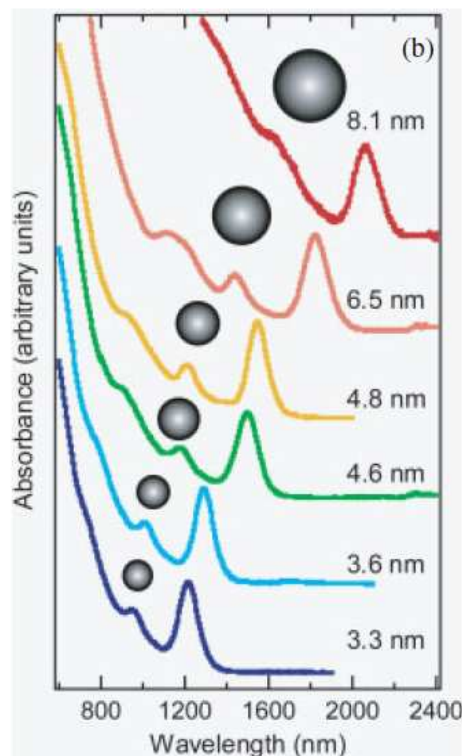

Figure 2.18: Absorption spectra of a series of PbSe QDs, from [15]. As the semiconductor QDs are confined to smaller sizes the absorption spectrum showing the 1*s* exciton state (illustrated in figure (2.17)) blue-shifts, and the band gap energy increases.

important and need to be understood well in order to fabricate such a solar cell.

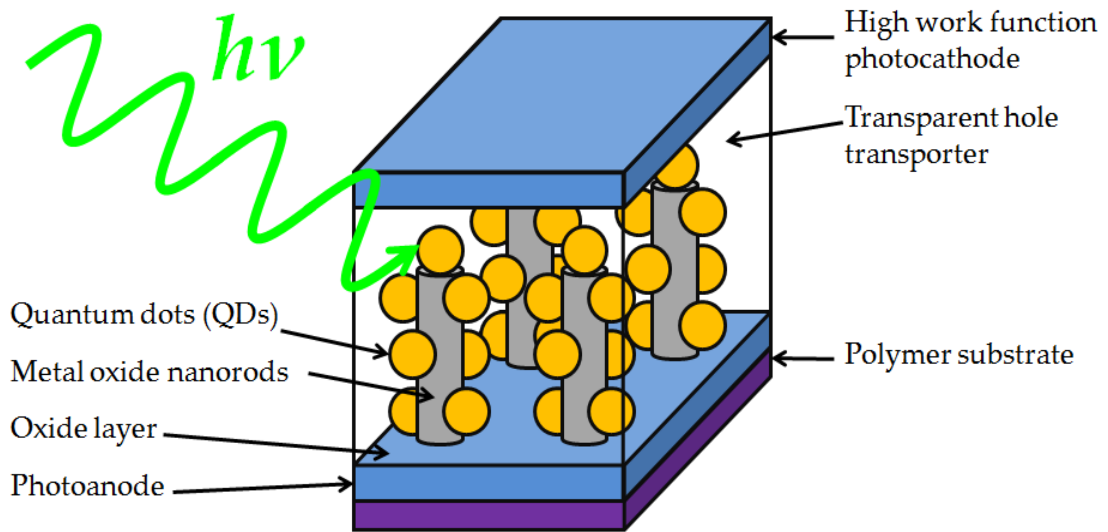

Figure 2.19: A model for a hybrid solar energy cell, adapted from [65]. Quantum dots and metal oxide nanorods are used for the creation and transportation of charge carriers respectively. The photon illustrated is absorbed by a quantum dot, creating an exciton. The electron is then transported to the photoanode through a nanorod, and the hole is transported to the photocathode through a material that is transparent to the incoming photons.

It has been previously mentioned that if absorption of a photon with an energy greater than the band gap occurs in a bulk semiconductor, the excess energy is lost as heat and only one exciton is generated. However, this is not strictly correct because multiple excitons will be generated when the photon energy is multiple times the band gap. The process of generating multiple excitons is thought to be due to impact ionization as illustrated in figure (2.20), where the excess energy of an electron or hole is transferred to promote other electrons across the band gap. $2E_g$ is the minimum photon energy required for impact ionization under the conservation of energy, in that the excess energy of a photoexcited electron will itself be E_g, which can then be transferred so as to photoexcite a second electron across the band gap. The excess energy can therefore generate additional excitons rather than being absorbed as heat. The impact ionization process occurs at a rate much faster than the exciton lifetime [66].

The quantum efficiency of bulk silicon is given in figure (2.21). At higher photon energies multiple excitons are generated from each photon. However, in the case of bulk silicon this potential enhancement in efficiency is useless in the context of solar cells because the energy range it occurs in is outside the solar emission spectrum. Indeed, carrier multiplication does not occur in silicon until photon energies greater than $3E_g$.

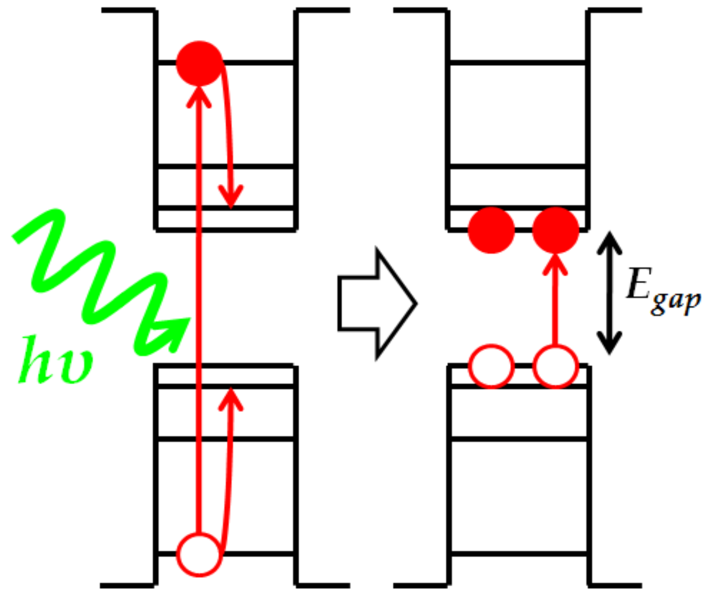

Figure 2.20: Impact ionization is one theory to explain carrier multiplication, after an exciton is formed by the absorption of a photon with energy, $h\nu$, greater than the band gap energy, E_{gap} [14]. The excess energy of the electron (filled circles) and / or hole (empty circles) is used to create one or more additional electron-hole pairs when $h\nu \geq 2E_{gap}$. Impact ionization is the opposite of the Auger recombination process [66].

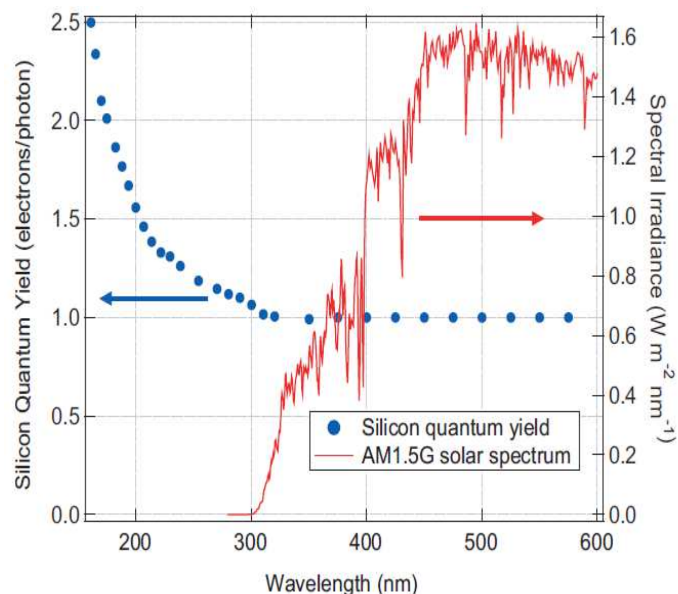

Figure 2.21: The solar spectrum (AM1.5G) versus the quantum yield of bulk silicon, from [15]. Multiple excitons are generated in silicon at lower wavelengths (higher energies). The band gap energy of silicon is approximately 1.1 eV and so $2E_g$ is at a wavelength of approximately 550 nm, and $3E_g$ at approximately 370 nm.

It has been suggested that in quantum-confined structures, the conservation of translational momentum will be relaxed and so the threshold energy for carrier

multiplication will be closer to $2E_g$ than in bulk materials. In the impact ionization model it is assumed that one or other of the charge carriers (electron or hole) must individually create an additional pair of charge carriers. This model considers a simple bulk-like picture of impact ionization rather than considering the complex energy level system in a quantum dot. Photon energy in excess of the band gap energy is partitioned between the electron and hole depending on their effective masses:

$$E_e/E_h = m_h^*/m_e^*, \tag{2.98}$$

where E_e and E_h are the excess energies of the electron and hole such that $E_e + E_h = (h\nu - E_g)$. The threshold energy for carrier multiplication using this so-called energy partition model is [15]:

$$h\nu_{th} = \left(2 + \frac{m_e^*}{m_h^*}\right) E_g, \tag{2.99}$$

and was first introduced by Schaller *et al.* [67, 68]. The threshold energy for carrier multiplication will therefore vary depending on m_e^* and m_h^*. For example, in the case of $m_h^* \gg m_e^*$, where the energy levels in the valence band will be much more closely spaced than the energy levels in the conduction band, the carrier multiplication threshold energy will be lower than the case of $m_h^* \approx m_e^*$, where $h\nu_{th} \approx 3E_g$ [26].

The process of carrier multiplication in quantum dots is still debated, although a recent publication has compared carrier multiplication results in bulk PbS and PbSe quantum dots to theoretical calculations based on this impact ionization mechanism with very good agreement [17]. The energy partition model of equation (2.99) also fits very well with experimental data. For example, lead materials such as PbS and PbSe have similar electron and hole effective masses, meaning that an energy threshold of $h\nu_{th} \approx 3E_g$ is expected. Indeed, the threshold energy for PbS has been measured to be approximately $3.2E_g$ [69] and $2.9E_g$ in PbSe [68]. For materials where $m_h^* > m_e^*$, a lower a threshold energy is observed: approximately $2.1E_g$ in InP [18] and $2.5E_g$ in CdSe [68].

It is also speculated that the efficiency of carrier multiplication is enhanced in quantum dots compared to bulk materials [14, 70], due to the presence of discrete, widely-spaced energy levels. This is because the impact ionization process is more competitive with non-radiative decay processes in quantum dots due to a lower density of phonon states. Phonon states will mismatch with the widely-spaced electronic density of states, effectively slowing the decay process. Impact ionization is also speculated to be enhanced by a larger Coulomb interaction present in quantum dots. However, these hypotheses remain controversial, and as such

there is great interest to study carrier multiplication in quantum dots and to fully understand the processes by which it occurs, especially because it has been calculated that carrier multiplication could lead to the fabrication of a solar cell with a maximum power efficiency of 44.4% [71].

Carrier multiplication has been shown to occur in several types of quantum dot: Si [72], CdSe [25, 73, 74], CdTe [74], PbSe [75, 76, 77], PbS [77, 76], InAs [26, 78] and recently InP [18]. However, a recent publication has suggested that carrier multiplication in PbSe and PbS is not enhanced in quantum dots, and that it is actually more efficient in bulk material [16]. However, in this work the quantum efficiency is plotted against absolute photon energy. It has been shown that the data, once plotted instead against an energy-gap-normalized energy scale (*i.e.* $h\nu/E_g$ instead of simply $h\nu$) illustrate that quantum dots are far more energy efficient than bulk material of the same band gap [17]. This relative energy scale seems more appropriate because the band gap energy of quantum dots can be varied so easily. There is clearly a need for more measurements on bulk materials to directly compare to quantum dots to ascertain whether or not carrier multiplication is enhanced by quantum confinement. This thesis contains quantum efficiency measurements of bulk InP measured by time-resolved terahertz spectroscopy (§4.2) to compare to recent data on InP quantum dots [18]. There is also effort being put into the study of charge transfer and photoconductivity in nanoparticles compared with bulk phenomena [79, 80], as this is clearly another important factor should quantum dots be used to fabricate a solar cell.

2.7 Terahertz absorption and photoconductivity

The terahertz (THz) spectral region lies between 300 GHz ($\lambda = 1$ mm) and 10 THz ($\lambda = 30$ μm), between the infrared and microwave regions of the electromagnetic spectrum. However, the technological development in this region is in no way as advanced as those in optical and microwave (or electronic) frequencies due to the difficulty involved in the generation and detection of THz frequencies [20]. It is now being used in a wide variety of applications including the study of biomolecular systems and pharmaceuticals [81].

$$1\ \text{THz} \equiv 1\ \text{ps} \equiv 0.3\ \text{mm} \equiv 4\ \text{meV}. \tag{2.100}$$

For this reason the region was known as the ‘THz gap’. It is now accessible due to technological advances in ultrafast laser systems [22]; the generation and detection of THz pulses will be discussed in §3.3.2.

Photons with energies within the THz spectrum are suitable for probing the

internal energy levels of an exciton [82]. In bulk materials, phonon modes also fall into this energy range, and so THz radiation is an ideal probe of semiconductor physics. Moreover, the method of time-domain THz spectroscopy (THz-TDS) involving detection via electro-optic sampling (§3.3.2) allows direct measurement of the electric field of THz pulses [22]. This allows changes in the phase of the probe pulse to be measured as well as changes in magnitude, unlike more traditional spectroscopic techniques such as transient absorption (TA) spectroscopy.

The electric fields of THz pulses are directly measured in the time domain, and are Fourier transformed according to

$$E(\omega) = \frac{1}{2\pi} \int_{-\infty}^{\infty} E(t) e^{-i\omega t} dt, \tag{2.101}$$

where $E(\omega)$ is the complex field amplitude and $E(t)$ the experimentally-measured pulse in the time domain. The optical properties of a sample can therefore be determined in the THz frequency range: the complex refractive index of a sample, $\tilde{n}$, is defined as

$$\tilde{n}(\omega) = n(\omega) + ik(\omega), \tag{2.102}$$

where $n(\omega)$ is the frequency-dependent refractive index and $k(\omega)$ the frequency-dependent wave vector of the sample. The complex refractive index is related to the complex dielectric constant, ϵ, by:

$$\epsilon = \epsilon_1 + i\epsilon_2 = (n + ik)^2, \tag{2.103}$$

so that $\epsilon_1 = n^2 - k^2$ and $\epsilon_2 = 2nk$. The electric field for a wave propagating in the z-direction becomes

$$\begin{aligned} E = E_0 \exp\left[i\omega\left(\frac{\tilde{n}z}{c} - t\right)\right] &\Rightarrow E_0 \exp\left[i\omega\left(\frac{nz}{c} + \frac{ikz}{c} - t\right)\right] \\ = E_0 \exp\left[-\frac{k\omega z}{c}\right] &\exp\left[i\omega\left(\frac{nz}{c} - t\right)\right], \end{aligned} \tag{2.104}$$

where $k\omega/c = \alpha/2$, where α is defined as the absorption coefficient. Eq. (2.104) shows that the refractive index n gives rise to a time delay $t_D = nz/c$, or phase change, in the THz waveform as it travels through the sample, and the wave vector k results in absorption according to

$$k = \frac{c\alpha}{2\omega}, \tag{2.105}$$

where $\omega = 2\pi\nu$. The intensity of the wave, $I = E^2$, propagating through a sample

is therefore affected by the absorption coefficient according to:

$$I = I_0 e^{-\alpha z}. \tag{2.106}$$

This is the Beer-Lambert law for the absorption of radiation. The length $1/\alpha$, or the sample depth at which the intensity has diminished to $1/e$ of its original intensity ($\approx 36.7\%$) is defined as the penetration depth of the sample, δ:

$$\delta = \frac{1}{\alpha}. \tag{2.107}$$

The absorbance of a sample, A, is thus

$$A = \log_{10}\left(\frac{I}{I_0}\right) = \alpha d, \tag{2.108}$$

where d is the sample thickness.

The transmission coefficient of a sample is given by the ratio of the Fourier-transformed fields through the sample, $E_S(\omega)$, compared to a reference, $E_0(\omega)$:

$$T(\omega) = \frac{E_S(\omega)}{E_0(\omega)}. \tag{2.109}$$

This complex, frequency-dependent transmission coefficient is related to the complex refractive index, $\tilde{n}$, according to the Fresnel transmission coefficients [83]:

$$T(\omega) = \frac{4\tilde{n}}{(1+\tilde{n})^2} \exp\left[\frac{i\omega d}{c}(\tilde{n}-1)\right]. \tag{2.110}$$

It is important to note that the right-hand term desribes transmission through the sample, and that multiple reflections of the THz pulses at the sample interfaces are ignored because they are truncated in the time domain before being transformed into the frequency domain. This truncation is performed by applying a Gaussian window function to the time-domain data, centred on the main THz peak such that the data are reduced to zero at the point where reflections occur. From the measured fields $E_0(\omega)$ and $E_S(\omega)$, the complex refractive index $\tilde{n}$ is extracted numerically as described in §3.3.7.

Once the complex refractive index of a sample is known, optical-pump THz-probe experiments can be undertaken to measure the frequency-dependent photoconductivity of the sample. A pump beam photoexcites the sample at a pump-probe delay time, τ, before the THz probe. This leads to the creation of an electron-hole plasma with a characteristic plasma frequency, ω_p, in the THz spectrum [84, 85, 86]. Here, the complex, frequency-dependent photoconductivity of the

sample, $\tilde{\sigma}(\omega)$, is determined from the ratio of the Fourier-transformed change in the THz field upon photoexcitation, $\Delta E(\omega)$, to the THz field through the sample, $E_S(\omega)$ [87, 86, 88, 89, 90, 91]:

$$\tilde{\sigma}(\omega) = -\frac{2\epsilon_0 c\tilde{n}}{\delta}\frac{\Delta E(\omega)}{E_S(\omega)}, \tag{2.111}$$

where ϵ_0 is the permittivity of free space and δ is the penetration depth of the pump beam. Equation (2.111) is for the case of a thick sample where $d \gg \delta$. For layered media or for the case of thin-filmed materials, the determination of the photoconductivity becomes much more complicated, requiring a thorough analysis of the terahertz wave propagation through the photoexcited sample [92, 93, 94]. It also assumes that the change in the electric field is small in comparison to the initial electric field.

The photoconductivity of a sample will be mainly due to electrons for the case when the electron effective mass is much less than the hole effective mass ($m_e^* \ll m_h^*$), in that the electrons will have a much higher mobility. The complex photoconductivity of the sample at a particular pump wavelength can be modeled by the Drude model which describes the photoexcited electrons within the sample as a free electron gas which oscillates at THz frequencies [95]:

$$\tilde{\sigma}(\omega) = \frac{\epsilon_0 \omega_p^2 \tau_S}{1 - i\omega\tau_S}, \tag{2.112}$$

where ω_p is the plasma frequency of the free electron gas resulting from oscillations in the electron density, and τ_S is the electron relaxation time. The mean free path of electrons, l, is therefore

$$l = v\tau_S \tag{2.113}$$

where v is the electron velocity. Although the Drude model is naïve in that it does not take into account the periodic potentials of the lattice, the model does consistently fit experimental data well. There are several modifications of the Drude model, however, including the Drude-Smith model which includes an additional term to account for back-scattering [96].

The plasma frequency is related to the electron density, N_e, by:

$$\omega_P = \sqrt{\frac{N_e e^2}{\epsilon_0 m_e^* \delta}} \tag{2.114}$$

where e is the electron charge and m_e^* the effective mass of the electron. For the case when the effective hole mass is much less than that of the electron, the pho-

toconductivity would be mainly due to holes rather than electrons and the hole effective mass would be used in eq. (2.114). However, for the case when the effective mass of the electron is equivalent to the effective mass of the hole, and thus the THz-induced photoconductivity is due to the presence of electrons and holes equally, a factor of 2 would be introduced into the square root of eq. (2.114). This effectively accounts for the use of the exciton effective mass, $1/\mu = 1/m_e^* + 1/m_h^*$, in that $\mu \approx m_e^*$ for $m_e^* \ll m_h^*$ and $\mu = 2m_e^*$ for $m_e^* = m_h^*$.

Equation (2.114) demonstrates how useful time-resolved THz spectroscopy can be, in that the carrier density is directly measured. The Drude model is fitted to the measured photoconductivity (obtained via Eq. (2.111)) so as to extract the plasma frequency and relaxation time. The quantum efficiency, η, or the number of electrons generated per photon, of the sample at a particular pump wavelength can therefore be determined from the ratio of electron to photon densities:

$$\eta = \frac{N_e}{N_\gamma} \tag{2.115}$$

where the photon density, N_γ, is calculated using:

$$N_\gamma = \frac{P}{\pi r^2}\frac{(1-R)}{E_\gamma} \tag{2.116}$$

where P is the pump beam energy, r is the beam radius, R is the sample reflectivity and E_γ is the pump photon energy. Therefore only knowledge of the absorption coefficient, reflectivity and thickness of the sample are required, as well as the size and power of the pump beam.

By varying the pump-probe delay time, the frequency-dependent photoconductivity can be deduced on the subpicosecond timescale. This is particularly useful for novel nanoparticulate samples where more traditional techniques of assessing photoconductivity, for instance using electrodes, are not viable. In the context of the proposed next-generation solar cell in figure (2.19), the conductive properties of nanowires [97], nanocrystal films [98, 99, 100], hole-transporting materials [101] and quantum dots [102, 103, 104, 105] can be studied with time-resolved THz spectroscopy, as well as phenomena such as carrier multiplication discussed in §2.6 [26, 25, 16].

Chapter 3

Experimental.

This chapter details the experimental methods used to investigate photovoltaic materials. The surface photovoltage effect (SPV as detailed in §2.5, figure (2.14)) is investigated using laser-pump synchrotron-probe measurements on bulk *n*-type Si(111), where the X-ray probe beam from the Synchrotron Radiation Source (SRS, formerly at Daresbury Laboratory) is measured using X-ray Photoelectron Spectroscopy (XPS) of the Si 2*p* core level. Pump-probe experiments at the SOLEIL synchrotron radiation source, Paris, using a portable 375 nm laser to investigate PbS quantum dots deposited on a ZnO substrate are also described. The table-top time-resolved THz spectrometer that has been built in the Photon Science Institute is then detailed along with the experimental challenges involved. For both the SRS and THz work a femtosecond laser system, funded by the North West Development Agency (NWDA), is used.

3.1 Laser system

The main components of the laser system include a titanium-sapphire (Ti:sapphire, or Ti:Al_2O_3) oscillator (Tsunami, Newport) which produces ultrafast pulses (typically with ≈100 fs pulse durations) at a repetition rate of approximately 80 MHz, and a Ti:sapphire regenerative amplifier (§3.1.4, Spitfire, Spectra-Physics) producing high-powered pulses at a repetition rate of 1 kHz, which is seeded with the output from the Tsunami. Both the oscillator and amplifier produce near-infrared light at 800 nm. Both systems are also pumped with an external laser: the Tsunami is pumped with a continuous wave (CW) laser at 532 nm (Millennia Pro, Spectra-Physics) where the laser medium is Nd:YVO_4, pumped by an additional diode laser in a rack off the optical table, delivered through a fibre-optic cable (shown in black in figure (3.1)). The Spitfire that is seeded by the oscillator is also pumped with a pulsed laser at 527 nm (Empower, Spectra-Physics), as shown in figure

(3.2), which has Nd:YLF as its medium. The Empower is also diode-pumped with intracavity frequency doubling.

The output of the Tsunami is attenuated by a wave-plate/polarizer combination (described in §3.1.2) before proceeding to the pulse-picker and frequency doubler/tripler, and finally the output is taken off the table by periscope 2. This is the setup used for the laser-pump synchrotron-probe measurements. The tunability of the oscillator, where the laser cavity length can be chosen so as to change the repetition rate, makes it ideal for pump-probe experiments where the the laser needs to be synchronized to an external radiation source. The terahertz spectrometer, however, uses the output from the amplifier on the bottom tier: the Tsunami output is taken to the bottom tier directly with periscope 1 to seed the amplifier. The terahertz spectrometer also uses a wavelength-tunable output from an optical parametric amplifier (§3.1.5, TOPAS, Light Conversion), which uses the Spitfire output.

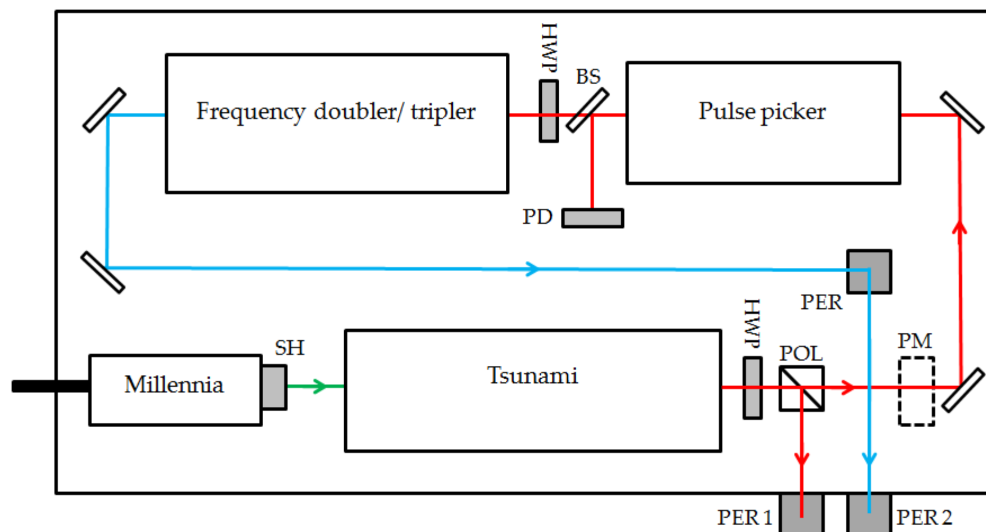

Figure 3.1: A schematic layout of the top tier of the portable laser system. HWP: half wave plate; BS: A beam sampler which can be inserted to reflect some of the pulse-picked beam onto the photodiode (PD) in order to ascertain the contrast ratio of the pulses. SH: mechanical shutter; POL is a polarizer used to attenuate the beam; PM shows a position where a power meter can be placed; PER shows the position of three periscopes, one to take vertically polarised light to the lower tier (PER1), one used to take the frequency doubler/tripler output off the table below the Tsunami beam (PER), and one to take the output beam off the optical table (PER2). The output from the top tier taken off the table using PER2 is used in pump-probe measurements with the SRS, explained in §3.2 .

The laser system is split across two levels which can be mounted on wheels to transport it around a facility, such as the Synchrotron Radiation Source (SRS) at Daresbury Laboratory. A photograph of the system on beamline 6.1 at the now de-commissioned SRS is shown in figure (3.3).

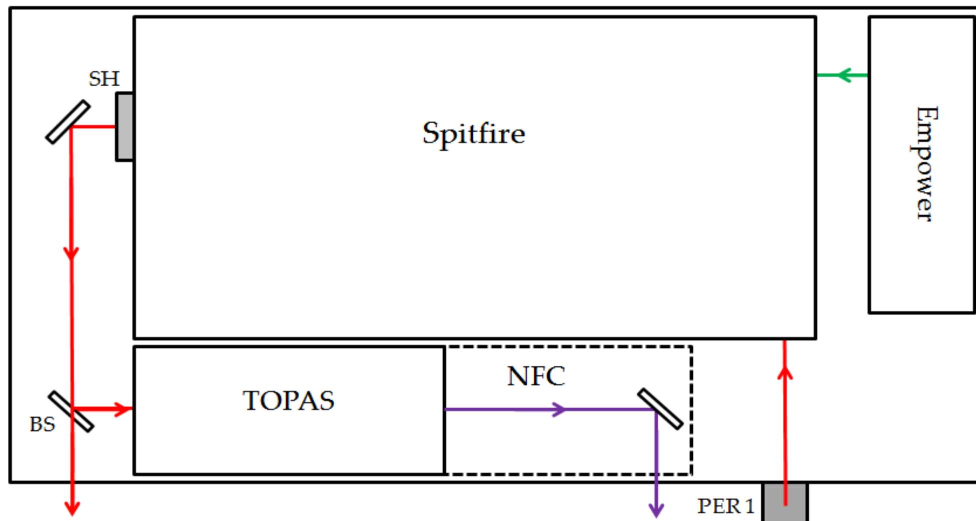

Figure 3.2: Schematic layout of the bottom tier of the mobile laser system. The Spitfire regenerative amplifier takes input from Periscope 1 from the top tier, and is pumped by the Empower laser as described in §3.1.4. A beam-splitter (BS) takes the majority of the output of the amplifier (approximately 90%) to pump the TOPAS optical parametric amplifier. The output of the TOPAS is subject to nonlinear frequency conversion (NFC), as described in §3.1.5, before being taken off the table. The remainder of the output of the Spitfire is used in the generation and detection of THz pulses, explained in §3.3.

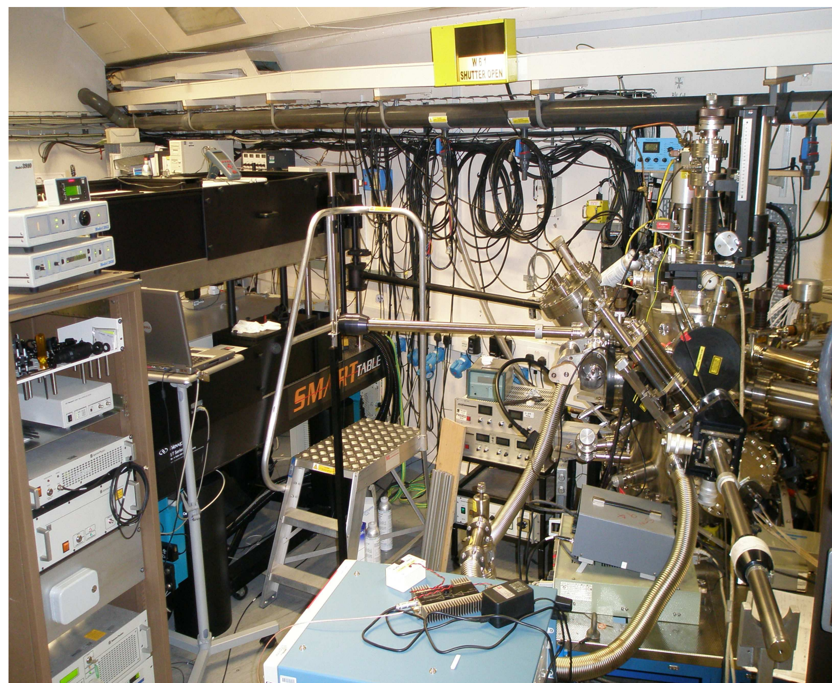

Figure 3.3: Photograph of the laser system on beamline 6.1 at the SRS. The ultra-high-vacuum (UHV) apparatus housing the sample can be seen to the right of the laser system.

3.1.1 Mode-locking and pulse-picking

Mode-locking is the method via which short pulses can be created, and is achieved by introducing active or passive elements which modulate the loss/gain of the laser cavity. This modulation must occur at a frequency equal to the inter-mode separation:

$$\Delta\nu = c/2L \tag{3.1}$$

where L is the cavity length. A train of pulses is created within the cavity due to the interference of longitudinal modes (standing waves at frequencies $\nu = nc/2L \quad (n = 1, 2, 3, \ldots)$) in the cavity. The fact that there are a large number of modes leads to a very short pulse duration of the resultant pulses.

Active methods modulate the cavity losses inside the resonator using a radio frequency (RF) device such as an acousto-optic modulator (AOM), which is implemented in the Ti:sapphire oscillator (Tsunami) system. A piezoelectric transducer periodically creates a standing acoustic wave within the modulator, which can be understood as a weak shutter to the light in the resonator (when an acoustic wave is induced in the modulator, light is refracted at an angle θ to the straight-through path, and only this light is allowed to propagate away). If the rate of this modulation is equal to cavity round-trip time τ_c ($= 2L/c$), then one single pulse of light will travel through the cavity, and the laser will be mode-locked. Mode-locking typically occurs at a frequency of approximately 80 MHz for Ti:sapphire oscillator systems. AOMs are also used to pulse pick: if the frequency at which a standing wave is created is equal to a fraction of the Tsunami pulsed output frequency, a beam (containing, for example, one pulse for every twenty-six originally generated) will be diffracted away from the main output beam, which can then be blocked.

A problem with this active method of mode-locking is that the RF modulation needs to be locked exactly to the length of the cavity according to Eq. (3.1). This means that any misalignment of the laser beam, or any small change in cavity length, will cause mode-locking to be lost. The Tsunami therefore uses a 'regenerative' mode-locking technique. A beamsplitter takes a small amount of the output beam to a photodiode which monitors the frequency of the pulses oscillating within the cavity, and relays this to the RF generator used for the AOM, so any changes in alignment *etc.* over time do not affect the mode-locking because the RF modulation is altered accordingly.

Because the pulse frequency is changed by the cavity length according to eq. (3.1), the frequency is to an extent tunable simply by having some of the cavity mirrors on motorized delay stages (for the Tsunami, the range is tunable across approximately 80-83 MHz). The cavity length can thus be chosen for the appli-

cation. In the case of synchronizing the laser system to the SRS which operated at 3.123 MHz, the cavity length was chosen so that the frequency range included 81.198 MHz, or twenty-six times the SRS periodicity. The method of synchronization is described in §3.2.2.

3.1.2 Waveplates and the Pockels effect

It is important to be able to manipulate the polarization of a laser beam. In the case of pump-probe measurements, the polarization of the pump and probe beams can affect the sample in different ways. In certain samples, when a probe beam is polarized parallel to the pump beam, it will preferentially probe the excited entities whose transition moment is polarized in the same direction. Measurements will be perturbed by the reorientation process [106]. To rid measurements of such perturbations, the pump and probe polarization angles should differ by a 'magic-angle' of $\theta_M = \arctan\sqrt{2} = 54.7^\circ$, the angle of the space diagonal in a cube [107]. An example is in nuclear magnetic resonance (NMR) spectroscopy, where the dipolar coupling of two nuclei subjected to a magnetic field is removed when the magnetic field is orientated at the magic-angle to the internuclear vector. Another advantage of changing the polarization of a pump beam is that it can then be rejected after the sample very easily, using a polaroid filter to reject its orientation. It is therefore highly necessary to be able to adjust the angle of polarization: one way in which this is achieved uses waveplates.

Waveplates introduce a phase difference (*i.e.* a delay) between the ordinary and extraordinary polarizations of a laser beam, which leads to a net rotation of the polarization as the beam travels through the plate. The amount of delay, Γ, that a crystal induces is related to its thickness L and its birefringence Δn:

$$\Gamma = \frac{2\pi \Delta n L}{\lambda}, \tag{3.2}$$

where λ is the wavelength of incident light [108].

A quarter wave plate (QWP or $\lambda/4$) induces a 90° delay between the ordinary and extraordinary wave components (parallel and perpendicular to the optical axis): if the plane of incident light is adjusted so that it makes an angle of 45° to the optical axis of the crystal, the polarization of the light will be converted from linear to circular polarization. A half wave plate (HWP or $\lambda/2$) is used to rotate the orientation of linearly polarized light by inducing a phase delay of 180°. If incident light has its plane at an angle ϕ to the optical axis of the crystal, the polarization will be rotated by 2ϕ. Zero-order waveplates, used to create a phase retardance, are constructed out of two individual plates with their optical axes crossed so that the

effect of the first is canceled by the second, except for the residual phase difference between them.

Waveplates are very useful and are used in many applications. The output of the Tsunami can be attenuated using a HWP followed by a polarizing beam splitter: the angle between the plane of the laser beam and the optical axis of the HWP is adjusted, varying the amounts of horizontally and vertically polarized light transmitted. A polarizing beamsplitter separates the two components, one of which is taken off the table down a periscope to the Ti:sapphire regenerative amplifier on the lower tier. A simple rotation stage controlling the angle of the optical axis of the HWP then becomes an easy-to-use variable attenuator, the output of which is

$$I = I_0 \cos^2 \vartheta, \tag{3.3}$$

where I_0 is the input intensity and ϑ the angle between the laser light polarization and the optical axis of the HWP. This is known as *Malus' Law* for a perfect polarizer.

A voltage-controlled waveplate uses the Pockels, or electro-optic, effect, which is a second-order nonlinear phenomenon. The electro-optic effect occurs when a nonlinear crystal is subject to a static electric field ξ_0 as well as the field $\xi(t)$ of a laser pulse. The first two orders of the polarization, $P(t)$ are given by

$$P(t) = \epsilon_0 \left(\chi_1 \xi(t) + \chi_2 \xi_0 \xi(t)\right) = \epsilon_0 (\chi_1 + \chi_2 \xi_0) \xi(t), \tag{3.4}$$

where χ_1 and χ_2 are the first and second-order electric susceptibilities of the material, and ϵ_0 is the permittivity of free space. The relative permittivity, ϵ_r, is related to the susceptibility by

$$\epsilon_r = \epsilon_0 (1 + \chi), \tag{3.5}$$

and so the refractive index, $n = \sqrt{\epsilon_r}$ from eq. (2.103), depends on the susceptibility according to

$$n = \sqrt{1 + \chi}. \tag{3.6}$$

Expressing the electric field as $\xi(t) = \xi_0 \sin \omega t$ and substituting into eq. (3.4) gives

$$P(t) = \epsilon_0 \sin \omega t (\xi_0 + \chi_1 \xi_0 + \chi_2 \xi_0^2), \tag{3.7}$$

and so the second-order susceptibility leads to a variation of the refractive index of the material, proportional to the static field ξ_0 because $n = \sqrt{1 + \chi}$.

The resulting change in refractive index appears as a rotation of the polarization of the laser beam which can be observed with balanced detection [109]. This forms the basis of the detection of THz pulses (known as free space electro-optic sam-

pling), where the two electric fields focused onto the crystal, as discussed in in Eq. (3.4), are from the THz and laser pulses. As the THz electric field ξ_0 changes, so does the refractive index in the crystal, and thus the polarization of the laser beam travelling through it. A polarizing beamsplitter then allows the varying amounts of horizontally and vertically polarized laser light to be detected. This method of detection allows the THz electric field ξ_0 to be measured.

3.1.3 Frequency doubling and phase matching

The process of frequency doubling, or second harmonic generation (SHG) is a nonlinear optical effect: materials that can be used to halve the wavelength of a laser beam do not have a linear dependence of polarization, P, on electric field $\xi(t)$, which can be written as a Taylor expansion:

$$P = \epsilon_0(\chi_1\xi(t) + \chi_2\xi(t)^2 + \chi_3\xi(t)^3 + \cdots), \tag{3.8}$$

where χ_1 is the linear susceptibility with χ_2, χ_3, *etc.* being nonlinear optical coefficients. Expressing the electric field as $\xi(t) = \xi_0 \sin \omega t$ gives

$$P = \epsilon_0(\chi_1\xi_0 \sin \omega t + \chi_2\xi_0^2 \sin^2 \omega t + \chi_3\xi_0^3 \sin^3 \omega t + \cdots) \tag{3.9}$$

of which the second term can be rewritten as

$$P_2 = \frac{1}{2}\epsilon_0\chi_2\xi_0^2(1 - \cos 2\omega t), \tag{3.10}$$

which shows that a nonlinear dependency of polarization leads to the generation of a wave oscillating at a frequency twice that of the incident electromagnetic wave [109]. The ratio between the amount of light at a frequency 2ω and the amount at ω is simply the ratio of the coefficients of the first two terms in Eq. (3.9):

$$R(2\omega : \omega) = \chi_2\xi_0/\chi_1, \tag{3.11}$$

thus being dependent on the properties of the material and the intensity of the laser radiation.

For laser light incident normally on such a material, the conversion efficiency can be incredibly small (as low as $10^{-6}\%$) [106]. Famously, the first detection of this phenomenon by Franken *et al.* in 1961 by doubling a ruby laser output at 694.30 nm to 347.15 nm (by focusing the laser beam onto a quartz plate) was removed from publication due to the editor mistaking the incredibly dim spot of frequency-doubled laser light for a speck of dirt on the photograph [110]. The reason is that

the nonlinear materials used in this process are also dispersive, *i.e.* the refractive index is dependent on wavelength. The fundamental and second harmonic travel at different speeds: with the fundamental continuously generating the second-order beam. The latter cannot remain in phase with itself, and is thus susceptible to destructive interference. In order to gain as high a ratio of doubled beam to fundamental as possible, *phase matching* must be achieved. This is possible by choosing to send the fundamental beam in a specific direction through the crystal (*i.e.* at a specific angle with respect to the crystal surface) so that both beams travel with the same velocity. This can make laser alignment difficult because small deviations from this angle can cause dramatic loss in the power of the second harmonic (today, this angle is usually specified by manufacturers). Once achieved, the power of the second-order beam can be 50% that of the fundamental, and it will still be coherent (this preservation of coherence is a major advantage of using non-linear crystals for this purpose).

The doubling crystal used to double the laser output at 800 nm to 400 nm (for the sample pump beam in the table-top THz spectrometer) is BBO (beta barium borate, $\beta - BaB_2O_4$) which is one of the most widely used materials. The preferential use of this crystal is due its properties: it is phase-matchable to a broad range of frequencies, from 400 nm to 3500 nm with transmission down to UV wavelengths at 200 nm. It also has a large SHG coefficient and a relatively high damage threshold. BBO in particular has superior properties for ultrafast lasers, so that, for example, frequency doubling of a 50 fs pulse at 496 nm can be achieved with a crystal 0.07 mm thick [111].

3.1.4 Regenerative amplifier

A Spitfire Pro Ti:sapphire regenerative amplifier (where the term 'regenerative' refers to the amplified pulse being trapped in a laser resonator) is used to generate high power pulses of energy >1 mJ at a repetition rate of 1 kHz. They are ultrafast with typical pulse durations of 85-90 fs at a wavelength of 800 nm. A schematic diagram of the amplifier is shown in figure (3.4). Approximately 450 mW ($\approx$ 6 nJ) from the Tsunami oscillator on the top tier of the laser system is used to seed the amplifier. The seed pulses are prevented from leaving the cavity the way they entered with the use of a Faraday isolator that only allows the laser pulses to travel through it in one direction due to the Faraday effect:

$$\beta = vBd, \tag{3.12}$$

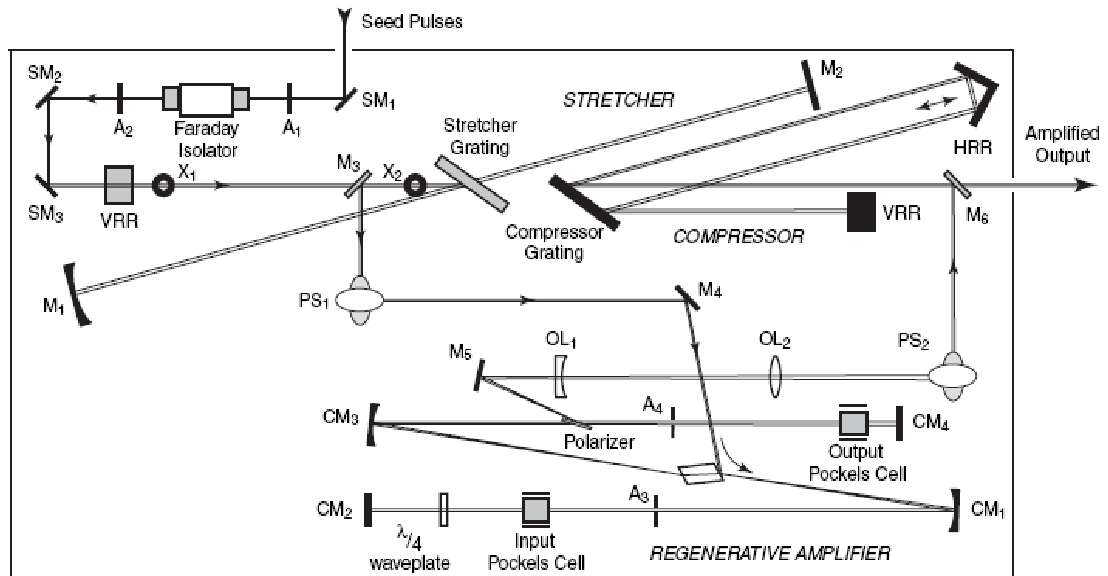

Figure 3.4: Schematic layout of the Spitfire Ti:sapphire regenerative amplifier. A: apertures; M: mirrors; SM: seed input mirrors; CM: amplifier mirrors; OL: expanding telescope lenses; PS: polarizing periscopes; VRR: vertical retro-reflectors; HRR: horizontal retro-reflector; X: position of removable iris alignment tools. The Pockels cells are used to trap and eject laser pulses in the amplifier. The Ti:sapphire crystal is shown in the centre of the amplifier section, where it is cut at the Brewster angle for horizontal polarization so that only horizontally polarized laser radiation is transmitted, and vertically polarized light is reflected. The Empower laser pump beam is focused and brought over mirror CM_3 to excite the Ti:sapphire crystal.

where β is the angle through which the polarization of the laser pulses are changed, v is the Verdet constant of the material (describing the strength of the Faraday effect in a material, which is wavelength dependent), B is the magnetic field applied, and d is the length of the rotator. A magnetic field is applied causing a 45° rotation in the polarization of the laser pulses. Polarizers before and after the rotator allow this changed polarization to propagate into the amplifier. Pulses travelling retrograde will gain another 45° rotation, meaning a total rotation of 90° compared to the input pulses. The first polarizer therefore prevents the pulses leaving, meaning no regenerative output can propagate back to the oscillator [112]. This would cause feedback to occur in the oscillator.

The seed pulses first pass through the stretcher, before being trapped in, or ejected back out of, the amplifier by the use of a Pockels cell. An amplified pulse is then extracted with another Pockels cell before passing through the compressor. This is called a *chirped pulse amplification* technique. The laser used to pump the Ti:sapphire gain medium is the Empower laser which gives an average power of 6 W at 527 nm.

The stretcher is required so that the peak pulse intensity is greatly reduced so

as to prevent damage of the Ti:sapphire crystal during amplification [113, 114]. The input beam first travels through a gap in the vertical retro-reflector VRR and above mirror M_3 to hit the stretcher grating. The grating causes dispersion of the frequencies of the laser pulse so that red wavelengths travel further than blue ones, causing temporal and spatial broadening. Gold mirror M_1 is concave and tilted to send the stretched beam above the grating to the long stretcher end mirror M_2. The beam is reflected back onto M_1, back onto the grating and then down onto the vertical retro-reflector VRR. The pulse then retraces its path through the stretcher where more temporal stretching occurs. On its return to the grating the spatial stretching is reversed to reform a circular beam but the temporal stretching of the beam is doubled (*i.e.* it has hit the grating four times in total, each time creating temporal stretching, and every other time it is incident on the grating the spatial stretching is reversed). After the beam travels through the stretcher the second time, it is taken out by mirror M_3 (the vertical retro-reflector is also at a vertical tilt).

A polarizing periscope PS_1 converts the polarization of the laser pulses from horizontal to vertical. A vertically-polarized laser pulse is sent to the Ti:sapphire crystal with mirror M_4. Because the Ti:sapphire rod is cut at the Brewster angle for horizontal polarization, the laser pulse is reflected to mirror CM_1 before travelling through the input Pockels cell. It is reflected by CM_2 and so travels through the quarter wave-plate ($\lambda/4$) and the Pockels cell (which is switched off) twice. Each time the polarization is rotated by 45° by the quarter wave plate so as it returns to the Ti:sapphire crystal the pulse is now horizontally polarized: it travels through the crystal for first-pass gain. As the output Pockels cell is also switched off at this point the laser pulse then travels back through the Ti:sapphire crystal for second-pass gain.

A laser pulse is trapped in the cavity by switching on the input Pockels cell after the pulse has passed through it a third time. A further two passes through the quarter wave plate rotate the polarization back to vertically polarized, and if the input Pockels cell is now turned on (giving another change in polarization of 90°) the laser pulse is again horizontally polarized and can continue to pass through the gain medium.

If a laser pulse arrives at the input Pockels cell for a third time and the cell is already on, two further passes through it leave the polarization unchanged: the laser becomes vertically polarized after the laser pulse travels through the quarter wave plate twice. The same happens if the Pockels cell is switched off throughout. The Ti:sapphire crystal reflects the laser pulse out of the amplifier to mirror M_4, and it is prevented from leaving the amplifier by the Faraday isolator.

The input Pockels cell is therefore switched on and off rapidly so as to keep

the laser pulse horizontally polarized. All other pulses will be rejected. Typically after 20 to 25 passes through the gain medium the output Pockels cell is switched on (this timing is computer controlled so as to control to the output power of the amplifier). Again, if the cell is turned on after the laser pulse has passed through it to mirror CM_4, the polarization will be rotated by 90° to become vertically polarized on its return, and will be extracted by the plate polarizer, where (like the Ti:sapphire crystal) horizontally polarized light is transmitted and vertically polarized light is reflected. The extracted pulse is then sent through a second polarizing periscope to return the laser pulse to horizontally polarized. The extracted pulses are also sent through an expanding telescope made from lenses OL_1 and OL_2 in order to reduce the beam intensity in the compressor.

The compressor reverses the temporal stretching of the laser beam. Longer wavelengths travel less distance than shorter wavelengths and so the pulse peak power is regained [115]. A horizontal retro-reflector (HRR) is mounted on a mechanical delay stage that can be controlled so as to optimize the temporal compression to achieve the highest possible peak power [106]. The dispersing beam from the grating travels first through the HRR before being reflected by another vertical retro-reflector VRR. The beam is therefore incident upon the grating four times as was the case in the stretcher, so all stretching is reversed. The VRR sends the beam at a slight vertical tilt so that on its exit from the compressor the beam travels over mirror M_6. The whole process occurs at a repetition rate of 1 kHz and the average power of the amplified pulse is approximately 1 W.

There is a timing delay generator (TDG) that controls the input and output Pockels cells with a high voltage supply, as well as controlling the time delay of the pump beam in the Empower laser. This means that a seed pulse is trapped in the cavity so that it passes through the Ti:sapphire crystal when the crystal is excited by the pump beam [112].

A bandwidth detector (BWD) is placed in the stretcher so as to ensure that none of the optics in the amplifier become damaged. The BWD is made of two photodiodes that are placed at the position of a weaker, high order reflection from the stretcher grating (only the zero order reflections propagate through the stretcher). After the laser beam is incident on the grating it becomes spatially as well as temporally stretched. This spatial stretching is detected by placing the two photodiodes of the BWD a set distance apart. Only when enough temporal stretching has occurred will both photodiodes be illuminated. The alignment of the seed beam, as well as its initial bandwidth, will also have to be optimum for this to occur. The TDG used for the trapping of a laser pulse within the amplifier will only be allowed to trigger when the BWD photodiodes are both illuminated. Therefore if insufficient stretching has occurred, and thus the laser pulses have peak intensities

that could damage the optics in the amplifier, the amplifier is inactive.

The gain of the Ti:sapphire amplifier, g_0 is given by

$$g_0 = \frac{J_{stored}}{J_{sat}}, \tag{3.13}$$

where J_{stored} is the pump fluence (energy density) stored in the gain medium and J_{sat} is the saturation fluence [106]. The stored fluence is given by

$$J_{stored} = \frac{E_p \alpha}{S} \frac{\lambda_p}{\lambda_s}, \tag{3.14}$$

where S is the cross-section of the pump, E_p the pump energy incident on the gain medium, α the total absorption of the pump radiation, and λ_p and λ_s are the wavelengths of the pump and seed beams. The seed pulse with low energy E_{in} will be amplified as

$$E_{out} = E_{in} e^{g_0} \tag{3.15}$$

for each pass through the amplifier cavity. Once the fluence of the seeded pulse becomes comparable to the saturation fluence of the gain medium, however, the amplified pulse energy becomes [116]:

$$E_{out} = S J_{sat} \ln \left\{ g_0 \left[\exp\left(\frac{J_{in}}{J_{sat}} \right) - 1 \right] + 1 \right\}, \tag{3.16}$$

where J_{in} is the input fluence of the seed beam. The saturation fluence for a Ti:sapphire crystal is typically 1 Jcm^{-2} [106].

3.1.5 Optical parametric amplifier

The advent of ultrafast lasers with pulse widths in the range 50 - 150 fs has allowed spectroscopic techniques at previously unobtainable temporal resolutions to be developed. In addition to ultrafast timescales, there is a need for lasers with wide wavelength tunability so that many different states of matter can be investigated - for example, electronic transitions in the ultraviolet and vibrational modes in the infrared, probed using one laser. This has led to be development of Optical Parametric Oscillators (OPOs) and Amplifiers (OPAs), the latter of which are examined here.

Optical parametric generation (OPG) was first demonstrated in 1965 [117]. A high-frequency, high-intensity pump beam (at angular frequency ω_p) amplifies a lower-frequency, lower-intensity signal beam (ω_s) in a nonlinear crystal. A third beam, the idler, is generated in addition at frequency ω_i such that $\omega_i < \omega_s < \omega_p$

[118]. Energy conservation is satisfied such that

$$\hbar\omega_p = \hbar\omega_s + \hbar\omega_i \tag{3.17}$$

and for the interaction to be efficient, momentum conservation, or phase-matching, must be satisfied such that

$$\hbar k_p = \hbar k_s + \hbar k_i. \tag{3.18}$$

Three-wave interactions in nonlinear media are more generally described by the Manley-Rowe relations [119]:

$$\frac{1}{\omega_i}\frac{dI_i}{dz} = \frac{1}{\omega_s}\frac{dI_s}{dz} = -\frac{1}{\omega_p}\frac{dI_p}{dz}. \tag{3.19}$$

The interaction results in the flow of energy from the two lower-frequency fields to the sum-frequency field or *vice versa* [118]. In the case of sum-frequency generation, two high-intensity beams at ω_s and ω_i interact to produce a beam at $\omega_s + \omega_i$. Second harmonic generation occurs when $\omega_s = \omega_i$. Difference frequency generation occurs in the case of two high-intensity beams at ω_s and ω_p interacting, whereby the beam at ω_p transfers power to the beam at ω_s and to a generated difference frequency beam at ω_i. Optical parametric amplification is similar to difference frequency generation, except that the beam at ω_s is instead much less intense than ω_p and as such experiences a large amplification, while at the same time the idler beam ω_i is generated. The intensity of the signal and idler beams (I_s and I_i) after travelling through a nonlinear crystal of length L can be shown to be [118]:

$$\begin{aligned} I_s(L) &= I_{s0}\left[1 + \frac{\Gamma^2}{g^2}\sinh^2(gL)\right], \\ I_i(L) &= I_{s0}\frac{\omega_i}{\omega_s}\frac{\Gamma^2}{g^2}\sinh^2(gL). \end{aligned} \tag{3.20}$$

Here I_{s0} is the initial intensity of the signal beam and g and Γ are

$$\begin{aligned} g &= \sqrt{\Gamma^2 - \left(\frac{\Delta k}{2}\right)^2}, \quad \text{and} \\ \Gamma &= \frac{8\pi^2 d_{eff}^2 I_p}{n_i n_s n_p \lambda_i \lambda_s \epsilon_0 c}, \end{aligned} \tag{3.21}$$

where Δk is the wave-vector mismatch, $\Delta k = k_p - k_s - k_i$, d_{eff} is the effective nonlinear optical coefficient, n_i, n_s and n_p are the refractive indices of the nonlinear crystal at frequencies ω_i, ω_s and ω_p, λ_i and λ_s are the idler and signal beam wavelengths, and c is the speed of light. In the case of perfect phase-matching such that $\Delta k = 0$ and $g = \Gamma$, equation (3.20) simplifies to:

$$\begin{aligned} I_s(L) &\cong \frac{1}{4} I_{s0} \exp{(2\Gamma L)}, \\ I_i(L) &\cong \frac{\omega_i}{4\omega_s} I_{s0} \exp{(2\Gamma L)}. \end{aligned} \tag{3.22}$$

The ratio of signal to idler intensities is such that an equal number of signal and idler photons are generated. A parametric gain factor can be defined by

$$G = \frac{I_s(L)}{I_{s0}} = \frac{1}{4} \exp{(2\Gamma L)}, \tag{3.23}$$

where the gain grows exponentially with the crystal length L and nonlinear coefficient Γ.

Equations (3.20) through to (3.23) describe monochromatic, continuous waves. For the case of ultrafast pulsed lasers,

$$E(z,t) = \Re\{A(z,t) \exp{[j(\omega t - kz)]}\}, \tag{3.24}$$

where j is the imaginary unit and $A(z,t)$ is the amplitude of the electric field. The three-wave interaction is now described by three fields, each described by eq. (3.24) moving through a nonlinear crystal with different group velocities, v_g, where

$$v_g = \frac{1}{\hbar}\frac{dE}{dk} = \frac{d\omega}{dk} \tag{eq:Vg}$$

The signal, idler, and pump beams can thus be described in terms of the group velocities, v_{gs}, v_{gi} and v_{gp} and amplitudes A_s, A_i and A_p [118, 120]:

$$\begin{aligned} \frac{\partial A_s}{\partial z} + \frac{1}{v_{gs}}\frac{\partial A_s}{\partial t} &= -j\frac{\omega_s d_{eff}}{n_s c} A_i^* A_p \exp(-j\Delta kz), \\ \frac{\partial A_i}{\partial z} + \frac{1}{v_{gi}}\frac{\partial A_i}{\partial t} &= -j\frac{\omega_i d_{eff}}{n_i c} A_s^* A_p \exp(-j\Delta kz), \\ \frac{\partial A_p}{\partial z} + \frac{1}{v_{gp}}\frac{\partial A_p}{\partial t} &= -j\frac{\omega_p d_{eff}}{n_p c} A_s A_i \exp(+j\Delta kz). \end{aligned} \tag{3.25}$$

These equations can be transformed into a frame of reference that is moving with the group velocity of the pump pulse by defining $\tau = t - z/v_{gp}$:

$$\frac{\partial A_s}{\partial z} + \left[\frac{1}{v_{gs}} - \frac{1}{v_{gp}}\right]\frac{\partial A_s}{\partial \tau} = -j\frac{\omega_s d_{eff}}{n_s c} A_i^* A_p \exp(-j\Delta kz),$$
$$\frac{\partial A_i}{\partial z} + \left[\frac{1}{v_{gi}} - \frac{1}{v_{gp}}\right]\frac{\partial A_i}{\partial \tau} = -j\frac{\omega_i d_{eff}}{n_i c} A_s^* A_p \exp(-j\Delta kz), \tag{3.26}$$
$$\frac{\partial A_p}{\partial z} = -j\frac{\omega_p d_{eff}}{n_p c} A_s A_i \exp(j\Delta kz).$$

Here it can be seen that the main issues of parametric amplification with ultrafast pulses are related to the group velocity mismatch (GVM) of the pulses, δv_{ga}:

$$\delta v_{ga} = \frac{1}{v_{ga}} - \frac{1}{v_{gp}} \qquad a = s, i. \tag{3.27}$$

The GVM between the pump and the signal/ idler beams limits the interaction length over which the amplification takes place. The GVM between the signal and idler beams limits the phase-matching bandwidth.

The pulse splitting length is defined as the propagation length through the nonlinear crystal after which the signal or idler pulse separate from the pump pulse in the absence of gain:

$$l_{ap} = \frac{\tau_p}{\delta v_{ga}}, \tag{3.28}$$

where τ_p is the pump pulse duration. The GVM will vary depending on the crystal type, the pump wavelength and the type of phase matching. For a crystal with length L shorter than the pulse splitting length, the gain expression for the case of continuous wave (CW) beams in Eq. (3.23) remains valid for ultrafast pulses as well. However, for crystal lengths comparable or greater than the pulse splitting length, GVM becomes important and the CW expressions become invalid.

A schematic diagram of the OPA is given in figure (3.5). A very small amount of the pump beam is used to generate a white light continuum in a sapphire plate. This white light gives the signal beam, whereas the rest of the beam is used as the pump in the optical parametric generation process in the BBO crystals. Wavelength tuning is achieved by changing the phase-matching angle of the BBO crystal so that a near-IR part of the white light spectrum is phase-matched to the 800 nm pump beam and amplification can occur. The amplification occurs in two stages: the first BBO crystal is the preamplifier, with the second BBO crystal being pumped by the majority of the amplifier output. This crystal is orientated so as to create saturation of the amplified signal and idler beams so that a high level of pulse-to-pulse stability is achieved.

The BBO crystals are type II, because type II phase matching has many advan-

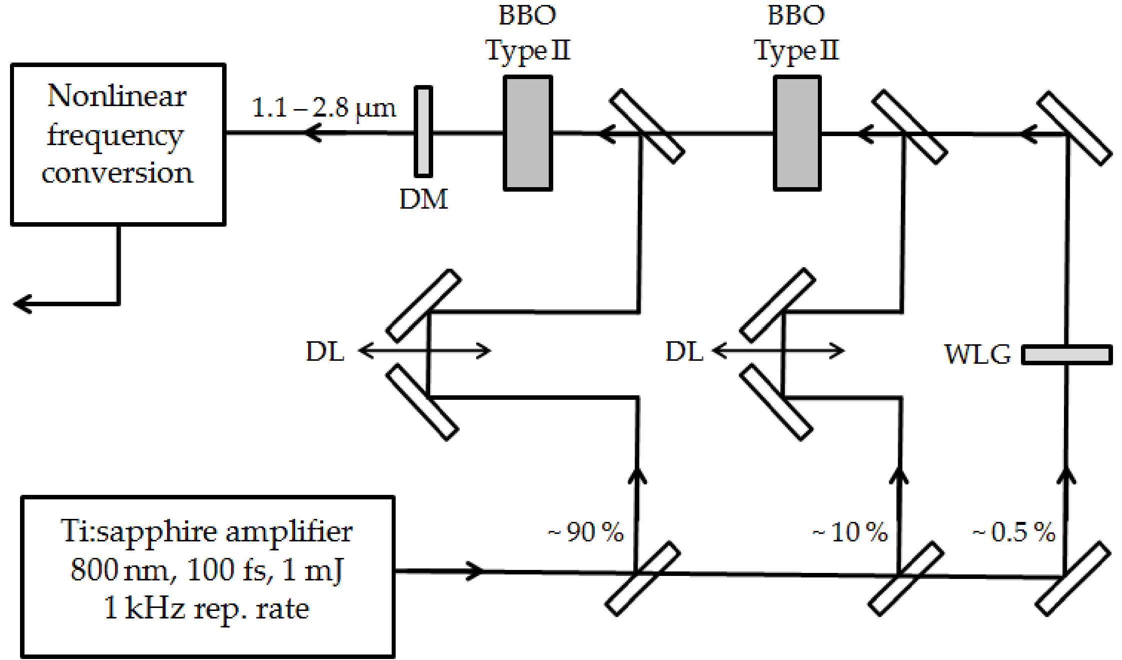

Figure 3.5: Near-infrared optical parametric amplifier using the 800 nm output from a Ti:sapphire regenerative amplifier. DL: delay line; WLG: white light continuum generation in a sapphire plate; BBO: beta barium borate nonlinear crystal; DM: dichroic mirror. The OPA creates a tunable wavelength range between 1100 and 2800 nm. Nonlinear frequency conversion (second harmonic generation *etc.*) is then used to create a tunable output ranging between 260 and 800 nm. A dichroic mirror is used on the output to remove any residual 800 nm pump beam (sent to a beam dump), although this is sometimes removed so as to use this residual pump for sum-frequency generation.

tages over type I phase matching [121]. Type II phase matching leads to the signal and idler waves having orthogonal polarizations. For instance, if the polarization of the pump is extraordinary (e), the idler will have extraordinary polarization and the signal will have ordinary (o) polarization:

$$e(\text{pump}) \rightarrow e(\text{idler}) + o(\text{signal}). \tag{3.29}$$

This means that the signal and idler beams can be separated easily using polarizing beam-splitters. Also, type II phase-matching in the BBO crystals means that the relative velocity with respect to the pump of the signal wave is opposite to that of the idler wave over most of the tuning range (*i.e.* the GVMs are of opposite signs). This means that the energy flow in the OPG process is mostly from pump to signal and idler waves so that the interaction has a higher conversion efficiency [121]. Another advantage is that the amplified bandwidth is almost independent of the signal wavelength, and so there is much better control over the bandwidth of the amplified pulses [122]. One drawback of using a type II interaction is a lower

effective nonlinearity, which means that a higher-intensity pump beam is required for the same gain in a type I interaction [121].

The output of the OPA gives up to 250 μJ of amplified light at 1400 nm, and is tunable between 1100 and 2800 nm. To achieve tunability to ultraviolet wavelengths, two nonlinear frequency conversion stages are used which also utilize BBO crystals for sum-frequency generation or second harmonic generation. For instance, to generate 700 nm, one of these stages would be used to frequency-double the 1400 nm signal beam. To achieve 350 nm, a second stage would frequency-double this again. The output energies over the Light Conversion TOPAS tuning range are shown in figure (3.6). This tuning curve is for a TOPAS-C, where Light Conversion manufacture many different versions with different wavelength tuning ranges. The dichroic mirror used on the output of the OPA to block the residual pump beam at 800 nm is sometimes removed so as to sum its frequency with either the signal or the idler beams, so as to extend the tuning range to 230 nm (≈ 5.4 eV).

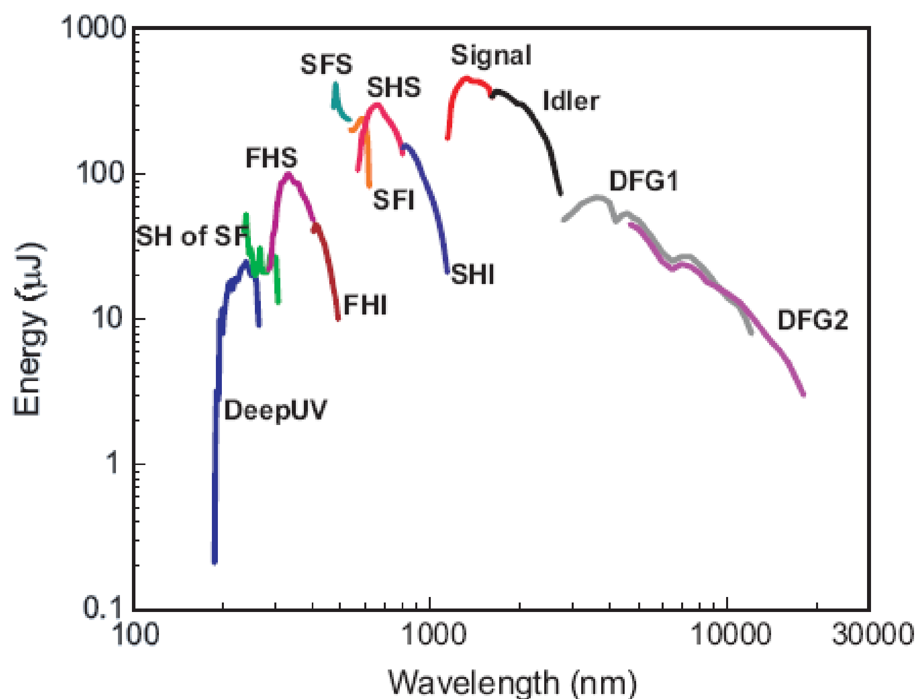

Figure 3.6: Tuning range for the Light Conversion TOPAS (www.lightcon.com), using a 2 mJ amplifier output. SHS: second harmonic of signal beam; SHI: second harmonic of idler beam; SFS: sum-frequency of signal and pump beam; SFI: sum-frequency of idler and pump beam; FHS: fourth harmonic of signal beam; FHI: fourth harmonic of idler beam; SH of SF: second harmonic of the sum-frequency of the pump and signal (blue) and idler (green) beams. DFG refers to a difference-frequency setup that can be installed to extend the tuning range further into the infrared, although this is not used here.

To summarise, the OPA gives a reproducible, stable output ($\pm$ 2% r.m.s. is specified) over a wide range of wavelengths to be used in pump-probe spectroscopies. It is also ideal for non-specialist users because most of the time it operates as a turn-key 'black box' requiring little maintenance.

3.1.6 Laser beam radius measurement

An accurate measurement of the laser beam diameter is achieved using a knife-edge method [123]. It is a simple and well-established technique that can be easily applied with minimal equipment and calculations, and has been found to be as accurate as similar slit and aperture methods [124]. Moreover, this low-cost method can yield a high spatial resolution that is limited only by the resolution of the mechanical stages used [125]. A knife-edge is mounted on a translation stage perpendicular to the path of a laser beam which is subsequently incident on a power meter. The knife-edge is translated across the beam, and the translation stage micrometer is measured at the points at which the knife-edge reduces the power incident on the power meter to 90 % and 10 % of its total power, P_{TOT}. The laser beam is assumed to have a Gaussian profile, and the beam width, w, is defined to be the radius at which the intensity is reduced to $1/e$ times its maximum.

The intensity, $I(x, y)$, of a Gaussian laser beam propagating in the z-direction is given by

$$I(x,y) = I_0 \exp\left[\frac{-r(x,y)^2}{w^2}\right], \tag{3.30}$$

where $r(x,y) = \left[(x-x_0)^2 + (y-y_0)^2\right]^{\frac{1}{2}}$, with x_0 and y_0 defining the position of the centre of the beam. The total power of the Gaussian beam, P_{TOT}, is the intensity integrated over the area of the laser beam according to:

$$P_{TOT} = \int_{-\infty}^{\infty} I(x,y)dxdy = \frac{\pi}{2} I_0 w^2. \tag{3.31}$$

By measuring the positions at which the knife-edge reduces the total power, P_{TOT}, as it is translated across the beam in one direction, to 90 % (at a point d_{90}) and 10 % (at d_{10}), the beam width is calculated according to [123]:

$$w = 0.552\left[d_{10} - d_{90}\right]. \tag{3.32}$$

The setup is illustrated in figure (3.7). Equation (3.32) demonstrates the simplicity of this technique, in that a complete profile of the beam shape is not required. This method is also advantageous because the measurements can be performed relatively quickly.

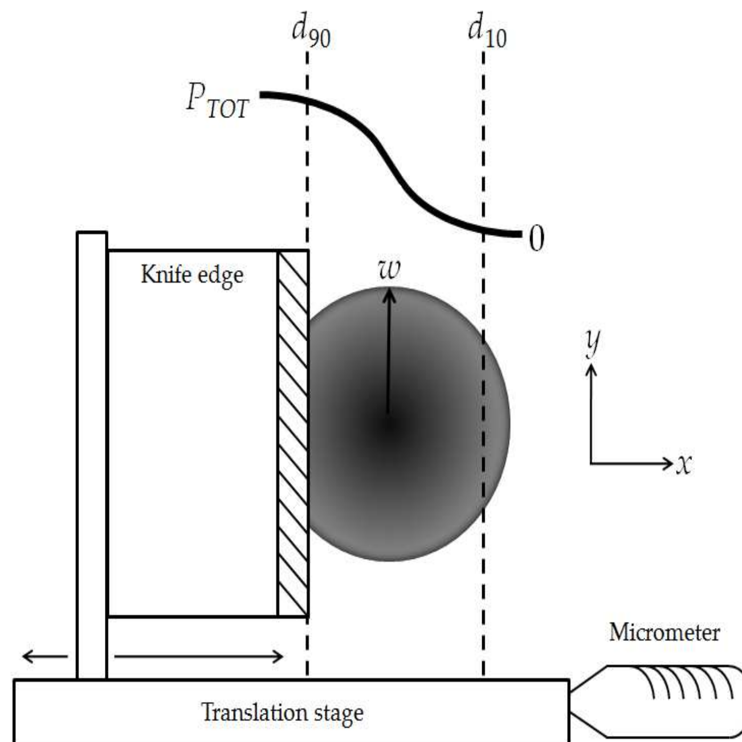

Figure 3.7: The knife-edge beam radius measurement. The knife-edge is translated across the laser beam as the laser power is monitored with a power meter. A micrometer is used to measure the points at which the power is reduced to 90 % (at d_{90}) and 10 % (at d_{10}) of the total power, P_{TOT}. The change in the laser power as the knife-edge translates across it is illustrated by the black curve.

3.2 Laser-pump synchrotron-probe experiments

The ability to synchronize the laser output with an external reference is a powerful tool when combining the laser system with an external light source for experimentation. A good example of this occurs in pump-probe experiments when an external synchrotron is used to generate the radiation for the probe [31, 32, 33, 34, 35]. In the case of the experiments synchronizing the laser system to the SRS at Daresbury Laboratory (presented in §3.2.2), the SRS is used as an X-ray source (with a pulse duration of 200 ps r.m.s.), and the samples are pumped with radiation from the laser in an ultra high vacuum (UHV) chamber (with pressures down to 1×10^{-10} mbar). It is essential to be able to synchronize the two sources so that the delay time between pump and probe pulses does not change uncontrollably. The delay time is then calibrated by introducing a fast photodiode into the UHV chamber at the sample position.

In the following sections, X-ray photoelectron spectroscopy (XPS) is discussed, whereby the X-ray synchrotron probe is used to study the core energy levels of a sample, followed by the methodology of synchronizing the laser system to the SRS

for pump-probe spectroscopy. Finally, pump-probe experiments carried out at the SOLEIL synchrotron facility in Paris using a portable 375 nm laser are introduced.

3.2.1 X-ray photoelectron spectroscopy (XPS)

A high energy X-ray photon probe with energy $h\nu$ frees electrons from a sample due to the photo-electric effect, where the electron kinetic energies are

$$KE = h\nu - BE - W, \tag{3.33}$$

where BE is the binding energy of the electrons and W is the workfunction of the electron analyser, which gives an intrinsic shift to the kinetic energies of the electrons. The high energy of the probe means that bound core level electrons are freed, and so an electron energy analyser is used: electrons at each kinetic energy are counted to determine the populations of the core levels in a sample, *i.e.* mapping the filled density of states. This technique probes the surface of the sample because it is this region from which the electrons can escape (electrons from within the bulk of the sample scatter and are re-absorbed) [43]. The depth from which electrons in a sample can escape is determined by the inelastic mean free path of electrons, λ, which is the distance travelled by an electron before a scattering event occurs [126]. The dependence of the inelastic mean free path of electrons on kinetic energy is described by the universal curve shown in figure (3.8). The intensity of an electron beam travelling through a solid decays according to the Beer-Lambert law:

$$I(z) = I_0 e^{-\frac{z}{\lambda}}, \tag{3.34}$$

where z is the distance through the solid and I_0 is the initial intensity of the electron beam. The inelastic mean free path length is thus defined as the distance the electron beam can travel before its intensity has decreased to $(1/e)$ of its initial intensity. In XPS this means that 63% of detected electrons escape from a surface depth λ, with 86% escaping from a depth 2λ and 95% escaping from a depth 3λ. For example, the inelastic mean free path of an electron with a kinetic energy of 10 eV is 1 nm.

An electron analyser is constructed from a hemispherical cavity subjected to an electrostatic field created by outer and inner plates at different potentials, typically kV. Theses voltages are calibrated to ensure passage of electrons at a certain energy (the pass energy) to the electron counter. An electron counter such as a Channeltron is an electron multiplier made from a glass funnel coated in a thin semiconducting layer, with a negative high voltage applied to the wider input end.

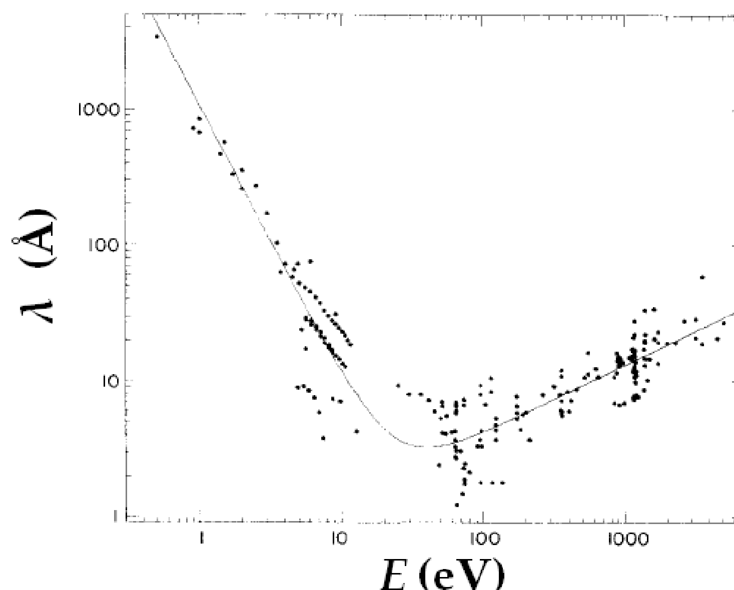

Figure 3.8: Inelastic mean free path of electrons, λ, versus kinetic energy [126]. Data points are elements: the even distribution around the curve makes it universal.

Electrons emitted through secondary emission are accelerated towards the narrow end where a separate anode collects the multiplied electrons. A schematic diagram of an XPS experiment is shown in figure (3.9). In fixed analyser transmission (FAT) mode, the voltages of the retarding lens create an electrostatic field that retards electrons of a certain kinetic energy to the analyser pass energy, as well as focusing the electrons on the analyser entrance slit. This mode is also known as constant analyser energy (CAE) mode. The voltages are then varied so as to sample electrons of different kinetic energies. Samples studied with XPS are usually solid because the experiment must take place under ultra high vacuum (UHV) in order to prevent surface contamination over the timescale of the experiment.

The energy distribution curves recorded in XPS are spectral functions that are affected by all the possible excitation processes in the sample. Typical XPS spectra include a background that increases with binding energy, due to inelastic scattering of electrons within the sample. Only 63% of detected electrons escape from a depth of up to one mean free path; other electrons will therefore undergo inelastic scattering events (leading to a loss in kinetic energy, where one electron can undergo multiple losses) before escaping the sample and being detected.

Photoemission peaks observed in an XPS spectrum for s-orbital ($l = 0$) electrons are singlets, whereas p-orbital ($l = 1$) peaks are doublets. This is due to spin-orbit splitting, in that there are two possible values for the total momentum quantum number $j = |l \pm s|$, where $s = 1/2$ is the electron spin (thus for p-orbitals j can be $\frac{1}{2}$ or $\frac{3}{2}$). The populations, and thus intensities, of each peak in a doublet is due to

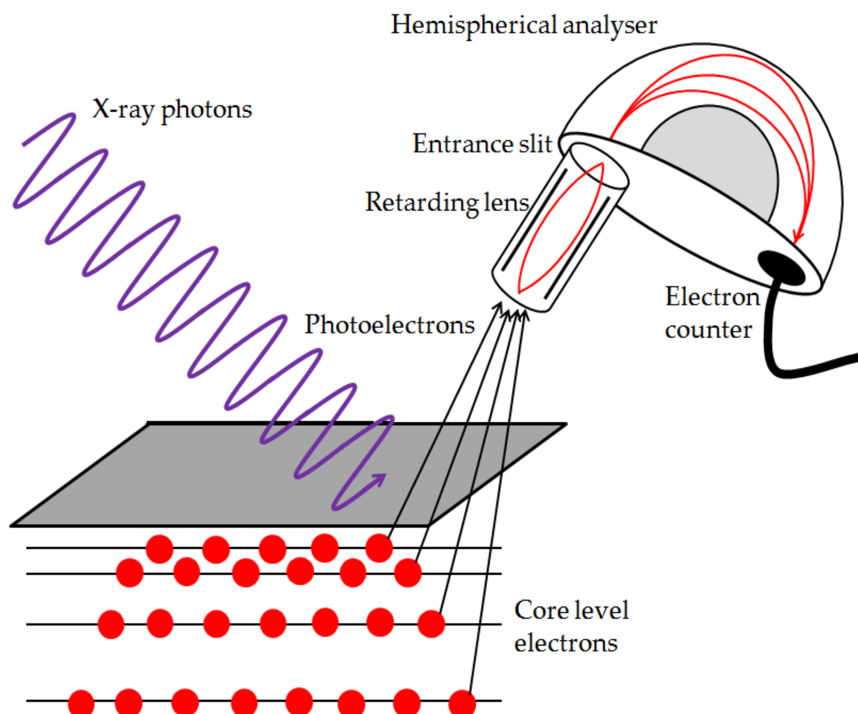

Figure 3.9: The X-ray photoelectron spectroscopy (XPS) experiment. In fixed analyser transmission (FAT) mode, the voltages of the retarding lens create an electrostatic field that retard electrons at a certain kinetic energy to the analyser pass energy. The voltages in the hemispherical analyser are fixed so that only electrons at the pass energy reach the electron counter, and a spectrum is obtained by scanning the retard potential. Only electrons from atoms close to the surface of the sample can reach the analyser due to the inelastic mean free path of electrons in a solid (figure (3.8)). The sample is held under ultra high vacuum to prevent surface contamination.

the degeneracy, $(2j+1)$, of each orbital. For p-orbitals this degeneracy is 2 and 4 for $j = \frac{1}{2}$ and $j = \frac{3}{2}$ respectively. This means 6 electrons occupy a p-orbital, and the relative populations of the doublet peaks will be 2:4 or 1:2. Table (3.1) summarises the electron populations and degeneracies of the s, p, d and f orbitals, and the filling of electronic levels up to the $4f_{7/2}$ orbital is shown in table (3.2).

l	Notation	$j = \lvert l+s \rvert$	$(2j+1)$	Electrons	Doublet ratio
0	s	$^1/_2$	2	2	-
1	p	$^1/_2\,,\,^3/_2$	2 , 4	6	1:2
2	d	$^3/_2\,,\,^5/_2$	4 , 6	10	2:3
3	f	$^5/_2\,,\,^7/_2$	6 , 8	14	3:4

Table 3.1: Degeneracy and population of the s, p, d and f electronic orbitals, and the ratio of the intensities of the doublet peaks observed in XPS.

The strength of the spin-orbit coupling will affect the energy spacing between the doublet peaks, *e.g.* the energy difference between the $2p_{1/2}$ and $2p_{3/2}$ states.

n	l	$(n+l)$	s	$j = \lvert l+s \rvert$	Orbital	X-ray notation
1	0	1	$\pm^1/_2$	$^1/_2$	$1s_{1/2}$	K
2	0	2	$\pm^1/_2$	$^1/_2$	$2s_{1/2}$	L_1
2	1	3	$-^1/_2$	$^1/_2$	$2p_{1/2}$	L_2
2	1	3	$+^1/_2$	$^3/_2$	$2p_{3/2}$	L_3
3	0	3	$\pm^1/_2$	$^1/_2$	$3s_{1/2}$	M_1
3	1	4	$-^1/_2$	$^1/_2$	$3p_{1/2}$	M_2
3	1	4	$+^1/_2$	$^3/_2$	$3p_{3/2}$	M_3
4	0	4	$\pm^1/_2$	$^1/_2$	$4s_{1/2}$	N_1
3	2	5	$-^1/_2$	$^3/_2$	$3d_{3/2}$	M_4
3	2	5	$+^1/_2$	$^5/_2$	$3d_{5/2}$	M_5
4	1	5	$-^1/_2$	$^1/_2$	$4p_{1/2}$	N_2
4	1	5	$+^1/_2$	$^3/_2$	$4p_{3/2}$	N_3
5	0	5	$\pm^1/_2$	$^1/_2$	$5s_{1/2}$	O_1
4	2	6	$-^1/_2$	$^3/_2$	$4d_{3/2}$	N_4
4	2	6	$+^1/_2$	$^5/_2$	$4d_{5/2}$	N_5
5	1	6	$-^1/_2$	$^1/_2$	$5p_{1/2}$	O_2
5	1	6	$+^1/_2$	$^3/_2$	$5p_{3/2}$	O_3
6	0	6	$\pm^1/_2$	$^1/_2$	$6s_{1/2}$	P_1
4	3	7	$-^1/_2$	$^5/_2$	$4f_{5/2}$	N_6
4	3	7	$+^1/_2$	$^7/_2$	$4f_{7/2}$	N_7

Table 3.2: Electron configuration up to the $4f_{7/2}$ orbital. Energy levels are filled with increasing energy described by the quantum numbers $(n+l)$, where lower values of n are filled first when two or more states have the same value for $(n+l)$. X-ray nomenclature is also included.

For a given value of $(n+l)$ this separation increases with the atomic number of the atom. For a given atom, the doublet separation increases with both n and l [127].

The peaks observed in an XPS spectrum include photoelectron peaks from atomic core levels and Auger emission. Whereas the kinetic energies of observed photoemission peaks (of fixed binding energies) will change depending on the X-ray photon energy according to eq. (3.33), Auger emission peaks occur at fixed kinetic energies. This is because Auger emission occurs when a core level electron relaxes to a lower atomic state made available after a primary photoelectron is emitted following X-ray photoexcitation. This excess energy is emitted either as a photon (X-ray fluorescence), or is used in exciting another electron (Auger emission). Auger emission for the case of a 1s electron (or K state in X-ray notation) ejected upon photoexcitation leads to an internal transition from the 2p to the 1s state (the 2p state is labelled $L_{2,3}$ in X-ray notation), thus ejecting another 2p electron, is shown in figure (3.10). The Auger emission energy for this transition, $E_{KL_{2,3}L_{2,3}}$ is therefore approximately [127]:

$$E_{KL_{2,3}L_{2,3}} = E_K - E_{L_{2,3}} - E_{L_{2,3}}. \quad (3.35)$$

This energy is clearly independent of the X-ray energy, or indeed the primary beam composition (*i.e.* an electron or ion beam could create Auger emission in the same way as an X-ray beam).

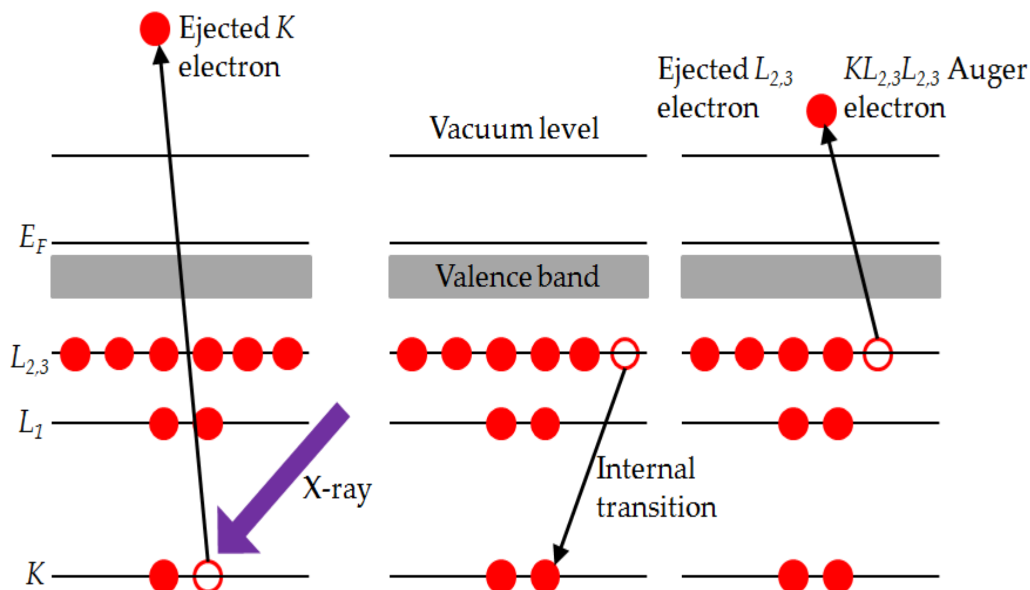

Figure 3.10: The Auger emission process for a $KL_{2,3}L_{2,3}$ Auger electron, adapted from [127]. The relaxation of the atom after photoexcitation leads to the emission of an Auger electron.

The intensity of a photoelectron peak in an XPS spectrum is given by [127]

$$I = J\rho\sigma K\lambda, \quad (3.36)$$

where J is the X-ray photon flux, ρ is the atomic concentration, σ is the cross section for photoelectron production (a probability for the photoelectric effect to occur for a particular orbital in a particular atom), K is an attenuation due to instrumental factors, and λ is the attenuation length of electrons in the solid (analogous to the mean free path length). Photoelectron peaks in an XPS spectrum can thus be used to determine the atomic composition of a material being studied, in that the ratio of XPS peak intensities for an element (adjusted by relevant cross sections *etc.*) gives the percentage atomic composition. If N_A is the amount of a particular atom in a sample, the percentage amount of A can be calculated using

$$N_A\% = \frac{I_A/F_A}{\Sigma(I/F)} \times 100\% \quad (3.37)$$

where F is the sensitivity factor for a particular electron orbital (a conglomeration

of the factors in eq. (3.36)).

XPS can also probe the valence band of a material. This occurs at low binding energies (typically 0-20 eV) and is due to electrons involved in bonding orbitals rather than core levels at much higher binding energies [128]. Measuring the valence band spectrum allows for the Fermi energy, E_F, of a sample to be determined from the low binding energy cut-off of a metal in electrical contact with the sample. Core levels appear in the XPS spectrum at binding energies greater than the valence band. In the case of zinc, for example, the first core level seen at higher binding energies than the valence band is the 3d state.

The photoelectron peak shapes are determined by a Lorentzian contribution, caused by the limited natural lifetime of the core hole state, and a Gaussian broadening contribution caused by the line shape of the X-ray beam exciting the sample as well as electron scattering and detection in the analyser, *i.e.* by instrumental factors [129]. The Lorentzian contribution $L(E)$ is given by

$$L(E) = \left\{ 1 + \left[\frac{E - E_0}{\beta} \right]^2 \right\}^{-1} \tag{3.38}$$

and the Gaussian contribution $G(E)$ is given by

$$G(E) = \exp \left\{ - \ln 2 \left[\frac{E - E_0}{\beta} \right]^2 \right\}, \tag{3.39}$$

where both are characterized by the peak position E_0 and the full-width at half-maximum height (FWHM) of the peak, where $\beta = \frac{1}{2}$ FWHM. The convolution of these two contributions, the Voigt function, gives the best description of the spectral peaks:

$$f(E) = hf(L^*G) = h \int_{-\infty}^{+\infty} L(E')G(E - E')dE', \tag{3.40}$$

where h is the peak height, or maximum intensity. It is important to note that the Voigt function contains independent full-width at half-maximum heights for the Lorentzian and Gaussian contributions [129]. Calculating this convolution can be computationally time consuming, and so two approximations to the Voigt function are often used, whereby the spectral line function $f(E)$ is determined by either a product or a summation of the two contributions. The product approximation is determined by

$$
\begin{aligned}
f(E) =& h\left\{1 + M_V\left[\frac{E - E_0}{\beta + \alpha(E - E_0)}\right]^2\right\}^{-1} \\
& \times \exp\left\{-(1 - M_V)\ln 2\left[\frac{E - E_0}{\beta + \alpha(E - E_0)}\right]^2\right\},
\end{aligned} \tag{3.41}
$$

and the sum approximation by

$$
\begin{aligned}
f(E) =& hM_V\left\{1 + \left[\frac{E - E_0}{\beta + \alpha(E - E_0)}\right]^2\right\}^{-1} \\
& + h(1 - M_V)\exp\left\{-\ln 2\left[\frac{E - E_0}{\beta + \alpha(E - E_0)}\right]^2\right\}.
\end{aligned} \tag{3.42}
$$

Here M_V is the mixing ratio (1 for purely Lorentzian, 0 for purely Gaussian, typically set to 0.7, dependent on the ratio of natural to instrumental broadening), and α is the asymmetry index. These approximations set the full-width half-maximums to be equal for both contributions. Hesse *et al.* have shown that the sum approximation is closer to the true Voigt function [129], and this is implemented in the XPS analysis software CasaXPS (www.casaxps.com) in this work.

A good visual indication of the goodness of the peak fitting is given by plotting the residual of the fit $R(i)$:

$$
R(i) = \frac{S(i) - M(i)}{\sqrt{M(i)}} \tag{3.43}
$$

where $S(i)$ is the fit and $M(i)$ is the data.

3.2.2 Synchronization of the laser system to the SRS

The aim of the experiments at the SRS is to measure the change in the surface photovoltage (SPV, eq. (2.91)), induced by laser photoexcitation (the pump), over the time period of the synchrotron repetition rate (for the SRS, 320 ns). Therefore the laser pulses must be synchronized to coincide at the sample at the same time as the X-ray probe beam and at the same repetition rate. The pump-probe delay time, τ, then needs to be controlled and varied to measure the change in the SPV over time.

A Spectra-Physics 'Lok-2-Clock' electronics module for the Tsunami Ti:sapphire oscillator allows the laser output to be synchronized to an external reference such as a synchrotron light source, with time jitters reduced to 1 ps r.m.s. as monitored by a fast photodiode, using a motorized mirror to correct coarse changes, as well

as a mirror mounted to a piezoelectric motor for fine changes, in the repetition rate. In the case of the SRS, the repetition rate is 3.123 MHz in which there are 160 RF buckets available to be filled with electrons, approximately 2 ns apart (at 499.68 MHz, which is the external reference used). Because this frequency is too high for the Tsunami to operate (the tuning range of the Tsunami is approximately 80 to 83.3 MHz), some electronics is implemented to divide the external reference to within this range. The Tsunami oscillator frequency was chosen so that the operating frequency range would allow an integer division (by a pulse picker) to give the synchrotron repetition rate.

The SRS has two modes of operation: single-bunch (SB) and multi-bunch (MB). Whereas approximately 80% of the RF buckets are filled with electrons in MB, SB has only one bunch every 320 ns.

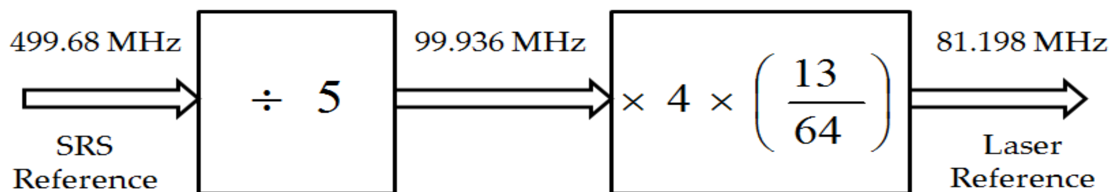

Figure 3.11: A schematic diagram of the electronics used to divide the SRS reference frequency to one that can be used to synchronize the laser to it. The pulse picker can then be used to 'divide' this frequency so that one pulse is generated for each SRS pulse in single-bunch mode. The Direct Digital Synthesiser (DDS) can introduce a time delay between laser probe and SRS pump pulses.

A frequency divider is used to divide the SRS reference by five, after which a Direct Digital Synthesiser (DDS) is used to convert the signal to match 81.198 MHz that the Tsunami oscillator is capable of generating (a separate frequency divider of five is used because the DDS can only perform multiplications or divisions by numbers which can be expressed as 2^x). A DDS is used to implement complex multiplication and divisions of RF signals, by storing points of a waveform digitally before recalling them in order to generate a new waveform (after multiplications). A digital to analogue converter (DAC) is then used to create an output voltage (the process is illustrated in figure 3.11). A pulse picker is then employed so that one pulse in every twenty-six is used, meaning that one laser pulse will be generated every 320 ns, synchronized to the SRS. The DDS then becomes a powerful tool as the phase increment between the points it samples can be adjusted, leading to a delay in the output laser pulse (a phase difference of 30° leads to a 1 ns delay). This means that the delay time between the oscillator laser and synchrotron pulses can be varied easily and accurately, thus laser-pump synchrotron-probe experiments can be carried out. The use of the DDS is far superior than the use of a mechanical delay stage: for a 320 ns time delay, a mechanical stage would need

to be 96 m long. A mechanical delay stage would also be highly sensitive to laser alignment errors as the time delay could not be accurately known unless the stage was aligned so that the input and output beams were exactly parallel.

The laser system is now synchronized to the synchrotron, and the delay time between the pump and probe is controlled by the direct digital synthesiser (DDS) that introduces a phase shift into the laser output. This phase shift is analogous to a traditional delay line as shown in figure (3.12).

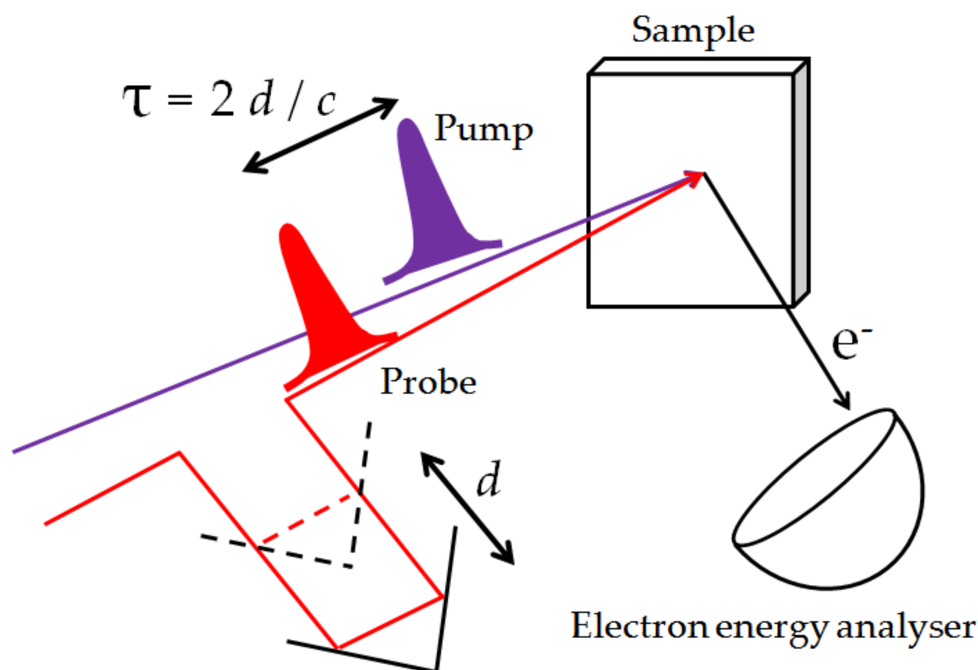

Figure 3.12: A laser-pump synchrotron-probe experiment using an optical delay line to introduce a pump-probe delay time. A Direct Digital Synthesiser can be used to generate this time delay electronically rather than mechanically.

The first material studied in these experiments was a wafer of *n*-type Si (111), the most common semiconductor used in traditional solar energy cells. The laser pump beam at 800 nm (1.55 eV) excites valence band electrons across the band gap (E_g = 1.12 eV in silicon [130]) and so the band bending at the surface interface changes as described in section 2.4. This change in the amount of band bending at the surface, the surface photovoltage change, is determined using XPS of the *Si* 2*p* core level. XPS is an ideal method for studying the SPV as the analysed photoelectrons come mainly from the surface atoms, where the band bending will be experienced in the space charge layer, as shown in figure (3.13). The SPV change is revealed as a shift in the kinetic energy of the photoemission spectrum.

For an n-type semiconductor the spectrum will shift to lower kinetic energies (higher binding energy), and for a p-type semiconductor the spectrum will shift to higher kinetic energies. The laser photoexcites electrons into the conduction

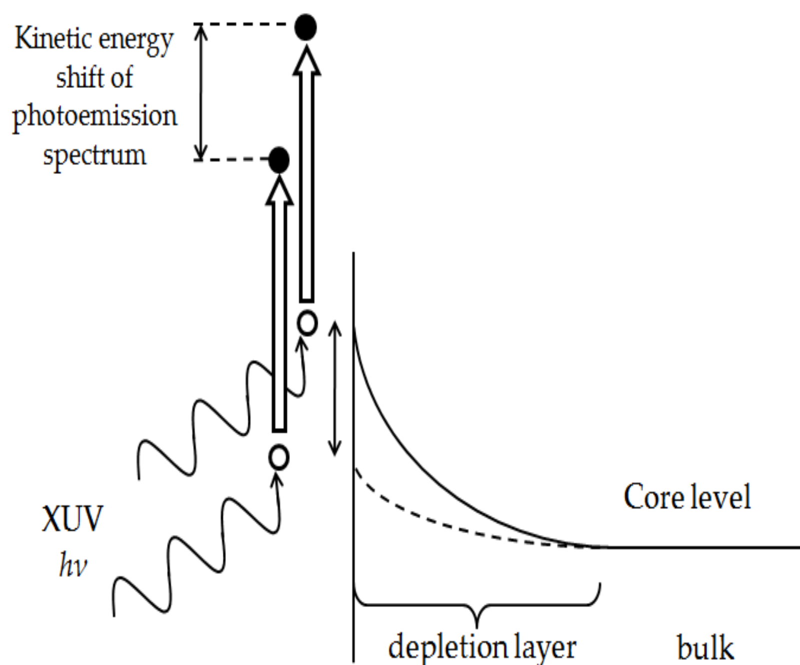

Figure 3.13: Determination of the surface photovoltage using XPS. Here the semiconductor is *n*-type and so upon laser illumination to the photoemission spectrum will shift to lower kinetic energies, as the surface band bending is reduced by charge injection (see figure (2.14)).

band, which then separate across the space charge region, with electrons drifting towards the bulk and the holes towards the surface in an *n*-type semiconductor (and vice versa for a *p*-type semiconductor), which suppresses the band bending. As the electrons recombine with holes radiatively, the amount of kinetic energy shift observed decays.

3.2.3 Pump-probe experiments at SOLEIL

For these experiments, a portable 375 nm CUBE laser by Coherent was used at the TEMPO beamline at the SOLEIL synchrotron radiation source [131]. A signal generator with a variable period, T, was used to turn the laser on and off at each half-period as shown in figure (3.14). This TTL output is used to trigger in-house software that captures a narrow XPS energy range centred on a particular core level of the sample under study. 20,000 XPS spectra are captured over the period T, so for example, setting the TTL period to 1 ms will mean an XPS spectra is captured every 50 ns, with the laser turning on and off every 0.5 ms. There are very few counts recorded per capture, and so many accumulations of these XPS spectra are recorded to achieve a good signal-to-noise ratio (typically requiring of the order of 10,000 accumulations). The surface photovoltage effect (SPV) on a particular core energy level can be measured with good temporal resolution, as the

core level shifts in energy as the laser is turned on and decays back to its original energy once the laser is turned off.

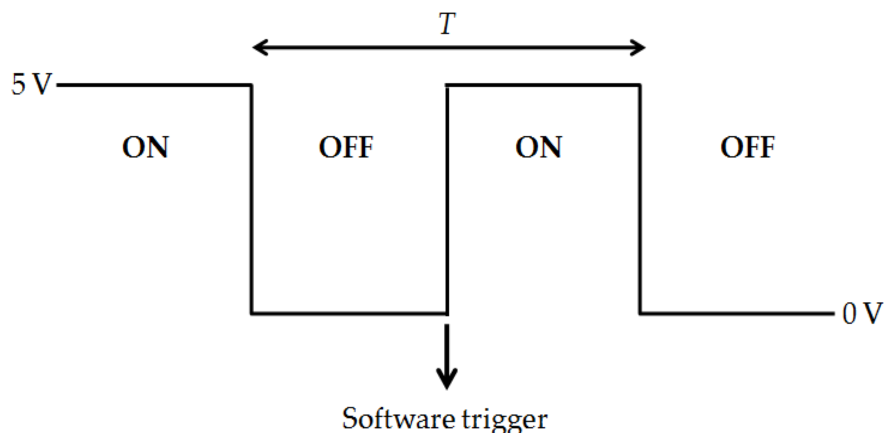

Figure 3.14: A signal generator creates a TTL signal to control the CW laser: 5 V for on, 0 V for off. The period, T, is variable and typically set to 1 ms. The signal generator is used to trigger the pump-probe software which captures 20,000 XPS spectra over the period.

The technological advances required to be able to record a narrow XPS spectrum up to every 5 ns were first made at the ELETTRA synchrotron radiation source at Trieste, Italy [132]. Instead of using a charge-coupled device (CCD) for detection on the electron analyser, a two-dimensional array of microchannel plate detectors (MCPs) is used, whereby electron multiplication occurs in an applied electric field. A cross-delay anode detector is used to measure the electron signals: spatial information is measured using a delay line where the time-delay signal is converted to spatial information using a combination of constant fraction discriminators (CFDs) and time-to-digital converters (TDCs) [133]. CFDs are used so that the start and stop signals from the delay lines are unaffected by peak amplitude variations. The TDCs allow XPS signals of the order of megacounts per second to be acquired. Data acquisition and computer interfacing are automated by a field programmable gate array (FPGA) which controls the pump-probe experiment using a trigger from the pump [132]. At TEMPO there is a 150 ns time resolution limit due to the time difference in the signals from the delay line detector (the so-called 'transit time spread' of electrons travelling through the analyser), and the speed of the electronics.

XPS spectra were also recorded with much greater signal-to-noise ratios on a variety of core energy levels when the laser was permanently off and permanently on. Additionally, the power of the laser was controllable, and so it was possible to study the SPV effect at a variety of different laser powers.

3.3 Time-resolved THz spectrometer

This section details the table-top time-resolved THz spectrometer (TRTS) that has been built in the Photon Science Institute, starting from a layout of the spectrometer before explaining the non-linear optical phenomena utilized in the generation and detection of the THz beam. The setup of ultraviolet/visible/near-infrared-pump THz-probe experiments is then explained before detailing the various experimental challenges that have been overcome in fabricating the spectrometer. The output of the Spitfire regenerative amplifier is used to generate and detect THz pulses. The pump used in the experiments comes either from the TOPAS-C optical parametric amplifier, or by frequency-doubling a portion of the 800 nm amplifier output. Both of these setups are described.

The THz spectrometer was designed, built and commissioned by the author of this work, in consultation with Dr. Darren Graham.

3.3.1 Schematic layout

The spectrometer has three main components: THz generation, THz detection, and pump beam. One of the main logistical problems of the setup is the matching of path lengths of both the generation and detection beam paths, and the pump and probe (or generation) beam paths to the sample. Measuring the THz probe beam alone essentially involves a pump-probe technique involving a delay line, and is one of the reasons why THz spectroscopy is more challenging than other more traditional techniques such as transient absorption (TA) spectroscopy, where the probe beam is simply detected by a photodiode, photodiode array, or CCD (charge-coupled device) camera.

Initial studies of quartz (§4.1.1), two solvents (§4.1.2) and GaAs (§4.1.3) were carried out using the setup in figure (3.15). The output of the Spitfire regenerative amplifier (1 W average power at a 1 kHz repetition rate, with a wavelength of 800 nm) is used for THz generation and detection, as well as for the photoexciting pump beam. In this case, the path length of the pump and THz generation beams from the first beamsplitter (BS1) to the sample is matched. The THz generation and detection beams from the second beamsplitter (BS2) to the ZnTe detection crystal is also matched. Delay line DL1 is used to scan the THz pulse, and delay line DL2 is used to vary the pump-probe delay time τ. The pump beam is either the 800 nm (1.55 eV) amplifier output, or a doubling crystal is inserted to generate a 400 nm (3.10 eV) pump beam.

For studies on bulk InP (§4.2), a variable pump beam energy was required as opposed to simply 800 and 400 nm in the previous setup. The output from

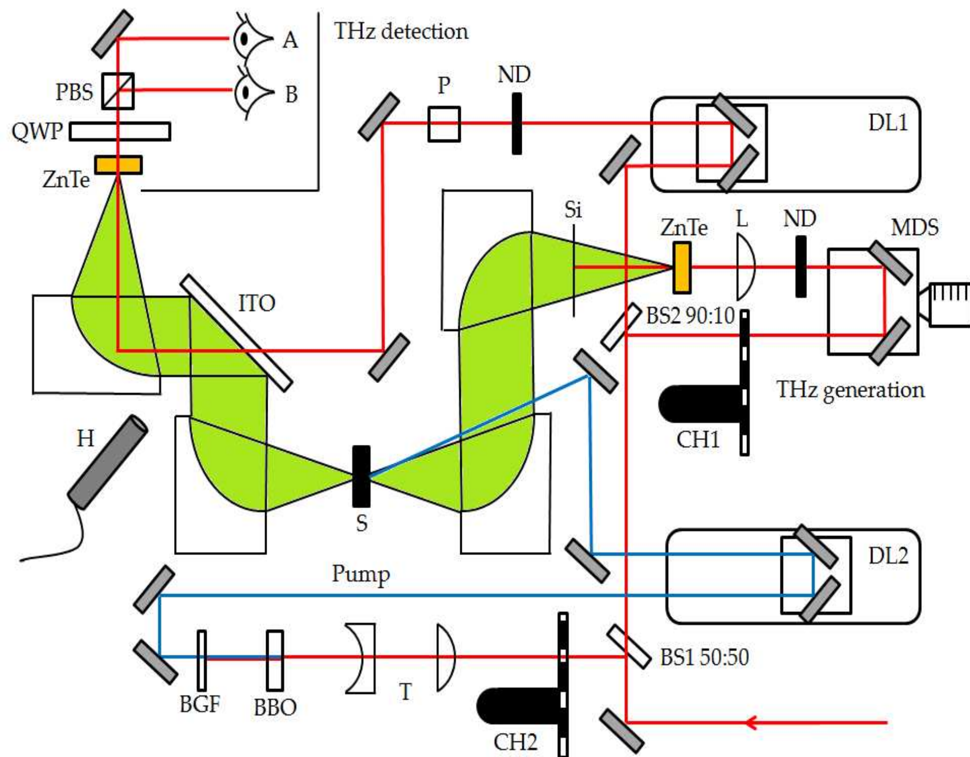

Figure 3.15: Layout of the time-resolved THz spectrometer made of three sections: THz generation, THz detection, and a pump beam. The large mirrors used to reflect and focus the THz beam are gold parabolic mirrors. BBO: beta-barium-borate crystal for frequency doubling of the pump beam. BGF: blue glass filter to reject the 800 nm after frequency doubling; CH1 and CH2: optical choppers; DL1 and DL2: optical delay lines; MDS: manual delay stage; ND: neutral density filter; T: telescope; L: lens; BS1 and BS2: beam splitters; ZnTe: THz generation and detection crystals; Si: high resistivity silicon filter; P: polarizer; ITO: indium-tin-oxide coated glass; QWP: quarter wave-plate; PBS: polarizing beam splitter; A and B: photodiodes; H: humidity monitor; S: sample.

the regenerative amplifier is then split on the main laser table to be used in an optical parametric amplifier (OPA). This new setup is illustrated in figure (3.16). This is additionally challenging because the path lengths of the pump and THz probe now need to be matched to the point at which the beams are split on the main laser table. The THz generation/ detection beam needs to be taken on an additional delay to compensate for the complicated route the pump beam takes through the OPA. The OPA gives a continuous range of pump wavelengths from 230 nm - 20 μm, of which 370 - 800 nm are used to study InP. The OPA setup also includes the use of a diffuser: a fused-silica plate that has been polished with a coarse abrasive. This creates a homogeneous beam free from any potential hot-spots in the OPA output. The diffuser causes the beam to defocus rapidly, and so lenses are used before and after it so as to collect and recollimate the beam. This modified setup also uses a pellicle beam splitter to bring the pump beam collinear

with the THz probe before the sample. A photograph of the THz experiment is shown in figure (3.17).

Figure 3.16: Layout of the time-resolved THz spectrometer utilizing an OPA for the pump beam. D: diffuser; PEL: pellicle beam-splitter; PM: gold parabolic mirrors. The difference signal of the photodiodes is measured using the lock-in amplifier, which is read by the PC which simultaneously controls the THz detection and pump delay lines (DL1 and DL2).

Figure 3.17: Photograph of the time-resolved terahertz spectrometer.

3.3.2 THz generation and detection

Broadband terahertz radiation can now be generated due to advances in ultrafast laser technology. The output from the Spitfire regenerative amplifier gives 1 mJ at a 1 kHz repetition rate, with a pulse duration of 100 fs, which means the wavelength of the pulse is Gaussian, centred at 800 nm with a full width half maximum (FWHM) of approximately 10 nm. This large spectral bandwidth, $\Delta\omega$, gives rise to the generation of THz pulses when incident on a nonlinear ZnTe (110) crystal [134].

The electric field of the laser pulse is given by

$$E = A\cos\omega t \tag{3.44}$$

which adheres to the wave equation:

$$\left[-\frac{\partial^2}{\partial z^2} + \frac{1}{c^2}\frac{\partial^2}{\partial t^2}\right] E(z,t) = -\mu_0 \frac{\partial^2}{\partial t^2} P(z,t) - \mu_0 \frac{\partial}{\partial t} j(z,t), \tag{3.45}$$

where $P(z,t)$ is the polarization and $j(z,t)$ the charge density. The large spectral bandwidth of the pulses is best described as the interaction of two waves at frequencies ω_1 and ω_2, with $\Delta\omega = \omega_1 - \omega_2$. The Pockels effect (Eq. (3.4)) leads the polarization of the crystal to oscillate at THz frequencies [135]: the second order polarization $P^{(2)}(t)$ is given by

$$\begin{aligned} P^{(2)}(t) &= \chi^{(2)} E_1(t) E_2(t) \\ &= \chi^{(2)} A_1 A_2 \cos\omega_1 t \cos\omega_2 t \\ &= \frac{1}{2}\chi^{(2)} A_1 A_2 \left[\cos(\omega_1 - \omega_2)t + \cos(\omega_1 + \omega_2)t\right] \\ &= P^{(2)}_{\Delta} + P^{(2)}_{\Sigma}, \end{aligned} \tag{3.46}$$

where $P^{(2)}_{\Delta}$ is the difference term and $P^{(2)}_{\Sigma}$ the sum term. The sum term corresponds to sum frequency generation and hence frequency-doubling when $\omega_1 = \omega_2$. The difference term corresponds to optical rectification: the change in the polarization leads to the emission of a THz field that can be derived by solving the wave equation [136]:

$$E_{THz}(t) = -\frac{\mu_0}{4\pi}\frac{S}{z}\left(\frac{\partial P}{\partial t}\right), \tag{3.47}$$

where S is the emitting area and z is the distance between the emitter and the detector. Rotation of the 1 mm thick ZnTe generation crystal is required to obtain the maximum THz field $E_{THz}(t)$ [137]. This is achieved when the angle between the polarization of the generation beam and the [001] plane of the crystal is 54.7°

[137, 138].

A 1 mm thick (100) silicon filter is used after the ZnTe generation crystal to block any transmitted 800 nm radiation (shown as Si in the layout (figure (3.15))). The wafer is synthesized using the float zone technique, with n-type phosphorus doping and a resistivity greater than 10,000 Ωcm. Unfortunately this filter of course absorbs THz and some of the signal is lost, but it is a necessary evil because this remnant generation beam could reach the sample, potentially photoexciting it, or reach the detection crystal and photodiodes. Another filter is used after the sample to block the pump beam for pump-probe experiments, where it will also block any fluorescence from the sample.

The process of detecting THz radiation also utilizes the Pockels effect: as the THz field is transmitted through a second nonlinear, 0.5 mm thick, ZnTe crystal it becomes birefringent, and so its refractive index changes. A weak 800 nm detection beam is sent colinearly through the crystal, and as the refractive index of the crystal changes, the polarization of the detection beam changes. A quarter wave plate is then used to convert the polarization from linear to circular (or rather, elliptical). A polarizing beam splitter then separates the two components of the polarization, and they are monitored by two photodiodes, as shown in figure (3.18). This process is called electro-optic sampling, for the delay time between the THz beam and the detection beam is changed by a delay line so that different parts of the THz pulse are sampled depending on which part reaches the ZnTe crystal at the same time as the detection beam [139, 140].

The efficiency of this electro-optic sampling is also affected by the angle between the polarization of the detection beam and the [001] axis of the crystal, and varies depending on whether the polarization of the detection beam is parallel or perpendicular to that of the THz beam [141].

The two photodiodes are balanced such that when there is no THz beam present, the amounts of light reaching the two photodiodes are equal: this is achieved by rotating the quarter-wave plate. When a THz beam is present the refractive index of the ZnTe crystal is changed, changing the polarization of the 800 nm detection beam, and so there is a difference in the signals measured by the two photodiodes.

The THz signal, or rather the changes in polarization, are detected using a lock-in amplifier and a chopper. An optical chopper synchronized to the laser system chops the generation beam (CH1 in figure (3.15)) so that a THz pulse is only generated every other input pulse (*i.e.* the generation beam is chopped at 500 Hz because the repetition rate of the regenerative amplifier is 1 kHz).

If $\Delta I = I_1 - I_2$ is the difference in signal intensity reaching the two photodiodes and the intensity of the detection beam is $I_{det} = I_1 + I_2$, the measured signal can

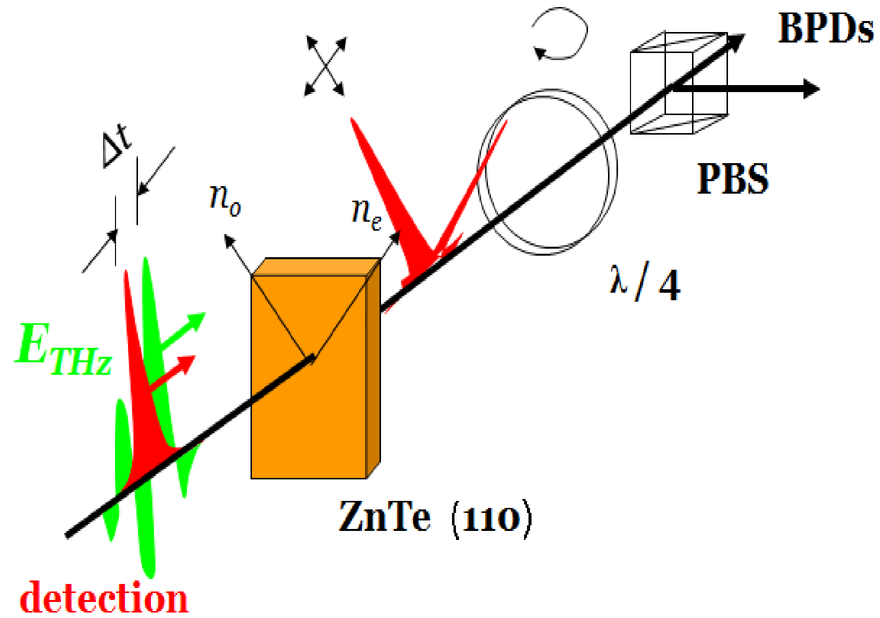

Figure 3.18: Electro-optic sampling technique, where n_o and n_e are the ordinary and extraordinary components of the ZnTe refractive index, $\lambda/4$ is a quarter wave plate for conversion to circularly (elliptically) polarized light, PBS is a polarizing beam splitter and BPDs are the pair of balanced photodiodes.

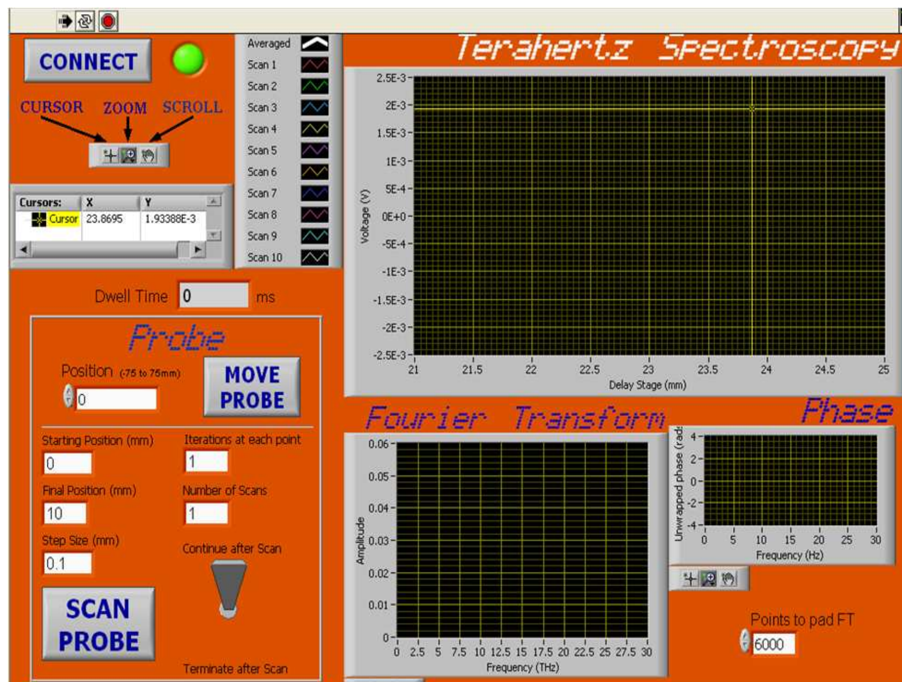

Figure 3.19: Screen shot of the THz automation software written in LabView.

be used to determine the THz field E_{THz} by:

$$\frac{\Delta I}{I_{det}} = \frac{\omega n^3 E_{THz} r_{41} L}{c}, \tag{3.48}$$

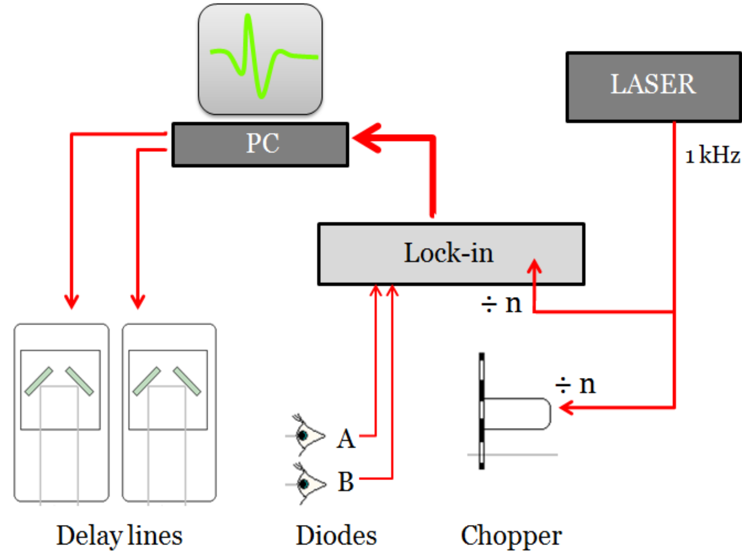

Figure 3.20: Data acquisition in the THz spectrometer. Both the lock-in amplifier and the optical chopper are synchronized to a subharmonic of the laser repetition rate (1 kHz / n, *i.e.* 500 Hz, 333.3 Hz, 250 Hz for $n = 2, 3, 4$ *etc.*).

where the electro-optic coefficient $r_{41} = 4.04$ pm/V for ZnTe [142], the near-infrared refractive index is $n = 3.22$ for ZnTe at 800 nm [143], L is the length of the crystal (0.5 mm) and ω is the angular frequency of the detection beam. The terahertz electric field is thus calculated from the voltage signal of the lock-in amplifier:

$$E_{THz} = 2\frac{\Delta V}{V_{max}} \frac{\lambda}{2\pi n^3 r_{41} L} = \frac{\Delta V}{V_{max}} \cdot 3.78 \times 10^4 \quad (\mathrm{V} \quad \mathrm{cm}^{-1}) \tag{3.49}$$

where V_{max} is the total voltage from each diode in the absence of a THz field such that $\Delta V = 0$. Typically peak electric fields in excess of 300 V cm^{-1} are measured.

The generation and detection of THz pulses using nonlinear optical crystals is fast becoming the most popular way to generate THz due to the commercial availability of the electro-optic materials and the bandwidths achievable from them. However, there are other ways to generate and detect THz radiation such as using photoconductive antennas [20].

An electro-optically sampled THz pulse (obtained with no sample present) is shown in figure (3.21). The inset of the figure shows a magnified section from which it can be seen that the signal to noise ratio (S/N) is greater than 1000:1. This is a single scan where eight accumulations were taken at each point. The lock-in amplifier time constant (§3.3.3) is set at 300 ms.

The power spectrum of the pulse is obtained from the square of the amplitude of the Fourier transform of the time-domain data (Eq. (2.101)) and is shown in

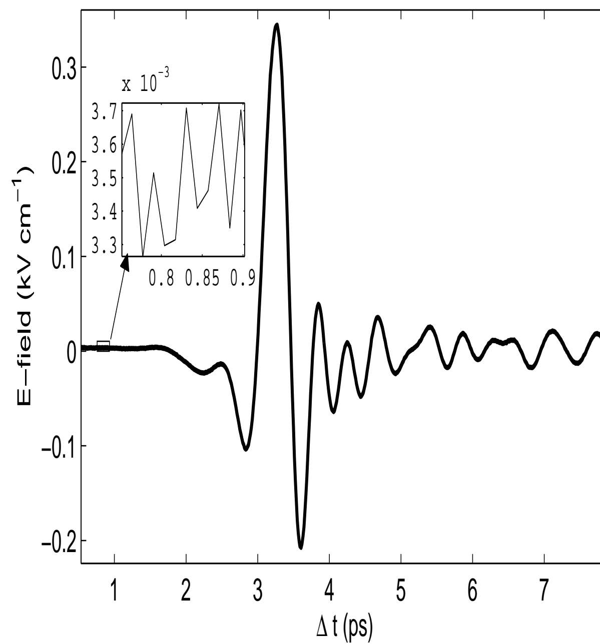

Figure 3.21: A THz pulse scanned over 8 ps, with an inset illustrating the noise level. The electric field was calculated using Eq. (3.48). The achieved signal to noise ratio here is $\approx$ 1600:1.

figure (3.22). A bandwidth of 3 THz is achieved, where the bandwidth is limited by the lack of phase matching of the frequency difference mixing in the ZnTe crystal [144].

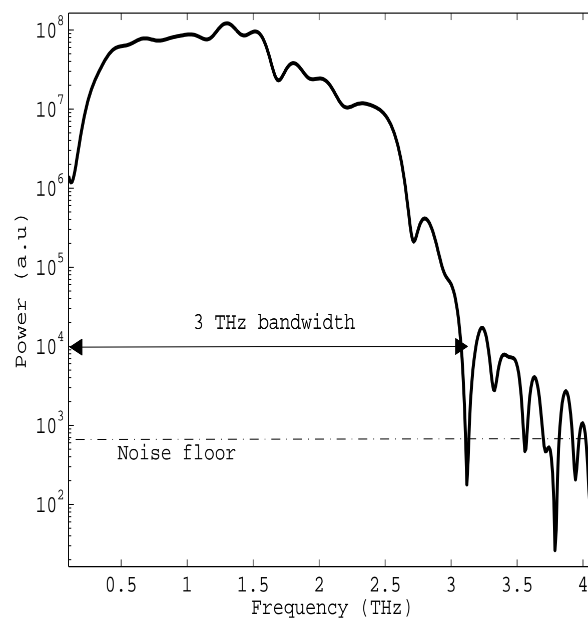

Figure 3.22: The THz power spectrum corresponding to figure (3.21), with a bandwidth of 3 THz. The dynamic range is over five decades.

The time-domain data are padded with zeros before Fourier transforming in order for the frequency spectrum to contain more points. The resolution of the frequency spectrum is given by

$$\Delta f = \frac{1}{N}\frac{1}{dt}, \tag{3.50}$$

where N is the number of data points (the Fourier transform will be most effective when $N = 2^x$) and dt is the time step [20]. Here the time step is 33.3 fs, and the time-domain data contained 480 data points, giving a spectral resolution of $\Delta f \approx 62$ GHz. In theory, should the entire range of the delay line be scanned (150 mm), the resolution can be improved to approximately 1 GHz.

It is important that the time step used in the time domain measurement is sufficiently small that the cut-off frequency, f_c, given by

$$f_c = \frac{1}{2dt}, \tag{3.51}$$

is greater than the bandwidth of the power spectrum, because if not the power spectrum becomes aliased, *i.e.* it is 'folded over' at the cut-off frequency [145]. The cut-off frequency in this case is $\approx$ 37 THz. The phase of the Fourier transform is given by

$$\phi(\omega) = \arg(E(\omega)) = \arctan\left(\frac{\Re E(\omega)}{\Im E(\omega)}\right), \tag{3.52}$$

where $\Re E(\omega)$ and $\Im E(\omega)$ are the real and imaginary components of the frequency spectrum. However, these 'raw' phase data only take values between $\pm\pi$ radians, and so the phase must be *unwrapped* whereby 2π is added to each discontinuity. A phase-unwrapping module is present in most mathematical software packages such as MATLAB. The raw unwrapped phase data are shown in figure (3.23).

The balanced detection technique is used so that fluctuations in the laser fluence (pulse to pulse fluctuations) will not perturb the measurements. However, it is important to note that this will only hold true should the two photodiodes be perfectly balanced. How well the photodiodes can be balanced will therefore effect the noise level in the measurements. A polarizer is used to 'clean up' the polarization of the detection beam (which, again, can fluctuate) because this would not be suppressed by the balanced detection. The spectrometer therefore incorporates many subtle techniques in an attempt to minimise the noise level in the spectrometer.

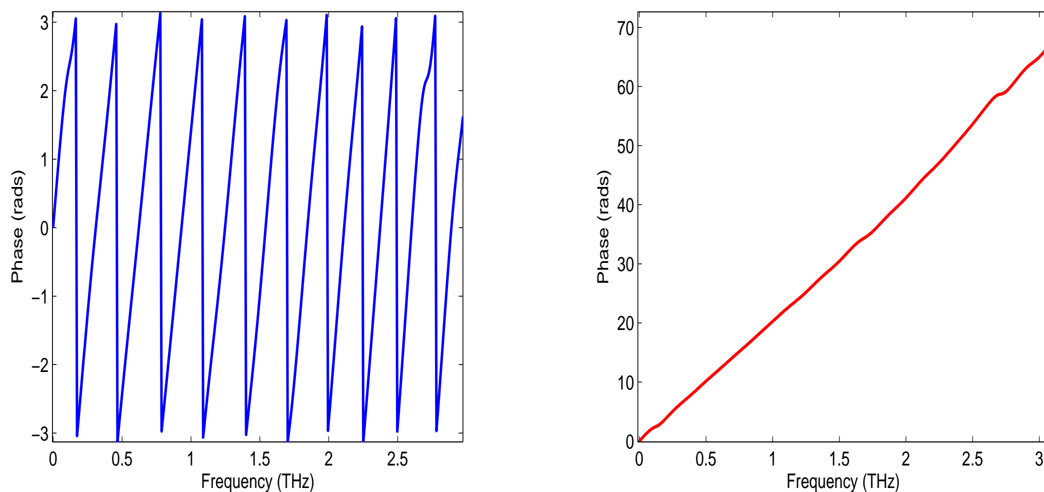

Figure 3.23: Raw (left) and unwrapped (right) phase data of the THz pulses.

3.3.3 Lock-in amplifier

A lock-in amplifier is used to detect the change in the difference of the signals from the two photodiodes ($A - B$) occurring at the frequency of the chopper. The lock-in uses a reference signal that is the same as that used for the choppers, namely a subharmonic of the 1 kHz reference from the laser.

If a THz pulse is created every two, three or four laser pulses (for the subharmonics $n = 2, 3, 4$), a change in the photodiode difference signal will be measured in the presence of a THz pulse. However, this change in the signal from the photodiodes may be very small compared to the actual photodiode signal, and as such is very difficult to detect. Moreover, the change in the photodiode signal may be equivalent or even smaller than the noise level of the photodiode signal, making measurements impossible. However, a lock-in amplifier is a phase-sensitive detector, and given the same reference as the chopper, will only detect a signal occurring at that reference frequency, with all other signals being rejected. The actual photodiode signal is removed, and only the change in the difference of the photodiode signals ($A - B$) occurring at a subharmonic of the laser reference frequency will be measured. The reference voltage sent to the lock-in amplifier does not have to be sinusoidal, because the lock-in amplifier has a voltage-controlled oscillator (VCO) which creates a sinusoidal voltage synchronized to the reference. The reference input simply needs to be periodic and synchronous with the desired signal.

A simplified circuit diagram for a lock-in amplifier is given in figure (3.24). The main components of the lock-in amplifier are [146]: (*i*) An AC amplifier which gives a voltage gain $G_a c$ determined by the sensitivity settings of the lock-in, which are user-specified; (*ii*) A voltage-controlled oscillator which is used to create a sinusoidal voltage synchronized to an input reference in frequency and phase. This

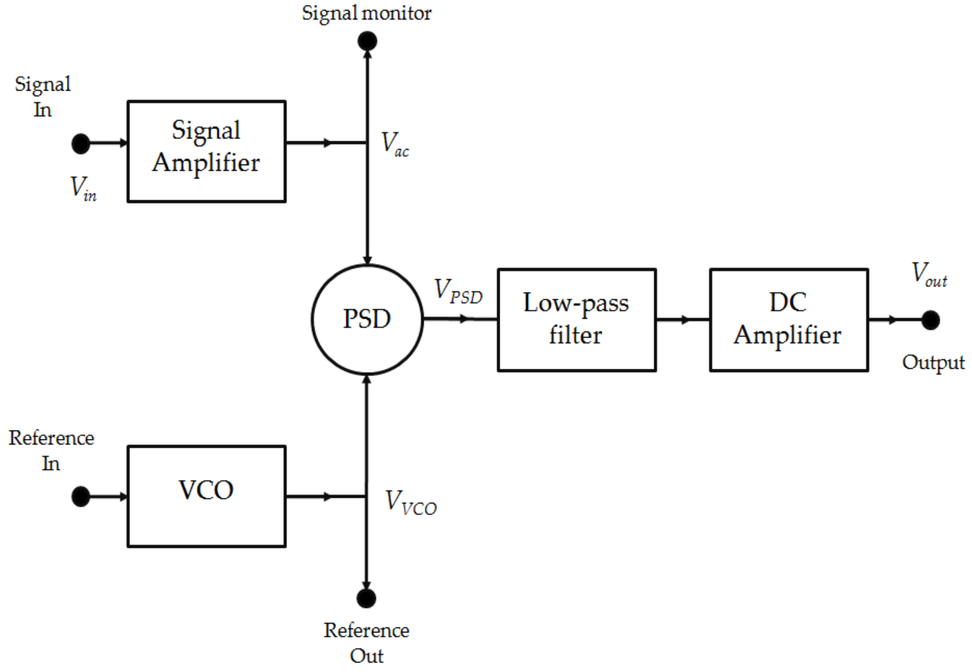

Figure 3.24: Circuit diagram of a lock-in amplifier, adapted from [146]. A voltage-controlled oscillator (VCO) generates an oscillating voltage, V_{VCO}, synchronized to an external reference. The AC amplifier amplifies the input signal, V_{in}, with variable filters specified by the user. This amplified signal, V_{ac}, is then multiplied with the reference voltage in the phase sensitive detector (PSD). The DC output of this, V_{PSD}, is then passed through a low-pass filter and a DC amplifier to give the output measurement V_{out}.

VCO also contains a phase-shifting circuit that allows the user to shift its signal phase from 0° to 360°; (*iii*) A phase sensitive detector (PSD). This is a specialised multiplier that creates the product $V_1^* V_2$ from inputs V_1 and V_2; (*iv*) A low-pass filter with a user-controlled time constant that has up to two stages that can be used; (*v*) A DC amplifier which is different to an AC filter in that it works at zero frequency.

For an input voltage V_{in}:

$$V_{in}(t) = V_0 \sin(\omega_0 t + \theta) + V_n(t), \tag{3.53}$$

where V_0 is the amplitude of the signal which is to be measured, θ is the signal phase and $\omega_0 = 2\pi\nu_0$ where ν_0 is the ordinary frequency of the signal, in this case the frequency at which the chopper is set. However, the signal 'sits' on a much larger signal, V_n such that $V_n^2 \gg V_0^2$, that may as well be considered to be a large background noise. If there were no large background noise, an oscilloscope or simple AC voltmeter could be used to measure V_0.

The output voltage from a lock-in amplifier is [146, 147]:

$$V_{out} = \frac{1}{2} G_{ac} G_{dc} V_0 E_0 \cos(\theta - \phi), \tag{3.54}$$

where E_0 and ϕ are the amplitude and phase of the VCO signal and G_{ac} and G_{dc} are gains applied by the AC and DC amplifiers.

Modern-day lock-in amplifiers are, of course, digital, and so the multiplication and filtering stages are now performed by digital signal processing (DSP) chips, although the principle is the same [148]. Input voltages are now first sent through analog-to-digital converters. One particular advantage of digital lock-ins is the ability to be able to *autophase* onto the signal, that is, for the general case of $\theta \neq \phi$, the reference signal phase ϕ is adjusted so that $\theta = \phi$ and the entire signal is in phase and measured.

3.3.4 Water absorption

Frequency (THz)	Intensity (log I)	Frequency (THz)	Intensity (log I)
0.557	-0.8145	2.196	-0.2034
0.752	-0.9942	2.222	-0.1960
1.097	-0.3182	2.264	-0.0563
1.113	-0.8352	2.344	-0.6247
1.163	-0.2790	2.366	-0.6328
1.207	-0.7824	2.391	-0.0565
1.229	-0.8504	2.463	-0.0712
1.411	-0.3734	2.631	-0.6111
1.602	-0.6907	2.640	+0.5355
1.661	-0.2731	2.664	-0.7818
1.670	+0.1020	2.686	-0.5744
1.795	-0.9527	2.774	+0.4693
1.797	-0.8294	2.880	-0.2760
1.868	-0.3299	2.884	-0.7358
1.919	-0.5736	2.885	-0.9564
2.040	-0.6608	2.969	-0.0257
2.074	-0.8295	2.970	+0.0265
2.164	-0.1046		

Table 3.3: Water absorption lines in the THz spectral region up to 3 THz [149]. The greater log I, the greater the absorption, with the largest absorption occurring at 2.640, 2.774 and 1.670 THz.

One very important experimental consideration in THz spectroscopy is that THz radiation is heavily absorbed by water vapour at certain frequencies in the THz spectrum, in particular, those corresponding to the rotational modes of water

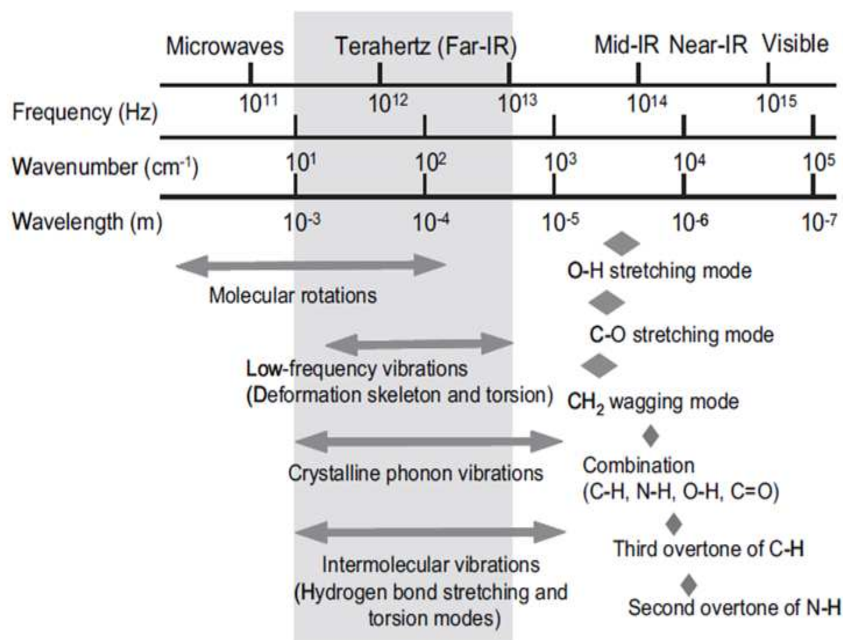

Figure 3.25: Characteristic absorptions in the infrared and terahertz regions, from [150].

vapour [150, 151]. Figure (3.25) illustrates the characteristic absorptions in the THz and infrared spectral regions. For this reason the spectrometer enclosure must be purged with either dry air or nitrogen (in this case the former). The main absorption lines of water are given in table (3.3) along with their intensity $\log I$, determined experimentally by NASA's molecular spectroscopy division [149].

The effect that water absorption has on the THz spectrum is shown in figure (3.26). Because experiments need to be conducted with the spectrometer enclosure purged with dry air, all important optics are controlled remotely. Two sample holders are mounted on a small delay stage so that a sample and its reference can be measured without disturbing the purge. The quarter-wave plate in the detection area (which needs to be rotated so as to achieve perfect balancing on the photodiodes) is mounted on a mechanical rotation stage; the THz generation beam and the pump beam can both be blocked with the use of mechanical shutters.

3.3.5 Etalon effect

Multiple reflections in the generation and detection ZnTe crystals (1.0 and 0.5 mm thick respectively) are seen in the time-domain data, as shown in figure (3.27). The thickness of the detection crystal leads to a reflection round-trip delay of 11.4 ps ($t = d/c$), and the generation crystal produces a delay double this. Reflections are also observed 'before' the main pulse due to reflections of the 800 nm THz detection beam in the detection crystal. These reflections manifest as a modulating

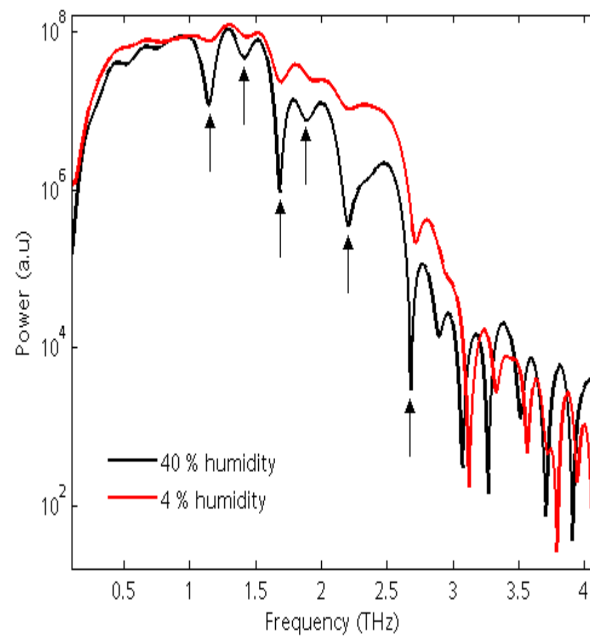

Figure 3.26: Power spectra with and without purging with dry air (humidity of 4% and 40% respectively, as measured with a humidity probe placed close to the sample location). The main regions of absorption (arrows) correspond to the strongest absorption lines (or group of lines) listed in table (3.3): 1.10, 1.41, 1.67, 1.87, 2.22 and 2.64 THz.

oscillation of approximately 65 GHz in the frequency domain, as shown in figure (3.28).

These reflections will not undermine measurements, however, because they can be cut off in the time domain (if, for example, the pulse is only recorded over roughly 8 ps). Reflections that will interfere with measurements are often those from the sample: for example, bulk semiconductor wafers are often less than 0.5 mm thick. Thin film samples, such as those epitaxially grown, are microns thick. This means that weak reflections will occur at smaller time shifts that cannot be easily identified in the time-domain data unlike the stronger reflections from the generation and detection crystals. Recording the time-domain data over less than 8 ps will lead to loss of information about the sample, such as its absorption, and a reduction in the spectral resolution [152]. Although these reflections are not obvious in the time-domain data, nor in the Fourier power spectrum, they often manifest when extracting the optical constants such as the absorption, when the ratio of the power spectra is computed and small differences in the frequency spectrum become important. These oscillations are accepted, and are often evident in literature data [153].

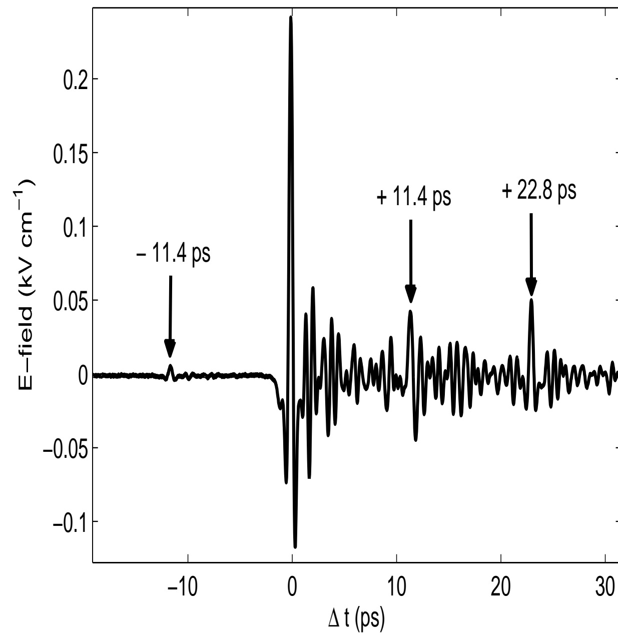

Figure 3.27: A wide scan over the THz pulse, where multiple reflections from the generation and detection crystals are seen in the time domain. Here the THz beam path is unpurged. Reflections are seen in the time domain at ±11.4 ps from the detection crystal, and 22.8 ps from the generation crystal (where a second, weaker reflection from the detection crystal also occurs).

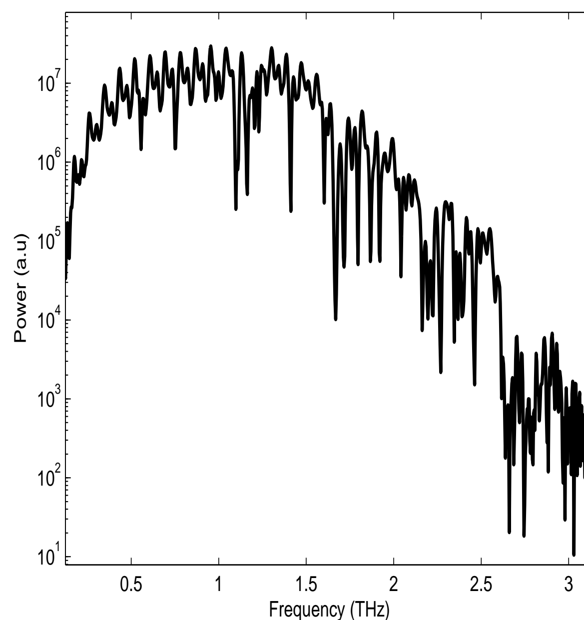

Figure 3.28: Multiple reflections in the time domain lead to a 65 GHz modulation of the power spectrum. This is most clear over the range 0.5 - 1 THz.

3.3.6 Pump-probe experiments

To understand the charge carrier dynamics in a semiconductor, THz radiation can be used to probe the exciton population because intra-excitonic transitions occur at THz frequencies (exciton binding energies are typically 1 - 100 meV, with 1 THz being 4.1 meV) [154]. The THz signal is also sensitive to free carriers and low-energy vibrational modes (phonons) [155]. The evolution of the system over time can be investigated by varying the pump-probe delay time [156, 157, 158], and the photoexcited optical constants, and thus the photoconductivity, can be studied [159, 160, 161, 162].

In the pump-probe setup, the pump beam, instead of the THz generation beam, is optically chopped (CH2 in figure (3.15)) so that a pump-induced change in the THz signal is measured by the lock-in amplifier. Therefore the detection delay line DL1 is kept fixed at some point on the THz pulse, and the pump delay time is changed using the second delay line DL2. A transient is then recorded by varying the pump-probe delay time. A THz difference scan, ΔE_{THz}, can also be recorded by scanning the detection delay line while chopping the pump beam: in fact, it is important to obtain this first, because only this scan can reveal the point on the detection delay line that gives the largest pump-induced change (*i.e.* the largest transient signal). For instance, a photoexcited sample may cause dispersion of the THz pulses and so the largest pump-induced change in the THz signal may not occur at the THz peak position when the sample is not photoexcited.

One important factor that must not be overlooked is the issue of beam sizes. The entire THz probe beam must experience excitation in the sample, and so the pump beam must be larger than the probe beam at the sample. Spot size is defined as the point where the intensity of the Gaussian beam falls by a factor of $1/e$. If not, the spectrum will be skewed to higher frequencies as shown in figure (3.29) from [161]. This is because the higher frequency components of the THz beam occur at smaller radii than lower frequencies.

Initial studies were carried out on GaAs(100) (§4.1.3), where the pump beam was brought to the sample at an angle using the setup shown in figure (3.15). The pump beam was later generated using the OPA (the setup shown in figure (3.16)), brought to the sample using a pellicle beam splitter to bring the pump beam colinear with the terahertz probe beam. The main drawback of using such a beam splitter is that pellicles have relatively low damage thresholds (typically 20 mW), and so less pump power can be used. In the first setup the pump beam was measured to be approximately 4 mm in diameter with the THz probe beam having a diameter of 2.5 mm. The use of a diffuser in the second setup leads to a much larger beam size, typically 9 - 10 mm in diameter.

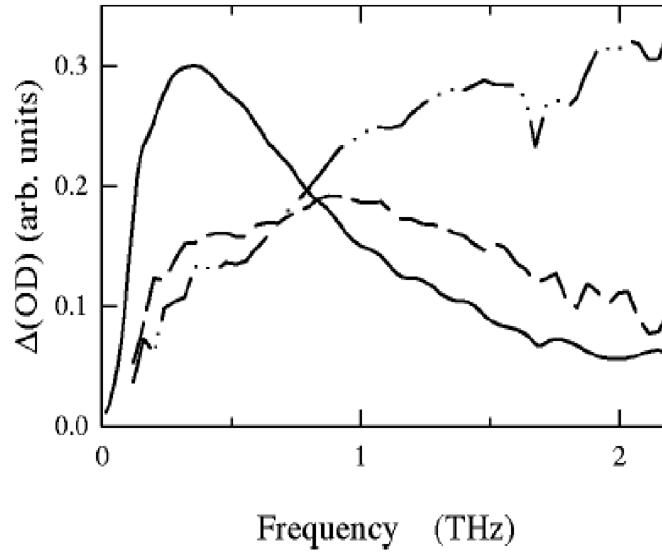

Figure 3.29: Change in optical density spectra as a function of frequency for varying beam sizes, from [161]. The THz beam size here is 2.3 mm: the pump sizes are 6 mm (solid line), 1.7 mm (dashed line) and 1.1 mm (dot-dashed line).

3.3.7 Material parameter extraction

The first step in the analysis of the THz data is the extraction of the optical parameters of a sample, namely its complex refractive index, $\tilde{n}(\omega)$:

$$\tilde{n}(\omega) = n(\omega) + ik(\omega), \tag{2.102}$$

where n is the refractive index and k is the wave vector, related to the absorption coefficient of the sample, α, by

$$k = \frac{c\alpha}{2\omega}, \tag{2.105}$$

where c is the speed of light. The refractive index of a material gives rise to a time delay of the THz pulses, whereas the wave vector gives rise to an attenuation of the THz pulses.

Before analysis takes place using the time-domain signals, any offset of the recorded pulses from zero (due to not-quite perfect balancing of the photodiodes) is quantified and removed. Then a Gaussian window, centred on the peak of the THz pulses, is applied so as to suppress the time-domain signal at the end of the scan to zero. This is to remove any offset in the time-domain signal at the end of the scan which might otherwise lead to an oscillation in the frequency domain.

For the case when the thickness of a sample, d, is known, the complex refractive index of a sample can be computed using a fixed-point iteration method [163]. The iterative process is guaranteed to converge within a few iterations, and as such the

method is computationally fast and undemanding. The method involves iterating the real and imaginary components of the complex refractive index separately at each frequency, beginning with initial values. The transmission function of the sample, $T(\omega)$, can be fitted in terms of the complex refractive index of the sample from the Fresnel transmission coefficient:

$$T(\omega) = \frac{E_S(\omega)}{E_0(\omega)} = \frac{4\tilde{n}\tilde{n_0}}{(\tilde{n} + \tilde{n_0})^2} \cdot \exp\left[-i(\tilde{n} - \tilde{n_0})\frac{\omega d}{c}\right] \cdot FP(\omega), \tag{3.55}$$

where $E_S(\omega)$ is the Fourier-transformed time-domain THz signal through the sample, $E_0(\omega)$ is the Fourier-transformed time-domain THz reference signal through air, $\tilde{n}$ is the frequency-dependent complex refractive index of the sample, $\tilde{n_0}$ is the frequency-dependent complex refractive index of air, and $FP(\omega)$ is a Fabry-Pérot term. This term accounts for multiple reflections of the THz pulses at the sample interfaces, which is here ignored because the time-domain data are truncated to remove such reflections. Equation (3.55) can be simplified so as to separate $\tilde{n}$ into n and k, as well as using $\tilde{n_0} \cong 1$ for air:

$$\frac{E_S(\omega)}{E_0(\omega)} = \frac{4\tilde{n}}{(\tilde{n} + 1)^2} \cdot \exp\left[-i(n-1)\frac{\omega d}{c}\right] \cdot \exp\left[-k\frac{\omega d}{c}\right]. \tag{3.56}$$

Taking the argument of equation (3.56) allows for new values of n to be iterated:

$$\arg\left[\frac{E_S(\omega)}{E_0(\omega)}\right] = \arg\left[\frac{4\tilde{n}}{(\tilde{n}+1)^2}\right] - (n-1)\frac{\omega d}{c}, \tag{3.57}$$

$$n = -\frac{c}{\omega d}\left\{\arg\left[\frac{E_S(\omega)}{E_0(\omega)}\right] - \arg\left[\frac{4\tilde{n}}{(\tilde{n}+1)^2}\right]\right\} + 1. \tag{3.58}$$

Taking the logarithm of the absolute of equation (3.56) allows for new values of k to be iterated:

$$\ln\left|\frac{E_S(\omega)}{E_0(\omega)}\right| = \ln\left|\frac{4\tilde{n}}{(\tilde{n}+1)^2}\right| - k\frac{\omega d}{c}, \tag{3.59}$$

$$k = -\frac{c}{\omega d}\left\{\ln\left|\frac{E_S(\omega)}{E_0(\omega)}\right| - \ln\left|\frac{4\tilde{n}}{(\tilde{n}+1)^2}\right|\right\}. \tag{3.60}$$

The initial values, n_i and k_i, to be used for the first iterations computed with equations (3.58) and (3.60), are derived from the case where the Fresnel transmission coefficient is set to 1:

$$\begin{aligned} n_i &= -\frac{c}{\omega d}\arg\left[\frac{E_S(\omega)}{E_0(\omega)}\right] + 1, \\ k_i &= -\frac{c}{\omega d}\ln\left|\frac{E_S(\omega)}{E_0(\omega)}\right|. \end{aligned} \tag{3.61}$$

More complex algorithms can be used for the case when the thickness of the sample is unknown [164].

Chapter 4

Time-resolved terahertz spectroscopy of photovoltaic materials

4.1 Commissioning the spectrometer

The building and implementation of the time-resolved terahertz (THz) spectrometer included many refinements, as did the process of data analysis. Absorption measurements were carried out on two solvents, toluene and hexane, that are commonly used to suspend quantum dot samples, to obtain the refractive index and absorption spectra for the solvents. These solvent samples were held in a 1 mm path length quartz cuvette. Absorption measurements were taken to compare to literature data for quartz [165], toluene [166] and hexane [167]. A time-resolved study of GaAs was then carried out to compare to identical studies in the literature [168, 161]. This allowed the spectrometer to be benchmarked before novel time-resolved studies on InP began.

4.1.1 Terahertz absorption of quartz

Toluene and hexane samples were held in a quartz cuvette with a path length of 1 mm. Quartz was used because it has a much lower absorption coefficient over terahertz frequencies than borosilicate glass (Schott BK7) commonly used in optical experiments [165]. The outer length of the cuvette was 3.5 mm, meaning the quartz cuvette walls are 1.25 mm thick (a total quartz sample thickness of 2.5 mm). Time-domain THz scans through air (the reference) and the empty quartz cuvette are shown in figure (4.1). The time delay of the THz pulses through quartz is due to the higher refractive index for quartz compared to air, and the decrease in the THz signal is due to absorption by the quartz sample.

It is important to note that the experiment enclosure is purged of water vapour

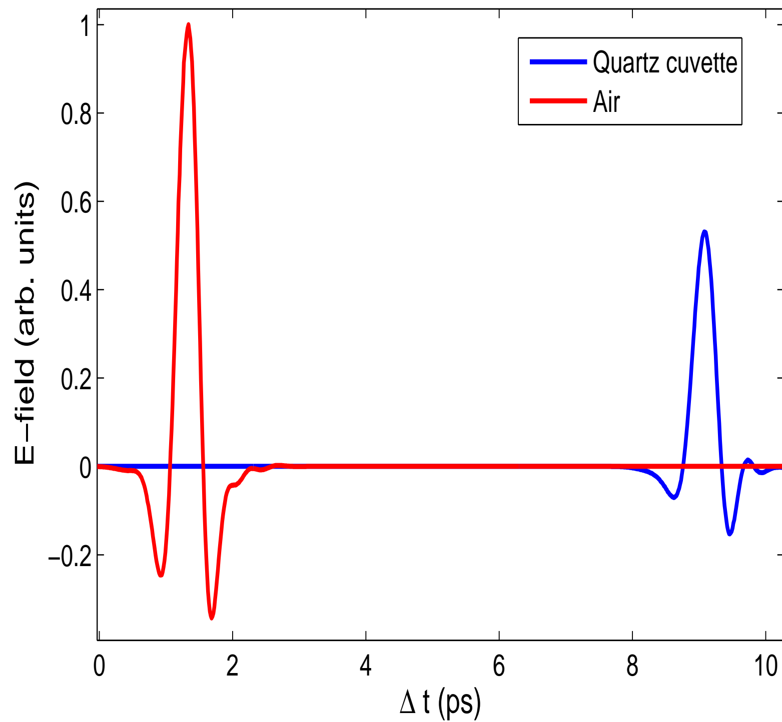

Figure 4.1: Time-domain THz data for an empty quartz cuvette compared to the air reference.

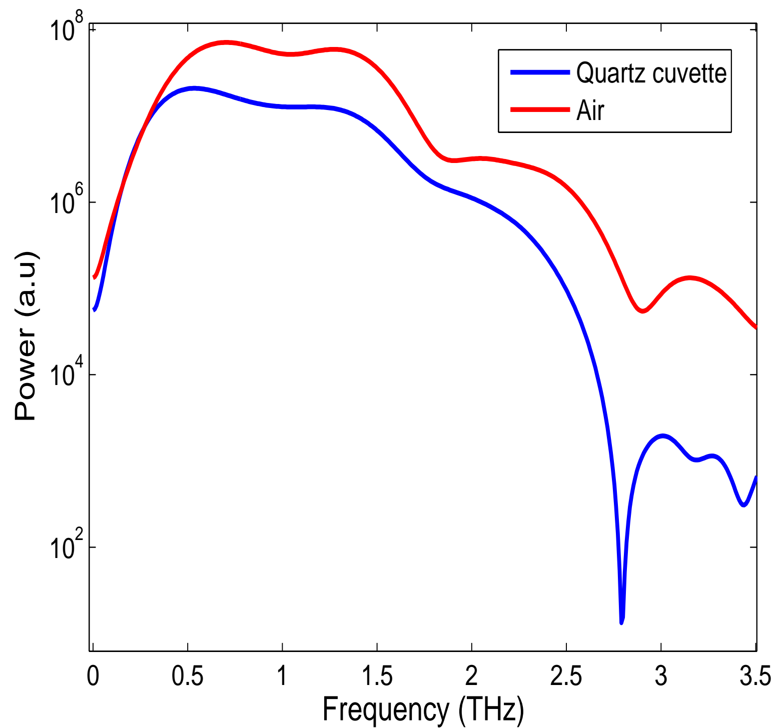

Figure 4.2: Power spectra of THz pulses through an empty quartz cuvette compared to the air reference, showing that the absorption of the THz radiation by quartz reduces the THz bandwidth.

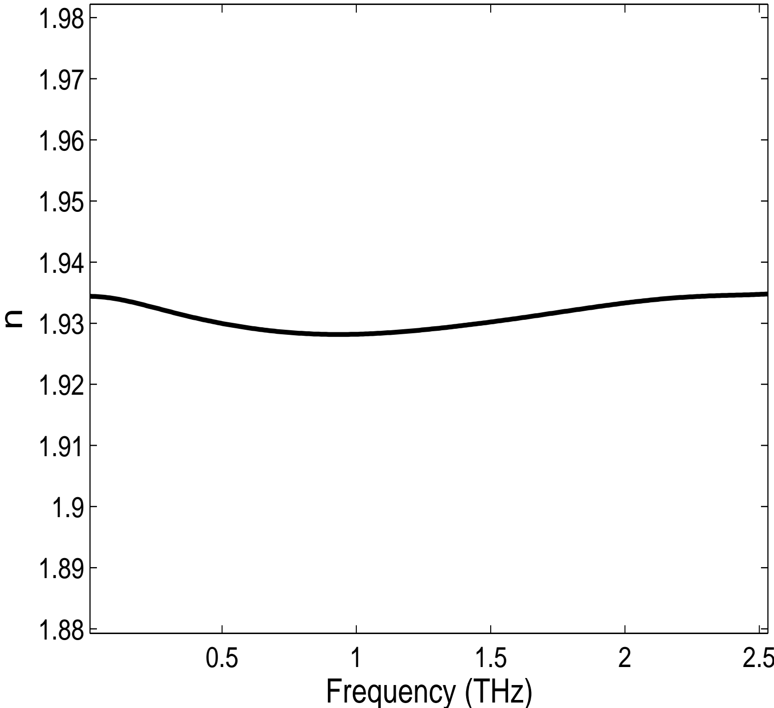

Figure 4.3: The refractive index of quartz over terahertz frequencies, calculated using the experimental data shown in figure (4.1).

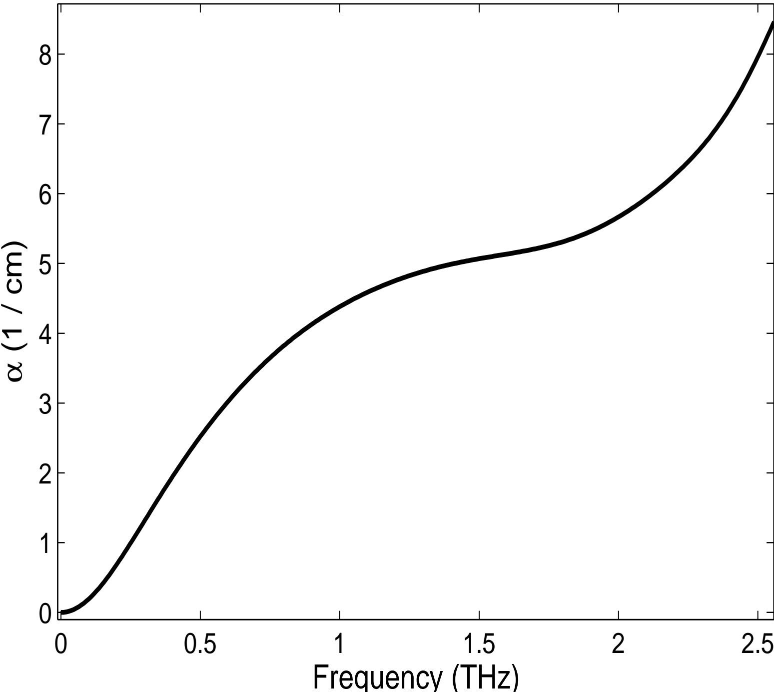

Figure 4.4: Absorption coefficient of quartz over terahertz frequencies, calculated using the experimental data shown in figure (4.1).

in the air using an external dry air supply. A humidity probe was used to ensure that the relative humidity in the experiment enclosure was never more than 5%; the air in the laboratory is usually greater than 40% relative humidity.

The power spectral density over THz frequencies was calculated from the square of the modulus of the Fourier-transformed time-domain electric field $E(t)$:

$$P_{THz} = |\mathscr{F}\{E(t)\}|^2. \tag{4.1}$$

The power spectra for the air reference and the empty quartz cuvette sample are given in figure (4.2), showing a narrowing of the THz bandwidth due to absorption by the quartz cuvette.

The refractive index and absorption coefficient of quartz over THz frequencies, calculated from this experiment using the fixed-point iteration method (§3.3.7), are given in figures (4.3) and (4.4) respectively.

The refractive index and absorption coefficient of quartz over terahertz frequencies compare well with data in the literature. Naftaly and Miles show that the refractive index of quartz at 2 THz is approximately 1.95, and the absorption coefficient is 5 cm^{-1} at 2 THz [165]. This illustrates that the methodology used for extraction of material parameters works well.

4.1.2 Terahertz absorption of toluene and hexane

Absorption measurements of toluene and hexane samples were carried out by recording time-domain THz scans through the empty quartz cuvette (reference) before repeating the measurements with solvent added to the cuvette. The refractive index and absorption spectra were then derived through the fixed-point iteration method described in §3.3.7. Figure (4.5) shows the time-domain terahertz pulses recorded after passing through the empty cuvette reference, toluene and hexane. The time-domain data show that there is a greater absorption of the THz pulses in toluene than in hexane, as well as a greater time shift, illustrating that the refractive index of toluene over THz frequencies is also larger.

The power spectra for toluene and hexane compared to the cuvette reference are shown in figure (4.6) over a THz bandwidth of approximately 3 THz. Again, less power is transmitted through toluene. The unwrapped phase of the Fourier transform (explained in §3.3.2) is shown in figure (4.7). The larger increase in the phase of the toluene data with frequency is because of the greater time shift observed in the time-domain electric field shown in figure (4.5).

The refractive index and absorption spectra over terahertz frequencies, obtained from the fixed-point iteration method, are shown in figures (4.8) and (4.9)

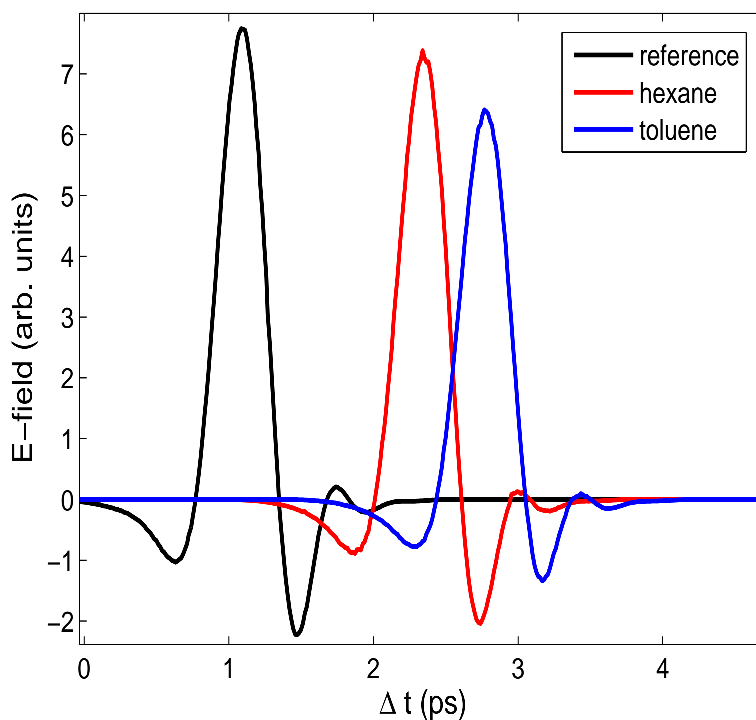

Figure 4.5: Time-domain THz pulses for toluene and hexane compared to an empty quartz cuvette reference. Clearly greater absorption occurs in toluene, as well as a greater time shift, meaning the THz refractive index of toluene is greater than that of hexane.

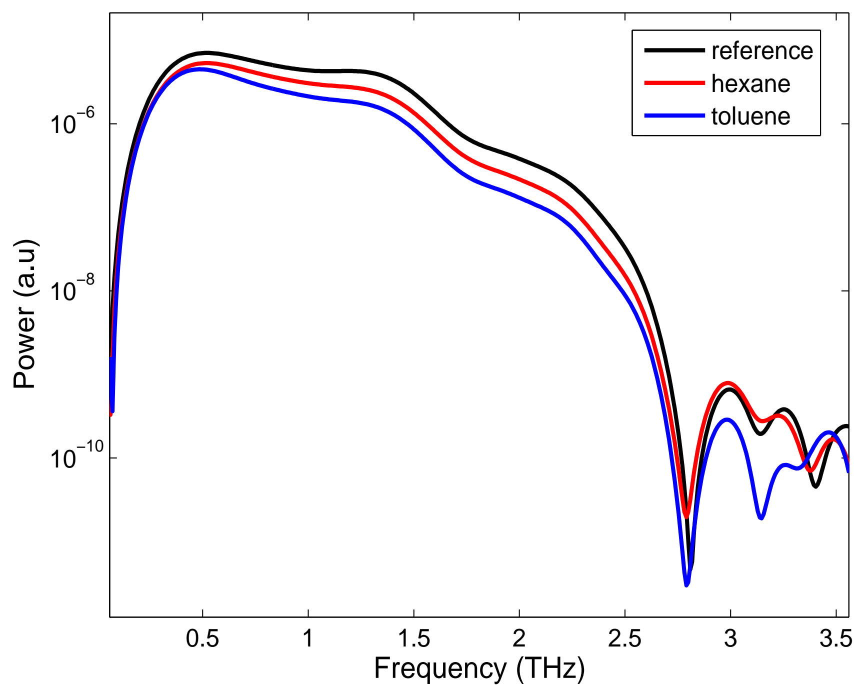

Figure 4.6: Power spectra for toluene and hexane over a bandwidth of 3 THz, showing greater absorption by toluene than by hexane.

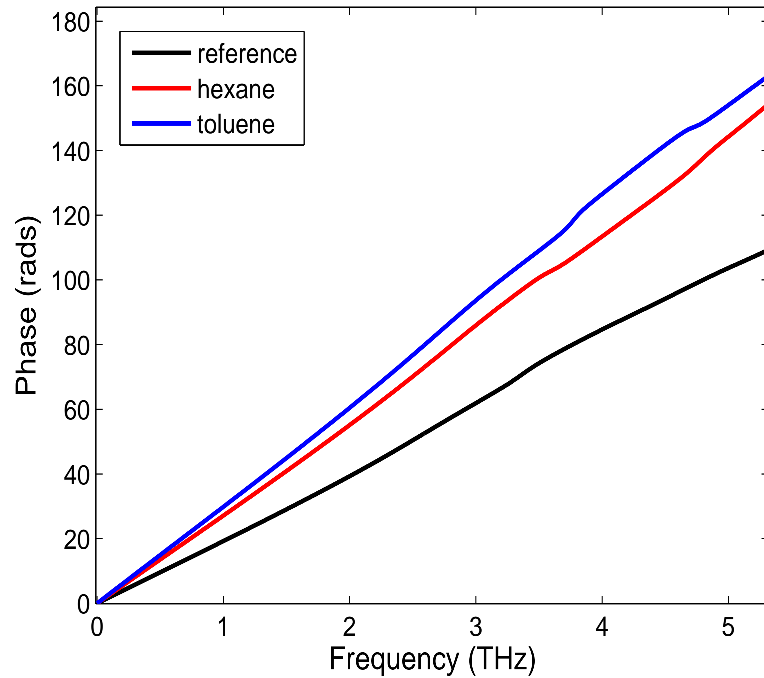

Figure 4.7: Unwrapped Fourier transform phase spectra for toluene and hexane compared to the quartz cuvette reference. A greater increase in the Fourier-transform phase for toluene is due to a greater time shift in the time-domain data, corresponding to a higher refractive index.

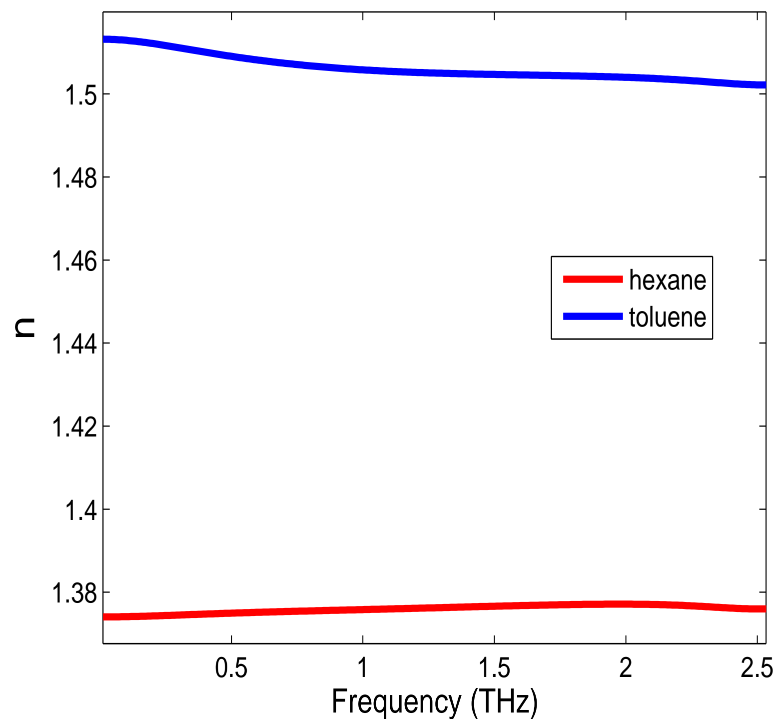

Figure 4.8: Refractive indices of toluene and hexane, showing little variation over the terahertz bandwidth.

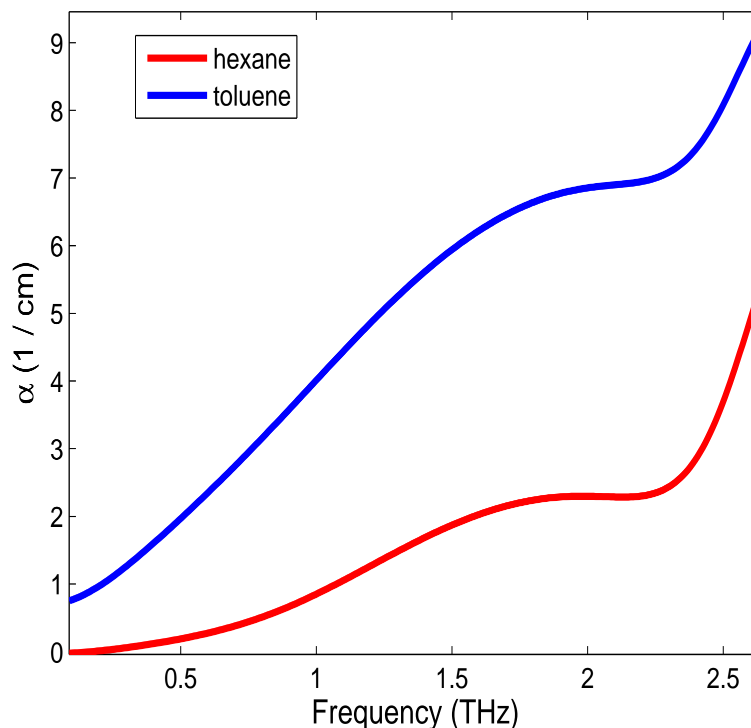

Figure 4.9: Absorption spectra for toluene and hexane, showing higher absorption by toluene than by hexane.

respectively. There is little change in the refractive indices of the two solvents over the terahertz bandwidth, where the refractive index of toluene is approximately 1.51 and the refractive index of hexane is approximately 1.38. Toluene therefore has a similar refractive index to benzene ($n = 1.5$) and hexane has a refractive index similar to water ($n = 1.33$) [83]. The refractive index of toluene over terahertz frequencies agrees well to the value of 1.50 reported in the literature [166], as does the value of 1.37 for hexane [167]. The absorption spectrum for toluene in figure (4.9) also compares well to that reported in the literature, where an absorption coefficient of approximately 5 cm^{-1} is measured at 2 THz [166]. The absorption spectrum over terahertz frequencies for hexane is lacking in the literature.

The absorption spectra of the two solvents shows that toluene exhibits greater absorption of terahertz radiation. Hexane is therefore a more suitable solvent to be used for quantum dot samples to be studied by terahertz spectroscopy. Indeed, terahertz studies of quantum dot samples usually employ hexane as the sample solvent [24, 23, 25], although toluene has been used as well [26, 27]. It is important that the THz absorption of these solvents is characterised, because measuring a change in the THz waveform when quantum dots have been added is highly challenging [169].

4.1.3 Time-resolved terahertz spectroscopy of GaAs

To benchmark the laser-pump terahertz-probe setup and establish the pump-probe technique, a GaAs(100) wafer was used due to the availability of literature data [168, 161]. The sample was un-doped, semi-insulating (with high resistivity) and 0.35 mm thick. THz difference scans (ΔE_{THz}, obtained by chopping the pump beam and scanning the THz delay line) were obtained at different pump-probe delay times so as to build-up a two-dimensional plot of pump-probe delay time, τ, versus the time over the THz pulse, Δt, as shown in figure (4.10).

As the pump and probe beam overlap in time, a smearing in the 2D Δt / τ plot

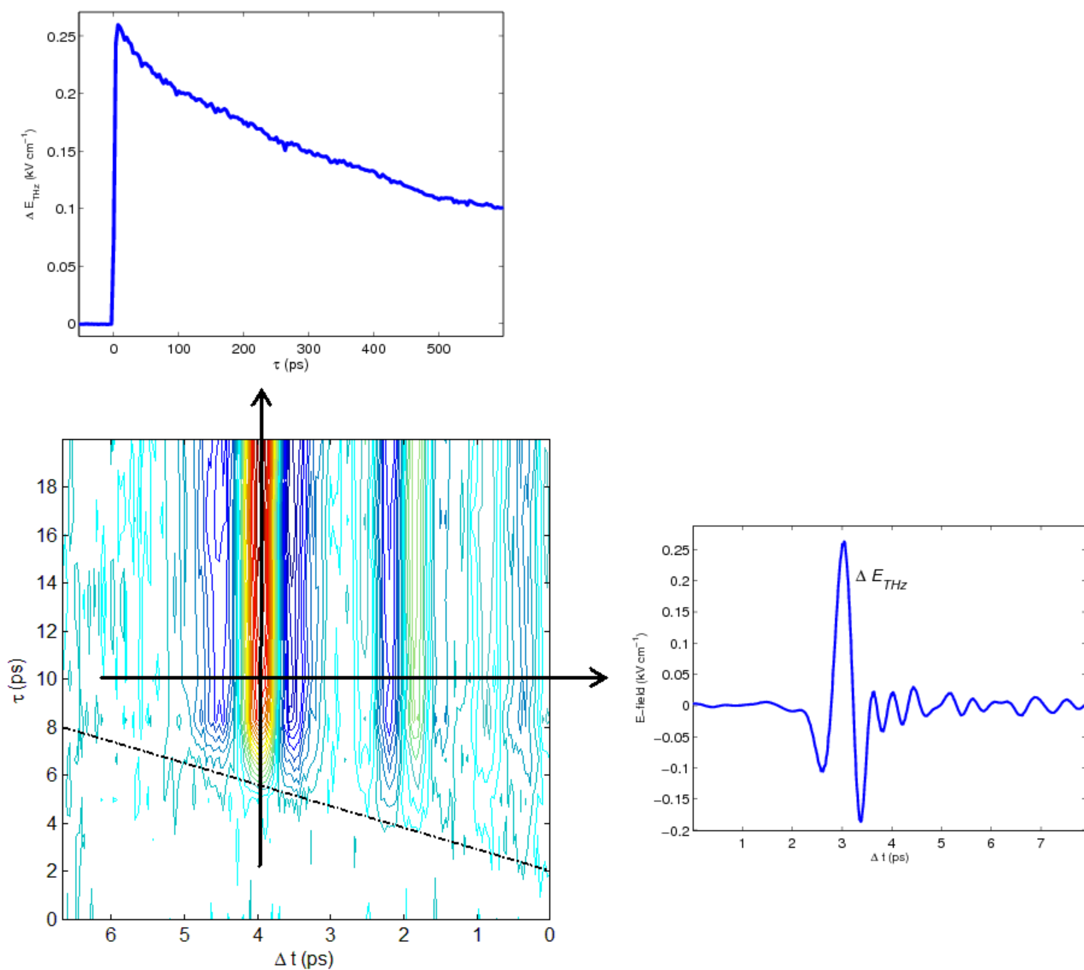

Figure 4.10: A GaAs wafer is photoexcited with a 400 nm (3.10 eV) pump at a time delay τ to the probe beam. The pump is optically chopped so that the change of the THz signal is detected by the lock-in amplifier. The pump delay line is then scanned at a certain point on the THz pulse, yielding a transient that decays over time as pump-induced excitons recombine (top). A scan of the change in the THz pulse, ΔE_{THz}, is taken by scanning the detection delay line at a fixed pump-probe delay time (right). Taking these scans at various pump-probe delay times allows a 2-dimension plot of Δt against τ to be constructed (left).

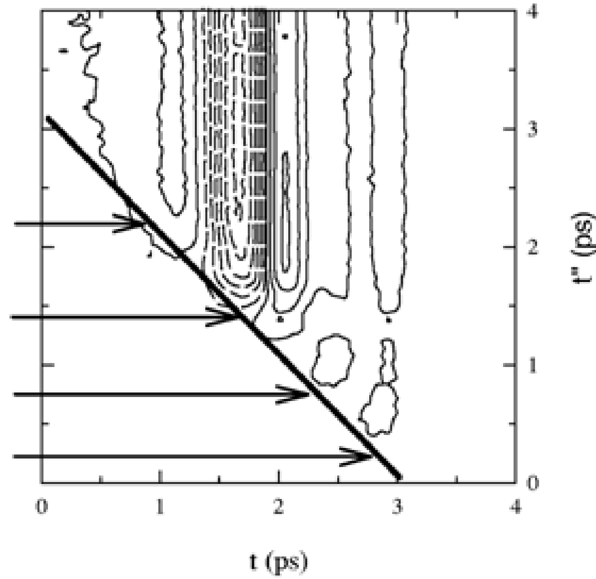

Figure 4.11: 2D contour plot for GaAs photoexcited with 400 nm radiation (3.10 eV), from reference [161]. Here, t is equivalent to Δt and t" to τ in figure (4.10). The arrows show the points at which the pump and probe overlap.

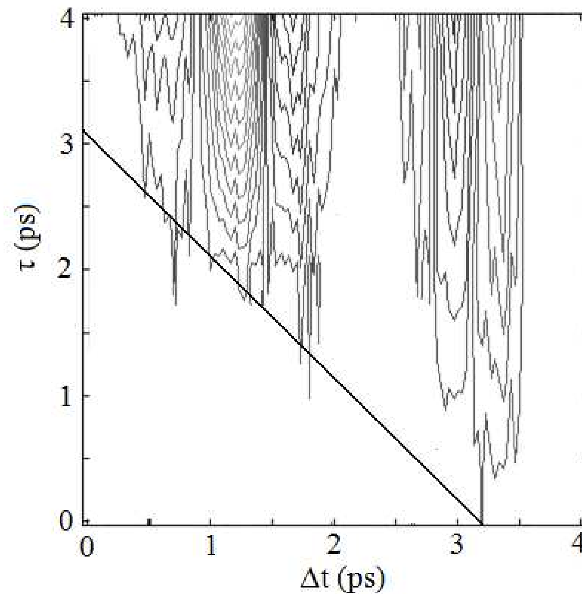

Figure 4.12: 2D contour plot for GaAs photoexcited with 400 nm radiation (3.10 eV), plotted to closely match the aspect ratio of figure (4.11). The black line shows the temporal smearing due to the overlap of pump and probe pulses. At $\tau = 1$ ps, only the 'tail' of the THz waveform overlaps with the pump laser pulse.

is observed such that a complete ΔE_{THz} scan cannot be obtained until a pump-probe delay time of $\tau \approx 3$ ps. This is because the pump and probe beams are not completely overlapped until roughly 3 ps after they first intercept (*i.e.* at $\tau = 1$ ps only the 'tail' of the THz pulse overlaps with the pump laser pulse). This shows strong agreement with what is seen by Beard *et al.*: the 2D plot from reference

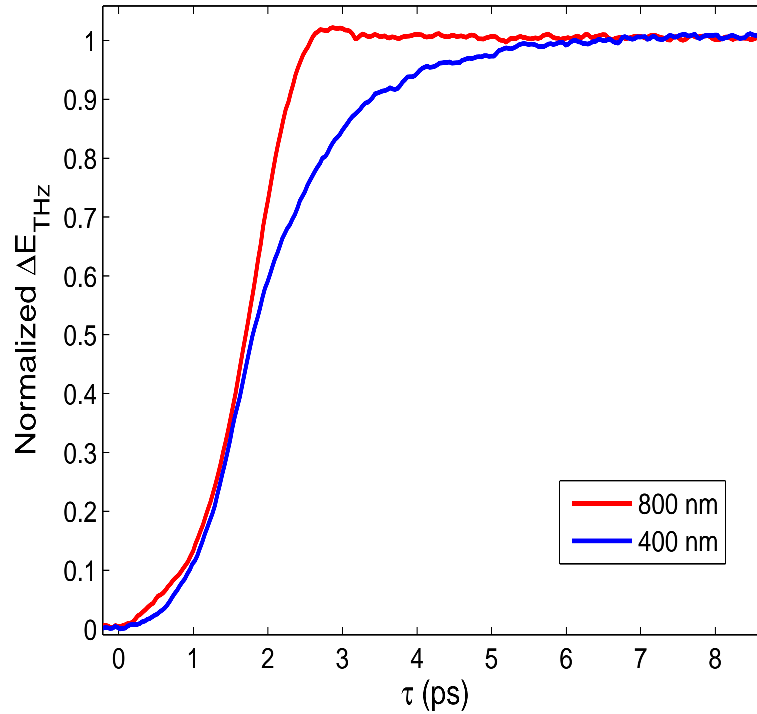

Figure 4.13: Rising edge of the change in the THz waveform for GaAs photoexcited with 400 and 800 nm laser pulses. When photoexcited with 400 nm radiation, the rising edge is delayed due to the intervalley scattering of electrons.

[161] is shown in figure (4.11) for comparison. The gradients of the smearing in figures (4.10) and (4.11) are the same. To show this explicitly, the contour plot of figure (4.10) was adjusted so as to match that of figure (4.11), and is illustrated in figure (4.12).

The rising edge of the change in the THz waveform was measured using two different photoexcitation wavelengths, 800 nm (1.55 eV) and 400 nm (3.1 eV), as shown in figure (4.13). The band gap energy of GaAs is 1.43 eV and the band structure is shown in figure (4.14) [170]. The rising edge of the change in the THz waveform under photoexcitation with 400 nm is delayed because of intervalley scattering [171]. At a higher photon energy the photoexcited electrons, injected at the zone centre (Γ), scatter into neighbouring conduction band valleys (minima), such as the L valley at $\approx$ 2 eV in figure (4.14), within 100 fs [171]. Electrons then scatter back to the conduction band minimum at the band gap, although this occurs over several picoseconds [171]: it is this electron population that contributes to the conductivity of the material. The conductivity therefore increases to reach a steady-high value until electron-hole recombination begins to reduce the carrier density on a much longer timescale.

The THz is attenuated by electrons at the zone centre (Γ conduction band valley) because these electrons contribute to the conductivity of the sample due to

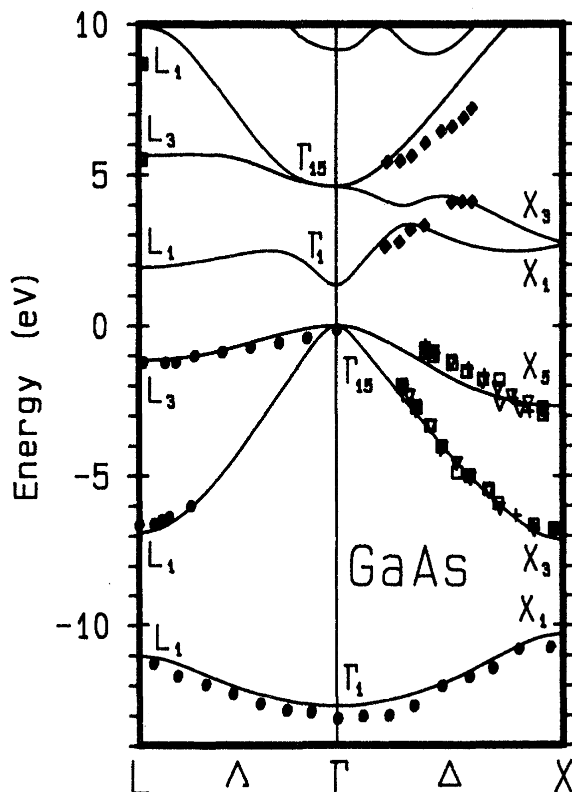

Figure 4.14: Band structure of GaAs, from [170].

having a much lower effective mass than electrons in the satellite L and X valleys. The effective mass of electrons at Γ in GaAs is $0.067m_e$ compared to $0.56m_e$ and $0.85m_e$ for the L and X valleys respectively, *i.e.* an order of magnitude less [172]. The L and X valleys lie at 1.82 and 1.98 eV above the valence band maximum, meaning both satellite valleys are accessed when GaAs is photoexcited with a 400 nm pump beam (3.10 eV). The relatively large effective mass of electrons in the L and X valleys means that they have relatively low mobilities, which explains why non-radiative decay by phonon emission to the zone centre takes several picoseconds. Once at the zone centre, electrons have higher mobilities and can therefore contribute to the sample conductivity, hence absorbing the THz probe. A much slower rising edge in the change of the THz pulses is therefore observed when photoexciting with 400 nm because electrons are injected into the satellite valleys (which does not happen with a 1.55 eV pump).

GaAs has a similar band structure to InP, which is the material of interest in §4.2, and the effective masses of electrons in the Γ, L and X valleys, as well as the band gaps of these valleys above the valence band maximum, are given in table 4.1. Electrons in the L and X valleys in InP also have much greater effective masses, and so a similar effect is expected upon photoexcitation with energies greater than 2 eV.

Material	GaAs		InP	
Conduction band	E_g (eV)	m_e^* (m_e)	E_g (eV)	m_e^* (m_e)
Γ	1.43	0.067	1.34	0.08
L	1.82	0.560	2.01	0.47
X	1.98	0.850	2.38	0.88

Table 4.1: Effective electron masses for the Γ, L and X conduction band valleys, as well as the energy gaps above the valence band maximum, in GaAs and InP, from [172]. The larger effective masses of electrons in the L and X satellite valleys, with relatively lower mobilities, means that scattering back to the Γ zone centre typically takes several picoseconds. The relatively lower effective mass of electrons at the zone centre means that it is these electrons that contribute to the sample conductivity.

4.2 Time-resolved terahertz spectroscopy of InP

4.2.1 Motivation

Stubbs *et al.* have measured carrier multiplication in indium phosphide (InP) colloidal quantum dots using ultrafast transient absorption spectroscopy [18], a study that involved the author. At photon energies greater than two times the band gap energy, the quantum efficiency, η, increases beyond unity. For example, at 2.6 E_g, the quantum efficiency was measured to be 1.18 ± 0.03 [18], because not each high-energy photon creates an extra electron-hole pair. The threshold energy for carrier multiplication, $h\nu_{th}$, depends on the electron and hole effective masses, m_e^* and m_h^*, of the material according to the energy partition model discussed in §2.6:

$$h\nu_{th} = \left(2 + \frac{m_e^*}{m_h^*}\right) E_g. \tag{2.99}$$

Whereas the threshold energy for carrier multiplication in bulk semiconductors is dictated by energy and momentum conservation such that $h\nu_{th}$ can be as much as $4E_g$, it is proposed that translational momentum conservation is relaxed in nanoparticles due to quantum confinement [68]. For example, in the case of $m_h^* \gg m_e^*$, where the energy levels in the valence band will be much more closely spaced than the energy levels in the conduction band, the carrier multiplication energy will be lower than the case of $m_h^* \approx m_e^*$ [26].

The process of carrier multiplication in quantum dots is still debated. The energy partition model of equation (2.99), however, does fit well with experimental data. For example, lead materials such as PbS and PbSe have similar effective masses, meaning that an energy threshold of $h\nu_{th} \approx 3E_g$ is expected. Indeed, the threshold energy for PbS has been measured to be approximately $3.2E_g$ [69] and $2.9E_g$ in PbSe [68]. For materials where $m_h^* > m_e^*$, a lower a threshold energy is

observed: approximately $2.1E_g$ in InP [18] and $2.5E_g$ in CdSe [68].

A lower threshold energy is desired should such quantum dots be utilized in a solar cell [15], especially because the band gap energy can be tuned to best overlap the solar spectrum by simply adjusting the size of the quantum dots [71]. InP is therefore a very interesting material: moreover, indium is a relatively benign substance compared to other quantum dot systems containing lead, cadmium, or arsenic, meaning it is also a commercially interesting material.

The fundamental physical processes involved in carrier multiplication are controversial. Indeed, it is still uncertain as to whether carrier multiplication is enhanced in quantum dots due to quantum confinement. Pijpers *et al.* have used time-resolved terahertz spectroscopy to measure the quantum efficiency of bulk lead sulphide (PbS) and lead selenide (PbSe), and have found that the bulk quantum efficiencies are in fact higher than those measured in PbS and PbSe quantum dots [16] when plotted on an absolute energy scale. These results conflict with the hypothesis that the quantum confinement of semiconductors leads to the enhancement of carrier multiplication due to the relaxation of the conservation of translational momentum. However, plotting on a relative energy scale, $h\nu/E_g$, as discussed in §2.6, shows that the quantum dots are more energy efficient that a bulk material with the same band gap energy. However, fewer excitons may be created in a quantum dot sample than in a bulk material at a particular photon energy due to a difference in band gap energies of the quantum confined and bulk materials [17].

The recent studies of carrier multiplication in bulk PbS and PbSe using time-resolved terahertz spectroscopy show that accurate measurements of bulk quantum efficiencies are necessary so as to understand the physical process involved in carrier multiplication in analogous quantum dot systems [16]. The fact that InP quantum dots have recently been shown to exhibit carrier multiplication, with one of the lowest threshold energies measured [18], means that measurements of bulk InP quantum efficiencies are urgently required for comparison, and this is the aim of this study.

Time-resolved terahertz spectroscopy offers an ultrafast measurement of the internal quantum efficiency. This technique is superior to traditional measurements involving the contact of electrodes, because in THz experiments the photoexcited carriers are not required to travel large distances to the electrodes over which scattering and recombination may occur.

Terahertz spectroscopy measures the photoexcited carrier density, obtained from fitting the experimentally-measured complex photoconductivity with the Drude model for a free electron-hole gas. In the case of InP, where the effective hole mass is approximately eight times the effective electron mass [18], the

THz response is due primarily to photoexcited electrons. The Fourier-transformed time-domain terahertz signal transmitted through the sample, $E_S(\omega)$, as well as the Fourier-transformed change in the terahertz signal upon photoexcitation, $\Delta E(\omega)$, is used to determine the complex photoconductivity $\tilde{\sigma}(\omega)$ as explained in §2.7:

$$\tilde{\sigma}(\omega) = -\frac{2\epsilon_0 c\tilde{n}}{\delta}\frac{\Delta E(\omega)}{E_S(\omega)}. \tag{2.111}$$

This calculation first requires the complex refractive index of the unphotoexcited sample, $\tilde{n}$, which is determined from THz scans with and without the sample by the method described in §3.3.7. These photoconductivity data are then fitted with the Drude model:

$$\tilde{\sigma}(\omega) = \frac{\epsilon_0 \omega_p^2 \tau_S}{1 - i\omega\tau_S}, \tag{2.112}$$

where the free parameters available to fit are the plasma frequency, ω_p, and the scattering time τ_S. A lower limit for the scattering time is determined by the electron mobility for a material, μ_e:

$$\mu_e = \frac{e\tau_S}{m_e^*}, \tag{4.2}$$

where e is the fundamental charge of the electron and m_e^* is the electron effective mass. The mobility for bulk InP with a similar doping level to the sample used here is 2000 $cm^2V^{-1}s^{-1}$ [173], which was also quoted by the wafer manufacturer, giving a lower limit scattering time of approximately 90 fs, in that the scattering time cannot be faster than that dictated by the electron mobility within a material.

The Drude model is fitted to the data using a simple minimum-least-squares method with two variables. The plasma frequency is then used to obtain the photoexcited electron density, N_e, according to eq. (2.114). The quantum efficiency, η, is then obtained from the ratio of electron to photon densities:

$$\eta = \frac{N_e}{N_\gamma}, \tag{2.115}$$

where the photon density is calculated using eq. (2.116), and the pump beam radius is measured using the knife-edge method (§3.1.6). The only knowledge required of the sample is therefore the absorption coefficient, reflectivity and thickness. For InP this information was obtained from [174]. The InP(100) wafer used was Fe-doped and semi-insulating. Semi-insulating semiconductors with low densities of free carriers and thus high resistivities allow for good transmission of THz radiation which would otherwise be heavily attenuated in the presence of free carriers. The band gap energy of bulk InP is 1.34 eV [174, 175]. The wafer was bought

from MTI Corporation, quoting a carrier concentration as low as 0.1 - 1.0 cm^{-3} and a resistivity of 10^7 - 10^8 Ωcm. The iron doping compensates for the *n*-type free carrier density, caused by lattice impurities *etc.*, due to a deep acceptor state that is formed.

4.2.2 Photoconductivity spectra

The refractive index and absorption coefficient of InP over THz frequencies are shown in figures (4.15) and (4.16), as calculated using the fixed-point iteration method of material parameter extraction (§3.3.7). The refractive index compares well with another terahertz study of InP using a different parameter extraction method, where the refractive index was determined to be 3.50 at 1 THz [176], compared to 3.41 measured here. This difference may be due to the doping of the sample. The InP sample used here is Fe-doped, whereas the doping of the sample studied by Dorney *et. al* [176] is not known. The infrared refractive index of InP is 3.12 at 2.39 μm [177].

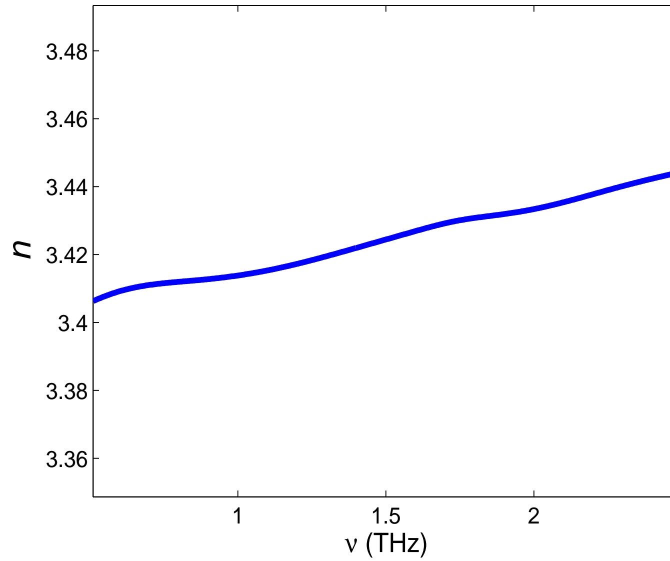

Figure 4.15: Refractive index of InP over terahertz frequencies extracted from the THz time-domain spectroscopy experiment.

It should be noted that in analysis of terahertz spectroscopy the spectral dependence of the refractive index of a sample is often neglected, and it is simply determined from the time delay of the terahertz pulses, Δt, observed:

$$\Delta t = \frac{(n - n_{ref})d}{c}, \tag{4.3}$$

where n_{ref} is the the refractive index of the reference (*i.e.* for air $n_{ref} = 1$) and d is

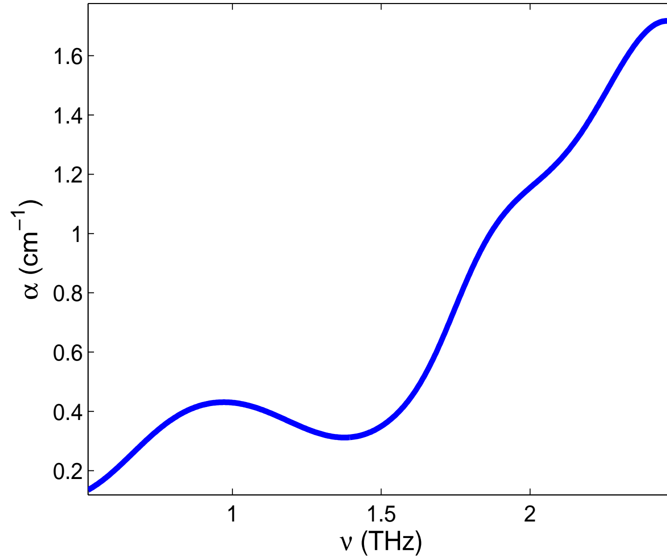

Figure 4.16: Absorption coefficient of InP over terahertz frequencies extracted from the THz time-domain spectroscopy experiment.

the sample thickness. The spectral analysis here is therefore a refinement to this.

An example time-domain trace of a THz pulse through the InP sample, E_S, and the change in the THz pulse upon photoexcitation with an 800 nm pump beam, ΔE, are shown in figure (4.17), and the Fourier transforms of these time-domain traces are shown in figure (4.18). The temporal shift of the time-domain trace of ΔE is due to a small change in the refractive index of the sample induced by the charge carriers created by the absorption of the pump over the penetration depth. It is these spectra that are used to calculate the complex photoconductivity of the sample. For the 800 nm pump beam (in this case with an energy density of 7.6 nJ mm^{-2}), the complex photoconductivity spectrum is shown in figure (4.19). The photoconductivity data are fitted with the Drude model using a minimum least squares method with two free parameters, the plasma frequency, ω_p, and scattering time τ_S. Another example photoconductivity spectrum using a 450 nm pump beam (with an energy density of 11.8 nJ mm^{-2}) is shown in figure (4.20), where a similar scattering time to that of the 800 nm case is obtained. Higher plasma frequencies result from higher pump energy densities, as well as higher pump photon energies due to the electron-hole plasma occupying a smaller portion of the sample because of a higher absorption coefficient and hence smaller penetration depth. It should be noted that all scattering times obtained from the fitting process are larger than the minimum value of 90 fs obtained from the mobility, but very consistent with it (of the same order of magnitude).

A power dependence study was carried out using a 511 nm pump beam, with energy densities ranging between 2.86 and 14.3 nJ mm^{-2}. The photon density, N_γ,

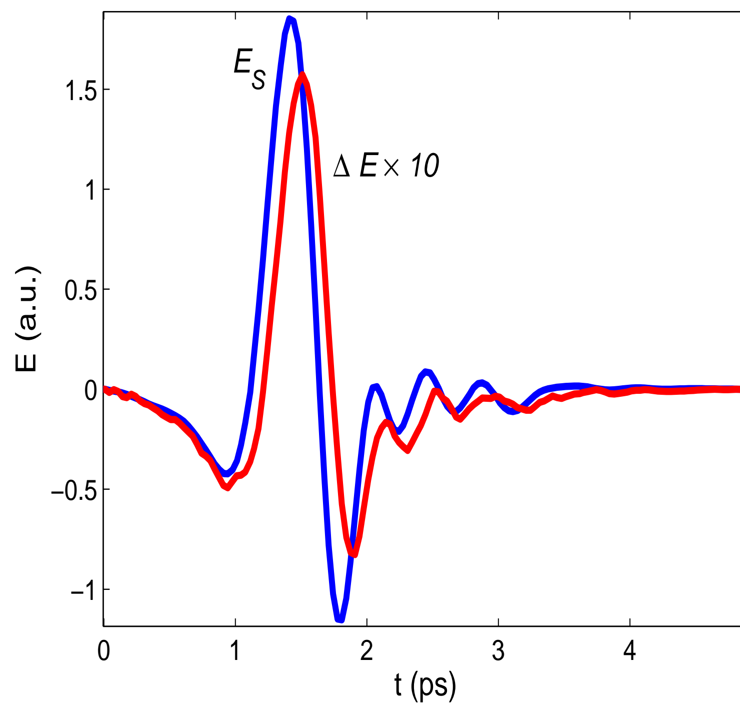

Figure 4.17: Time-domain trace of THz pulses through the InP sample, E_S, and the change in the THz pulses, ΔE, upon photoexcitation with an 800 nm pump beam with an energy density of 7.6 nJ mm^{-2}.

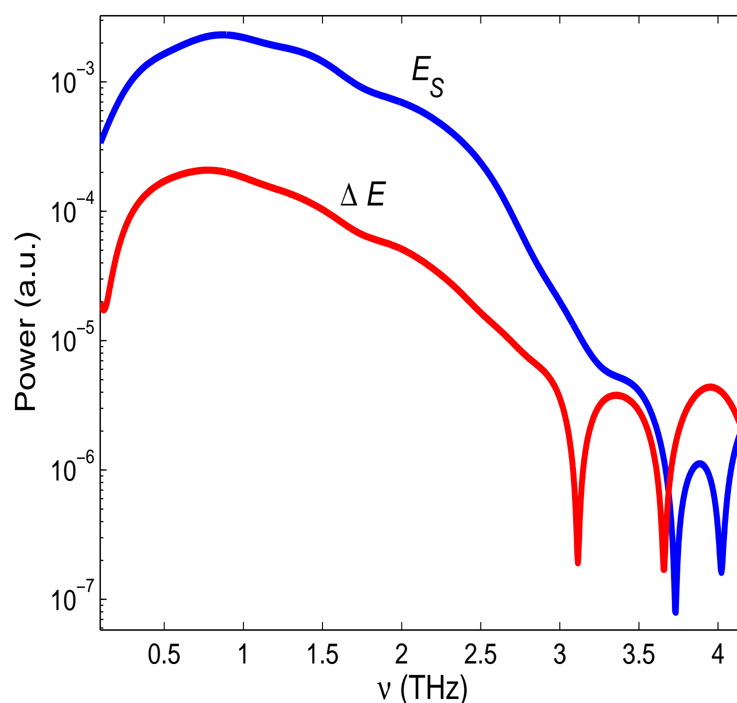

Figure 4.18: Fourier transforms of the time-domain traces shown in figure (4.17) to give the power spectrum of THz pulses through the InP sample, E_S, and the change in the power spectrum upon photoexcitation, ΔE, with a 7.6 nJ mm^{-2}, 800 nm pump beam.

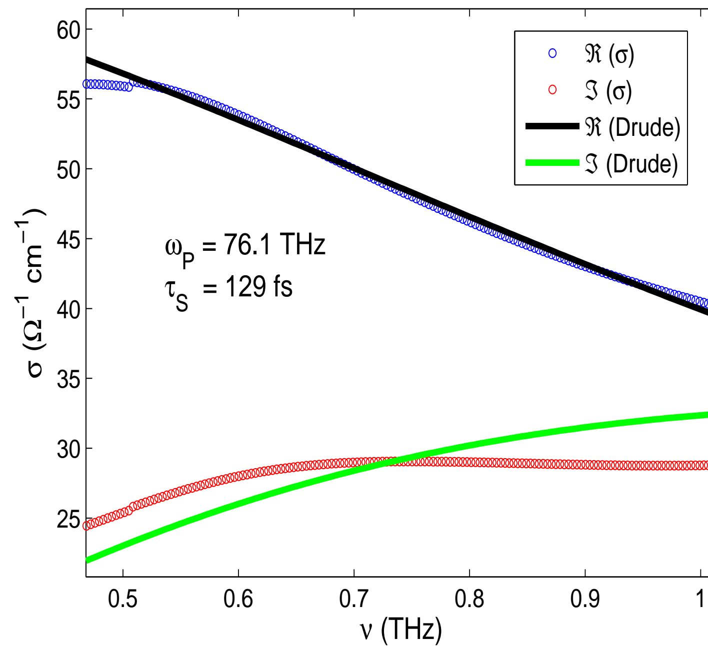

Figure 4.19: Complex photoconductivity of InP upon photoexcitation with an 800 nm pump beam with an energy density of 7.6 nJ mm^{-2}, obtained using the power spectra shown in figure (4.18). The data are fitted with the Drude model using a plasma frequency, ω_p, of 76.1 THz and a scattering time, τ_S, of 129 fs.

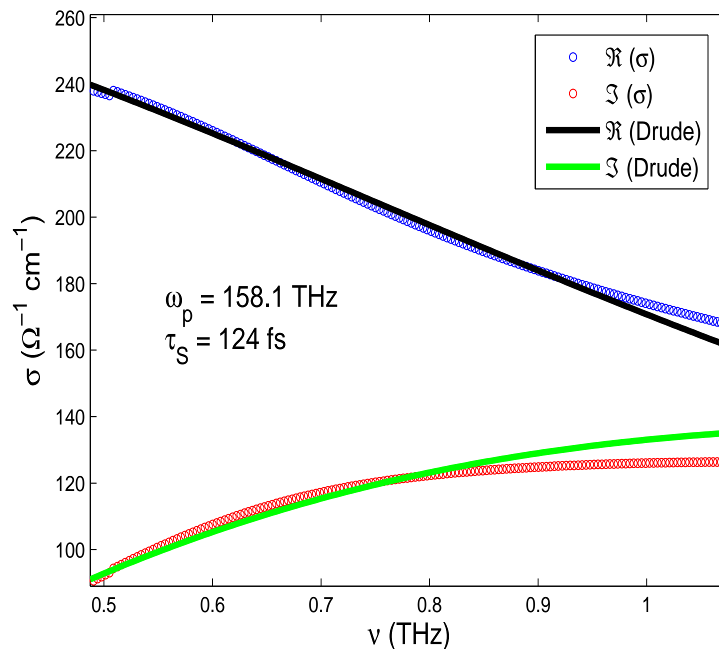

Figure 4.20: Complex photoconductivity of InP with a 450 nm pump beam (energy density of 11.8 nJ mm^{-2}). The data are fitted with the Drude model using a plasma frequency, ω_p, of 158.1 THz and a scattering time, τ_S, of 124 fs.

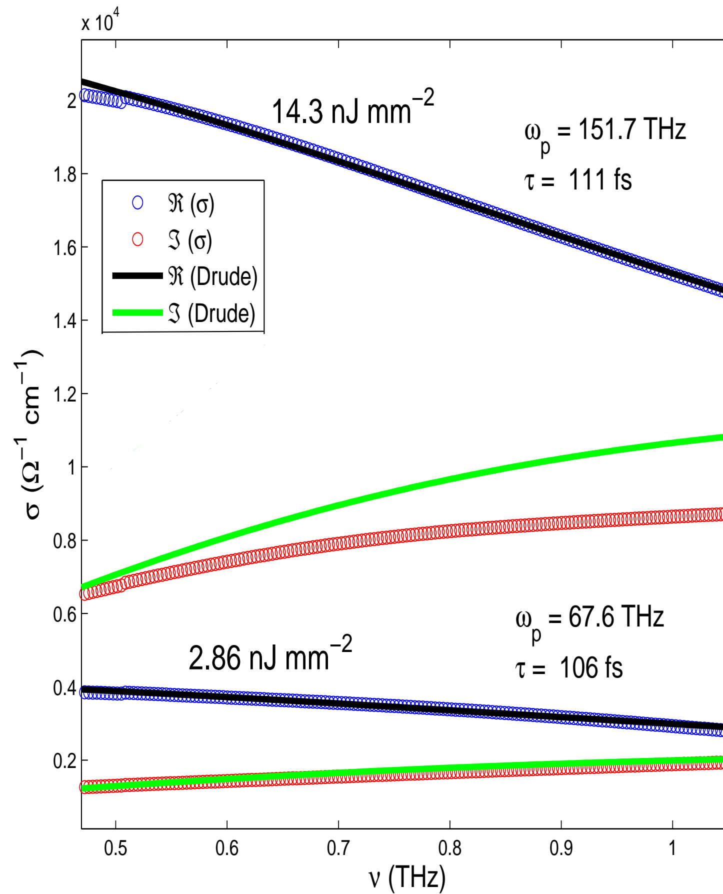

Figure 4.21: Complex photoconductivity spectra of InP with a 511 nm pump beam and two different energy densities, 2.86 and 14.3 nJ mm^{-2}.

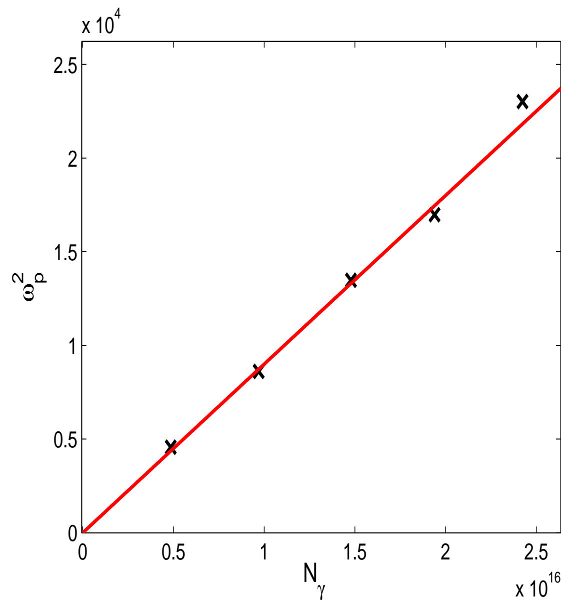

Figure 4.22: Power dependence of the square of the plasma frequencies obtained from the Drude model fitting of photoconductivity spectra for InP with a 511 nm pump beam. The linear fit is $\omega_p^2 = 9 \times 10^{-13} N_\gamma$, where $\omega_p^2 = 0$ at $N_\gamma = 0$.

is related to the square of the plasma frequency ω_p according to:

$$\omega_P = \sqrt{\frac{2N_e e^2}{\epsilon_0 m^* \delta}}, \tag{2.114}$$

where the photoexcited electron density is proportional to the photon density ($N_e \propto N_\gamma$). The power dependence study was therefore carried out to ascertain if this was the case for the plasma frequencies obtained by the Drude model fitting. The complex photoconductivity spectra at the highest and lowest energy densities are shown in figure (4.21), whilst a plot of the square of the plasma frequencies obtained from fitting against photon densities is given in figure (4.22). Indeed, the relationship is linear as expected and the intercept occurs at the origin (no electron-hole plasma created at zero fluence). This also means that there are no band filling effects occurring with increased fluence, for this would change the effective electron mass and hence the plasma frequency [178].

The photoconductivity spectra were taken at a pump-probe delay time, τ, of approximately 10 ps after photoexcitation. This was to ensure that the maximum change in the THz pulses, ΔE, had been reached but also that no recombination of charge carriers had occurred. Pump-probe delay scans for the case of a 511 nm pump beam at energy densities of 2.9, 8.6 and 14.3 nJ mm^{-2} are shown in figure (4.23). These pump scans illustrate that ΔE is proportional to fluence, and that 10 ps is an appropriate pump-probe delay time at which to measure the photoconductivity.

It is important to measure the change in the terahertz waveform at least 10 ps after photoexcitation because the intervalley scattering of electrons at high pump photon energies means that the full change in the THz pulse, ΔE_{THz}, is not attained for several picoseconds after photoexcitation [171]. This is revealed in the rising edge of the pump scans, as shown in figure (4.24). In the same way as in GaAs, at higher photon energies the rising edge of the change in the terahertz waveform becomes delayed due to electrons scattering back to the band edge. The fact that this effect occurs at similar photon energies in InP as GaAs is due to the two materials having very similar band structures, with similar band gap energies of 1.34 and 1.43 eV respectively. The band structure of InP is shown in figure (4.25) to compare with that of GaAs in figure (4.14). These similarities also lead to very similar impact ionization coefficients in the two materials [179].

The photoconductivity spectra in figures (4.19), (4.20) and (4.21) show that the Drude model does not fit the imaginary component of the complex photoconductivity as adequately as it does the real component. However, the aim of the fitting is to obtain the plasma frequency, ω_p, which is related to the photoexcited electron

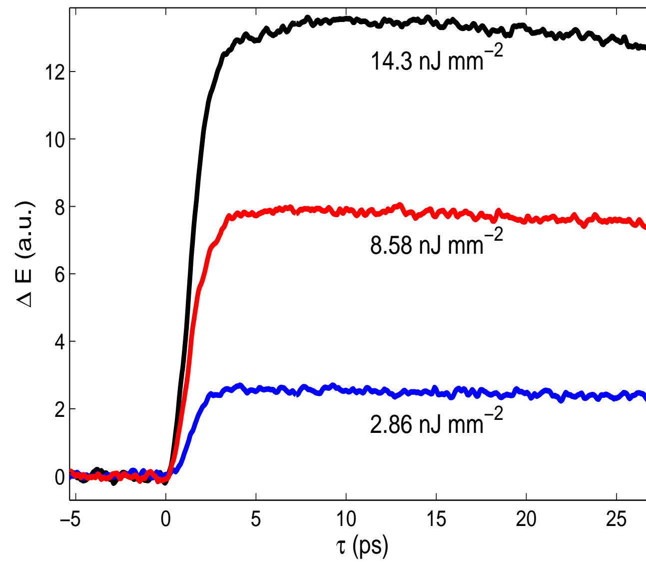

Figure 4.23: Pump scans showing the change in the THz pulse, ΔE, as a function of pump-probe delay time τ, with photoexcitation by a 511 nm pump beam at various energy densities. The photoconductivity spectra were all measured at a pump-probe delay time of approximately $\tau = 10$ ps.

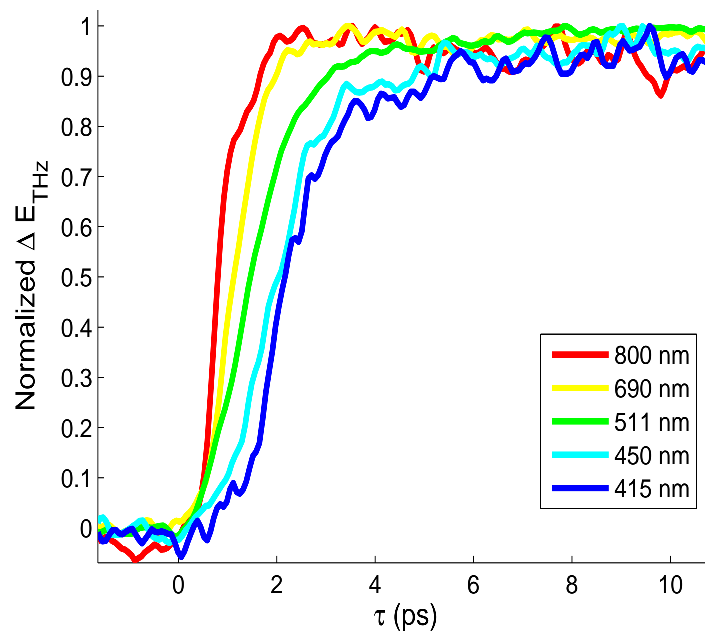

Figure 4.24: Pump scans showing the rising edge of the change in the THz pulse, ΔE, as a function of pump-probe delay time τ, with various pump wavelengths: 800 nm (1.55 eV), 690 nm (1.80 eV), 511 nm (2.42 eV), 450 nm (2.76 eV) and 415 nm (2.99 eV). At higher energies the rising edge is delayed due to charge carriers scattering back to the band edge.

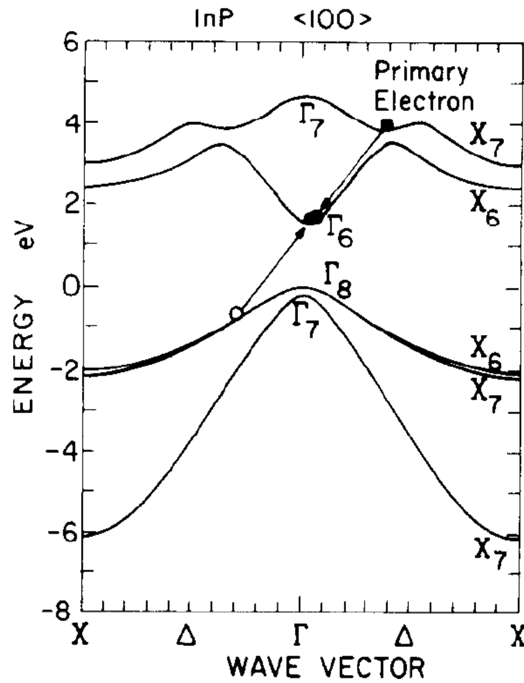

Figure 4.25: Band structure of InP, illustrating electron-initiated impact ionization in InP, from [180]. A high energy photon photoexcites an electron into the conduction band. Energy is then transferred to another valence band electron, promoting it into the conduction band, leading to two photoexcited electrons at the band edge.

density. This is sufficiently extracted from the real component fitting, and indeed the Drude model is generally observed to fit poorly to the imaginary component of the photoconductivity in the literature: an example is shown in figure (4.26) taken from reference [16]. However, there is no discussion of this problem in the literature. Terahertz photoconductivity spectra are also frequently displayed only up to frequencies of 1 THz as shown in figure (4.26). Modifications to the Drude model, such as the Drude-Smith model which is adjusted to account for electron back-scattering [96], were tested and were found not to improve the fits.

It is important to note that InP can be used to generate THz radiation in the same way ZnTe is used in the THz time-domain spectrometer [181, 182]. However, the excitation densities used in this experiment were far below those required for THz generation [181]. To confirm this, a check was performed where the THz probe delay line was scanned with the pump beam photoexciting the InP sample whilst the THz generation beam was blocked, in order to establish that no THz radiation was being created. No change was observed, confirming that no THz radiation was generated by the InP wafer during the experiment.

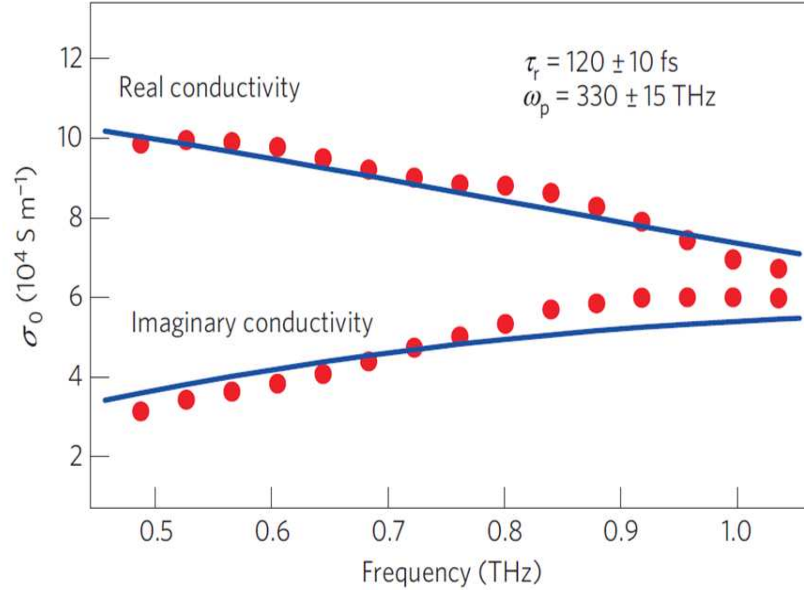

Figure 4.26: Complex photoconductivity spectrum for bulk PbS taken from reference [16]. The imaginary component is not fitted as adequately as the real component.

4.2.3 Efficiency of bulk InP

The optical parametric amplifier was used to provide a pump beam at various wavelengths such that an energy range between 1 and 2.5 times the band gap energy of InP could be investigated. This range was chosen so as to compare to the $h\nu/E_g$ energy range investigated for InP quantum dots [18]. The use of this relative energy scale best demonstrates the energy efficiency of the material [17].

The efficiency of bulk InP calculated using eq. (2.115) is shown in figure (4.27). Here, efficiency is defined as the ratio of the measured photoexcited carrier density to the input pump photon density at a pump-probe time delay of 10 ps. This should not be confused with the internal quantum efficiency of the material, because the instantaneous change in the THz probe upon photoexcitation cannot be measured due to the intervalley scattering of electrons to the zone centre (as discussed in §4.1.3). The pump-probe delay time of 10 ps was chosen so that all intervalley scattering effects would be finished, yet before any significant carrier recombination had occurred.

The bulk measurements are compared to the quantum efficiency of InP quantum dots from Stubbs *et al.* [18] and measurements from an InP photovoltaic device [183]. The InP device included a 4 µm thick Zn-doped (1×10^{17} cm^{-3}) absorber. Whereas the quantum dots show carrier multiplication above $h\nu = 2.1E_g$, the bulk shows no carrier multiplication [184]. Moreover, the efficiency of the bulk material decreases at energies higher than approximately $2E_g$. This is, however, in agreement with measurements on an InP photovoltaic device. These device

measurements also agree with previous measurements on InP devices [185, 186].

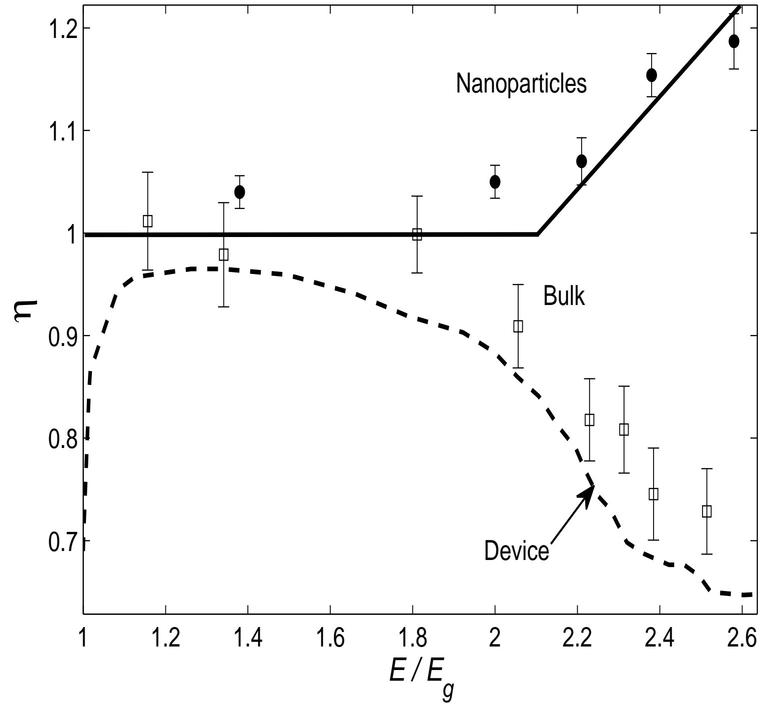

Figure 4.27: Efficiency, η, of bulk InP measured using time-resolved terahertz spectroscopy [184] (squares). The bulk measurements agree with measurements on an InP photovoltaic cell, from Schimper *et al.* [183] (dashed line). The bulk material shows no carrier multiplication in contrast to measurements on InP quantum dots [18] (filled circles), where the quantum efficiency increases above $h\nu = 2.1E_g$, illustrated by the solid line (a guide for the eye).

The THz quantum efficiency measurements are consistently slightly higher than those from the device. This may be because device measurements use electrodes in contact with the device, and so charge carriers travel large distances to be detected, over which scattering and recombination can occur. This underestimation in the efficiency of a material as measured with electrodes was also observed by Pijpers *et al.*, where time-resolved THz measurements on bulk PbS are compared to measurements of a PbS device [16]. The PbS device efficiency measurements, from Smith and Dutton [187], were consistently lower than those obtained from ultrafast THz spectroscopy.

The errors in the efficiency measurements are calculated according to:

$$\left(\frac{\sigma_\eta}{\eta}\right)^2 = \left(\frac{\sigma_{N_e}}{N_e}\right)^2 + \left(\frac{\sigma_{N_\gamma}}{N_\gamma}\right)^2, \tag{4.4}$$

where the error in the electron density is determined by the error in the plasma

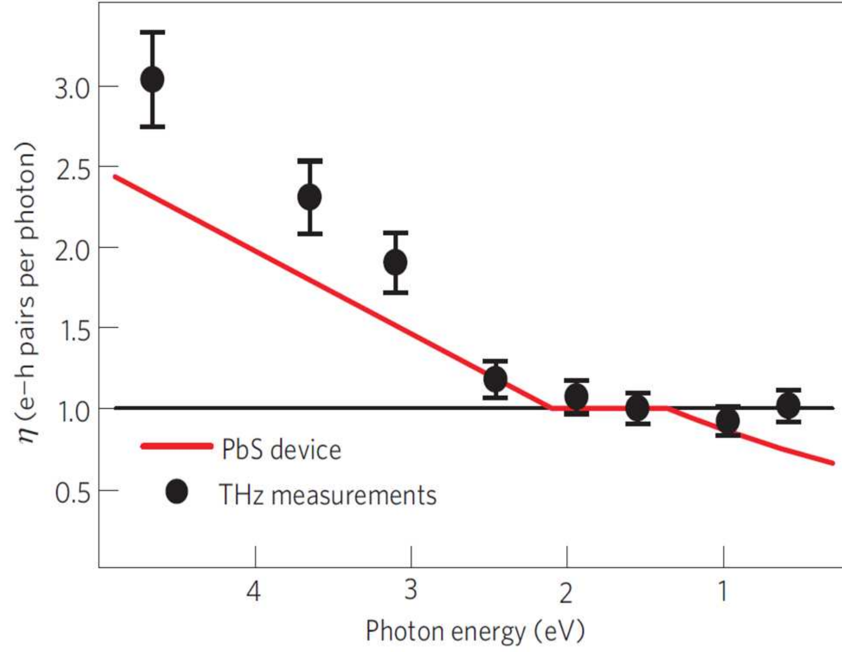

Figure 4.28: Quantum efficiency of bulk PbS, as measured with terahertz spectroscopy (dots), compared to measurements from a PbS device, from [16].

frequency that is extracted by Drude model fitting:

$$\left(\frac{\sigma_{N_e}}{N_e}\right)^2 = 2\left(\frac{\sigma_{\omega_p}}{\omega_p}\right)^2, \tag{4.5}$$

because $N_e \propto \omega_p^2$. The error in the photon density is due to the error in the power meter reading and in the measured radius of the pump beam ($N_\gamma \propto P$ and $N_\gamma \propto 1/r^2$):

$$\left(\frac{\sigma_{N_\gamma}}{N_\gamma}\right)^2 = \left(\frac{\sigma_P}{P}\right)^2 + 2\left(\frac{\sigma_r}{r}\right)^2. \tag{4.6}$$

The error in the extracted plasma frequency was 0.2 THz, the range over which a small adjustment of the scattering frequency would allow for a similar least-squares residual to be obtained. The error in the power meter reading was 20 μW and the error in the radius measurement (using the knife-edge technique) was 0.2 mm. The largest contribution to the error is the error in the photon density such that $\sigma_{N_\gamma} \gg \sigma_{N_e}$, of which the error in the beam radius is the largest contributor.

The measurements on bulk InP do not illustrate carrier multiplication, with a drop in efficiency occurring towards UV wavelengths [184]. This is in contrast to similar measurements on bulk PbS, as shown in figure (4.28), where carrier multiplication - an increase in quantum efficiency - is found to occur as the photon energy is increased.

The observed drop in efficiency observed in GaAs and InP devices is due to

surface recombination [188]. Surface recombination is the process whereby surface states act as recombination centres for charge carriers. The effect of these surface recombination centres is to dramatically reduce the minority carrier (for *n*-type semiconductors, holes) lifetime τ_M [189]:

$$\frac{1}{\tau_M} = \frac{1}{\tau_R} + \frac{1}{\tau_D} + \frac{1}{\tau_S}, \tag{4.7}$$

where τ_R, τ_D and τ_S are the radiative, defect-state-initiated and surface-state-initiated recombination lifetimes respectively. This leads to limited quantum efficiency of a material [189, 190]. Moreover, at higher energies, a greater absorption coefficient means that photoexcited charge carriers are more concentrated at the surface: the absorption region is the penetration depth, $\delta = 1/\alpha$, where approximately 63% of photons are absorbed over δ, and 95% over 3δ. An increase in the absorption coefficient is analogous to a decrease in the diffusion length of the charge carriers, or the length over which a carrier can travel before recombination occurs [191]. Therefore a drop in efficiency occurs at higher photon energies. The role of surface recombination as the cause of a loss of quantum efficiency is widely accepted, and the energy dependence of quantum efficiency observed in InP is typical to solar cell devices [188].

The drop in efficiency with photon energy in bulk InP, as opposed to an increase in efficiency in bulk PbS [16], may be due to the differences in the band structures of the two materials. For example, a drop in quantum efficiency is also observed in GaAs devices [192, 193], as shown in figure (4.29), with the efficiency decreasing at ultraviolet energies greater than $2E_g$. InP has a very similar band structure to GaAs, whereas the band structure of PbS, as shown in figure (4.30), is quite different [194]. For instance, the minimum band gap in PbS does not occur at the zone centre (the Γ point). One other factor may be that surface recombination effects are missing due to the sample being optically thin. The PbS sample studied was an epitaxial layer with a thickness of 1 μm [16]. This is of the same order of magnitude as the penetration depth for PbS at lower energies ($\delta = 1$ μm at 1.24 eV [195]). However, $d > \delta$ will still hold true at higher photon energies. InP has a penetration depth of $\delta = 0.3$ μm at 1.55 eV [174], and the sample was 0.5 mm thick meaning it was optically thick.

Figure 4.29: Quantum efficiency of GaAs substrates with and without a Bragg reflector, from [193].

Figure 4.30: Band structure of PbS, from [194].

4.3 InP Quantum Dot measurements

Assessment of carrier multiplication in quantum dot samples is traditionally measured using transient absorption spectroscopy where a visible probe beam creates interband transitions of the photoexcited electrons (for example, see studies on PbSe[75], InP [18] and PbS [69]). The THz equivalent of these measurements can complement these studies, and the frequency dependent conductivity can give understanding into the behaviour of charge carriers within the quantum dots, for example, whether the photoconductivity is Drude-like or not [22].

Carrier multiplication in quantum dot samples is determined from the transient change (measured by a pump scan) in the THz pulse (or other probe, such as a white light continuum in transient absorption experiments), which is indicative of the excitonic population in the sample. A biexciton is revealed as an ultrafast (tens of picoseconds) component in this transient. Although this will be seen at high fluence due to multi-photon absorption, carrier multiplication is judged to be present when this fast transient still occurs in the regime of low fluence (*i.e.* when one photon or less is absorbed per quantum dot). Thus photoexcitation with a pump beam with energies above the carrier multiplication threshold with low fluence will show a fast transient if carrier multiplication is present, and this fast transient will not be present if the pump beam has an energy below the threshold.

Colloidal quantum dots (nanoparticles encased in ligands that prevent consolidation) are often dispersed in solution in toluene or hexane, or other solvents including chloroform. Initial studies show that hexane is a more suitable solvent for THz measurements due to a lower absorption coefficient than toluene (figure (4.9)). Quartz is the most suitable material for the sample cuvette, with much greater absorption occurring in glass materials.

The concentration of the solution is an important factor when carrying out time-resolved laser-pump THz-probe experiments. It is important that all of the pump energy is absorbed by the quantum dots upon photoexcitation so that the greatest change in the THz waveform, ΔE, is achieved. The absorbance of InP quantum dots in hexane (1 mm path length) was therefore measured as shown in figure (4.31). The absorbance, or optical density, at a particular wavelength is defined as:

$$A = \log\left(\frac{I_0}{I}\right) \tag{2.108}$$

where I is the intensity of the probe transmitted through the sample and I_0 is the initial intensity. The absorbance at the pump wavelength of 400 nm (3.10 eV) was 2.1: Beard *et al.* state that in these type of THz experiments an absorbance of at least 2 at the pump wavelength is desirable so as to measure a change in the THz

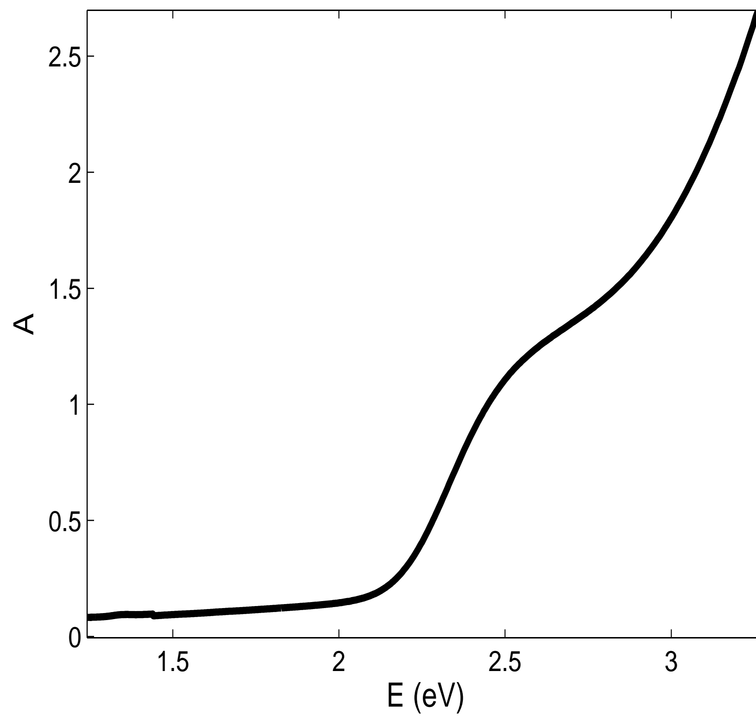

Figure 4.31: Visible absorbance spectrum of 6 nm InP quantum dots suspended in hexane. At 400 nm (3.10 eV) the sample has an absorbance of approximately 2.1. The non-zero absorbance at lower energies is due to sample defects.

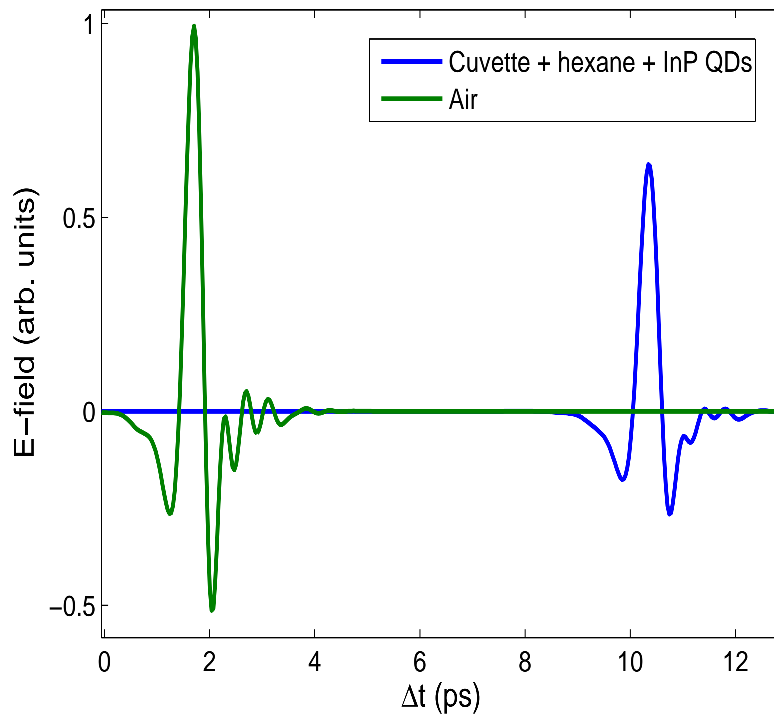

Figure 4.32: Time-domain traces of THz pulses through 6 nm InP quantum dots held in a solution of hexane in a 1 mm path length quartz cuvette.

waveform [22]. The greatest possible concentration was achieved by allowing the hexane solvent to evaporate over $\approx$ 48 hours, before redissolving the quantum dots in a minimal amount of solvent (*i.e.* enough to fill the 1 mm path length cuvette, approximately 0.4 ml). The absorbance spectrum in figure (4.31) is non-zero at lower energies, suggesting that the quantum dots contain defects which create states within the band gap giving rise to sub band gap absorption. However, the clear absorbance feature of the 1*s* exciton state at $\approx$ 2.5 eV shows that the size dispersion of the majority of the quantum dots is acceptable: a very large size dispersion would lead to this state being unidentifiable. The fluence of the pump beam is another issue to consider in the experiment, because greater changes will be measured at greater fluences.

A time-domain trace through the quantum dot sample is compared to an air reference signal in figure (4.32). Because an air reference was used, the absorption spectrum of the quantum dot sample is calculated in the usual way, before the absorption coefficients of the quartz cuvette (figure (4.4)) and hexane (figure (4.9)) are subtracted. The result is shown in figure (4.33). The absorption coefficient is small and comparable to that of the hexane solvent ($\approx$ 2 cm^{-1} at 2 THz) over terahertz frequencies, due to a dramatically lower number of free carriers compared to an undoped bulk sample. The absorption edge for the 1*s* exciton state at $\approx$ 2.5 eV means that the diameter of the quantum dots can be estimated to be 6 nm, by comparing to a literature study carried out on a variety of different sizes of InP quantum dots [196]. The absorption coefficient increases with frequency due to absorption by phonon modes as seen in the literature [105], although absorption spectra over terahertz frequencies are often omitted in literature studies of quantum dots.

Upon photoexcitation of the quantum dot sample with a 400 nm pump beam, a change in the terahertz waveform, ΔE, was not detected as shown in figure (4.34). Moreover, 16 scans were recorded and averaged so as to enhance the signal-to-noise ratio by a factor of 4. The ΔE scan was taken at a pump-probe delay time of approximately 10 ps, determined previously using the bulk InP sample. Clearly the change in the terahertz waveform is less than 1 in 1000.

The lack of a detected change in the terahertz waveform is not unexpected. Dakovski measured a THz change of 1 in 5000 in a PbSe sample [24] and Hendry *et al.* measured a THz change of 1 in 2000 in a CdSe sample [25, 23]. An InP quantum dot sample has not been measured before, and it is difficult to predict how large the signal will be. Moreover, the ligand and optical density of the samples can affect the measurements [22]. Whereas Hendry *et al.* measured a change of 1 in 2000 from colloidal CdSe quantum dots, a similar study of a CdSe sample by Wang *et al.* showed a change in the THz waveform of 1 in 200, an order

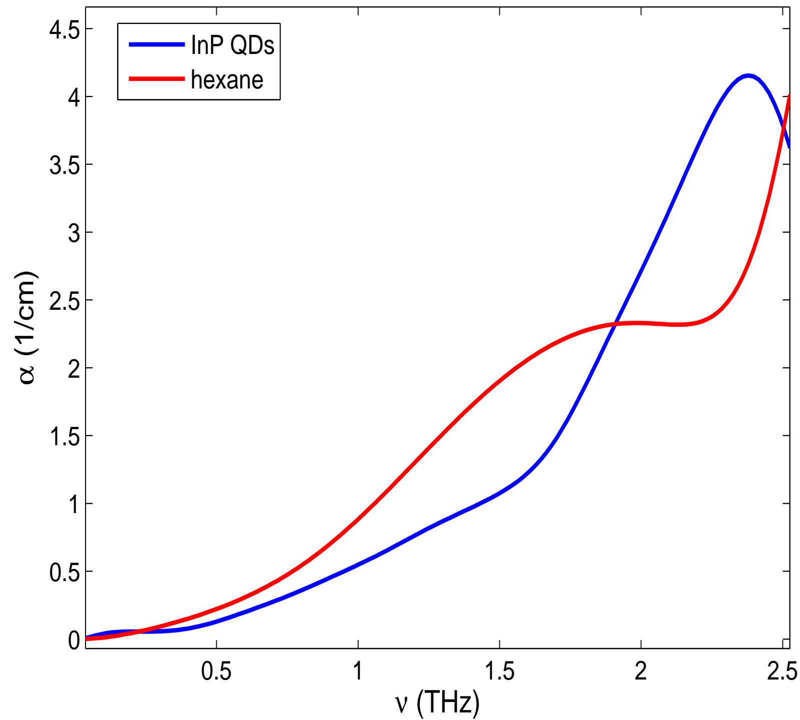

Figure 4.33: Absorption spectrum of 6 nm InP quantum dots over THz frequencies.

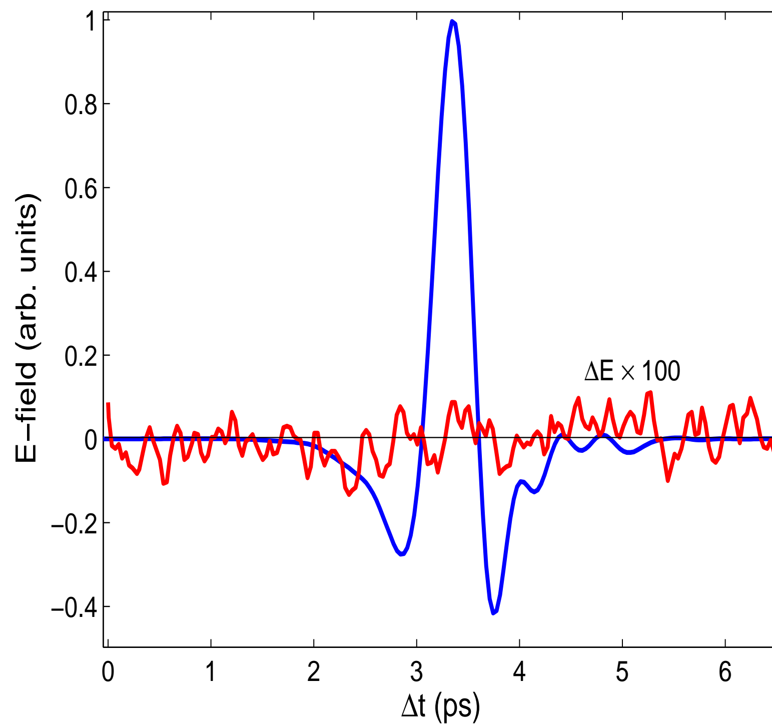

Figure 4.34: The change in the THz waveform, ΔE (red line), upon photoexcitation with a 400 nm pump with an energy density of 3.4 μJ cm^{-2}. A change in the InP quantum dot sample is not detected, as the ΔE scan appears as a flat noise line. The noise of this line is approximately $\pm 0.1/100$, and so the change in the THz waveform is less than 1 in 1000 compared to the THz waveform before excitation, illustrated by the blue line.

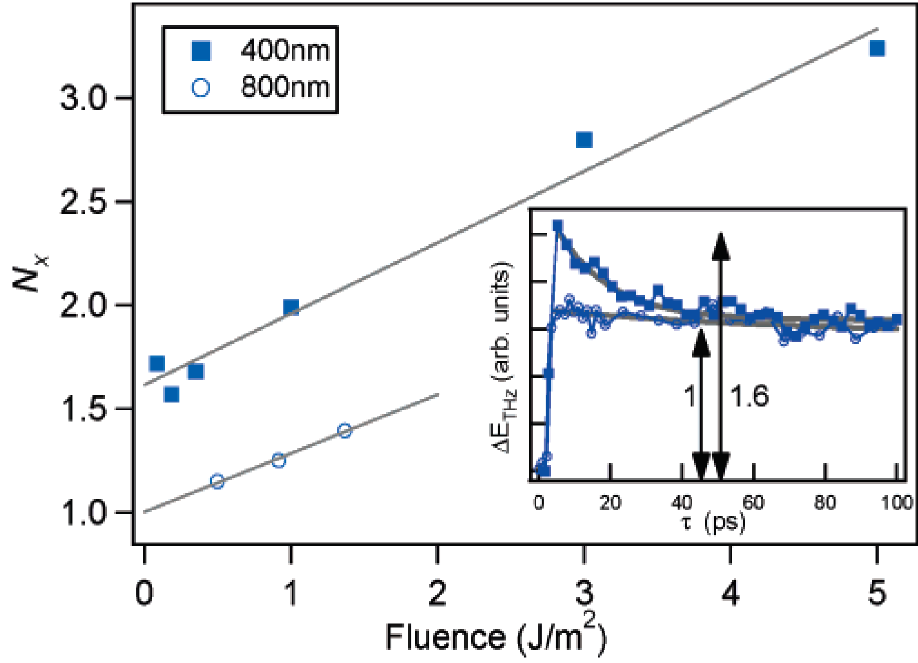

Figure 4.35: Carrier multiplication studied in InAs quantum dots with time-resolved THz spectroscopy [26]. 800 and 400 nm radiation are below and above the threshold for carrier multiplication. In the regime of low fluence, a fast biexciton component to the ΔE_{THz} transient is observed when photoexcitation occurs with 400 nm radiation.

of magnitude greater [27]. Pijpers *et al.* have studied InAs quantum dots in toluene with a change in the THz waveform of approximately 1 in 400 as shown in figure (4.35) [26].

The lowest fluences used in these experiments in the literature are 30 μJ cm^{-2} [25] and 88 μJ cm^{-2} [26]. These fluences are an order of magnitude greater than used here, where a fluence of 3.4 μJ cm^{-2} was measured at 400 nm. To achieve a higher fluence, several major changes need to be made. Rather than use the optical parametric amplifier to generate the pump beam, the pump beam could be generated in a doubling crystal, as was used in the original terahertz setup (3.15). However, at higher fluences the pellicle beam splitter cannot be used to bring the pump beam to the sample colinear to the THz probe due to a low damage threshold. Therefore in this setup the pump was brought to the sample at an angle around the gold parabolic mirrors, and hence was not colinear with the probe. In a new experimental arrangement, a hole could be drilled in the parabolic mirror that focuses the THz beam to the sample. This would, however, make the experimental set-up challenging to optimize because the alignment of the THz beam could not then be checked using a reference laser beam (*i.e.* removing the ZnTe generation crystal and following the 800 nm generation beam through the spectrometer).

Time-resolved THz measurements on quantum structures that are not quantum

confined in all three dimensions, such as self-assembled quantum dots grown on a substrate [169] or linked arrays of nanoparticles [80, 173], are more successful. Indeed, there are many THz studies on nanowires in the literature, for example on ZnO [97], GaAs [197] and Ge [198]. Therefore, an epilayer of the InP quantum dot sample could be deposited on a substrate as an alternative study.

4.4 Conclusions

The time-resolved THz spectrometer has been commissioned and benchmarked. Part of the commissioning process involved THz absorption measurements of two solvents, hexane and toluene, commonly used as solvents for quantum dots. It is found that toluene is a greater absorber of THz radiation, and so hexane is the more suitable solvent. The THz refractive indices for toluene and hexane agree well with literature data, as does the THz absorption spectrum of toluene, although the THz absorption spectrum of hexane is absent in the literature. Indeed, some terahertz measurements of colloidal quantum dot samples have used toluene as a solvent [26, 27], which unnecessarily reduces the THz signal.

A laser-pump THz-probe experiment was then conducted on a 0.35 mm thick GaAs(100) wafer to benchmark the pump-probe technique against an identical study in the literature. Measuring the change in the THz waveform at various pump-probe delay times allowed a two-dimensional plot of pump-probe delay time versus the THz probe delay time to be plotted. An identical smearing of the data was observed compared to the literature, which is caused by the overlap of the pump and probe pulses over approximately 3 ps. Pump scans at two different wavelengths, 800 nm and 400 nm, showed that the rising edge of the change in the THz waveform was delayed at a higher pump energy. This delay is attributed to the intervalley scattering of photoexcited conduction band electrons. This intervalley scattering effect was also observed in a bulk InP wafer. For this reason, measurements of the photoconductivity of semiconductors should be taken at a pump-probe delay time of at least 10 ps, at which time all electrons will have returned to the band edge.

A time-resolved study of bulk InP was carried out to measure the internal quantum efficiency of the material across a range of pump photon energies [184]. This was an important study because recently published transient absorption measurements on InP quantum dots show carrier multiplication at photon energies greater than twice the band gap energy [18]. An analogous study on bulk PbS showed that, although carrier multiplication had been found to occur in PbS quantum dots, the efficiency of the process was less than that of the bulk [16].

Quantum efficiency measurements on bulk InP showed that no carrier multiplication occurs, and that the efficiency actually decreases at higher photon energies [184]. This is due to surface recombination effects that are enhanced at higher photon energies due to the change in the absorption coefficient (and hence the penetration depth of the radiation) of the sample. The unusual results previously observed in PbS [16] may therefore be due to a very different band structure, or it may be due to the fact that the sample was optically thin. It would certainly be interesting to conduct a study of a bulk PbS sample that was optically thick so that the sample thickness was much greater than the pump penetration depth ($d >> \delta$).

Absorption measurements over terahertz frequencies have been taken for InP quantum dots suspended in hexane. A visible absorbance spectrum was first measured to estimate the diameter of the quantum dots to be approximately 6 nm, and to ensure that the optical density of the sample was sufficient for pump-probe experiments. The THz absorption was found to be small and of the same order of magnitude as the hexane solvent. Increased absorption at higher THz frequencies was attributed to absorption by phonon modes as suggested in the literature. Time-resolved measurements of the quantum dots using a 400 nm pump beam were unsuccessful: a change in the THz waveform was not detected, and so a transient of this change (used to assess whether or not carrier multiplication is occurring) could not be measured. However, these measurements have ascertained that the change in the THz waveform was less than 1 in 1000. The experiment was limited by the signal-to-noise ratio of the system as well as a limitation in the pump fluence available. Rather than using an optical parametric amplifier to generate a pump beam, a doubling crystal could be used. However, this will require several significant modifications of the system, including bringing the pump beam to the sample colinear with the THz probe beam through a hole drilled in one of the gold parabolic mirrors. This is clearly the next step that should be taken in the development of the THz spectrometer.

Chapter 5

Laser-pump synchrotron-probe experiments of bulk and nanoparticulate photovoltaic materials.

5.1 Surface photovoltage in *n*-type Si(111)

The laser system was synchronized to the Synchrotron Radiation Source (SRS) at Daresbury Laboratory, Cheshire, UK. An extreme ultraviolet (XUV) beam of energy $h\nu = 140$ eV was used to probe the Si 2p core level of the Si(111) (7×7) surface using XPS. The surface photovoltage (SPV) was observed as a shift in kinetic energy of this core level with illumination from the laser operating at a wavelength of 800 nm (1.55 eV, where the band gap of silicon is 1.12 eV) causing excitation of valence band electrons into the conduction band.

The 0.5 mm thick silicon sample was n-phosphorous doped with a resistivity of 5 Ωcm corresponding to a doping level of approximately 10^{15} cm^{-3}. The (7×7) surface reconstruction of the silicon leads to partially-occupied surface states within the band gap. This creates a depletion layer at the surface and the Fermi energy is pinned by the surface states. The n-type bulk means that the conduction and valence band edges bend at the surface. Upon photoexcitation, charge carriers are injected into the depletion layer which causes a change in the band bending. Because XPS is a surface-sensitive technique, the change in the surface band bending, the surface photovoltage, is measured using the Si 2p core level.

This section gives a brief description of the sample preparation, or cleaning, performed under ultra-high vacuum (UHV), before explaining how the XPS spectral peaks of the Si 2p core level have been fitted. The changes under laser illumi-

nation are then extracted to measure the change in the surface photovoltage.

5.1.1 Surface preparation

The reconstructed Si(111) (7×7) surface is prepared under UHV by annealing: the sample was repeatedly annealed by an electron beam so that the surface reached approximately 800 °C for twenty minutes before 'flashing' briefly at 1000 °C. The temperature of the sample was monitored using an optical pyrometer through a glass window on the vacuum chamber. The silicon surface atoms reconstruct under these temperatures into a more energetically stable configuration, the (7×7) reconstruction. The atomic arrangement on the first few atomic layers is relatively complicated involving several types of atomic position [199] as shown by the dimer-adatom-stacking-fault model (DAS) [200] in figure (5.1).

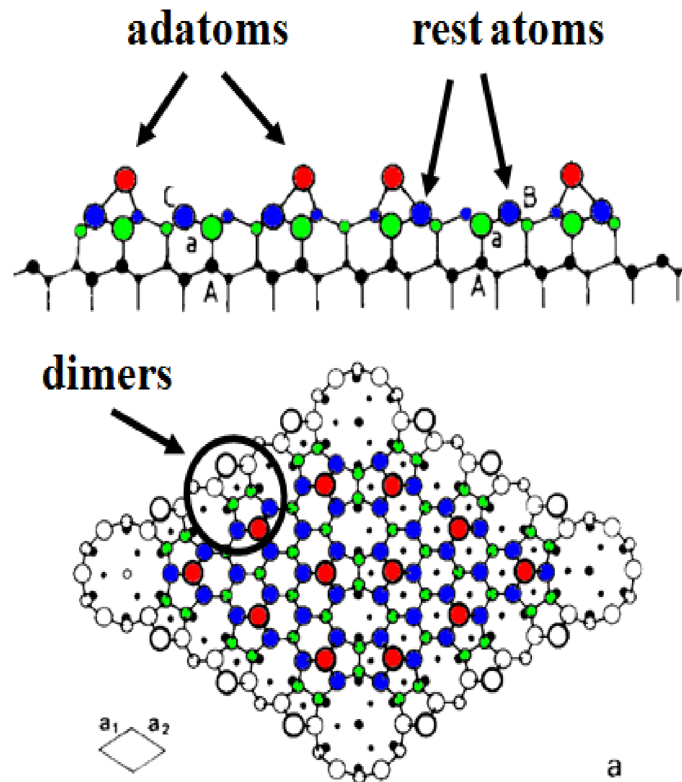

Figure 5.1: The DAS model for the Si(111) (7×7) surface, from [200].

The surface was diagnosed as clean (uncontaminated) using low energy electron diffraction (LEED) and XPS (a lack of photoelectrons at binding energies associated with carbon). In LEED, a low energy electron beam incident on the surface leads to the backscattering of diffracted electrons which are detected using a fluorescent screen. The diffraction occurs because the de Broglie wavelength of the electron (Eq. (2.45)) is similar to the interatomic separation of the sample.

Only elastically scattered electrons are detected, as other low energy electrons are removed by energy-filtering grids in front of the screen. A well-resolved LEED pattern can only be achieved with a very well-ordered surface, and so if a well-resolved LEED pattern is observed the surface is deemed to be clean and ordered. The (7×7) structure was revealed in the LEED pattern shown in figure (5.2).

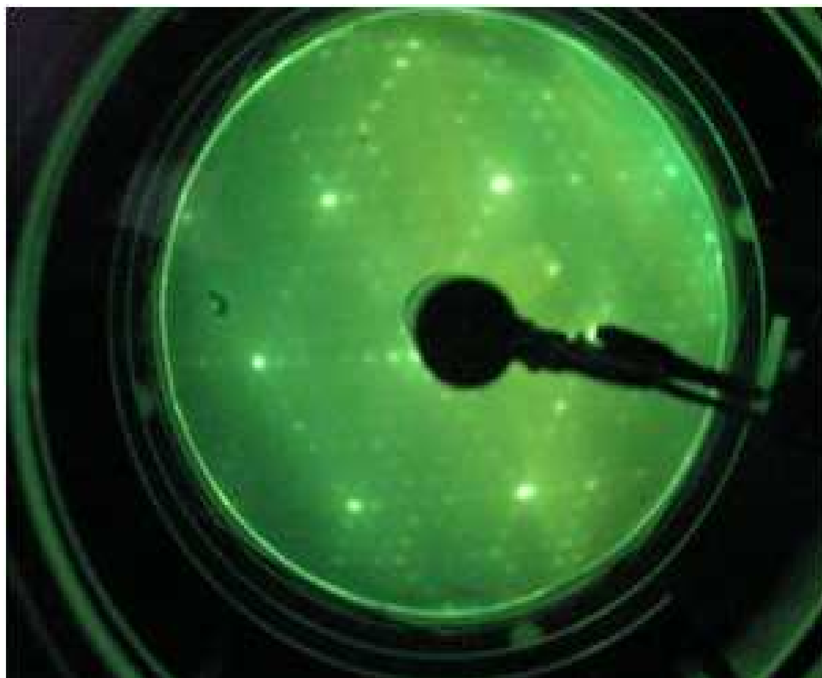

Figure 5.2: Photograph of the LEED pattern of Si(111) (7×7) after annealing. The well-resolved pattern is a diagnostic that the sample is now clean and ordered.

5.1.2 Spectral analysis

The silicon 2*p* core level has been well-studied by XPS, and the fitting parameters used by three different experimental groups are given in [201, 202, 203]; all three were published in same volume of *Physical Review B*, and are reviewed in [204]. The fitting parameters used in this study were those of the Le Lay group [201]: the fit is comprised of six doublets, one doublet assigned to bulk Si atoms, with the others assigned to surface states which are detailed in table (5.1). These surface states are well studied: their physical origins can be explained by the geometrical structure of the Si(111) (7×7) surface described by the DAS model in figure (5.1). The main surface state contributing to the energy spectrum is S_3, due to the back bonds between the adatoms and the underlying crystal shown in figure (5.1). Only the physical origin of the S_1 surface state is still debated: it is speculated that it reflects a continuum of excitations due to the metallic nature of the surface [205], or else a shake-up structure [201, 206].

Surface state	Shift from bulk (eV)	Physical origin
S_1	+0.90	excitation continuum
S_2	+0.50	adatoms
S_3	+0.24	back bonds
S_4	-0.10	dimers
S_5	-0.70	rest atoms

Table 5.1: Binding energy shifts from that of the bulk of five surface states of the Si 2p core level, with their physical origins [201].

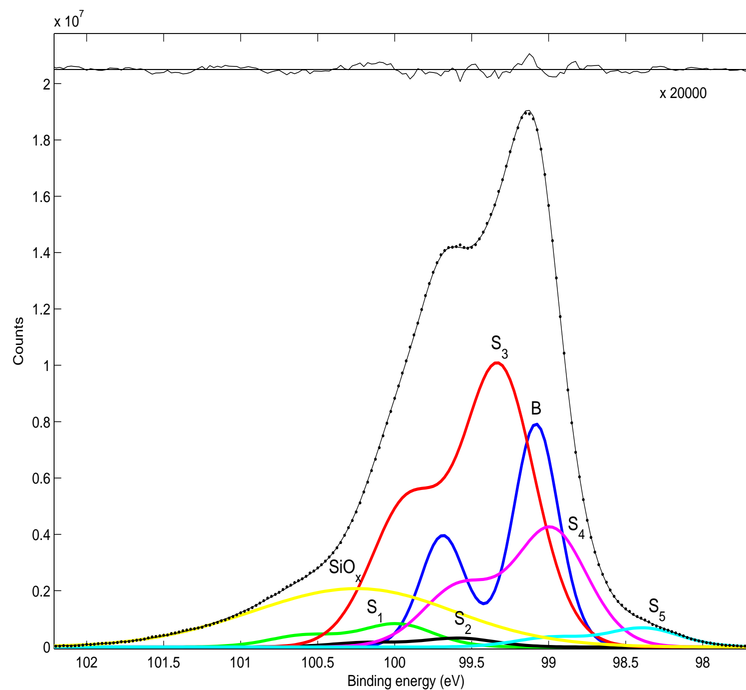

Figure 5.3: Fitting of Si 2p core level before photoexcitation. Each energy state is spin-orbit split by 0.605 eV, forming doublets, which, for p shells, have relative intensities of 2:1 for the $2p_{3/2}$ and $2p_{1/2}$ states. The FWHM of the surface states S_1 to S_5 are equal, and are greater than that of the bulk due to surface defects. The black points are raw data, with the black line through them being the fit (total of all the doublets). The magnified residual is shown above, indicating the fit is satisfactory.

The fitting of the Si 2p energy spectrum of the sample is shown in figure (5.3), where the sum approximation to the Voigt function was used for the Gaussian-Lorentzian peaks (Eq.(3.42)) in CasaXPS (www.casaxps.com). The fit uses the five surface state doublets described by Le Lay [201], and the fit residual illustrates it is successful. The width of the surface peaks, the full width at half maximum (FWHM), are fixed and are fitted to be broader than the bulk doublet. This is due to surface defects, where small differences in the reconstructed surface cause localized changes in the surface state energies within the area sampled by the XUV

probe beam. Other constraints used in the fitting are the separation between the doublet peaks, set at 0.605 eV between the Si $2p_{3/2}$ and $2p_{1/2}$ states [201], and the relative intensities of the doublet peaks which is 2:1 for p orbitals.

Laser excitation with 1.55 eV photons at a fluence of 58 nJ cm^{-2} causes charge carriers to be injected into the depletion layer at the surface as illustrated in figure (5.4). Electrons in the conduction band then migrate into the bulk and holes in the valence band migrate to the surface. This changes the electric field across the space charge region and so the band bending is reduced. This causes a shift to higher binding energies of core level electrons, and so the kinetic energy of photoelectrons created in XPS decreases due to eq. (3.33), $KE = h\nu - BE - W$. The XPS spectra of the Si $2p$ core level with and without photoexcitation are shown in figure (5.5). The spectrum is also broadened. The peak fitting of the 'laser on' spectrum is shown in figure (5.6).

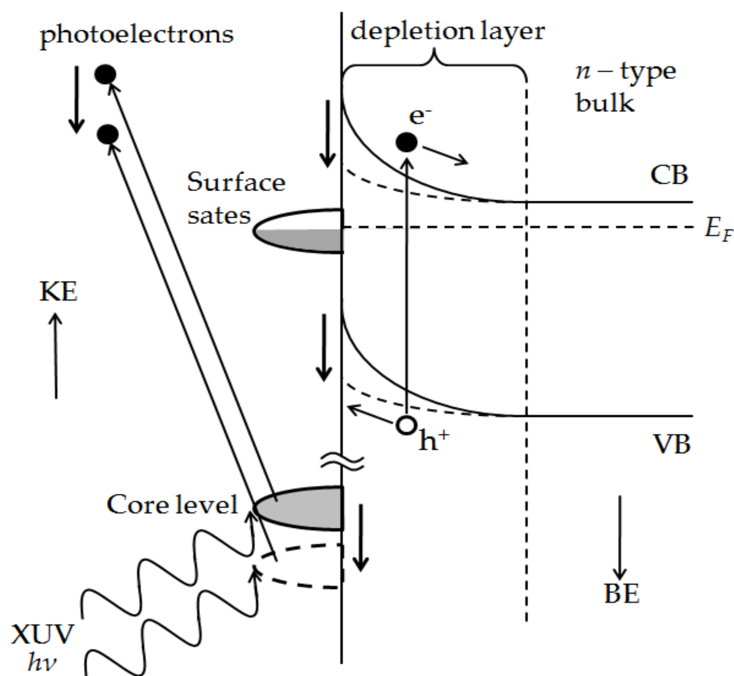

Figure 5.4: Surface photovoltage in an n-type semiconductor studied with XPS. Photoexcitation by a laser injects electron (e$^-$) into the conduction band (CB). Electrons then migrate into the bulk material due to the presence of the depletion layer, and holes (h$^+$) in the valence band (VB) migrate to the surface. This changes the electric field within the space charge region which reduces the band bending at the surface, illustrated by dashed lines. The binding energy (BE) of core electron energy levels thus increases, and so the kinetic energy (KE) of photoelectrons created in XPS is reduced.

The spectral fitting of the photoexcited sample in figure (5.6) shows a much larger contribution from the S_4 dimer state compared to the unphotoexcited case. In this fit the bulk peak broadens upon photoexcitation while the surface states do not. It is difficult to propose a physical mechanism that would result in a change in

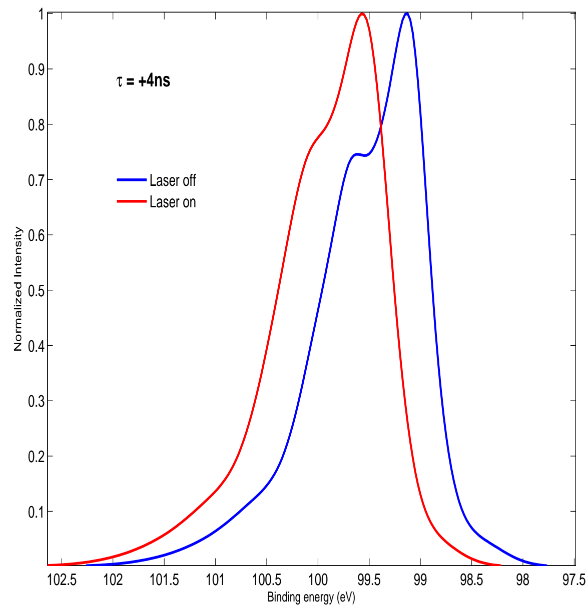

Figure 5.5: The Si 2p spectrum is shifted to higher binding energies (lower kinetic energies) upon laser excitation at a delay time of 4 ns between pump and probe. The peaks also appear to have broadened, as seen by loss in resolution of the doublet splitting in the 'laser on' signal.

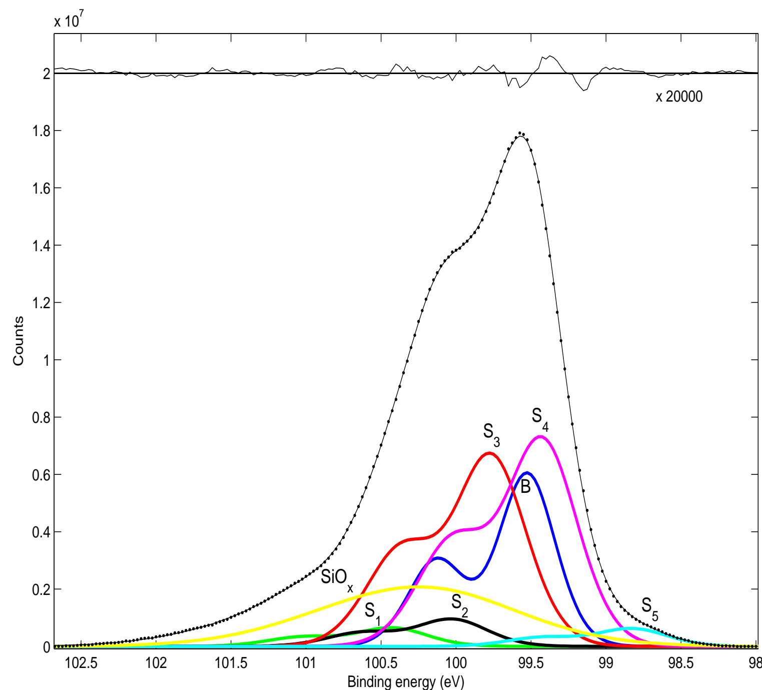

Figure 5.6: Fitting of the Si 2p core level 4 ns after photoexcitation. The bulk signal has broadened (revealed in an increase in the FWHM) and the relative intensities of the surface states has changed. The magnified residual shows that the fit is satisfactory.

the relative populations of surface states upon photoexcitation. Therefore, another fit was applied to the 'laser on' energy spectra, whereby the heights (and thus the percentage contributions) of the bulk and surface peaks were kept fixed at those determined in the 'laser off' spectrum, to determine if the apparent broadening could be explained purely by an increase in the spectral widths (FWHM). This fit is given in figure (5.7). Here the goodness of fit appears to have suffered, although not greatly. The broadening of the 'laser on' spectrum may be induced by the pump beam because the beam profile is Gaussian, and so more carriers will be generated at the centre of this beam where there is higher fluence. Therefore the amount of SPV shift will vary across the pump beam, which had a spot size (diameter) of 2 mm so that it was larger than the XUV probe beam, leading to the broadening of the spectral lines. These changes in the FWHMs of the bulk and surface states upon photoexcitation are given in table (5.2).

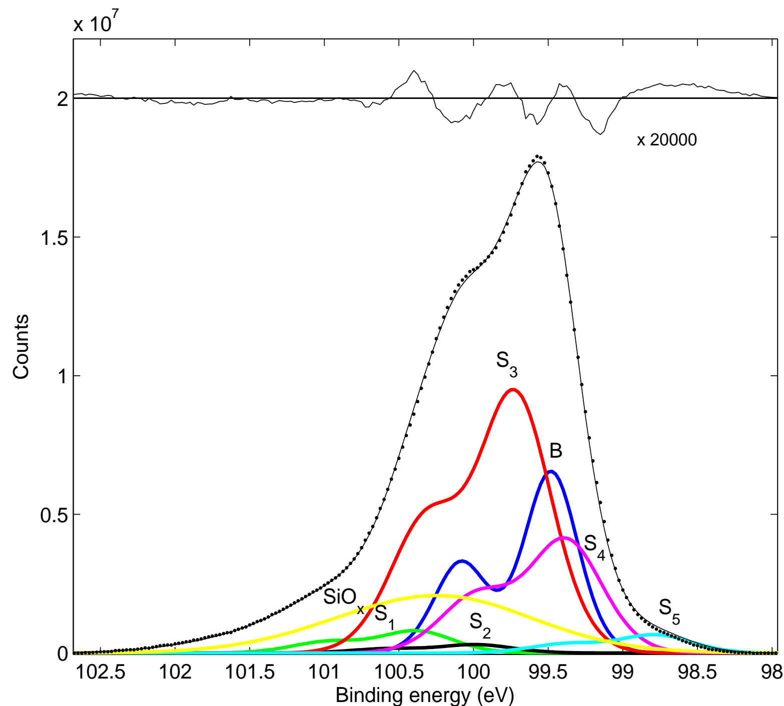

Figure 5.7: Fitting of the Si 2p core level 4 ns after photoexcitation. In contrast to figure (5.6), the % contribution of each bulk and surface state has been fixed to that obtained from the corresponding 'laser off' spectrum.

State	'Laser off' FWHM (eV)	'Laser on' FWHM (eV)
Bulk	0.32	0.44
Surface	0.54	0.58

Table 5.2: FWHM of bulk and surface Si 2p states for the 'laser off' and 'laser on' spectra shown in figure (5.3) and (5.7).

One difficulty with the spectral fits shown in figures (5.3) and (5.6) is the presence of a large 'tail' at higher binding energies. This is fitted by a very broad (FWHM > 1 eV) doublet labelled SiO_x, referring to silicon oxides, because the tail appears to be similar to the oxide surface states that have been reported in the literature [207, 208, 209, 210, 211]. This suggests that the UHV surface preparation did not completely remove all the surface oxide naturally present in an air-exposed Si wafer. The large FWHM seems unphysical, and so this may suggest the presence of other contaminants at the surface that were not removed by annealing, or it may be linked to the excitation continuum proposed as the physical origin of the S_1 state.

5.1.3 Surface photovoltage analysis

The laser-induced surface photovoltage (SPV) is revealed as the change in the shift of the energy spectrum at different time delays (Eq. (2.92)) and is shown in figure (5.8). A laser-induced SPV of 95 meV is measured, and the decay of the laser-induced SPV is measured across the 320 ns time window of the SRS (the repetition rate of the SRS is single-bunch mode was 3.123 MHz) by varying the pump-probe delay time.

The decay of the laser-induced SPV is modelled as a constant deceleration, in that the change in the band bending at the surface reduces as soon as recombination starts to occur, as discussed in §2.4, [52]:

$$SPV(t) = -\alpha k_B T \ln \left[\exp \frac{-\Delta V}{\alpha k_B T} + \frac{t}{\tau_\infty} \right] \tag{5.1}$$

where α is a material parameter, in this case 2 [55], ΔV is total change in the surface photovoltage, here 95 meV, and τ_∞ is the dark carrier lifetime.

The decay of the laser-induced SPV after excitation with the laser pump is determined to have a lifetime, τ_∞, of 0.41 μs, which differs from previous measurements in the literature [58], where τ_∞ is measured to be 14 μs from band-gap luminescence experiments. The doping of the n-type Si wafer was in this case 1.1 x 10^{16} cm^{-3}, roughly an order of magnitude greater than the sample used in this study.

The 95 meV change in the SPV appears on top of a 'background' of approximately 345 meV. This is most likely due to accumulation of the SPV created with subsequent laser pump pulses every 320 ns. The complete recovery of the band bending to that of the unexcited case is therefore not achieved over 320 ns. However, the value for the change in the SPV of 95 meV leads to sensible conclusions for the physics occurring at the silicon surface as detailed below.

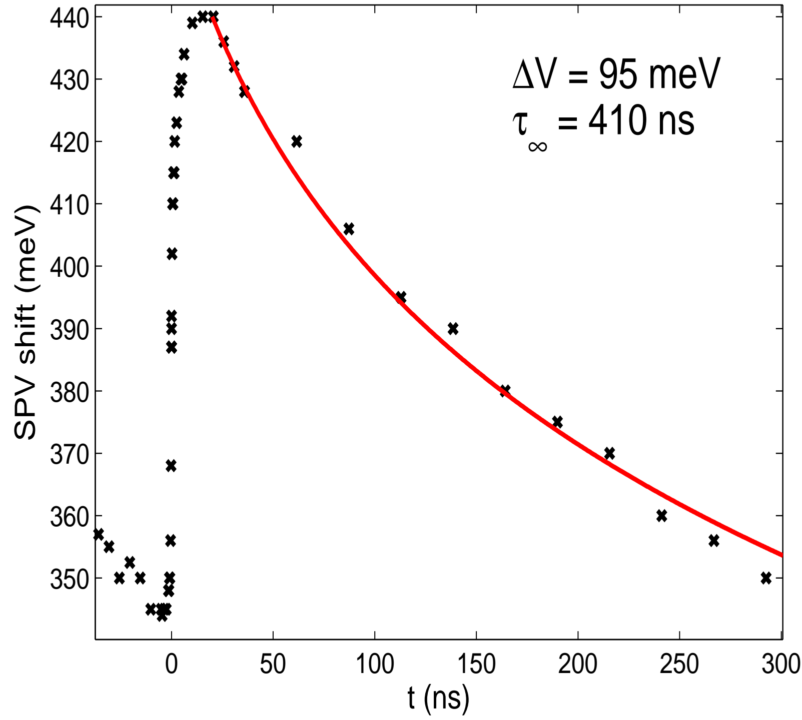

Figure 5.8: The change in the SPV, where the decay of the recovery of the band bending after excitation is fitted with a lifetime, τ_∞, of 0.4 μs, using a thermionic emission model for the recombination of electrons and holes. The pump beam was at an energy of 1.55 eV with a fluence of 58 nJ cm^{-2}.

It has also been suggested that the photoemission measurement process may influence the observed SPV decay, due to the changing surface potential affecting the kinetic energy of the photoelectrons during flight [52]. However, this would therefore effect any photoemission measurement.

The electronic structure of the Si(111) (7×7) surface is shown in figure (5.9). The band gap energy of silicon, 1.12 eV, is such that the 800 nm pump beam (1.55 eV) can photoexcite electrons into the unoccupied U_1 surface state [212], as well as across the band gap. The decay time for electrons from the U_1 state into the bulk has been measured using two-photon photoemission spectroscopy (2PPE) to be 140 ps [212], much faster than the decay time measured here. The fluence used in the 2PPE measurements was also orders of magnitude greater than used in these studies (0.8 mJ cm^{-2} compared to 58 nJ cm^{-2} here). Thus the measurements here are unlikely to be influenced by photoexcitation of electrons into the U_1 state. The laser beam can also photoexcite electrons from O_2 to U_1 and from O_1 to U_2, but similarly fast decay times would again be expected. Thus the primary process influencing the data is expected to be the recombination of carriers excited across the band gap.

The position of the Fermi level relative to the conduction band is calculated

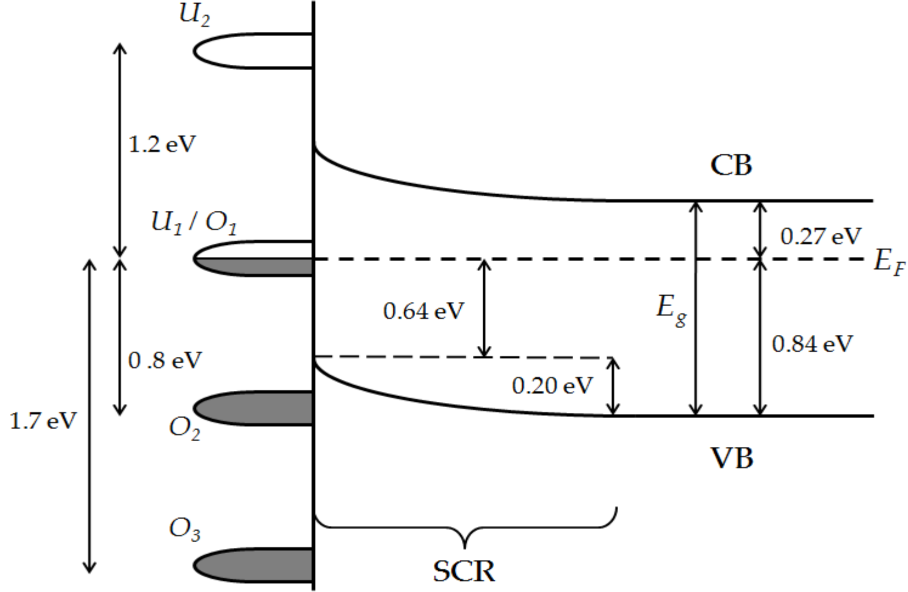

Figure 5.9: Electronic structure at the silicon surface. The band gap energy $E_g = 1.1$ eV, is such that the 1.55 eV pump beam can photoexcite electrons into the unoccupied U_1 surface state [212]. U: unoccupied surface state; O: occupied surface state; CB: conduction band; VB: valence band; SCR: space-charge region; E_g: band gap energy; E_F: Fermi energy.

using [213]:

$$E_C - E_F = k_B T \ln \left(\frac{N_C}{N_D} \right) \tag{5.2}$$

where $E_C - E_F$ is the energy gap between the conduction band minimum and the Fermi level, N_C is the effective density of states in the conduction band and N_D is the carrier concentration (or doping level). For n-type, phosphorous-doped silicon, N_C is 2.8×10^{19} cm^{-3} [213]. The carrier concentration, N_D, can be obtained from the resistivity of the sample: n-type silicon with a resistivity of 5 Ωcm corresponds to a carrier concentration of 8.95×10^{14} cm^{-3} [214]. The result is $E_C - E_F = 0.27$ eV.

The equilibrium band bending is obtained from:

$$\frac{\Delta V}{k_B T} \exp \left(\frac{\Delta V}{k_B T} \right) = \frac{n_P}{n_0} \exp \left(\frac{V_0}{k_B T} \right) \tag{2.91}$$

where ΔV is the total SPV shift upon photoexcitation (95 meV), n_0 is the carrier concentration, n_P is the photoexcited carrier concentration and V_0 is the equilibrium band bending. n_P is determined as being approximately 5×10^{13} cm^{-3}, given the laser fluence, energy and absorption coefficient (2000 cm^{-1} at 1.55 eV, giving a penetration depth of 5 μm [213]). This gves the equilibrium band bending, $V_0 = 0.203$ eV.

There are partially occupied surface states at the Fermi level, with a second unoccupied surface state 1.2 eV above the Fermi level, and there are two occupied states 0.8 and 1.7 eV below the Fermi level [215, 216]. The calculated Fermi level position and band bending, along with the unoccupied and occupied states at the surface, are given in figure (5.9). The Fermi level therefore lies approximately 0.64 eV above the valence band maximum at the surface. This agrees well with literature values for the pinning of the Fermi level at 0.63 - 0.65 eV above the valence band maximum at the surface [217, 218].

5.2 PbS quantum dots attached to ZnO

To study charge carrier dynamics in quantum dots they can be chemically attached to a substrate. A photon with energy $h\nu$ less than the band gap energy of the substrate but greater than the band gap energy of the quantum dots should photoexcite an electron into the quantum dot conduction band without photoexciting the substrate. If the energy level line-up of the quantum dot is such that the conduction band lies at energies within the conduction band of the substrate, this electron will be injected into the substrate on fast timescales. This allows for charge carriers to be captured before recombination occurs. This was recently shown with PbS quantum dots attached to TiO_2 by Sambur *et al.*, with electron injection from the quantum into the substrate occuring at approximately 50 fs, where the recombination lifetime of carriers in the quantum dot was estimated to occur at a much longer 50 ps [219]. Electron transfer across the interface of PbSe quantum dots attached to a TiO_2 substrate has also been measured to occur at approximately 50 fs [220]. Quantum dot-substrate systems can therefore form the basis of a solar energy cell, where the band gap energy of the quantum dot can be adjusted so as to absorb an optimum part of the solar spectrum.

PbS quantum dots attached to ZnO has a similar energy level line-up as the PbS-TiO_2 system in [219], as shown in figure (5.10). ZnO has a band gap energy of 3.4 eV [221], similar to the 3.05 eV band gap energy in TiO_2 [222]. Figure (5.10) shows how photoexcitation of the quantum dot leads to the injection of electrons into the conduction band of the ZnO. This substrate is *n*-type with a depletion layer, and hence band bending, at the surface. Injection of carriers into the depletion layer will lead to a change in the band bending, or surface photovoltage (SPV), similar to that observed in bulk silicon in §5.1.3. Thus measuring the transient change in the SPV of the ZnO gives insight into the charge carrier dynamics in the quantum dot-substrate system. Another reason for studying ZnO is that *n*-type ZnO nanorods have been proposed as a candidate material for electron

transportation in hybrid solar energy cells such as that shown in figure (2.19).

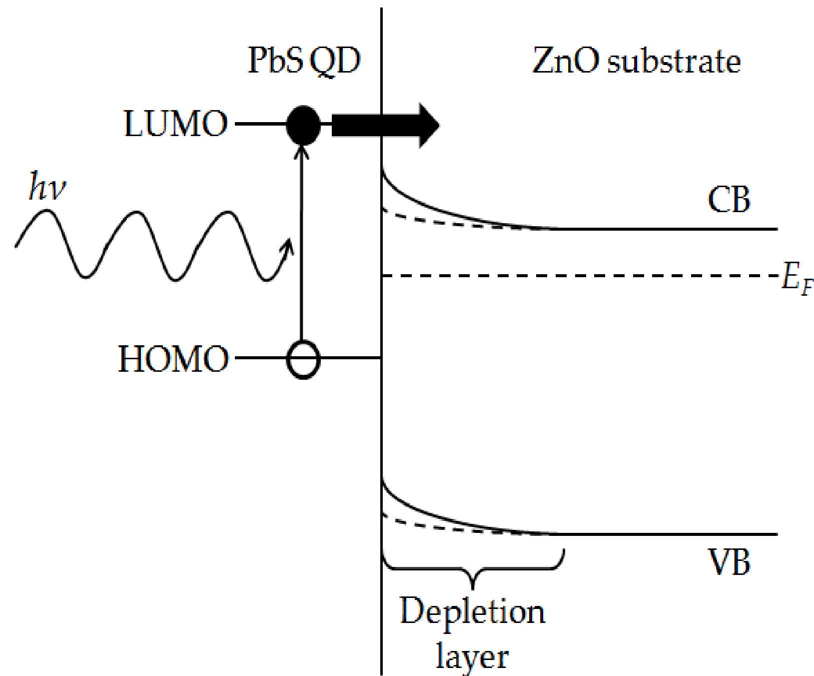

Figure 5.10: Energy level line-up of PbS quantum dots (QDs) on an *n*-type ZnO substrate. Photoexcitation of electrons from the highest occupied molecular orbit (HOMO) to the lowest unoccupied molecular orbit (LUMO) leads to the injection of electrons into the ZnO conduction band. The ZnO substrate is *n*-type and so this photoexcitation and subsequent injection of carriers into the depletion layer will change the amount of band bending at the ZnO surface (dashed lines).

This section outlines the method of sample preparation (§5.2.1) before giving XPS measurements of the PbS quantum dot-ZnO substrate sample (§5.2.2). An ultraviolet laser (375 nm) was used to photoexcite a clean ZnO sample, where XPS spectra of the Zn *3d* core level was used to measure the laser-induced change in the SPV. The PbS quantum dots were then chemically attached to the substrate, and the laser-induced SPV was measured again as detailed in §5.2.3.

5.2.1 Sample preparation

The *m*-plane ZnO(10$\bar{1}$0) crystal was prepared under ultra-high vacuum (UHV) by three repeated cycles of argon sputtering (Ar^+ ions bombarding the sample surface) and annealing (using an electron beam to heat the sample) [223]. A pyrometer was used to measure the temperature of the sample, which reached approximately 800 °C during the anneal cycles, causing the sample to glow orange (shown in a photograph in figure (5.11)). After the sputter/anneal cycles the sample was annealed in oxygen because the argon sputtering can create excessive oxygen vacancies at the surface [224]. The sample was then allowed to cool to room temperature

in the presence of oxygen before a long, low-temperature anneal (400 °C) followed by a short, high-temperature anneal (850 °C) to complete the reconstruction of the (1×1) surface. Low-energy electron diffraction (LEED) was used to diagnose the sample as clean, in that a sharp (1×1) LEED pattern of the surface was obtained as shown in figure (5.12) [225].

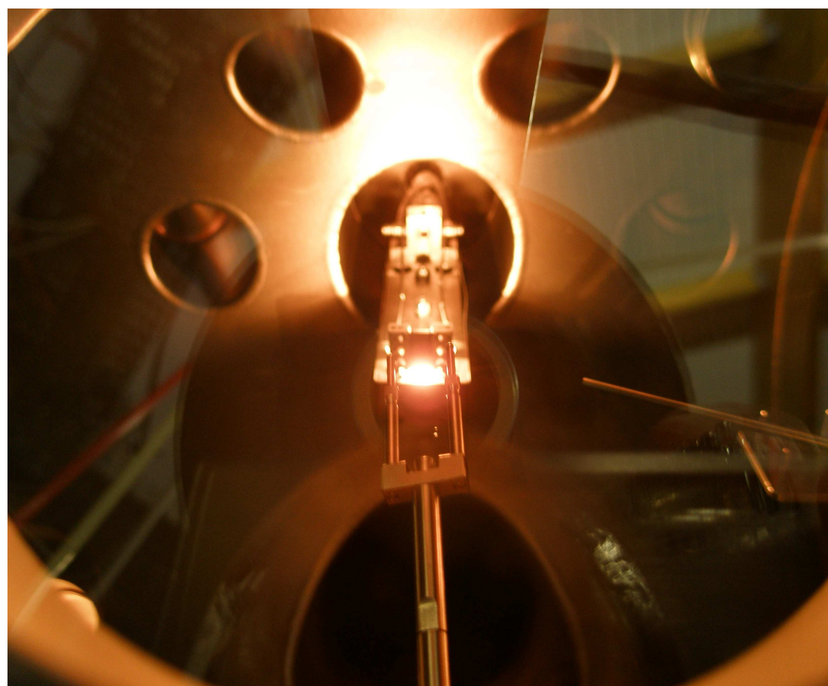

Figure 5.11: Photograph of the annealing of ZnO under ultra-high vacuum using e-beam heating. The anneal cycle heats the sample to 800 °C, causing it to glow orange.

The ZnO(10$\bar{1}$0) surface is shown in figure (5.13). The surface is non-polar in that the symmetry of the atomic bonding at the surface does not lead to any excess electronegativity and thus there is no net dipole moment perpendicular to the surface. ZnO has a Wurtzite structure where zinc atoms are tetrahedrally co-ordinated with oxygen atoms [226, 227]. The zinc-oxygen dimer distance is 1.992 Å and the back bonding distance is 1.974 Å [227].

This cleaning treatment of ZnO is required so as to enhance the *n*-type conductivity in the sample [224]: in particular, it has been found that plasma-induced damage from high ion density argon discharges has the greatest impact on the improvement of *n*-type ohmic contact resistivities in ZnO [228]. The *n*-type behaviour of ZnO is due to crystal defects [229]. Semiconductor defects include vacancies (an atom missing from the lattice) and interstitials (an extra atom within the lattice structure). Conductivity in ZnO is mainly attributed to oxygen vacancies ($V_O^{\bullet\bullet}$, with double positive charge), and less so from zinc interstitials ($Zn_i^{\bullet\bullet}$), although there is a great deal of complexity in the defect chemistry of ZnO, and

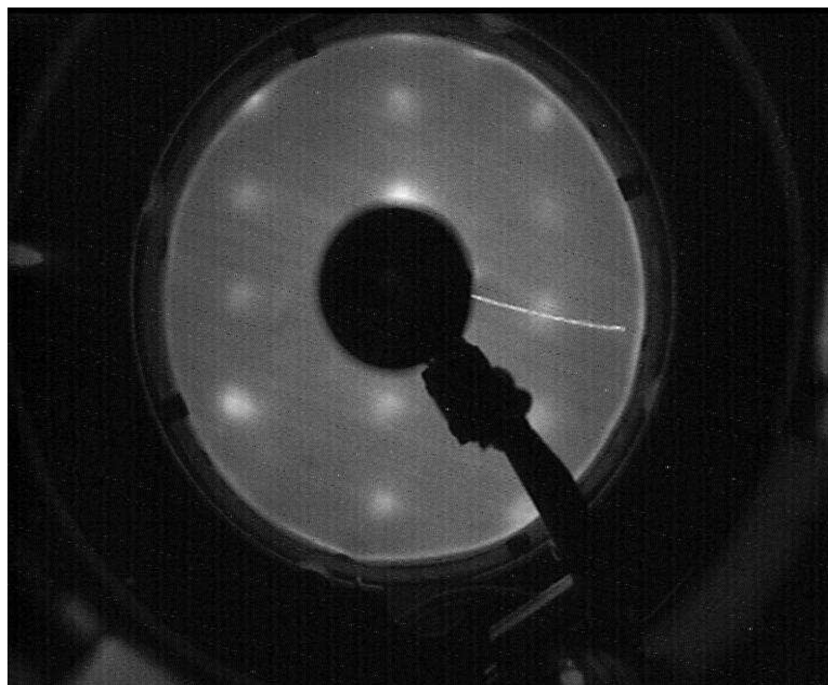

Figure 5.12: Photograph of the LEED pattern of the clean ZnO (1×1) surface.

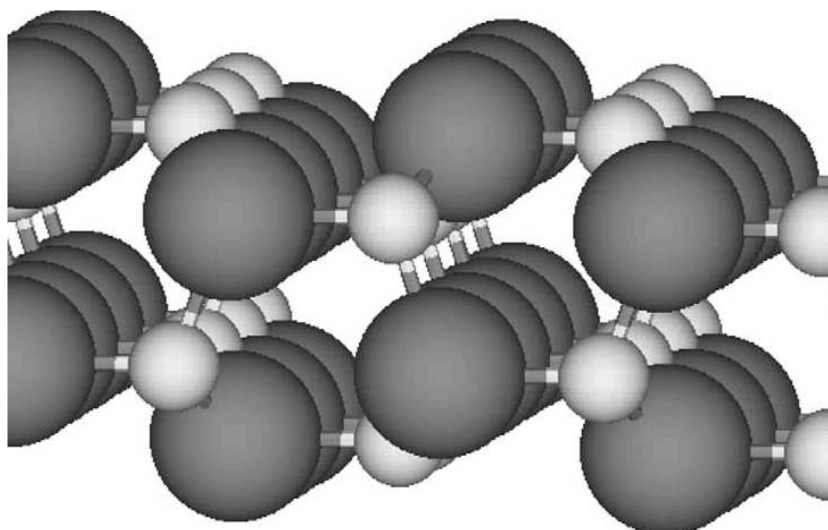

Figure 5.13: The ZnO($10\bar{1}0$) surface, from [226]. Darker circles represent Zn atoms with the smaller, lighter circles representing oxygen atoms.

possible defects include interstitial oxygen, complexes of oxygen vacancy and interstitial zinc, complexes of interstitial oxygen and zinc vacancies, and substitution of oxygen at zinc locations [230, 231, 232]. Sputtering leads to further removal of surface O^{2-} ions, which results in electronic charge being donated to the surface: it is this depletion layer that enhances the surface conductivity [229].

The method of preparation of the PbS quantum dots by colleagues in the chemistry department is detailed in [233]: the procedure involves a novel technique that is environmentally friendly in that olive oil (oleic acid) is used as both solvent and

capping agent. Initially, lead oxide and bistrimethylsilyl sulfide (TMS) are dissolved separately in olive oil. The TMS solution is then rapidly injected into the lead oxide solution, causing the formation of PbS nanoparticles. The concentration of the TMS solution and the growth time both affect the size of the nanoparticles created. This gives a unique advantage to the use of quantum dots in that the band gap, which varies with particle size as $E_g \propto 1/\text{size}^2$, is easily tuned. In the application to photovoltaics, this means a quantum dot can be created so that it can absorb the optimum part of the solar spectrum. The nanoparticles were precipitated by adding anhydrous acetone before centrifuging the solution. The product was then dissolved in dry toluene before being re-precipitated as before, and finally the nanoparticulate sample was dissolved in chloroform ($CHCl_3$).

Unfortunately the oleic acid capping agent, or ligand, that is attached to each nanoparticle so that the nanoparticles do not conglomerate, is highly insulating and was found to cause sample charging in XPS. This was rectified by exchanging these ligands for the shorter 3-mercaptopropionic acid (3-MPA, $HSCH_2CH_2COOH$, shown in figure(5.14)) which is commonly used as a capping agent in quantum dot samples [234], and also contains a carboxylate group suitable for linking to oxide surfaces. A recent study by Carlson *et al.* used this ligand to chemically link CdSe quantum dots to a ZnO substrate in this way so as to allow photoinjection of charge carriers created in the quantum dots into the substrate [235]. The thiol group was used to link to the PbS quantum dot, while the carboxylate group binds to the ZnO surface.

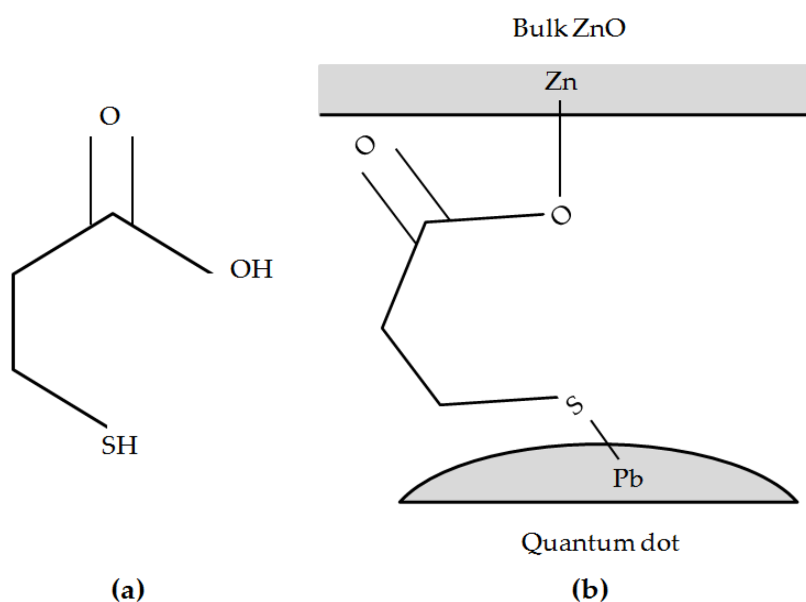

Figure 5.14: 3-mercaptopropionic acid (a), or 3-MPA ($HSCH_2CH_2COOH$). The thiol group links to the PbS quantum dot and the carboxylate group binds to the ZnO surface, where the H atoms are lost as shown in (b).

Upon removal of the clean ZnO sample from the UHV chamber, the PbS quantum dot solution was dropped onto the substrate. The chemical attachment of the quantum dot sample to the ZnO crystal was achieved by simply allowing the chloroform solvent to evaporate off the substrate, before rinsing the sample with additional chloroform. Chloroform is a ideal solvent for this purpose because it evaporates extremely quickly. This was performed over approximately 1.5 minutes before the PbS/ZnO sample was loaded back into the UHV sample transfer system to prevent contamination.

These PbS quantum dots have been shown to exhibit carrier multiplication by Hardman *et al.* [69] using the transient absorption experiment explained in detail in [18], with results similar to previous studies on the same material [77, 76, 236]. The threshold for carrier multiplication was found to be $3.2 \pm 0.1 \times E_g$. This is consistent with the energy partition model of eq. (2.99) which predicts a threshold of $3E_g$ when the electron and hole effective masses are similar as is the case in PbS [237]. The diameters of the quantum dots have been determined to be approximately 4.6 nm [69], with a size dispersion of ± 0.3 nm, or 6.5% [233].

5.2.2 XPS measurements

The first aim of X-ray photoemission spectroscopy (XPS) measurements was to ascertain whether or not the quantum dots had become attached to the ZnO surface. The sulfur $2p$ and lead $4f$ core level spectra are shown in figures (5.15) and (5.16) respectively. The XPS data were fitted using CasaXPS (www.casaxps.com). A Shirley background was subtracted from the spectra, and the FWHMs of the sulfur and lead states were determined to be 0.73 and 0.76 eV respectively. The spin orbit splitting of the peaks are well-defined as being 1.2 eV for sulfur $2p$ [238], and 4.9 eV for lead $4f$ [239], with the relative intensities of the doublets being 2:1 for p states and 4:3 for f states. The peaks shapes used are sum Gaussian-Lorentzian Voight approximations as described in §3.2.1.

The sampling depth of the XUV probe beam is defined as being 3λ, or three times the inelastic mean free path length of electrons (eq. (3.34)), over which 95% of electrons escaping the surface originate from. For measurements of the S *2p* and Pb *4f* core levels, an XUV photon energy of $h\nu = 230$ eV was used giving photoelectrons with kinetic energies ranging from 60 to 95 eV. These electrons have inelastic mean free path lengths of approximately 0.5 nm (figure (3.8)), giving a sampling depth of approximately 1.5 nm.

The components of the XPS spectra illustrate the presence of PbS as well as the 3-MPA ligand [69]. The Pb $4f$ spectra also contains a singlet Zn $3s$ peak from the ZnO substrate, suggesting that there is not a thick multilayer of quantum dots on

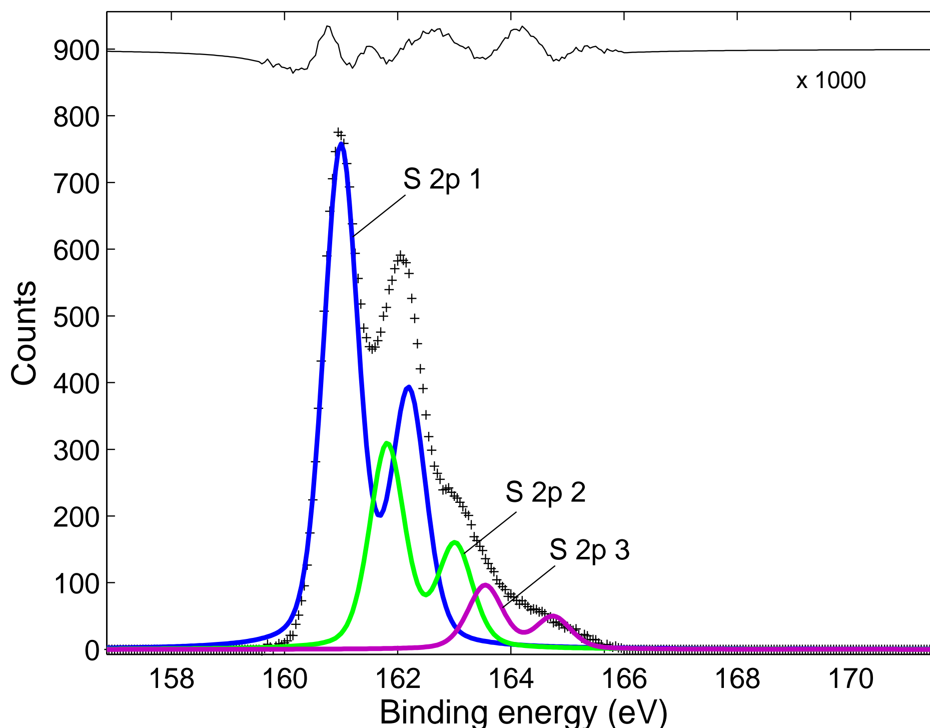

Figure 5.15: Fitting of the sulfur $2p$ core level for PbS quantum dots chemically attached to ZnO. The three species are sulfur found in PbS (S 2p 1, blue), neutral sulfur (S 2p 2, green) and sulfur associated with the ligand (S 2p 3, purple). The magnified residual is given above. An XUV photon energy of 230 eV was used, with a 1.5 nm sampling depth.

the surface (where no zinc signals could be measured). The binding energies of the components and their physical origins are given in table (5.3). The peak positions correlate well with those given in the literature.

Oxidized species of lead and sulfur are noticeably absent from the XPS spectra. Oxidized sulfur $2p$ states typically have binding energies between 168 and 170 eV, for example lead sulfate ($PbSO_4$) at 168.8 eV [244] and sulfur dioxide (SO_2) at 168.3 eV [245]: there are no signals in this energy range in figure (5.15). This means that the one-and-a-half minutes over which the PbS quantum dot sample was attached to the ZnO substrate was sufficiently fast that no significant oxidization could occur. In contrast, a large amount of oxidization has been observed in similar samples that were exposed to air for longer periods (from hours to weeks), an example of which is given in figure (5.17) which is taken from [69].

The coverage of PbS quantum dots across the ZnO surface was not uniform. By changing the region of the sample illuminated by the XUV probe beam, different proportions of the S $2p$ species are measured as shown in figure (5.18). Here, the S $2p$ 1 state corresponding to PbS is less than the S $2p$ 2 state of neutral sulfur, and the proportion of the S $2p$ 3 state corresponding to the 3-MPA ligand is also greater

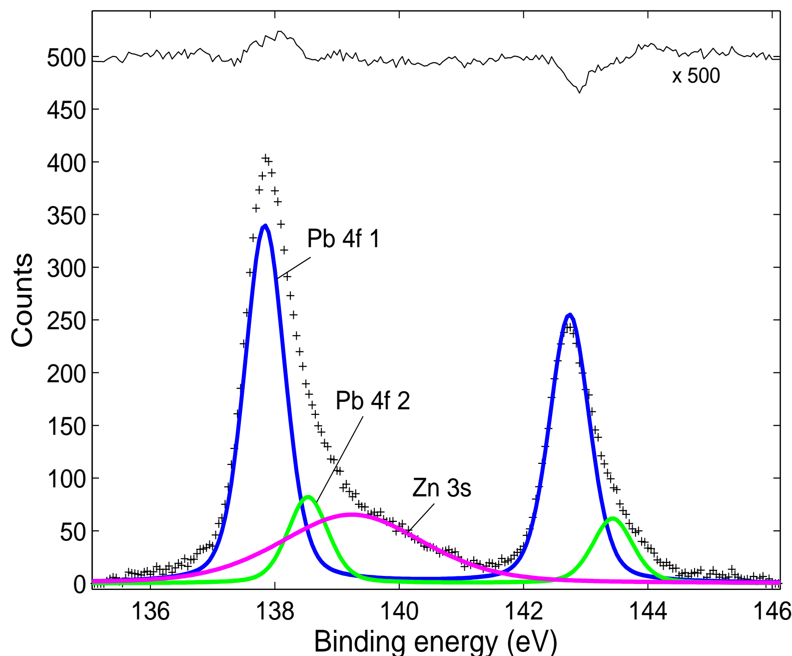

Figure 5.16: Fitting of the lead $4f$ core level for PbS quantum dots chemically attached to ZnO. The two species are lead found in PbS (Pb 4f 1, blue) and lead at the surface of the quantum dot linked to the ligand (Pb 4f 2, green). The Zn $3s$ core level for ZnO is also present (purple), meaning the X-ray probe is also sampling the substrate surface. The magnified residual is given above. An XUV photon energy of 230 eV was used, with a 1.5 nm sampling depth.

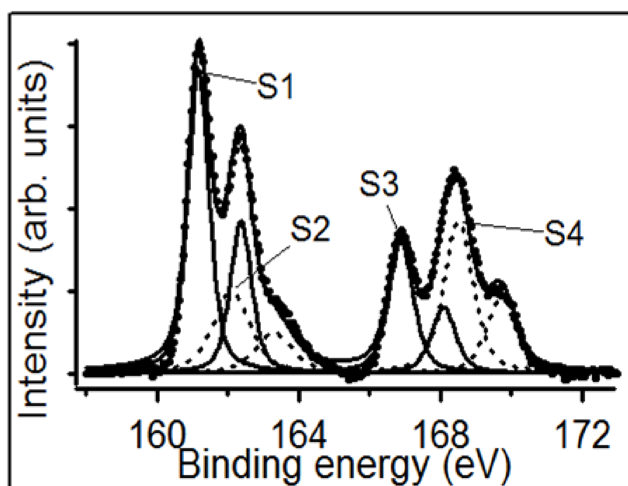

Figure 5.17: Oxidized species of the S $2p$ core level have binding energies ranging between 165 and 172 eV (labelled S3 and S4), from [69]. The PbS quantum dots in this case were attached to an indium tin oxide (ITO) substrate and had a mean diameter of 2.7 nm.

than the spectrum shown in figure (5.15). This suggests that in this area of the sample there are less quantum dots although ligands are still present. Figure (5.18) also contains three repeated XPS spectra, where each spectrum took approximately

State	Binding energy (±0.1 eV)	Physical origin	Reference
S 2*p* 1	160.9	PbS	[239]
S 2*p* 2	161.7	S	[239]
S 2*p* 3	163.5	ligand	[240]
Pb 4*f* 1	137.8	PbS	[241]
Pb 4*f* 2	138.5	ligand	[242]
Zn 3*s*	139.2	ZnO	[243]

Table 5.3: Binding energies for the states of lead, sulfur and zinc with their physical origins. Neutral sulfur is observed although neutral lead is not. The Pb and S spectra both include components associated with the 3-MPA ligand: the sulfur present in the ligand itself [240], and lead at the quantum dot surface attached to the ligand [242].

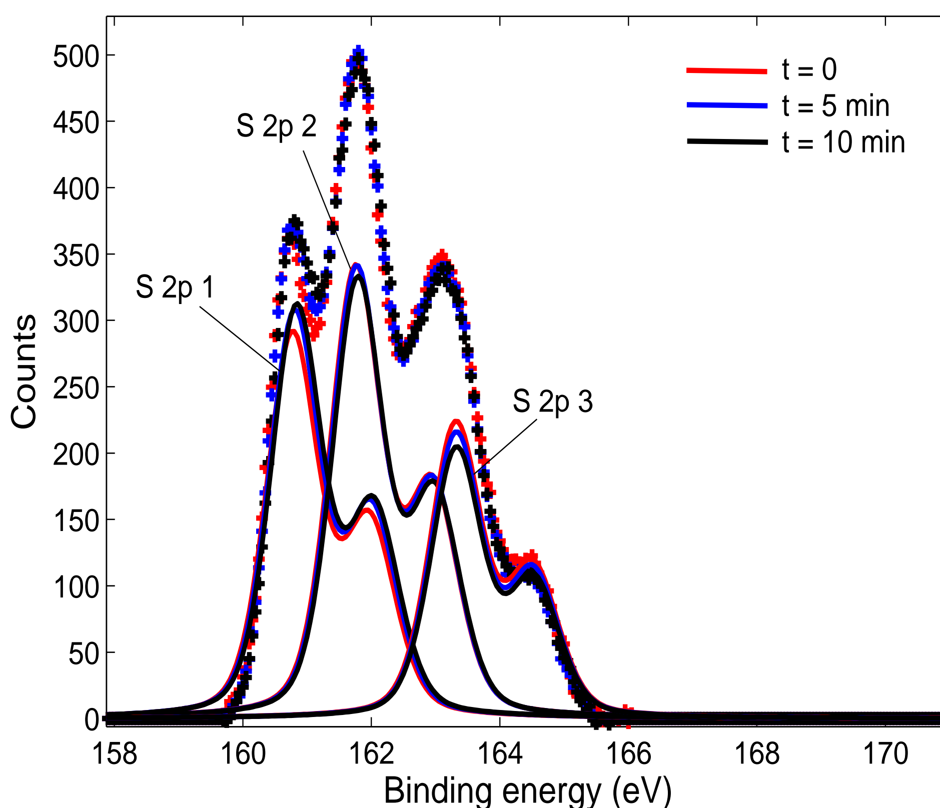

Figure 5.18: Degradation of the PbS quantum dot sample as illustrated by the change in the S 2*p* core level over three sequential XPS scans with each scan taking approximately 5 minutes. The change in the relative peak heights occurs as more of the neutral S (S 2p 2) species is created. An XUV photon energy of 230 eV was used, with a 1.5 nm sampling depth.

5 minutes. The proportions of the S 2*p* states changed over 10 minutes at which point the spectra stabilised. A lower proportion of the ligand state occurs after photodegradation leading to a higher proportion of the PbS state being present. This photodegradation explains the presence of the neutral sulfur (S 2*p* 2) state. However, the Pb 4*f* spectrum did not change upon X-ray exposure as shown in

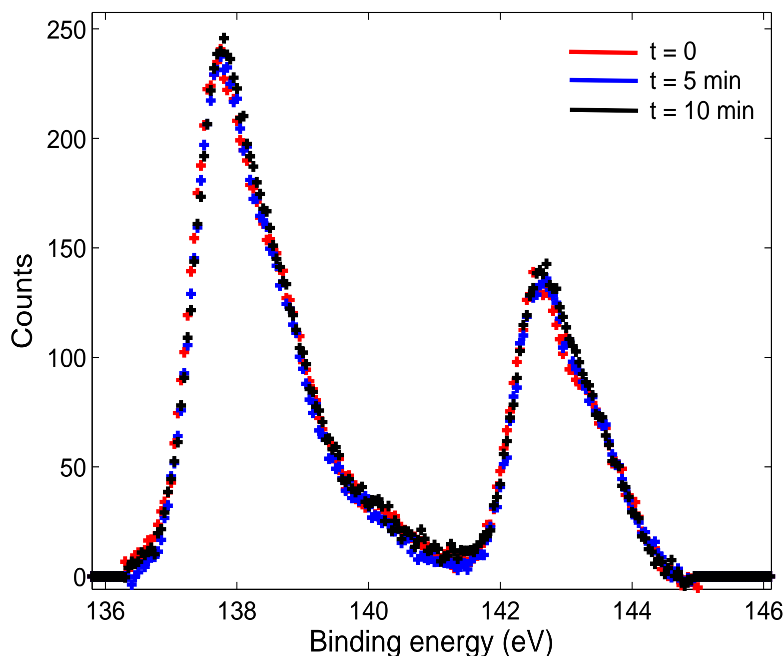

Figure 5.19: Three sequential XPS spectra of the Pb $4f$ core level, with each scan taking approximately 5 minutes (measured at the same time as the spectra shown in figure (5.18)). The Pb $4f$ spectrum does not change upon exposure to the X-ray beam meaning that the quantum dots are not degraded upon XUV illumination. An XUV photon energy of 230 eV was used, with a 1.5 nm sampling depth.

figure (5.19), hence the absence of neutral lead species in the XPS spectra. This suggests that the XUV beam may have only photodegraded the 3-MPA ligands.

Valence band scans of clean ZnO and of PbS quantum dots attached to ZnO are shown in figure (5.20). The changes at the valence band edge (over $\approx 1 - 3$ eV) are attributed to the quantum dots [69]. The valence band maximum corresponds to the highest occupied molecular orbit (HOMO) of the quantum dot, at a lower binding energy than the clean ZnO valence band maximum as is consistent with the energy level line-up diagram in figure (5.10). Changes in the valence band spectrum at binding energies over 4 - 8 eV are due to the 3-MPA ligands [233]. The Zn $3d$ core level is prevalent in both cases, although the signal is somewhat diminished when the quantum dots are attached as expected. A weak peak at 18.7 $\pm$ 0.1 eV is also present here, which is one of the Pb $5d$ doublet peaks. This binding energy is in good agreement within error to that of the Pb $5d_{5/2}$ level measured in PbS (18.52 eV, [246]). The doublet separation for the Pb $5d$ core level is 2.60 eV [239].

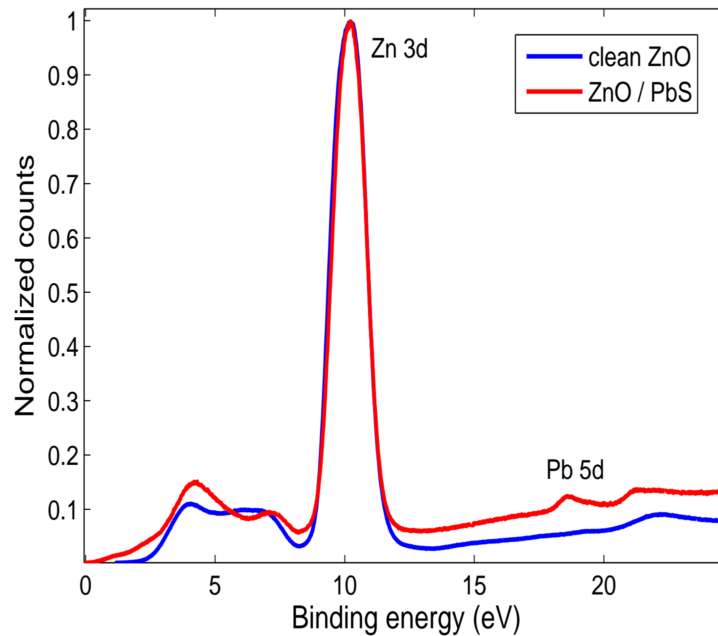

Figure 5.20: Normalized valence band scans for clean ZnO and PbS quantum dots attached to ZnO. The Zn 3*d* core level is prevalent in both scans. A weak signal corresponding to the Pb 5*d* core level doublet is present when the dots are attached where the Pb $5d_{5/2}$ level is at a binding energy of 18.7 eV. The valence band maximum occurs at lower binding energies when PbS quantum dots are attached, due to the highest occupied molecular orbit (HOMO) of the quantum dots. This is consistent with the energy level line-up shown in figure (5.10). An XUV photon energy of 200 eV was used, with sampling depths of approximately 2.4 nm.

5.2.3 Surface photovoltage measurements

The Zn 3*d* core level was used to measure the surface photovoltage of clean and quantum-dot-attached ZnO upon illumination with a pump laser. This is because it gives a strong XPS signal and it is straightforward to fit. It has a spin-orbit splitting of approximately 0.7 eV [247], and the relative intensities of the spin-orbit split doublet is 3:2. The peak fitting is shown in figure (5.21). Before the time-resolved measurements, the Zn 3*d* core level was measured with the pump laser permanently off, permanently on, and then off again. This was to ensure that the 'laser off' scans occurred the same binding energies, meaning that no charging effects were occurring. An example of this is shown in figure (5.22).

Surface photovoltage (SPV) measurements were first carried out on *m*-plane ZnO at the Synchrotron Radiation Source (SRS) at Daresbury laboratory, as described in §3.2.2. However, the 320 ns time window of the SRS in single bunch mode was too short to see any change in the SPV after photoexcitation as illustrated in figure (5.23). These measurements made it clear that the photoexcited

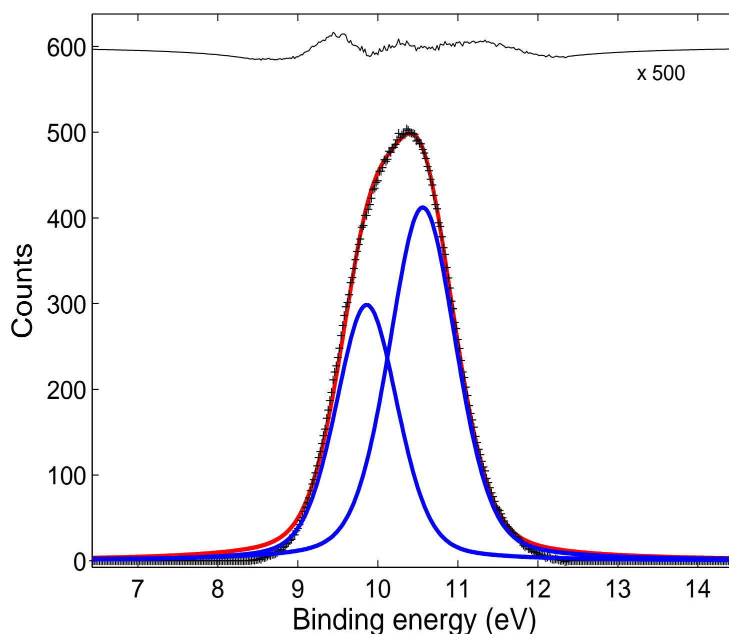

Figure 5.21: Fitting of the Zn 3*d* core level (laser off). The individual components of the doublet are shown in blue. A magnified residual is given above. A photon energy of 200 eV was used.

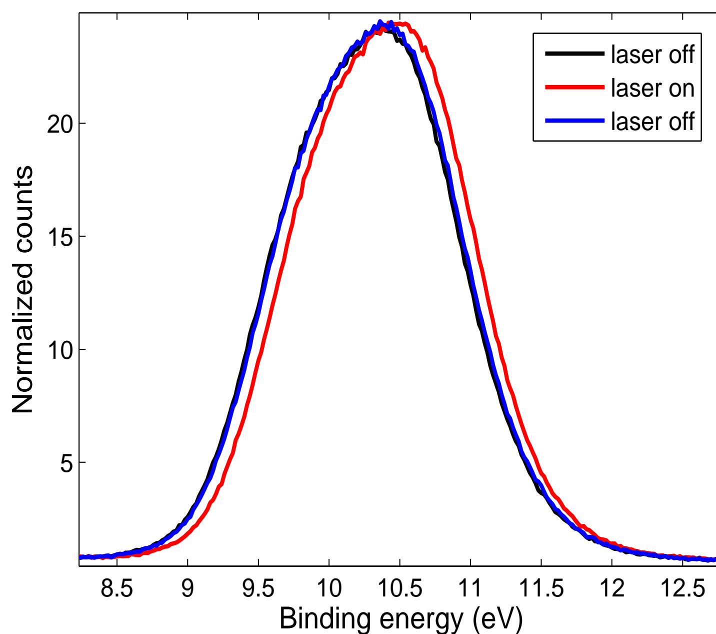

Figure 5.22: The Zn 3*d* core level with and without laser illumination. Upon photoexcitation with a 375 nm laser at a power of 10 mW, a shift in the core level of approximately 115 meV is measured. The core level returns to its original position when the laser is then turned off, meaning sample charging is not occurring. The spectra are normalized to the X-ray beam current. A photon energy of 200 eV was used.

transients in ZnO are long-lived, and that SPV measurements therefore needed to be carried out over much longer timescales. One other useful study carried out at the SRS was a fluence dependency study, shown in figure (5.24). The dependency of the SPV shift in the core energy levels on pump fluence, Φ, is described by [55]:

$$SPV(\Phi) = \alpha k_B T \ln\left[1 + \gamma\Phi\right], \tag{5.3}$$

where α and γ are material-dependent constants. Bröcker *et. al* state that α can take realistic values between 0.5 and 2: for the data here it was fitted that $\alpha = 0.63$ throughout. Equation (5.3) states that the relationship between the change in the SPV on fluence is logarithmic: the inset of figure (5.24) shows that plotting the change in SPV against $\ln \Phi$ gives a linear correlation.

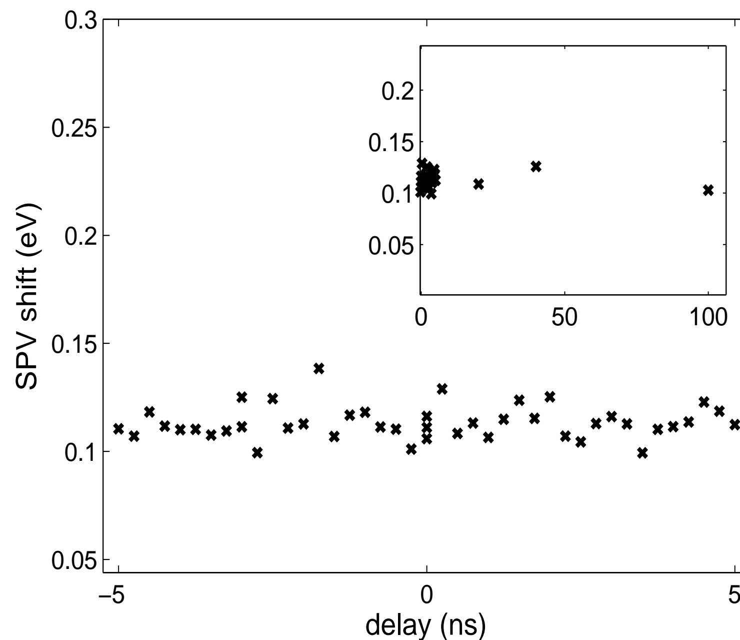

Figure 5.23: SPV shift of the Zn 3*d* core level studied at the SRS. An SPV shift of approximately 110 meV is measured with a laser fluence of 6 nJ cm^{-2}, although no noticeable change is measured over the timescale of the SRS single bunch mode. The inset shows delay times from 0 to 100 ns. A pump beam energy of 3.44 eV (360 nm) was used, with an XPS probe beam energy of 140 eV.

At the TEMPO beamline at the SOLEIL synchrotron, Paris, SPV measurements were repeated on the same ZnO crystal using the same cleaning recipe. However, the CW laser used here was controlled by a signal generator such that spectra of the Zn 3*d* core level were recorded every 50 ns over a period of 1 ms (20,000 XPS scans in total), with the laser being turned on at $t = 0$ s and turned off at $t = 0.5$ ms so as to measure the rise in the shift of the core level as well as its decay back to the original position. The fact that the XPS spectra are captured so quickly means

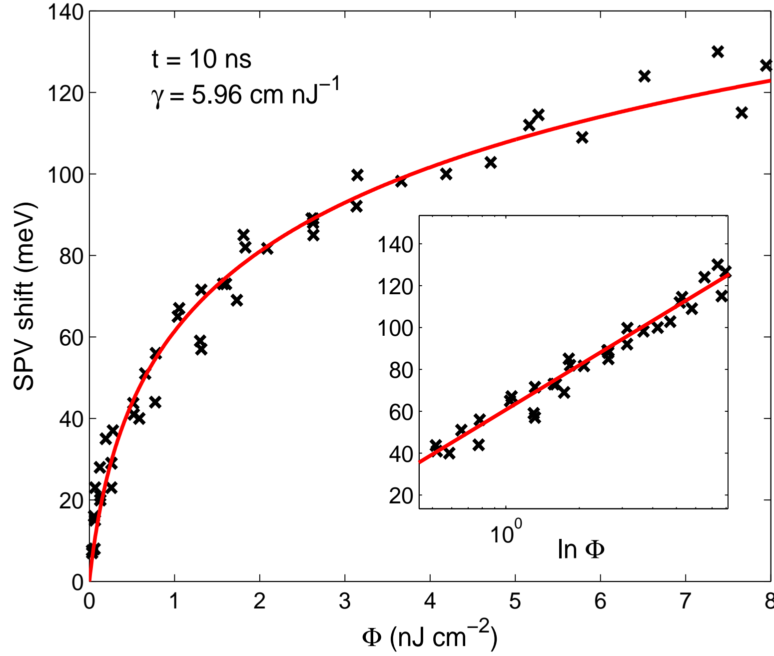

Figure 5.24: Power dependence of the surface photovoltage under photoexcitation with 3.44 eV at a pump-probe delay time of 10 ns, fitted according to eq. (5.3) with $\alpha = 0.63$ and $\gamma = 5.96$ cm nJ^{-1}. The inset shows the SPV shift plotted against $\ln \Phi$ where the fit becomes linear.

that the signal to noise ratio (S/N) suffers. To obtain an adequate S/N as many as 10,000 accumulations over the 1 ms time window are required.

The CW laser had a wavelength of 375 nm, or 3.30 eV. The intention was that the laser light would selectively photoexcite the quantum dot (with a band gap energy of 1.0 eV [69]) and not the ZnO substrate, because the band gap energy of ZnO is 3.4 eV [221]. This is to photoexcite charge carriers in the quantum dot that are then expected to be transported into the substrate on fast timescales as shown in the energy level line-up diagram in figure (5.10), following recent studies of PbS and PbSe quantum dots on TiO_2 substrates [219, 220].

The transient SPV data was extracted by fitting each of the 20,000 individual Zn 3*d* spectra as shown in figure (5.25) and recording the fitted peak position at each time delay. The signal to noise ratio was then improved by averaging the transient SPV data down to 1000 data points (corresponding to a time step of 1 µs), giving a S/N improvement of $\sqrt{20}$. The decay of the shift in the core level energy was then modelled using a least-squares method according to [55]:

$$SPV(t) = -\alpha k_B T \ln \left[1 - \exp \frac{-t}{\tau_\infty} \left(1 - \exp \frac{-\Delta V}{\alpha k_B T} \right) \right], \tag{5.4}$$

where ΔV is the total SPV shift, τ_∞ is the carrier lifetime and α is a material parameter, fitted to be 0.63 which was also obtained by fitting the power dependence

data taken at the SRS with eq. (5.3) (figure (5.24)). It is important to note that this model for the transient surface photovoltage differs from that used to model to transient SPV in bulk silicon (eq. (5.1)). Eq. (5.1) is a simplification of eq. (5.4) for the case where the total SPV shift is much greater than $k_B T = 25.85$ meV at 300 K, $\Delta V \gg k_B T$ [248]. The total SPV shift in bulk silicon was 95 meV on a 345 meV SPV background. The total SPV shift measured in bulk ZnO was $\approx$ 48 meV, and for the case of PbS quantum dots attached to ZnO, $\approx$ 16 meV. A satisfactory fit was obtained for the photoinduced SPV in Si using eq. (5.1), but it was found that this approximated model did not give a satisfactory fit to the ZnO data: instead, the general model of eq. (5.4) was found to fit the ZnO data well.

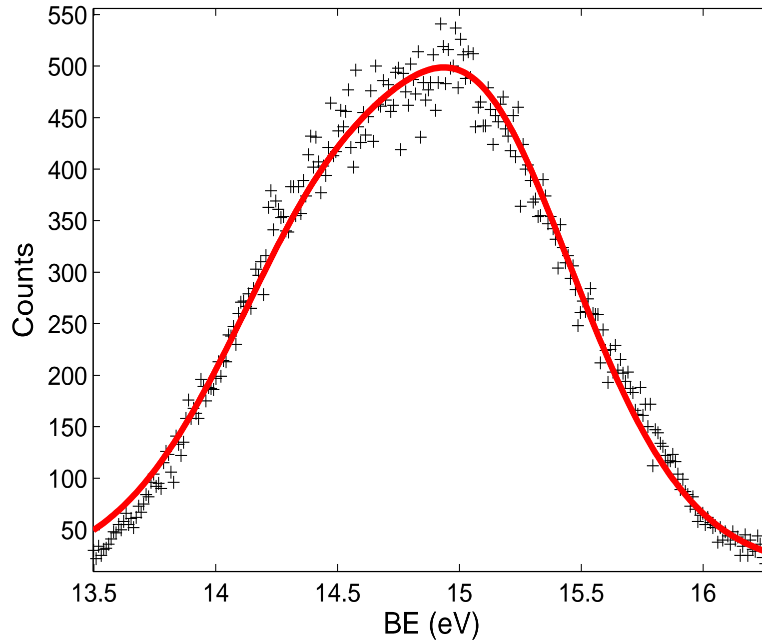

Figure 5.25: A typical scan of the Zn 3*d* core level taken at SOLEIL with a sum Gaussian-Lorentzian fit (the same as shown in figure (5.21)). This fitting is repeated at each 50 ns time step.

A surface photovoltage shift of the Zn 3*d* core level was observed in the clean ZnO sample as shown in figure (5.26). Although this was not anticipated because the pump beam did not have sufficient energy for direct photoexcitation across the band gap, the shift of the core level to higher binding energies is expected for an *n*-type semiconductor with band bending at the surface, due to the presence of a depletion layer. Photoexcitation leads to the injection of carriers into the depletion layer, creating a change in electric field across the depletion layer that suppresses the band bending as discussed in §2.4. The total SPV shift is 47.5 meV, and the decay lifetime is determined to be 0.134 ms by fitting according to eq. (5.4). This lifetime is surprisingly slow considering that electronic transfer may occur on fem-

tosecond timescales [219, 220]. Clearly a different, much slower process is being measured here. The data in figure (5.26) are repeated so as to illustrate the changes that occur when the excitation laser is turned on and off in figure (5.27).

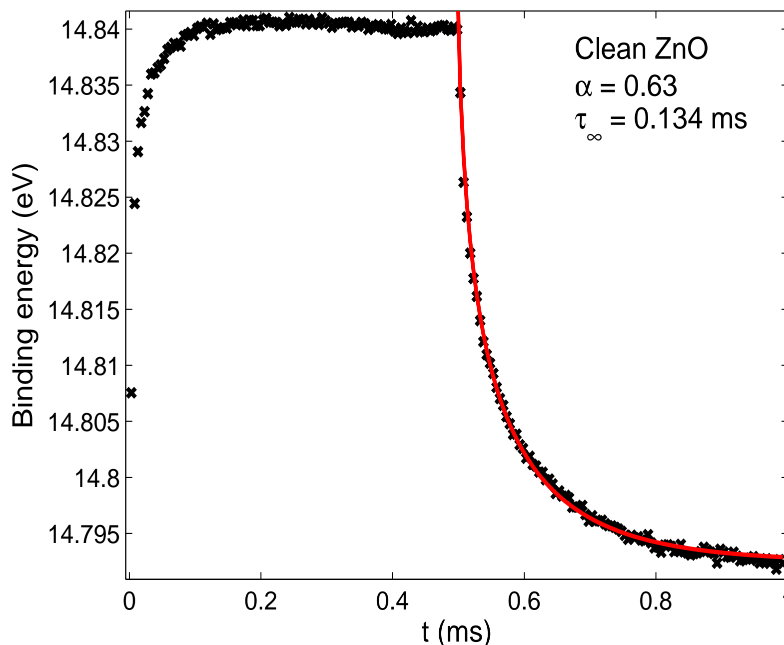

Figure 5.26: The SPV shift of the Zn 3d core level under laser excitation for clean ZnO. The laser is turned on a $t = 0$, creating a shift in the core level to higher binding energies. The laser is turned off at $t = 0.5$ ms at which point the core level decays back to its original position. The decay is fitted as a constant deceleration according to eq. (5.4) with a carrier lifetime of 0.134 ms.

A power dependence study was carried out by varying the CW laser power from 2 to 10 mW and recording XPS spectra with the laser constantly on, as shown in figure (5.28). Between each 'laser on' scan two 'laser off' scans were recorded to ensure that the core level had returned to the original binding energy. The laser-induced shift observed for the case of maximum power (10 mW), which was used in the time-resolved experiments, was approximately 100 meV. This is roughly twice as much as was found in the time-resolved experiments. It may be that there is a very long timescale process occurring that continues to increase the SPV shift over several minutes.

Similarly slow photoconductive responses in ZnO are reported in the literature [249, 250, 251, 252, 253]. In fact, the time constants reported are often much longer than measured here, often as long as minutes or hours. The rising edge of the SPV is also surprisingly slow compared to timescales expected for charge transfer, although it is faster than the SPV decay. This is also consistent with results in the literature. The rising edge of the SPV shown in figure (5.26) can be modelled by the inverse of eq. (5.4). This fitting is shown in figure (5.29) with a time constant

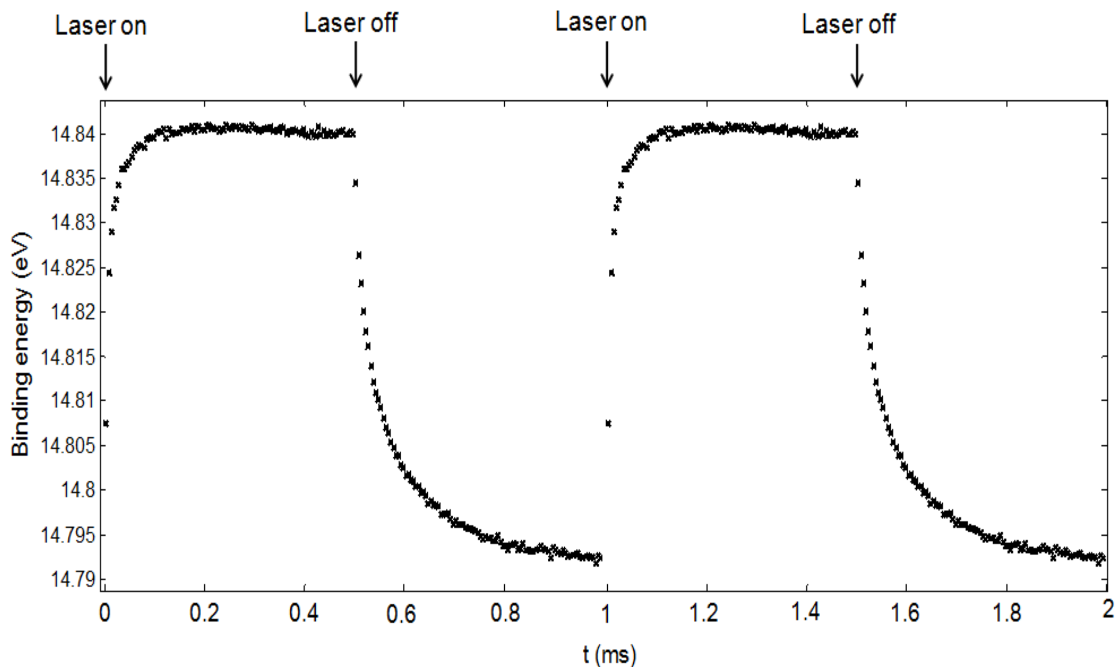

Figure 5.27: The SPV shift from figure (5.26) of the Zn 3*d* core level repeated to show the laser on and off timing. Photoexcitation with the laser leads to a shift of the core level to higher binding energies, which decays back to its original position once the laser is turned off.

of 50 µs.

The SPV response is caused by chemisorption and photodesorption of oxygen at the ZnO surface. This was first studied by Lagowski *et al.* in 1977 [254] and has been explained in detail in other studies since [255, 249, 250, 252]. Oxygen molecules chemisorb onto the ZnO surface primarily at oxygen vacancy sites [223, 231]. The molecules then become negatively charged ions (O_2^-) by capturing free electrons from the *n*-type ZnO, creating a depletion region at the surface that causes band bending. The amount of band bending is therefore affected by the amount of *n*-type doping (*i.e.* the concentration of oxygen vacancies) and the amount of occupancy at the vacancy sites [255]. This means that the experiments are heavily dependent on the cleaning process of the ZnO crystal. The differences between the timescales measured here and those measured in the literature are therefore attributed to the amounts of oxygen vacancies in the samples. Indeed, the cleaning process is such so as to enhance the photoconductivity of the sample by creating oxygen vacancies, and significant band bending may result from even a very narrow depletion layer. For example, Liu *et al.* have estimated that as much as 1 eV of band bending may be created from a 10 nm wide depletion region with a donor concentration of 10^{19} cm^{-3} [250].

When the laser is turned on, electron-hole pairs are created by the excitation of electrons into the conduction band ($h\nu \rightarrow e^- + h^+$). This is not obvious in this

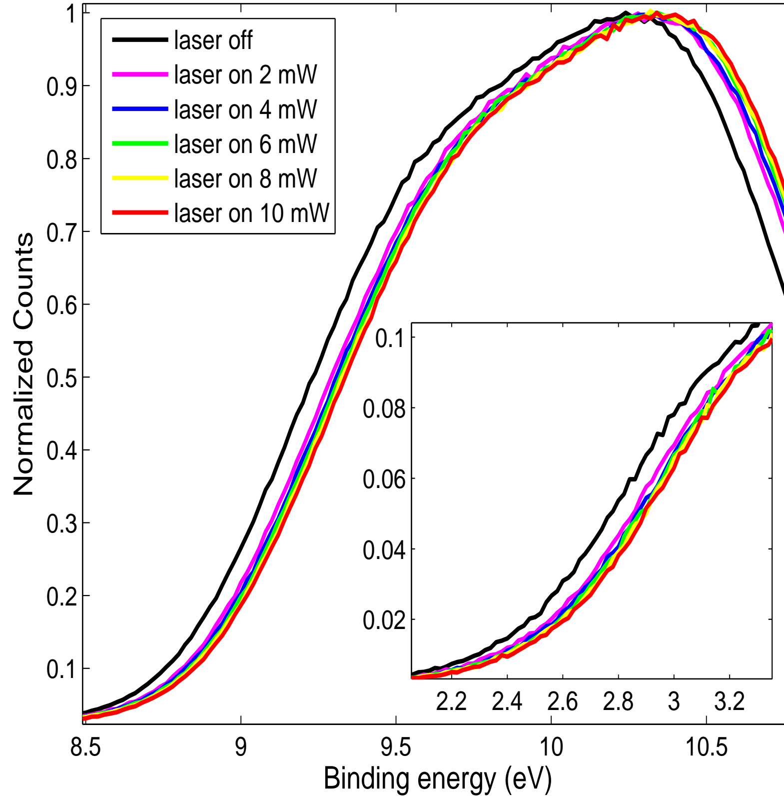

Figure 5.28: Power dependence of the SPV shift of the Zn 3*d* core level in clean ZnO photoexcited with a CW laser at 375 nm. Powers of 2, 4, 6, 8 and 10 mW were used, with the highest power giving a core level shift of approximately 100 meV. The inset shows the shift of the valence band edge at low binding energy. The XUV photon energy was 200 eV.

case, however, because the laser photon energy (3.2 eV) is less than the ZnO band gap energy (3.4 eV). This suggests that the pump beam photoexcites electrons into surface states within the band gap, and that a second excitation is required to promote electrons into the conduction band. This explains the slow rising edge of the change in the SPV, compared to that measured at the SRS in figure (5.23). At the SRS, a pump photon energy of 3.44 eV was used, which allowed for direct photoexcitation across the band gap, and an instantaneous SPV was observed.

Upon photoexcitation, the holes discharge the oxygen ions causing desorption [254]:

$$h^+ + O_2^- \rightarrow O_2(g), \tag{5.5}$$

where (g) denotes the gas phase. The *n*-type band bending at the ZnO surface leads to the migration of electrons into the bulk: the photoconductivity is now enhanced because the photoexcited conduction band electrons are separated from the surface.

When the laser is turned off, non-radiative recombination of electrons and holes

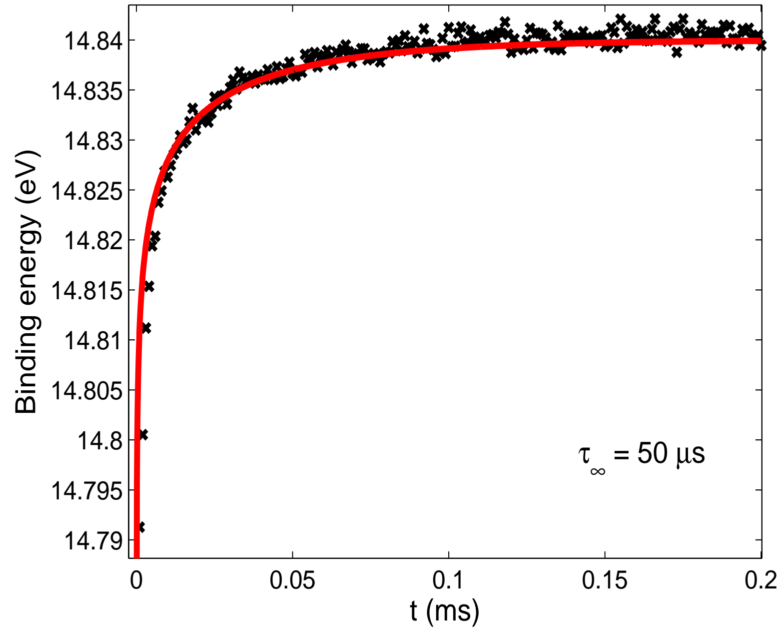

Figure 5.29: The rising edge of the SPV shift of the Zn 3*d* core level for clean ZnO, modeled with a time constant of 50 µs.

	ΔV (meV)	Rise τ_∞ (µs)	Decay τ_∞ (µs)
Clean ZnO	47.5	50	134
PbS / ZnO	15.0	5	75

Table 5.4: Fitting parameters for the SPV due to laser excitation of the Zn 3*d* core level for clean ZnO and PbS quantum dots attached to ZnO.

is limited by the absence of holes due to the oxygen desorption process. The band bending is then restored via the oxygen chemisorption process involving carrier capture across the depletion layer [254, 250, 252]. This cycle is illustrated in figure (5.30).

The PbS quantum dots were now chemically attached to the ZnO surface and the surface photovoltage of the Zn 3*d* core level was measured again. The amount of the SPV shift decreased to 15 meV (approximately a third of the SPV in clean ZnO, 47.5 meV), and the time constants associated with both the rise and decay of the SPV decreased, *i.e.* the rise and decay of the SPV occurred more quickly. The parameters are listed in table (5.4).

A comparison of the SPV data for clean ZnO and for PbS quantum dots attached to ZnO is given in figure (5.31). The signal to noise ratio for the PbS/ZnO data is worse because the magnitude of the SPV change is less than the clean case, and fewer accumulations were taken due to time constraints. Whereas figure (5.31) shows the averaged transient SPV data (where 20,000 data points across the 1 ms time window were averaged to 1,000 data points), the unaveraged transient SPV

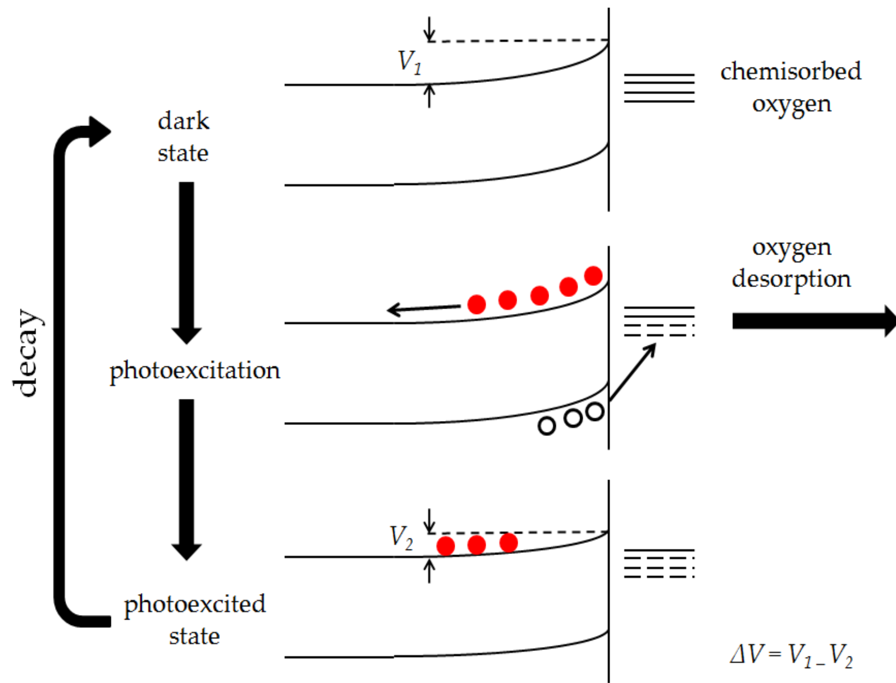

Figure 5.30: The SPV effect in ZnO caused by chemisorption and photodesorption of oxygen, adapted from [252]. Red filled circles denote electrons and unfilled black circles denote holes. The oxygen-related surface states are denoted by solid and dashed lines denoting filled and empty states respectively. The SPV decay is caused by the chemisorption of oxygen. The total SPV measured is the difference in the amount of band bending between the dark and photoexcited states.

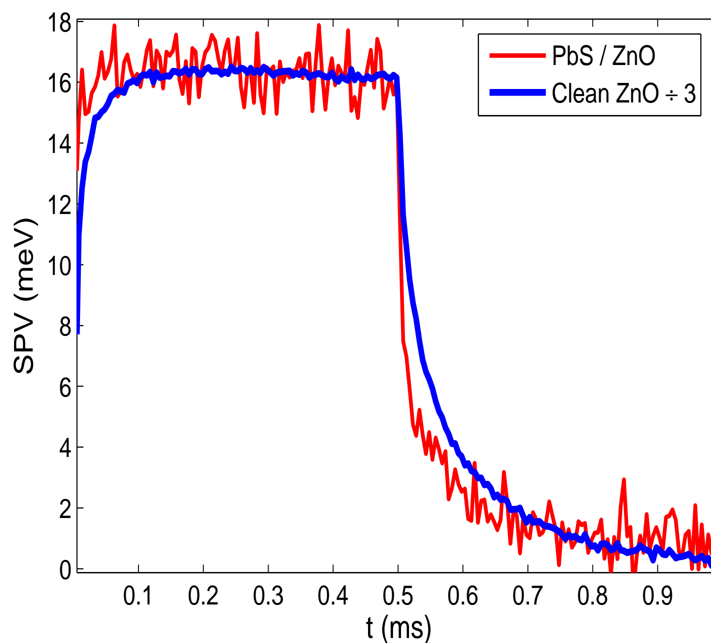

Figure 5.31: The SPV shift of the Zn *3d* core level for clean ZnO compared to PbS quantum dots attached to ZnO. The ZnO SPV shift is divided by three for comparison.

data set was used for the fitting of the SPV rise and decay. This was because the change in the SPV occurs much more quickly than the clean case: the unaveraged transient SPV data at 50 ns time steps was thus used for fitting instead of the averaged transient data that has 1 μs time steps. The decay of the SPV is shown in figure (5.32) and the rise in figure (5.33).

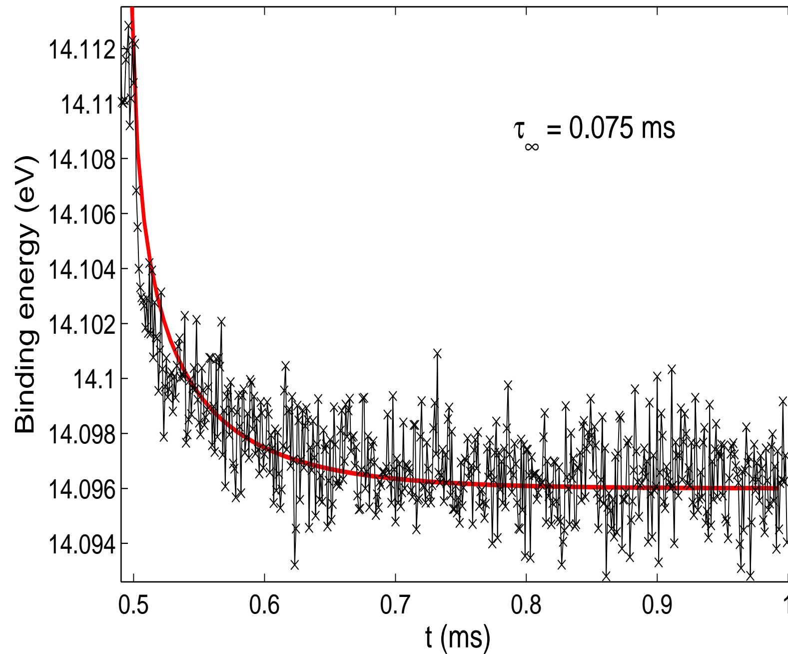

Figure 5.32: The decay of the laser-induced SPV of the Zn 3*d* core level for PbS quantum dots attached to ZnO, fitted with a decay constant of 75 μs.

The decrease in the total SPV change is attributed to a change in the ZnO surface depletion layer (and hence band bending) due to electron transfer from the PbS quantum dots as shown in figure (5.10). The attachment of PbS quantum dots to the ZnO surface therefore provides a direct photoexcitation route into the ZnO conduction band that was not present before. The presence of the quantum dots at the ZnO surface will also affect the Fermi level pinning which affects the amount of band bending in equilibrium.

It is intuitive that the rising edge of the change in the SPV upon photoexcitation should also occur on faster timescales because the quantum dots allow the direct injection of electrons into the ZnO conduction band. The rising edge therefore becomes instantaneous. Although figure (5.33) shows a fitted rising edge time constant of 5 μs, the signal to noise ratio is poor, and the rise may actually be occurring even more quickly that the current fitting suggests. The time resolution of the experiment was 150 ns due to the time difference in the signals from the delay line detector and the speed of the electronics, and it appears that the data are approaching this limit. Indeed, the timescale for electron transfer in analogous

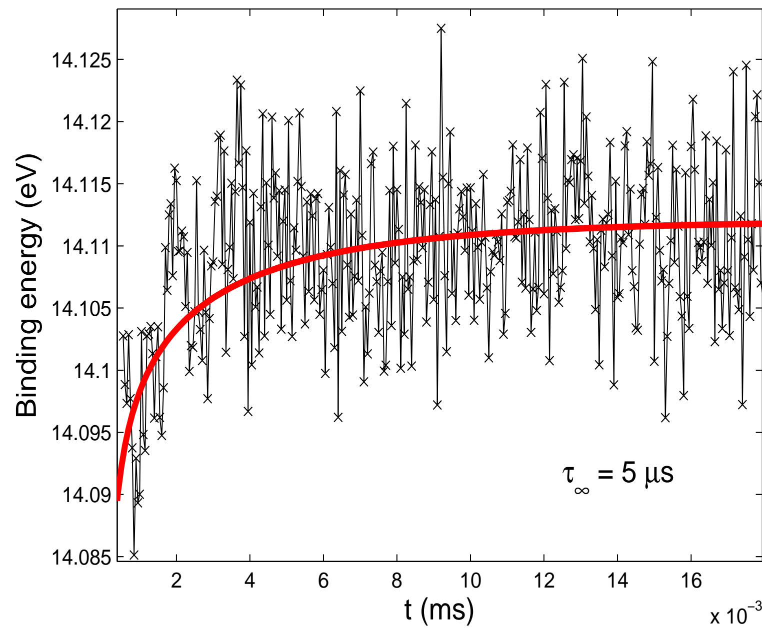

Figure 5.33: The rise of the laser-induced SPV of the Zn 3*d* core level for PbS quantum dots attached to ZnO, fitted with a time constant of 5 μs, approaching the time resolution of the experiment.

systems has been measured to be 50 fs [219, 220].

It is proposed that the attachment of the PbS quantum dots to the ZnO substrate leads to extra surface states within the ZnO band gap that provide additional routes for charge transfer in the oxygen chemisorption process. This explains the faster decay of the laser-induced SPV, with a time constant of 75 µs, when the quantum dots are attached. However, there is an absence of similar studies to this in the literature and further studies are clearly required.

5.3 Conclusions

X-ray photoelectron spectroscopy (XPS) and surface photovoltage (SPV) measurements have been carried out on silicon, zinc oxide and a sample of lead sulfide quantum dots chemically attached to zinc oxide.

SPV experiments on the Si(111) (7×7) surface show a change in the band bending at the surface of 95 meV upon illumination with 1.55 eV photons. The equilibrium band bending is determined to be 203 meV given the carrier concentration of the sample and the laser pump beam fluence, meaning that the Fermi level is pinned at 0.64 eV above the valence band maximum, agreeing well with literature measurements. The recombination process is proposed to be due to the recombination of photoexcited conduction band electrons with valence band holes across

the depletion layer, although the timescale for this recombination, determined to be ≈ 0.4 µs, does not agree well with literature estimations.

The experiments on Si took place at the Synchrotron Radiation Source at Daresbury Laboratory. The laser pump was synchronized to the synchrotron by a finite division of the laser repetition rate (81.198 MHz) to the 3.123 MHz (320 ns) repetition rate of the synchrotron by pulse picking every 26th laser pulse. A ZnO($10\bar{1}0$) crystal was also measured using the same system, although no transient change in the 110 meV SPV was observed over the SRS time window, meaning that changes in the SPV were occuring on much longer timescales. This lead to experiments at the SOLEIL synchrotron in Paris. Here, an external CW laser was controlled by a signal generator, with XPS spectra being measured every 50 ns over a 1 ms time window. The laser was turned on at the beginning of this time window and turned off after 0.5 ms.

SPV measurements on clean ZnO at SOLEIL showed an SPV shift of 47.5 meV. The timescale for the rising edge of the SPV change and the subsequent SPV decay were found to be relatively long: 50 and 134 µs respectively. The laser photon energy (3.3 eV) was insufficient to allow for direct photoexcitation of electrons into the conduction band. Electrons are promoted to band gap surface states before an additional absorption promotes them into the conduction band: hence a slow rising edge in the SPV change is observed. At the SRS similar experiments were carried out with a pump energy of 3.44 eV, *i.e.* greater than the band gap energy, which allowed direct photoexcitation across the ZnO band gap, and thus an instantaneous rise was observed.

The slow SPV decay rate is proposed to be due to chemisorption of oxygen at the surface once illumination ceases. The cleaning of ZnO, involving sputtering with argon ions, is itself designed to create oxygen vacancies at the surface which enhances the surface conductivity. There are many other defects within the ZnO lattice, including zinc interstitials, and there is a complex array of surface states at energies within the band gap. Because of this, ZnO is still under investigation today.

PbS quantum dots, previously measured to have diameters of approximately 4.6 nm, were chemically attached to the ZnO using a specially chosen ligand so that the energy level line-up would allow for direct injection of electrons from the quantum dot LUMO into the ZnO conduction band. XPS measurements of lead and sulfur core levels were carried out to ascertain that the quantum dots had been successfully attached. A slight degradation was observed in the sulfur 2*p* core level, although this ceased after approximately ten minutes, after which the sample was stable under the X-ray beam.

The SPV of the same Zn 3*d* core level was measured after chemical attachment

of the PbS quantum dots. The amount of the change in the SPV decreased by approximately a third to 15 meV, and the timescales of the rise and decay of the SPV decreased to 5 and 75 µs respectively. It is proposed that the PbS surface states lead to a change in the band bending at the ZnO surface and a change in the position of the Fermi level. This leads to a decreased amount of laser-induced surface photovoltage. The quantum dots create a direct route for the photoexcitation of electrons into the ZnO conduction band, and so the rising edge of the SPV becomes instantaneous. The results are limited by an experimental time resolution of 150 ns and a poor signal to noise ratio, and so a fitted time constant of 5 µs may be an overestimation. Further experimentation is clearly required because the effect of quantum dots attached to a substrate leading to changes in the SPV of that substrate is lacking in the literature.

Chapter 6

Conclusions and future work.

Laser-pump terahertz-probe and laser-pump synchrotron-probe experiments have been implemented to investigate the charge carrier dynamics in bulk and nanoparticulate photovoltaic materials.

A time-resolved THz spectrometer has been designed, built and commissioned. THz absorption measurements of toluene and hexane are made, and it is found that hexane is less absorbing over the THz frequency range of 0.1 - 2 THz, and is thus a more suitable solvent for solutions of quantum dot samples to be studied by THz spectroscopy. The THz refractive indices for toluene, hexane and quartz extracted are in strong agreement to literature results [165, 166, 167], meaning the fixed-point iteration method utilized in the extraction of the optical parameters is effective. The laser-pump THz-probe experiment was benchmarked using a GaAs wafer with good agreement to identical studies in the literature [161]. The intervalley scattering of photoexcited electrons in GaAs and InP at higher pump photon energies means that photoconductivity measurements in bulk semiconductors should only be taken at a pump-probe delay times of $\tau > 10$ ps, by which time all photoexcited electrons have returned to the band edge [171].

THz photoconductivity measurements of bulk InP have yielded the wavelength-dependent quantum efficiency of bulk InP to compare to a recent study of the quantum efficiency of InP quantum dots. Carrier multiplication is observed in InP quantum dots where quantum efficiencies exceeding unity are obtained at pump photon energies greater than twice the band gap energy [18]. In contrast, in this work, the quantum efficiency of bulk InP is found to decrease at higher photon energies [184]. Quantum efficiencies were plotted on a relative photon energy scale with respect to the band gap energy, $h\nu/E_g$, so as to compare bulk and quantum dot materials which have different band gap energies [17]. The efficiency decrease in the bulk is due to surface recombination effects which are dominant at higher photon energies due to a higher absorption coefficient and thus a decreased pene-

tration depth [191, 188]. In contrast, the quantum confinement of InP leads to an enhancement in quantum efficiency such that multiple electron-hole pairs can be generated from one photon with energy $h\nu \geq 2E_g$. A solar energy cell that utilizes these quantum dots could therefore benefit from an increase in efficiency. Moreover, the band gap energy and thus absorption of quantum dots can be adjusted so as to absorb the optimum amount of the solar spectrum, and the manufacture cost of quantum dots is greatly reduced compared to bulk materials where high purity is generally required [1].

The measurements of bulk InP follow a recent study of the quantum efficiency of bulk PbS measured with time-resolved THz spectroscopy [16]. This study found that the quantum efficiency of PbS quantum dots was not enhanced by quantum confinement, although here the plotting of quantum efficiencies on an absolute energy scale is misleading [17]. The fact that InP quantum dots have been shown in this thesis to be more efficient than the bulk on a $h\nu/E_g$ scale helps to resolve this controversy. Nevertheless, more studies are clearly required of bulk quantum efficiencies to compare to quantum dot measurements in order to understand the physical processes occurring, and to ascertain the effects caused by quantum confinement.

THz experiments of quantum dots can complement studies by other methods such as transient absorption experiments in the literature [73, 74, 75, 76, 77, 78, 18], because the frequency-dependent photoconductivity can give insight into the nature of the charge carrier dynamics. THz absorption measurements of 6 nm InP quantum dots suspended in hexane were performed, where the THz absorption was found to be small and similar to that of hexane. Laser-pump THz-probe measurements on InP quantum dots were unsuccessful because the change of the THz waveform upon photoexcitation was less than 1 in 1000. The experiment is limited by the signal-to-noise ratio of the experiment and the relatively low pump fluences generated by the optical parametric amplifier. In order for greater pump fluences to be used in photoexcitation, several upgrades to the THz spectrometer are required. The pump beam should be created using the output of the regenerative amplifier and a doubling crystal (although this will only give two possible pump wavelengths, 400 and 800 nm, with and without a doubling crystal), and the pump beam in this case should be brought to the sample colinear with the THz probe through a hole drilled in one of the parabolic mirrors, because the pellicle beam splitter currently used for this purpose has a low damage threshold.

It may be possible to study arrays of semiconductor nanorods such as the ZnO rods proposed for electron transportation in the hybrid solar cell design investigated here, where the photoconducting response will be larger than in isolated quantum dots held in solution. These would be good intermediate experiments

that could be carried out with the time-resolved spectrometer which may not require the invasive upgrades required to study colloidal quantum dot samples.

Photoinduced changes in the surface photovoltage (SPV) of bulk Si were measured at the SRS, Daresbury, UK, by synchronising a fs laser pump signal to the SRS, in the first such measurements of their kind in the UK. A total SPV change of 95 meV was measured, although this change occurred on a background of more than 300 meV. This is attributed to the fact that the change in the SPV did not completely decay over the 320 ns time-window of the SRS in single-bunch mode, and so an accumulation effect occurred. An SPV decay time constant of 0.4 μs was observed, and the decay of the SPV was attributed to the recombination of charge carriers across the depletion layer [52, 55, 248], rather than to effects of specific surface states [57, 58]. The total laser-induced SPV allowed for the pinning of the Fermi energy with respect to the valence band maximum at the surface to be determined as 0.64 eV, which was in strong agreement with values reported in the literature [217, 218].

Measurements of the SPV in bulk ZnO was also carried out at the SRS using a pump photon energy of 3.44 eV, which was greater than the band gap energy of ZnO (approximately 3.40 eV). An instantaneous change in the SPV of 110 meV was observed, although no decay was observed over the 320 ns time-window, meaning the charge carrier dynamics were occurring over much longer timescales. Measurements were next carried out at the Synchrotron SOLEIL, Paris, France, where time-resolved laser-pump synchrotron-probe experiments were carried out on much longer millisecond timescales. However, here a pump photon energy of 3.30 eV was used, meaning that direct photoexcitation across the ZnO band gap was not possible. As a result a slow onset of the photoinduced SPV was measured with a time constant of 50 μs, which may be due to the fact that two sequential photon absorptions were required to inject electrons into the ZnO conduction band, causing a delay in the onset of the photoinduced SPV. A longer time constant of 134 μs for the decay of the SPV change in bulk ZnO was measured when the laser was switched off. Here the SPV decay is dependent on an oxygen chemisorption process at the surface, and is consistent with that reported in the literature using different experimental techniques [254, 250, 252].

PbS quantum dots suspended in chloroform were then chemically attached to the ZnO surface using 3-MPA ligands [235]. This system is similar to that of PbS quantum dots linked to a TiO_2 substrate reported in the literature [219, 220], such that the energy level line-up allows for the direct injection of photoexcited electrons from the lowest unoccupied molecular orbit (LUMO) in the quantum dot into the conduction band of the ZnO substrate. The change in the SPV in ZnO was measured again, with faster decay (75 μs) and rising edge (5 μs) time constants

being observed. The SPV data suffer from a poorer signal-to-noise ratio than the clean ZnO results (approximately 3 times poorer), and, given this, it appears the time resolution of the experiment (150 ns) is approached at the rising edge (as there is significant error in fitting the onset of the data, and time-constants as short as the experimental resolution could be consistent with the fit). Thus it appears that the SPV change at the rising edge after linking PbS quantum dots to the surface may occur on a timescale that is close to or faster than the time resolution of the experiment. This suggests that the attachment of the quantum dots to the ZnO surface creates a direct route for photoexcited electrons in the quantum dot LUMO to be injected into the ZnO conduction band, as expected. The reduced decay time constant (when the laser is switched off) may be attributed to additional surface states within the ZnO band gap created by the PbS quantum dots that allow for additional routes for charge transfer in the oxygen chemisorption process.

Further studies of PbS quantum dots attached to ZnO could involve the use of a lower pump photon energy. The PbS quantum dots were reported to have a band gap energy of 1.0 eV [69], and so an 800 nm (1.55 eV) pump beam, for example, could be used to ensure photoexcitation of only the quantum dots and not the bulk ZnO (with a band gap energy of 3.4 eV). No SPV change should be observed in clean ZnO with this pump photon energy. The verification that charge carriers are directly injected from the quantum dot LUMO into the ZnO conduction band could therefore be achieved by observing an SPV change in the ZnO under photoexcitation of the PbS/ZnO system with a laser wavelength of 800 nm.

Another refinement of these SPV measurements could involve the use of so-called Type II quantum dots, where the quantum dot core and shell materials have different band gap energies. Selective photoexcitation of the core may be used to allow only one carrier (which may be either electrons or holes, depending on the band offsets at the core-shell interface) to be transferred to the shell of the dot, trapping the other. This could in principle lead to the selective injection of either an electron or hole into the substrate. These measurements would give further insight into the charge carriers dynamics occurring within quantum dots which is required to fabricate a highly efficient solar cell.

Bibliography

[1] O. Morton, "Solar energy: A new day dawning?: Silicon valley sunrise," *Nature*, vol. 443, pp. 19–22, 2006.

[2] R. Miles, G. Zoppi, and I. Forbes, "Inorganic photovoltaic cells," *Materials Today*, vol. 10, pp. 20–27, 2007.

[3] M. Powalla and D. Bonnet, "Thin-film solar cells based on the polycrystalline compound semiconductors CIS and CdTe.," *Advances in OptoElectronics*, vol. 2007, pp. 1–6, 2007.

[4] M. Grätzel, "Dye-sensitized solar cells," *Journal of Photochemistry and Photobiology C: Photochemistry Reviews*, vol. 4, pp. 145–153, 2003.

[5] M. Ohmori, T. Takamoto, E. Ikeda, and H. Kurita, "High efficiency InGaP/GaAs tandem solar cells," in *Techical Digest, International PVSEC-9*, p. 525–528, 1996.

[6] T. Takamoto, K. Sasaki, T. Agui, H. Juso, A. Yoshida, and K. Nakaido, "III–V compound solar cells.," *SHARP Technical Journal*, vol. 100, pp. 1–21, 2010.

[7] S. Wojtczuk, P. Chiu, X. Zhang, D. Derkacs, C. Harris, D. Pulver, and M. Timmons, "InGaP/GaAs/InGaAs concentrators using bi-facial epigrowth," in *Photovoltaic Specialists Conference, 2010. PVSC '10. 35th IEEE*, 2010.

[8] M. A. Green, K. Emery, Y. Hishikawa, and W. Warta, "Solar cell efficiency tables (version 36)," *Progress in Photovoltaics: Research and Applications*, vol. 18, p. 346–352, 2010.

[9] J. Zhao, A. Wang, M. A. Green, and F. Ferrazza, "19.8% efficient "honeycomb" textured multicrystalline and 24.4% monocrystalline silicon solar cells," *Applied Physics Letters*, vol. 73, pp. 1991–1993, 1998.

[10] C. J. Keavney, V. E. Haven, and S. M. Vernon, "Emitter structures in mocvd inp solar cells," in *Photovoltaic Specialists Conference, 1990., Conference Record of the Twenty First IEEE*, vol. 1, pp. 141 –144, 1990.

[11] I. Repins, M. Contreras, M. Romero, Y. Yan, W. Metzger, *et al.*, "Characterization of 19.9%-efficient CIGS absorbers," in *Photovoltaic Specialists Conference, 2008. PVSC '08. 33rd IEEE*, pp. 1 –6, 2008.

[12] X. Wu, J. C. Keane, R. G. Dhere, *et al.*, "16.5%-efficient CdS/CdTe polycrystalline thin-film solar cell," in *17th European Photovoltaic Solar Energy Conference*, p. 995–1000, 2001.

[13] Y. Chiba, A. Islam, K. Kakutani, R. Komiya, N. Koide, and L. Han, "High efficiency dye sensitized solar cells," in *15th International Photovoltaic Science and Engineering Conference*, p. 665–666, 2005.

[14] A. J. Nozik, "Quantum dot solar cells," *Physica E*, vol. 14, pp. 115–120, 2002.

[15] M. C. Beard and R. J. Ellingson, "Multiple exciton generation in semiconductor nanocrystals: Toward efficient solar energy conversion," *Laser & Photonics Reviews*, vol. 2, pp. 377–399, 2008.

[16] J. J. H. Pijpers, R. Ulbricht, K. J. Tielrooij, A. Osherov, Y. Golan, *et al.*, "Assessment of carrier-multiplication efficiency in bulk PbSe and PbS," *Nature Physics*, vol. 5, pp. 811–814, 2009.

[17] C. Delereu, G. Allan, J. J. H. Pijpers, and M. Bonn, "Carrier multiplication in bulk and nanocrystalline semiconductors: mechanism, efficiency, and interest for solar cells," *Physical Review B*, vol. 81, pp. 125306–1–125306–6, 2010.

[18] S. K. Stubbs, S. J. O. Hardman, D. M. Graham, B. F. Spencer, W. R. Flavell, *et al.*, "Efficient carrier multiplication in InP nanoparticles," *Physical Review B*, vol. 81, pp. 081303–1–081303–4(R), 2010.

[19] J. M. Hollander and W. L. Jolly, "X-ray photoelectron spectroscopy," *Accounts of Chemical Research*, vol. 3, pp. 193–200, 1970.

[20] S. L. Dexheimer, *Terahertz Spcetroscopy: Principles and Applications*. CRC Press, Boca Raton, 2008.

[21] C. A. Schmuttenmaer, "Exploring dynamics in the far-infrared with terahertz spectroscopy," *Chemical Reviews*, vol. 104, pp. 1759–1779, 2004.

[22] M. C. Beard, G. M. Turner, and C. A. Schmuttenmaer, "Terahertz spectroscopy," *Journal of Physical Chemistry B*, vol. 106, pp. 7146–7159, 2002.

[23] E. Hendry, *Charge carrier dynamics in novel semiconductors*. PhD thesis, University of Amsterdam, 2005.

[24] G. Dakovski, *Time-resolved terahertz spectroscopy of semiconductor quantum dots*. PhD thesis, Case Western Reserve University, 2008.

[25] E. Hendry, M. Koeberg, F. Wang, H. Zhang, C. de Mello Donegá, *et al.*, "Direct observation of electron-to-hole energy transfer in CdSe quantum dots," *Physical Review Letters*, vol. 96, pp. 057408–1–057408–4, 2006.

[26] J. J. H. Pijpers, E. Hendry, M. T. W. Milder, R. Fanciulli, J. Savolainenand, *et al.*, "Carrier multiplication and its reduction by photodoping in colloidal InAs quantum dots," *Journal of Physical Chemistry C*, vol. 111, pp. 4146–4152, 2007.

[27] F. Wang, J. Shan, M. A. Islam, I. P. Herman, M. Bonn, and T. F. Heinz, "Exciton polarizability in semiconductor nanocrystals," *Nature Materials*, vol. 5, pp. 861–864, 2006.

[28] P. U. Jepsen, D. G. Cooke, and M. Koch, “Terahertz spectroscopy and imaging – modern techniques and applications,” *Laser Photonics Review*, vol. 5, p. 124–166, 2011.

[29] J. A. Zeitler, P. F. Taday, D. A. Newnham, M. Pepper, K. C. Gordon, and T. Rades, “Terahertz pulsed spectroscopy and imaging in the pharmaceutical setting – a review,” *Journal of Pharmacy and Pharmacology*, vol. 59, pp. 209–223, 2007.

[30] A. G. Davies, A. D. Burnetta, W. Fana, E. H. Linfield, and J. E. Cunningham, “Terahertz spectroscopy of explosives and drugs,” *Materials Today*, vol. 11, pp. 18–26, 2008.

[31] F. J. Wuilleumier and M. Meyer, “Pump–probe experiments in atoms involving laser and synchrotron radiation: an overview,” *Journal of Physics B*, vol. 39, pp. R425–R477, 2006.

[32] J. Lacoursière, M. Meyer, L. Nahon, P. Morin, and M. Larzillière, “Time-resolved pump-probe photoelectron spectroscopy of helium using a mode-locked laser synchronized with synchrotron radiation pulses,” *Nuclear Instruments and Methods*, vol. 351, pp. 545–553, 1995.

[33] T. Quast, R. Bellmann, B. Winter, J. Gatzke, and I. V. Hertel, “Excited-state photoemission with combined laser/synchrotron pulse excitation from C_{60} chemisorbed on Ni(110),” *Journal of Applied Physics*, vol. 83, pp. 1642–1648, 1997.

[34] T. Gießel, D. Bröcker, P. Schmidt, and W. Widdra, “Time-resolving and energy-dispersive photoelectron detector for combined laser and synchrotron radiation experiments,” *Review of Scientific Instruments*, vol. 74, pp. 4620–4624, 2003.

[35] R. P. S. M. Lobo, J. D. LaVeigne, D. H. Reitze, D. B. Tanner, and G. L. Carr, “Subnanosecond, time-resolved, broadband infrared spectroscopy using synchrotron radiation,” *Review of Scientific Instruments*, vol. 73, pp. 1–10, 2002.

[36] D. J. Griffiths, *Introduction to Quantum Mechanics*. Prentice Hall, Englewood Cliffs, 1995.

[37] S. M. McMurry, *Quantum Mechanics*. Addison-Wesley Publishing Company, Wokingham, 1994.

[38] J. C. Phillips, *Bonds and Bands in Semiconductors*. Academic Press, New York, 1973.

[39] J. I. Pankove, *Optical Processes in Semiconductors*. Prentice-Hall, New York, 1971.

[40] A. J. Dekker, *Solid State Physics*. MacMillan & Co., London, 1958.

[41] R. B. Leighton, *Principles of Modern Optics*. McGraw-Hill, New York, 1959.

[42] C. Kittel, *Introduction to Solid Sate Physics*. John Wiley & Sons, New York, 7th ed., 1985.

[43] S. R. Elliott, *The Physics and Chemsitry of Solids*. John Wiley & Sons, Chichester, 1998.

[44] W. A. Harrison, *Electronic Structure and the Properties of Solids*. Freeman, San Francisco, 1980.

[45] H. M. Rosenberg, *The Solid State*. Oxford University Press, Oxford, 2003.

[46] P. A. Cox, *Electronic Structure and Chemistry of Solids*. Oxford University Press, Oxford, 1987.

[47] S. W. Koch, M. Kira, G. Khitrova, and H. M. Gibbs, "Semiconductor excitons in new light," *Nature Materials*, vol. 5, pp. 523–531, 2006.

[48] M. Balkanski and R. D. Waldron, "Internal photoeffect and exciton diffusion in cadmium and zinc sulfides," *Physical Review*, vol. 112, pp. 123–135, 1958.

[49] E. Yablonovitch, B. J. Skromme, R. Bhat, J. P. Harbison, and T. J. Gmitter, "Band bending, fermi level pinning, and surface fixed charge on chemically prepared GaAs surfaces," *Applied Physics Letters*, vol. 54, pp. 555–557, 1989.

[50] J. P. Long, "Surface space-charge dynamics and surface recombination on silicon (111) surfaces measured with combined laser and synchrotron radiation," *Physical Review Letters*, vol. 64, pp. 1158–1161, 1990.

[51] J. P. Long and V. M. Bermudez, "Band bending and photoemission-induced surface photovoltages on clean *n*- and *p*-gan (0001) surfaces," *Physical Review B*, vol. 66, pp. 121308–1–121308–4, 2002.

[52] W. Widdra, D. Bröcker, T. Gießel, I. V. Hertel, W. Krüge, *et al.*, "Time-resolved core level photoemission: surface photovoltage dynamics of the SiO_2/Si(100) interface," *Surface Science*, vol. 543, pp. 87–94, 2003.

[53] L. Kronik and Y. Shapira, "Surface photovoltage phenomena: theory, experiment, and applications," *Surface Science Reports*, vol. 37, pp. 1–206, 1999.

[54] M. H. Hecht, "Time dependence of photovoltaic shifts in photoelectron spectroscopy of semiconductors," *Physical Review B*, vol. 43, pp. 12102–12104, 1991.

[55] D. Bröcker, T. Gießel, and W. Widdra, "Charge carrier dynamics at the SiO_2/Si(100) surface: a time-resolved photoemission study with combined laser and synchrotron radiation," *Chemical Physics*, vol. 299, pp. 247–251, 2004.

[56] S. Tanaka, S. D. More, J. Murakami, M. Itoh, Y. Fujii, and M. Kamada, "Surface photovoltage effects on p-GaAs (100) from core-level photoelectron spectroscopy using synchrotron radiation and a laser," *Physical Review B*, vol. 64, pp. 155308–1–155308–6, 2001.

[57] M. Marsi, M. E. Couprie, L. Nahon, D. Garzella, T. Hara, *et al.*, "Surface states and space charge layer dynamics on Si(111)2 $\times$ 1: A free electron laser-synchrotron radiation study," *Applied Physics Letters*, vol. 70, pp. 895–897, 1997.

[58] J. P. Long, H. R. Sadeghi, J. C. Rife, and M. N. Kabler, "Surface space-charge dynamics and surface recombination on silicon (111) surfaces measured with combined laser and synchrotron radiation," *Physical Review Letters*, vol. 64, pp. 1158–1161, 1990.

[59] W. Shockley and H. J. Queisser, "Detailed balance limit of efficiency of p-n junction solar cells," *Journal of Applied Physics*, vol. 32, pp. 510–560, 1961.

[60] M. A. Green, K. Emery, Y. Hisikawa, and W. Warta, "Solar cell efficiency tables (version 30)," *Progress in Photovoltaics: Research and Applications*, vol. 15, pp. 425–430, 2007.

[61] K. Tanaka, T. Takahashi, T. Kondo, T. Umebayashi, K. Asai, and K. Ema, "Image charge effect on two-dimensional excitons in an inorganic-organic quantum-well crystal," *Physical Review B*, vol. 71, pp. 045312–1–045312–6, 2005.

[62] D. B. T. Thoai, R. Zimmermann, M. Grundmann, and D. Bimberg, "Image charges in semiconductor quantum wells: Effect on exciton binding energy," *Physical Review B*, vol. 42, pp. 5906–5909, 1990.

[63] R. L. Greene, K. K. Bajaj, and D. E. Phelps, "Energy levels of wannier excitons in GaAs-$Ga_{1-x}Al_x$As quantum-well structures," *Physical Review B*, vol. 29, pp. 1807–1812, 1984.

[64] P. Dawson, K. J. Moore, G. Duggan, H. I. Ralph, and C. T. B. Foxon, "Unambiguous observation of the 2s state of the light- and heavy-hole excitons in GaAs-(AlGa) As multiple-quantum-well structures," *Physical Review B*, vol. 34, pp. 6007–6010, 1986.

[65] O'Brian *et al.*, "EPSRC Materials for energy supply initiative," 2008.

[66] A. Franceschetti, J. M. An, and A. Zunger, "Impact ionization can explain carrier multiplication in PbSe quantum dots," *Nano Letters*, vol. 6, pp. 2191–2195, 2006.

[67] R. D. Schaller, M. A. Petruska, and V. I. Klimov, "Effect of electronic structure on carrier multiplication efficiency: Comparative study of PbSe and CdSe nanocrystals," *Applied Physics Letters*, vol. 87, pp. 253102–1–253102–3, 2005.

[68] R. D. Schaller, J. M. Pietryga, and V. I. Klimov, "Carrier multiplication in InAs nanocrystal quantum dots with an onset defined by the energy conservation limit," *Nano Letters*, vol. 7, pp. 3469–3476, 2007.

[69] S. J. O. Hardman, D. M. Graham, S. K. Stubbs, B. F. Spencer, E. A. Seddon, *et al.*, "Electronic and surface properties of PbS nanoparticles exhibiting efficient multiple exciton generation," *In Preparation*, 2011.

[70] R. D. Schaller and V. I. Klimov, "High efficiency carrier multiplication in PbSe nanocrystals: Implications for solar energy conversion," *Physical Review Letters*, vol. 92, p. 186601, 2004.

[71] M. C. Hanna and A. J. Nozik, "Solar conversion efficiency of photovoltaic and photoelectrolysis cells with carrier multiplication absorbers," *Journal of Applied Physics*, vol. 100, p. 074510, 2006.

[72] M. C. Beard, K. P. Knutsen, P. Yu, J. M. Luther, Q. Song, *et al.*, "Multiple exciton generation in colloidal silicon nanocrystals," *Nano Letters*, vol. 7, pp. 2506–2512, 2007.

[73] R. D. Schaller, M. Sykora, S. Jeong, and V. I. Klimov, "High-efficiency carrier multiplication and ultrafast charge separation in semiconductor nanocrystals studied via time-resolved photoluminescence," *Journal of Physical Chemistry B*, vol. 110, pp. 25332–25338, 2006.

[74] G. Nair and M. G. Bawendi, "Carrier multiplication yields of CdSe and CdTe nanocrystals by transient photoluminescence spectroscopy," *Physical Review B*, vol. 76, pp. 081304–1–081304–4(R), 2007.

[75] J. Minbiao, S. Park, S. T. Connor, T. Mokari, Y. Cui, and K. J. Gaffney, "Efficient multiple exciton generation observed in colloidal PbSe quantum dots with temporally and spectrally resolved intraband excitation," *Nano Letters*, vol. 9, pp. 1217–1222, 2009.

[76] R. J. Ellingson, M. C. Beard, J. C. Johnson, P. Yu, O. I. Micic, *et al.*, "Highly efficient multiple exciton generation in colloidal PbSe and PbS quantum dots," *Nano Letters*, vol. 5, pp. 865–871, 2005.

[77] G. Nair, S. M. Geyer, L.-Y. Chang, and M. G. Bawendi, "Carrier multiplication yields in PbS and PbSe nanocrystals measured by transient photoluminescence," *Physical Review B*, vol. 78, pp. 125325–1–125325–10, 2008.

[78] E. Rabani and R. Baer, "Distribution of multiexciton generation rates in CdSe and InAs nanocrystals," *Nano Letters*, vol. 8, pp. 4488–4492, 2008.

[79] S. K. E. Merchant, J. Lloyd-Hughes, L. Sirbu, I. M. Tiginyanu, P. Parkinson, *et al.*, "Conductivity of nanoporous InP membranes investigated using terahertz spectroscopy," *Nanotechnology*, vol. 19, pp. 395704–1–395704–7, 2008.

[80] M. C. Beard, G. M. Turner, J. E. Murphy, O. I. Micic, M. C. Hanna, *et al.*, "Electronic coupling in InP nanoparticle arrays," *Nano Letters*, vol. 3, pp. 1695–1699, 2003.

[81] H. H. Mantsch and D. Naumann, "Terahertz spectroscopy: The renaissance of far infrared spectroscopy," *Journal of Molecular Structure*, vol. 964, pp. 1–4, 2010.

[82] R. A. Kaindl, D. Hägele, M. A. Carnahan, R. Lövenich, and D. S. Chemla, "Exciton dynamics studied via internal THz transitions," *Physica Status Solidi B*, vol. 238, pp. 451–454, 2003.

[83] E. Hecht, *Optics*. Addison Wesley, Reading, 4th ed., 2002.

[84] R. Huber, F. Tauser, A. Brodschelm, M. Bichler, G. Abstreiter, and A. Leitenstorfer, "How many-particle interactions develop after ultrafast excitation of an electron-hole plasma," *Nature*, vol. 414, p. 286, 2001.

[85] S. Chatterjee, T. Grunwald, D. Köhler, K. Pierz, D. Golde, *et al.*, "THz measurements of the optical response in a two-dimensional electron gas," *Physica Status Solidi C*, vol. 6, p. 286, 2009.

[86] H.-K. Nienhuys and V. Sundström, "Influence of plasmons on terahertz conductivity measurements," *Applied Physics Letters*, vol. 87, p. 012101, 2005.

[87] H. Nienhuys and V. Sundström, "Intrinsic complications in the analysis of optical-pump, terahertz probe experiments," *Physical Review B*, vol. 71, p. 235110, 2005.

[88] J. E. Murphy, M. C. Beard, and A. J. Nozik, "Time-resolved photoconductivity of PbSe nanocrystal arrays," *Journal of Physical Chemistry B*, vol. 110, pp. 25455–25461, 2006.

[89] X. Ai, M. C. Beard, K. P. Knutsen, S. E. Shaheen, G. Rumbles, and R. J. Ellingson, "Photoinduced charge carrier generation in a poly(3-hexylthiophene) and methanofullerere bulk heterojunction investigated by time-resolved terahertz spectroscopy," *Journal of Physical Chemistry B*, vol. 110, pp. 25462–25471, 2006.

[90] G. Sharma, L. Razzari, F. H. Su, F. Blanchard, A. Ayesheshim, *et al.*, "Time-resolved terahertz spectroscopy of free carrier nonlinear dynamics in semiconductors," *IEEE Photonics*, vol. 2, pp. 578–592, 2010.

[91] P. Tiwana, P. Parkinson, M. B. Johnston, H. J. Snaith, and L. M. Herz, "Ultrafast terahertz conductivity dynamics in mesoporous $Ti0_2$: Influence of dye sensitization and surface treatment in solid-state dye-sensitized solar cells," *Journal of Physical Chemistry C*, vol. 114, pp. 1365–1371, 2010.

[92] F. Gao, G. L. Carr, C. D. Porter, D. B. Tanner, G. P. Williams, *et al.*, "Quasiparticle damping and the coherence peak in $YBa_2Cu_3O_{7-\delta}$," *Physical Review B*, vol. 54, pp. 700–710, 1996.

[93] H. Němec, F. Kadlec, and P. Kužel, "Methodology of an optical pump-terahertz probe experiment: An analytical frequency-domain approach," *Journal of Chemical Physics*, vol. 117, pp. 8454–8466, 2002.

[94] P. Kužel1, F. Kadlec, and H. Němec, "Propagation of terahertz pulses in photoexcited media: Analytical theory for layered media," *Journal of Chemical Physics*, vol. 127, pp. 024506–1–024506–11, 2007.

[95] P. Drude, "Zur elektronentheorie der metalle," *Annalen der Physik*, vol. 306, p. 566, 1900.

[96] N. V. Smith, "Classical generalization of the drude formula for the optical conductivity," *Physical Review B*, vol. 64, p. 155106, 2001.

[97] J. B. Baxter and C. A. Schmuttenmaer, "Conductivity of ZnO nanowires, nanoparticles, and thin films using time-resolved terahertz spectroscopy," *Journal of Physical Chemistry B*, vol. 110, pp. 25229–25239, 2006.

[98] D. G. Cooke, A. N. MacDonald, A. Hryciw1, J. Wang, Q. Li, *et al.*, "Transient terahertz conductivity in photoexcited silicon nanocrystal films," *Physical Review B*, vol. 73, pp. 193311–1–193311–4, 2006.

[99] M. Walther, D. G. Cooke, C. Sherstan, M. Hajar, M. R. Freeman, and F. A. Hegmann, "Terahertz conductivity of thin gold films at the metal-insulator percolation transition," *Physical Review B*, vol. 76, pp. 125408–1–125408–4, 2007.

[100] P. A. George, J. Strait, J. Dawlaty, S. Shivaraman, M. Chandrashekhar, *et al.*, "Ultrafast optical-pump terahertz-probe spectroscopy of the carrier relaxation and recombination dynamics in epitaxial graphene," *Nano Letters*, vol. 8, pp. 4248–4251, 2008.

[101] J. C. Brauer, K. Verner, K. Thorsmolle, and J.-E. Moser, "Terahertz time-domain spectroscopy study of the conductivity of hole-transporting materials," *Chimia*, vol. 63, pp. 189–192, 2009.

[102] J. Han, W. Zhang, W. Chen, L. Thamizhmani, A. K. Azad, and Z. Zhu, "Far-infrared characteristics of ZnS nanoparticles measured by terahertz time-domain spectroscopy," *Journal of Physical Chemistry B*, vol. 110, pp. 1989–1993, 2006.

[103] M. C. Beard, G. M. Turner, and C. A. Schmuttenmaer, "Size-dependent photoconductivity in CdSe nanoparticles as measured by time-resolved terahertz spectroscopy," *Nano Letters*, vol. 2, pp. 983–987, 2002.

[104] R. H. Groeneveld and D. Grischkowsky, "Picosecond time-resolved far-infrared experiments on carriers and excitons in GaAs-AlGaAs multiple quantum wells," *Journal of the Optical Society of America B*, vol. 11, pp. 2502–2507, 1994.

[105] P. K. Mandal and V. Chikan, "Plasmon-phonon coupling in charged n-type CdSe quantum dots: A THz time-domain spectroscopic study," *Nano Letters*, vol. 7, pp. 2521–2528, 2007.

[106] C. Rullière, *Femtosecond Laser Pulses: Principles and Experiments*. Springer, New York, 1998.

[107] G. R. Fleming, *Chemical Applications of Ultrafast Spectroscopy*. Oxford University Press, Oxford, 1986.

[108] J. Wilson and J. F. B. Hawkes, *Lasers: Principles and Applications*. Prentice Hall, New York, 1987.

[109] R. W. Boyd, *Nonlinear Optics*. Academic Press, Burlington, 2nd ed., 2003.

[110] P. A. Franken, A. E. Hill, C. W. Peters, and G. Weinreich, "Generation of optical harmonics," *Physical Review Letters*, vol. 7, pp. 118–119, 1961.

[111] G. Szabó and Z. Bor, "Broadband frequency doubler for femtosecond pulses," *Applied Physics B*, vol. 50, pp. 51–54, 1990.

[112] F. Zhou, I. P. Mercer, M. H. R. Hutchinson, C. N. Danson, and C. B. Edwards, "Double-side pumped Ti:sapphire regenerative pre-amplifier operating at 1.053 μm wavelength," *Electronics Letters*, vol. 31, pp. 1060–1061, 1995.

[113] T. Joo, Y. Jia, and G. R. Fleming, "Ti:sapphire regenerative amplifier for ultrashort high-power multikilohertz pulses without an external stretcher," *Optics Letters*, vol. 20, pp. 389–391, 1995.

[114] K. Yamakawa, A. Magana, and P. H. Chiu, "Tunable Ti:sapphire regenerative amplifier for femtosecond chirped-pulse amplification," *Applied Physics B*, vol. 58, pp. 323–326, 1994.

[115] A. M. Johnson, R. H. Stolen, and W. M. Simpson, "80 $\times$ single-stage compression of frequency doubled Nd:yttrium aluminum garnet laser pulses," *Applied Physics Letters*, vol. 44, pp. 729–731, 1984.

[116] L. M. Frantz and J. S. Nodvik, "Theory of pulse propagation in a laser amplifier," *Journal of Applied Physics*, vol. 34, pp. 2346–2349, 1963.

[117] J. A. Giordamaine and R. C. Miller, "Tunable coherent parametric oscillation in $LiNbO_3$ at optical frequencies," *Physical Review Letters*, vol. 14, p. 973, 1965.

[118] G. Cerullo and S. D. Silvestri, "Ultrafast optical parametric amplifiers," *Review of Scientific Instruments*, vol. 74, pp. 1–18, 2003.

[119] J. M. Manley and H. E. Rowe, "Some general properties of nonlinear elements," *Proceedings of the Institute of Radio Engineers*, vol. 44, pp. 904–913, 1956.

[120] S. A. Akhmanov, V. A. Vysloukh, and A. Chirkin, *Optics of femtosecond laser pulses*. American Institute of Physics, New York, 1992.

[121] K. R. Wilson and V. V. Yakovlev, "Ultrafast rainbow: tunable ultrashort pulses from a solid-state kilohertz system," *Journal of the Optical Society of America B*, vol. 14, pp. 444–448, 1997.

[122] R. Danielius, A. Piskarskas, A. Stabinis, G. P. Banfi, P. P. Di Trapani, and R. Righini, "Traveling-wave parametric generation of widely tunable, highly coherent femtosecond light pulses," *Journal of the Optical Society of America B*, vol. 10, pp. 2222–2232, 1993.

[123] J. M. Khosrofian and B. A. Garetz, "Measurement of a gaussian laser beam diameter through the direct inversion of knife-edge data," *Applied Optics*, vol. 22, pp. 3406–3410, 1983.

[124] D. Wright, P. Greve, J. Fleischer, and L. Austin, "Laser beam width, divergence and beam propagation factor- an international standardization approach," *Optical and Quantum Electronics*, vol. 24, pp. S993–S1000, 1992.

[125] W. Plass, R. Maestle, K. Wittig, A. Voss, and A. Giesen, "High-resolution knife-edge laser beam profiling," *Optics Communications*, vol. 134, pp. 21–24, 1997.

[126] M. P. Seah and W. A. Dench, "Quantitative electron spectroscopy of surfaces: A standard data base for electron inelastic mean free paths in solids," *Surface and Interface Analysis*, vol. 1, pp. 2–11, 1979.

[127] J. F. Watts and J. Wolstenholme, *An Introduction to Surface Analysis by XPS and AES*. Wiley, Chichester, 2003.

[128] D. Briggs and M. P. Seah, *Practical Surface Analysis. Volume 1: Auger and X-ray Photoelectron Spectroscopy*. Wiley, Chichester, 1990.

[129] R. Hesse, P. Streubel, and R. Szargan, "Product or sum: comparative tests of Voigt, and product or sum of Gaussian and Lorentzian functions in the fitting of synthetic Voigt-based X-ray photoelectron spectra," *Surface and Interface Analysis*, vol. 39, pp. 381–391, 2007.

[130] J. W. Precker and M. A. da Silva, "Experimental estimation of the band gap in silicon and germanium from the temperature–voltage curve of diode thermometers," *American Journal of Physics*, vol. 70, pp. 1150–1153, 2002.

[131] F. Baudelet, R. Belkhou, V. Briois, A. Coati, P. Dumas, *et al.*, "Soleil: a new powerful tool for materials science," *Oil and Gas Science and Technology*, vol. 60, pp. 849–874, 2005.

[132] G. Cautero, R. Sergo, L. Stebel, P. Lacovig, P. Pittana, *et al.*, "A two-dimensional detector for pump-and-probe and time resolved experiments," *Nuclear Instruments and Methods in Physics Research A*, vol. 595, pp. 447–459, 2008.

[133] M. Lampton, O. Siegmund, and R. Raffanti, "Delay line anodes for microchannel-plate spectrometers," *Review of Scientific Instruments*, vol. 58, pp. 2298–2305, 1987.

[134] S. L. Chuang, S. Schmitt-Rink, B. I. Greene, P. N. Saeta, and A. F. J. Levi, "Optical rectification at semiconductor surfaces," *Physical Review Letters*, vol. 68, pp. 102–105, 1992.

[135] L. Xu, X.-C. Zhang, and D. H. Auston, "Terahertz beam generation by femtosecond optical pulses in electro-optic materials," *Applied Physics Letters*, vol. 61, pp. 1784–1786, 1992.

[136] K. Wynne and J. J. Carey, "An integrated description of terahertz generation through optical rectification, charge transfer, and current surge," *Optics Communications*, vol. 256, pp. 400–413, 2005.

[137] Z. Zhen-Yu, H. Sophie, and T. Jérôme, "THz generation by optical rectification and competition with other nonlinear processes," *Chinese Physical Letters*, vol. 25, pp. 1868–1870, 2008.

[138] F. Blanchard, L. Razzari, H. C. Bandulet, G. Sharma, R. Morandotti, *et al.*, "Generation of 1.5 μj single-cycle terahertz pulses by optical rectification from a large aperture ZnTe crystal," *Optics Express*, vol. 15, pp. 13212–13220, 2007.

[139] Q. Wu, M. Litz, and X.-C. Zhang, "Broadband detection capability of ZnTe electro-optic field detectors," *Applied Physics Letters*, vol. 68, pp. 2924–2926, 1996.

[140] Y. Cai, I. Brener, J. Lopata, J. Wynn, L. Pfeiffer, *et al.*, "Coherent terahertz radiation detection: Direct comparison between free-space electro-optic sampling and antenna detection," *Applied Physics Letters*, vol. 73, pp. 444–446, 1998.

[141] P. C. M. Planken, H.-K. Nienhuys, H. J. Bakker, and T. Wenckebach, "Measurement and calculation of the orientation dependence of terahertz pulse detection in ZnTe," *Journal of the Optical Society of America B*, vol. 18, pp. 313–317, 2001.

[142] G. Zhao, R. N. Schouten, N. van der Valk, W. T. Wenckebach, and P. C. M. Planken, "Design and performance of a THz emission and detection setup based on a semi-insulating GaAs emitter," *Review of Scientific Instruments*, vol. 73, pp. 1715–1719, 2002.

[143] A. Nahata, A. S. Weling, and T. F. Heinz, "A wideband coherent terahertz spectroscopy system using optical rectification and electro-optic sampling," *Applied Physics Letters*, vol. 69, pp. 2321–2323, 1996.

[144] Y. C. Shen, P. C. Upadhya, E. H. Linfield, H. E. Beere, and A. G. Davies, "Ultrabroadband terahertz radiation from low-temperature-grown GaAs photoconductive emitters," *Applied Physics Letters*, vol. 83, pp. 3117–3119, 2003.

[145] P. M. Duffieux, *The Fourier transform and its applications to optics*. Wiley, New York, 1983.

[146] J. H. Scofield, "Frequency-domain description of a lock-in amplifier," *American Journal of Physics*, vol. 62, pp. 129–133, 1993.

[147] D. C. Champeney, *Fourier transforms and their physical applications*. Academic Press, New York, 1973.

[148] P.-A. Probst and A. Jaquier, "Multiple-channel digital lock-in amplifier with ppm resolution," *Review of Scientific Instruments*, vol. 65, pp. 747–750, 1993.

[149] NASA, *Jet Propulsion Laboratory, Molecular Spectroscopy*. Catalog, 18003.

[150] Y. Ueno and K. Ajito, "Analytical terahertz spectroscopy," *Analytical Sciences*, vol. 24, pp. 185–192, 2008.

[151] X. Xin, H. Altan, A. Saint, D. Matten, and R. R. Alfano, "Terahertz absorption spectrum of para and ortho water vapors at different humidities at room temperature," *Journal of Applied Physics*, vol. 100, pp. 094905–1–094905–4, 2006.

[152] M. Hoffmann, *Novel Techniques in THz-Time-Domain-Spectroscopy*. PhD thesis, Albert-Ludwigs-University Freiburg, 2006.

[153] K. Ikeda, A. Matsushita, Y. M. M. Tatsuno and, M. Yamaguchi, *et al.*, "Investigation of inflammable liquids by terahertz spectroscopy," *Applied Physics Letters*, vol. 87, pp. 034105–1–034105–3, 2005.

[154] R. A. Kaindl, R. Huber, B. A. Schmid, M. A. Carnahan, D. Hägele, and D. S. Chemla, "Ultrafast THz spectroscopy of correlated electrons: from excitons to Cooper pairs," *Physica Status Solidi B*, vol. 243, pp. 2414–2422, 2006.

[155] Y. S. Lee, *Principles of Terahertz Science and Technology*. Springer US, Boston, 2009.

[156] B. N. Flanders, D. C. Arnett, and N. F. Scherer, "Optical pump-terahertz probe spectroscopy utilizing a cavity-dumped oscillator-driven terahertz spectrometer," *IEEE Journal of Selected Topics in Quantum Electronics*, vol. 4, pp. 353–359, 1998.

[157] K. P. H. Lui and F. A. Hegmann, "Ultrafast carrier relaxation in radiation-damaged silicon on sapphire studied by optical-pump–terahertz-probe experiments," *Applied Physics Letters*, vol. 78, pp. 3478–3480, 2001.

[158] E. Knoesel, M. Bonn, J. Shan, and T. F. Heinz, "Charge transport and carrier dynamics in liquids probed by THz time-domain spectroscopy," *Physical Review Letters*, vol. 86, pp. 340–343, 2001.

[159] M. Schall and P. U. Jepsen, "Photoexcited GaAs surfaces studied by transient terahertz time-domain spectroscopy," *Optics Letters*, vol. 25, pp. 13–15, 2000.

[160] M. C. Beard, G. M. Turner, and C. A. Schmuttenmaer, "Subpicosecond carrier dynamics in low-temperature grown GaAs as measured by time-resolved terahertz spectroscopy," *Journal of Applied Physics*, vol. 90, pp. 5915–5922, 2001.

[161] M. C. Beard, G. M. Turner, and C. A. Schmuttenmaer, "Transient photoconductivity in GaAs as measured by time-resolved terahertz spectroscopy," *Physical Review B*, vol. 62, pp. 15764–15777, 2000.

[162] J. Kitagawa, , Y. Kadoya, M. Tsubota, F. Iga, and T. Takabatake, "Terahertz time-domain spectroscopy of photoinduced carriers in $YTiO_3$," *Journal of Magnetism and Magnetic Materials*, vol. 310, pp. 913–915, 2007.

[163] W. Withayachumnankul, B. Ferguson, T. Rainsford, S. P. Mickan, and D. Abbott, "Material parameter extraction for terahertz time-domain spectroscopy using fixed-point iteration," *Proceedings of SPIE*, vol. 5840, pp. 221–231, 2005.

[164] M. Scheller and M. Koch, "Fast and accurate thickness determination of unknown materials using terahertz time domain spectroscopy," *Journal of Infrared, Millimeter and Terahertz Waves*, vol. 30, pp. 762–769, 2009.

[165] M. Naftaly and R. E. Miles, "Terahertz time-domain spectroscopy: A new tool for the study of glasses in the far infrared," *Journal of Non-Crystalline Solids*, vol. 351, pp. 3341—-3346, 2005.

[166] G.-J. Kim, S.-G. Jeon, J.-I. Kim, and Y.-S. Jin, "Terahertz time domain spectroscopy of petroleum products and organic solvents," in *Infrared, Millimeter and Terahertz Waves*, pp. 1–2, IEEE, 2008.

[167] T. Ikeda, A. Matsushita, M. Tatsuno, Y. Minami, M. Yamaguchi, *et al.*, "Time dependence of photovoltaic shifts in photoelectron spectroscopy of semiconductors," *Applied Physics Letters*, vol. 87, pp. 034105–1–034105–3, 2005.

[168] N. Katzenellenbogen and D. Grischkowsky, "Electrical characterization to 4 THz of n- and p-type GaAs using THz time-domain spectroscopy," *Applied Physics Letters*, vol. 61, pp. 840–842, 1992.

[169] D. Turchinovich, *Study of Ultrafast Polarization and Carrier Dynamics in Semiconductor Nanostructures: a THz Spectroscopy Approach*. PhD thesis, Albert-Ludwigs-University Freiburg, 2004.

[170] M. Rohlfing, P. Krüger, and J. Pollmann, "Quasiparticle band-structure calculations for C, Si, Ge, GaAs, and SiC using Gaussian-orbital basis sets," *Physical Review B*, vol. 48, pp. 17791–17805, 1993.

[171] P. N. Saeta, J. F. Federici, B. I. Greene, and D. R. Dykaar, "Intervalley scattering in GaAs and InP probed by pulsed far-infrared transmission spectroscopy," *Applied Physics Letters*, vol. 60, pp. 1477–1479, 1992.

[172] I. Vurgaftman, J. R. Meyer, and L. R. Ram-Mohan, "Band parameters for III–V compound semiconductors and their alloys," *Journal of Applied Physics*, vol. 89, pp. 5815–5875, 2001.

[173] J. Lloyd-Hughes, S. K. E. Merchant, L. Sirbu, I. M. Tiginyanu, and M. B. Johnston, "Terahertz photoconductivity of mobile electrons in nanoporous InP honeycombs," *Physical Review B*, vol. 78, pp. 085320–1–085320–4, 2008.

[174] D. E. Aspnes and A. A. Studna, "Dielectric functions and optical parameters of Si, Ge, GaP, GaAs, GaSb, InP, InAs, and InSb from 1.5 to 6.0 eV," *Physical Review B*, vol. 27, pp. 985–1009, 1983.

[175] S. T. Thornton and A. Rex, *Modern Physics for Scientists and Engineers*. Saunders College Publishing, London, 1993.

[176] T. D. Dorney, R. G. Baraniuk, and D. M. Mittleman, "Material parameter estimation with terahertz time-domain spectroscopy," *Journal of the Optical Society of America A*, vol. 18, pp. 1562–1572, 2001.

[177] J. A. McCaulley, V. M. Donnelly, M. Vernon, and I. Taha, "Temperature dependence of the near-infrared refractive index of silicon, gallium arsenide and indium phosphide," *Physical Review B*, vol. 49, pp. 7408–7417, 1994.

[178] J. M. A. Gilman, A. Hamnett, and R. A. Batchelor, "Franz-keldysh and band-filling effects in the electroreflectance of highly doped p-type GaAs," *Physical Review B*, vol. 46, pp. 13363–13370, 1992.

[179] G. E. Stillman, V. M. Robbinsa, and K. Hess, "Impact ionization in InP and GaAs," *Physica B+C*, vol. 134, pp. 241–246, 1985.

[180] C.-W. Kao and C. R. Crowell, "Impact ionization by electrons and hole in InP," *Solid-Sate Electronics*, vol. 23, pp. 881–891, 1980.

[181] M. Nakajima, M. Takahashi, and M. Hangyo, "Temperature dependence of THz radiation from semi-insulating InP surface," *Journal of Luminescence*, vol. 94-95, pp. 627–630, 2001.

[182] M. Nakajima, Y. Oda, and T. Suemoto, "Competing terahertz radiation mechanisms in semi-insulating InP at high-density excitation," *Applied Physics Letters*, vol. 85, pp. 2694–2697, 2004.

[183] H.-J. Schimper, Z. Kollonitsch, K. Möller, U. Seidel, U. Bloeck, *et al.*, "Material studies regarding inp-based high-efficiency solar cells," *Journal of Crystal Growth*, vol. 287, pp. 642–646, 2006.

[184] B. F. Spencer, D. M. Graham, C. Lange, S. Chattopadhyay, and W. R. Flavell, "Developing InP-based solar cells: Time-resolved terahertz measurements of photoconductivity and carrier multiplication efficiencies," in *Infrared, Millimeter and Terahertz Waves*, pp. 1–3, IEEE, 2010. DOI: 10.1109/ICIMW.2010.5612377.

[185] C. Keavney, V. Haven, and S. Vernon, "Emitter structures in MOVCD InP solar cells," *Proceedings of the 21st IEEE PV Specialists Conference*, vol. 21, p. 141, 1990.

[186] T. Inoue, K. Kainosho, R. Hirano, H. Shimakura, T. Kanazawa, and O. Oda, "Characterization of high-purity InP by photoluminescence," *Journal of Applied Physics*, vol. 67, pp. 7165–7169, 1990.

[187] A. Smith and D. Dutton, "Behavior of lead sulfide photocells in the ultraviolet," *Journal of the Optical Society of America*, vol. 48, p. 1007, 1958.

[188] W. J. Yang, Z. Maa, X. Tanga, C. Fenga, W. Zhaoa, and P. Shi, "Internal quantum efficiency of solar cells," *Solar energy*, vol. 82, pp. 106–110, 2008.

[189] J. M. Langer and W. Walukiewicz, "Surface recombination in semiconductors," *Materials Science Forum*, vol. 196-201, pp. 1389–1394, 1995.

[190] D. E. Aspnes, "Recombination at semicoductor surfaces and interfaces," *Surface Science*, vol. 132, pp. 406–421, 1983.

[191] R. H. Wilson, "A model for the current-voltage curve of photoexcited semiconductor electrodes," *Journal of Applied Physics*, vol. 48, pp. 4292–4297, 1977.

[192] J. F. Geisz, S. Kurtz, M. W. Wanlass, J. S. Ward, A. Duda, *et al.*, "High-efficiency GaInP/GaAs/InGaAs triple-junction solar cells grown inverted with a metamorphic bottom junction," *Applied Physics Letters*, vol. 91, pp. 023502–023504, 2007.

[193] S. P. Tobin, S. M. Vemon, M. M. Sanfacon, and A. Mastrovito, "Enhanced light absorption in GaAs solar cells with internal bragg reflectors," *IEEE Photovoltaics Specialists Conference*, vol. 22, pp. 147–152, 1991.

[194] S. E. Kohn, P. Y. Yu, Y. Petroff, Y. R. Shen, Y. Tsang, and M. L. Cohen, "Band structure and optical properties of PbTe, PbSe and PbS," *Physical Review B*, vol. 8, pp. 1477–1488, 1973.

[195] E. D. Palik, *Handbook of Optical Constants of Solids*. Academic Press, Orlando, 1984.

[196] S. Gao, C. Zhang, Y. Liu, H. Su, L. Wei, *et al.*, "Lasing from colloidal InP/ZnS quantum dots," *Optics Express*, vol. 19, pp. 5528–5535, 2011.

[197] P. Parkinson, J. Lloyd-Hughes, Q. Gao, H. H. Tan, C. Jagadish, *et al.*, "Transient terahertz conductivity of GaAs nanowires," *Nano Letters*, vol. 7, pp. 2162–2165, 2007.

[198] R. P. Prasankumar, S. Choi, S. A. Trugman, S. T. Picraux, and A. J. Taylor, "Ultrafast electron and hole dynamics in germanium nanowires," *Nano Letters*, vol. 8, p. 1619–1624, 2008.

[199] C. Y. Su, P. Skeath, I. Lindau, and W. Spicer, "The nature of the 7×7 reconstruction of Si(111): As revealed by changes in oxygen sorption from 2×1 to 7×7," *Surface Science*, vol. 107, pp. L355–L361, 1981.

[200] K. Takayanagi, Y. Tanishiro, M. Takahashi, and S. Takahashi, "Structural analysis of Si(111)-7×7 by UHV-transmission electron diffraction and microscopy," *Journal of Vacuum Science and Technology A*, vol. 3, pp. 1502–1506, 1985.

[201] G. L. Lay, M. Göthelid, T. M. Grehk, M. Björkquist, U. O. Karlsson, and V. Y. Aristov, "Surface core-level shifts of Si(111)7×7: A fundamental reassessment," *Physical Review B*, vol. 50, pp. 14277–14282, 1994.

[202] C. J. Karlsson, E. Landemark, Y.-C. Chao, and R. I. G. Uhrberg, "Atomic origins of the surface components in the Si 2p core-level spectra of the Si(111)7×7 surface," *Physical Review B*, vol. 50, pp. 5767–5770, 1994.

[203] J. J. Paggel, W. Theis, K. Horn, C. Jung, C. Hellwig, and H. Petersen, "Correlation of surface core levels and structural building blocks for the Si(111)-7×7 reconstruction through high-resolution core-level spectroscopy," *Physical Review B*, vol. 50, pp. 18686–18689, 1994.

[204] G. L. Lay, A. Cricenti, C. Ottaviani, C. Haokansson, P. Perfetti, and K. Prince, "Surface core-level shifts of Si(111)7×7: a critical evaluation of the Si2p analysis," *Journal of Electron Spectroscopy and Related Phenomena*, vol. 88, pp. 711–715, 1998.

[205] C. J. Karlsson, E. Landemark, L. S. O. Johansson, U. O. Karlsson, and R. I. G. Uhrberg, "Hydrogen chemisorption on Si(111)7 $\times$ 7 studied with surface-sensitive core-level spectroscopy and angle-resolved photoemission," *Physical Review B*, vol. 41, pp. 1521–1528, 1990.

[206] U. Gelius, L. Asplund, E. Basilier, S. Hedman, K. Helenelund, and K. Siegbahn, "A high resolution multipurpose ESCA instrument with X-ray monochromator," *Nuclear Instruments and Methods in Physics Research B*, vol. 1, pp. 85–117, 1984.

[207] C. M. Garner, I. Lindau, C. Y. Su, P. Pianetta, and W. E. Spicer, "Electron-spectroscopic studies of the early stages of the oxidation of Si," *Physical Review B*, vol. 19, pp. 3944–3952, 1979.

[208] P. Morgen, U. Höfer, W. Wurth, and E. Umbach, "Initial stages of oxygen adsorption on Si(111): the stable state," *Physical Review B*, vol. 39, pp. 3720–3734, 1989.

[209] M. Nakazawa, S. Kawase, and H. Sekiyama, "Investigations of the SiO_2/Si interface. I. Oxidation of a clean Si(100) surface using photoemission spectroscopy with synchrotron radiation," *Journal of Applied Physics*, vol. 65, pp. 4014–4018, 1989.

[210] G. Hollinger and F. J. Himpsel, "Multiple-bonding configurations for oxygen on silicon surfaces," *Physical Review B*, vol. 28, pp. 3651–3653, 1983.

[211] G. Hollinger and F. J. Himpsel, "Probing the transition layer at the SiO_2-Si interface using core level photoemission," *Applied Physics Letters*, vol. 44, pp. 93–95, 1984.

[212] M. Mauerer and I. L. Shumay, "Ultrafast carrier dynamics in Si(111) 7$\times$7 dangling bonds probed by time-resolved second-harmonic generation and two-photon photoemission," *Physical Review B*, vol. 73, p. 245305, 2006.

[213] S. M. Sze, *Semiconductor Devices: Physics and Technology*. John Wiley & Sons, New York, 1985.

[214] W. F.Beadle, J. C. C. Tsia, and R. D. Plummer, *Quick Reference Manual for Semiconductor Engineers*. Wiley, New York, 1985.

[215] R. M. Tromp, R. J. Hamers, and J. E. Demuth, "Quantum states and atomic structure of silicon surfaces," *Science*, vol. 234, pp. 304–309, 1986.

[216] M. Jujita, H. Nagayoshi, and A. Yoshimori, "Electronic structure of the DAS model for the Si(111) 7$\times$7 reconstructed surface by energy band calculations," *Surface Science*, vol. 242, pp. 229–232, 1991.

[217] F. J. Himpsel, G. Hollinger, and R. A. Pollak, "Determination of the Fermi-level pinning position at Si(111) surfaces," *Physical Review B*, vol. 28, pp. 7014–7018, 1983.

[218] R. Losio, K. N. Altmann, and F. J. Himpsel, "Fermi surface of Si(111)7$\times$7," *Physical Review B*, vol. 61, pp. 10845–10853, 2000.

[219] J. B. Sambur, T. Novet, and B. A. Parkinson, "Multiple exciton collection in a sensitized photovoltaic system," *Science*, vol. 330, pp. 63–66, 2010.

[220] W. A. Tisdale, K. J. Williams, B. A. Timp, D. J. Norris, E. S. Aydil, and X.-Y. Zhu, "Hot-electron transfer from semiconductor nanocrystals," *Science*, vol. 328, pp. 1543–1547, 2010.

[221] J. A. McLeod, R. G. Wilks, N. A. Skorikov, L. D. Finkelstein, M. Abu-Samak, *et al.*, "Band gaps and electronic structure of alkaline-earth and post-transition-metal oxides," *Physical Review B*, vol. 81, pp. 245123–1–245123–9, 2010.

[222] J. Pascual, J. Camassel, and H. Mathieu, "Resolved quadrupolar transition in TiO_2," *Physical Review Letters*, vol. 39, pp. 1490–1493, 1977.

[223] O. Dulub, L. A. Boatner, and U. Diebold, "STM study of the geometric and electronic structure of ZnO(0001)-Zn, $(000\bar{1})$-O, $(10\bar{1}0)$, and $(11\bar{2}0)$ surfaces," *Surface Science*, vol. 519, pp. 201–207, 2002.

[224] S. J. Pearton, D. P. Nortona, K. Ipa, Y. W. Heoa, and T. Steiner, "Recent progress in processing and properties of ZnO," *Progress in Materials Science*, vol. 50, pp. 293—-340, 2005.

[225] M. M. C. Chou, L. Chang, D.-R. Hang, C. Chen, D.-S. Chang, and C.-A. Li, "Crystal growth of nonpolar m-plane ZnO on a lattice-matched(100) γ-$LiAlO_2$ substrate," *Crystal Growth and Design*, vol. 9, pp. 2073–2078, 2009.

[226] A. Wander and N. M. Harrison, "The structure of higher defective zno $(10\bar{1}0)$," *Surface Science Letters*, vol. 529, pp. 281–284, 2003.

[227] N. Jedrecy, S. Gallini, M. Sauvage-Simkin, and R. Pinchaux, "The zno non-polar $(10\bar{1}0)$ surface: an x-ray structural investigation," *Surface Science*, vol. 460, pp. 136—-143, 2000.

[228] J.-M. Lee, K.-K. Kim, S.-J. Park, and W.-K. Choi, "Low-resistance and nonalloyed ohmic contacts to plasma treated ZnO," *Applied Physics Letters*, vol. 78, pp. 3842—-3844, 2001.

[229] V. E. Henrich and P. A. Cox, *The Surface Science of Metal Oxides*. Cambridge University Press, Cambridge, 1994.

[230] W. Göpel and U. Lampe, "Influence of defects on the electronic structure of zinc oxide surfaces," *Physical Review B*, vol. 22, pp. 6447–6465, 1980.

[231] P. S. Xu, Y. M. Sun, C. S. Shi, F. Q. Xu, and H. B. Pan, "The electronic structure and spectral properties of ZnO and its defects," *Nuclear Instruments and Methods in Physics Research B*, vol. 199, pp. 286–290, 2003.

[232] C. G. V. de Walle, "Defect analysis and engineering in ZnO," *Physica B*, vol. 308-310, pp. 899–903, 2001.

[233] J. Akhtar, M. A. Malik, P. O'Brien, K. G. U. Wijayantha, R. Dharmadasa, *et al.*, "A greener route to photoelectrochemically active pbs nanoparticles," *Journal of Materials Chemistry*, vol. 20, pp. 2336–2344, 2010.

[234] S. S. Narayanan, S. S. Sinha, P. K. Verma, and S. K. Pal, "Ultrafast energy transfer from 3-mercaptopropionic acid-capped CdSe/ZnS QDs to dye-labelled DNA," *Chemical Physics Letters*, vol. 463, pp. 160–165, 2008.

[235] B. Carlson, K. Leschkies, E. S. Aydil, and X.-Y. Zhu, "Valence band alignment at cadmium selenide quantum dot and zinc oxide $(10\bar{1}0)$ interfaces," *Journal of Physical Chemisty C*, vol. 112, pp. 8419–8423, 2008.

[236] R. D. Schaller, M. Sykora, J. M. Pietryga, and V. I. Klimov, "Seven excitons at a cost of one: Redefining the limits for conversion efficiency of photons into charge carriers," *Nano Letters*, vol. 6, pp. 424–429, 2006.

[237] C. F. Barton, "Electron effective mass in PbS single crystals by infrared reflectivity measurements," *Journal of Applied Physics*, vol. 42, pp. 445–451, 1971.

[238] A. Barrie, I. W. Drummond, and Q. C. Herd, "Correlation of calculated and measured 2p spin-orbit splitting electron spectroscopy using monochromatic X-radiation," *Journal of Electron Spectroscopy and Related Phenomena*, vol. 5, pp. 217–225, 1974.

[239] R. B. Shalvoy, G. B. Fisher, and P. J. Stiles, "Bond ionicity and structural stability of some average-valence-five materials studied by X-ray photoemission," *Physical Review B*, vol. 15, pp. 1680–1697, 1977.

[240] G. Gonella, O. Cavalleri, S. Terreni, D. Cvetko, L. Floreano, *et al.*, "High resolution x-ray photoelectron spectroscopy of 3-mercaptopropionic acid self-assembled films," *Surface Science*, vol. 566-568, pp. 638–643, 2004.

[241] D. S. Zingg and D. M. Hercules, "Electron spectroscopy for chemical analysis studies of lead sulfide oxidation," *Journal of Physical Chemistry*, vol. 82, pp. 1992–1995, 1989.

[242] A. Lobo, T. Möller, M. Nagel, H. Borchert, S. G. Hickey, and H. Weller, "Photoelectron spectroscopic investigations of chemical bonding in organically stabilized PbS nanocrystals," *Journal of Physical Chemistry B*, vol. 109, pp. 17422–17428, 2005.

[243] B. R. Strohmeier and D. M. Hercules, "Surface spectroscopic characterization of the interaction between zinc ions and γ-alumina," *Journal of Catalysis*, vol. 86, pp. 266–279, 1984.

[244] V. I. Nefedov, Y. V. Salyn, P. M. Solozhenkin, and G. Y. Pulatov, "X-ray photoelectron study of surface compounds formed during flotation of minerals," *Surface and Interface Analysis*, vol. 2, pp. 170–172, 1980.

[245] B. J. Lindberg, K. Hamrin, G. Johansson, U. Gelius, A. Fahlman, *et al.*, "Molecular spectroscopy by means of esca ii. sulfur compounds. correlation of electron binding energy with structure," *Physica Scripta*, vol. 1, pp. 286–298, 1970.

[246] F. R. McFeely, S. Kowalczyk, L. Ley, R. A. Pollak, and D. A. Shirley, “High-resolution X-ray-photoemission spectra of PbS, PbSe, and PbTe valence bands,” *Physical Review B*, vol. 7, p. 5228–5237, 1973.

[247] C. J. Vesely and D. W. Langer, “Electronic core levels of the IIB-VIA compounds,” *Physical Review B*, vol. 4, pp. 451–462, 1971.

[248] D. Bröcker, *Zeitaufgelöste experimente zur oberflächen-photospannung an silizium*. PhD thesis, Martin-Luther-Universität Halle-Wittenburg, 2004.

[249] X. G. Zheng, Q. S. Li, W. Hu, D. Chen, N. Zhang, *et al.*, “Photoconductive properties of ZnO thin films grown by pulsed laser deposition,” *Journal of Luminescence*, vol. 122-123, pp. 198–201, 2007.

[250] M. Liu and H. K. Kim, “Ultraviolet detection with ultrathin zno epitaxial films treated with oxygen plasma,” *Applied Physics Letters*, vol. 84, pp. 173–175, 2004.

[251] T. E. Murphy, K. Moazzami, and J. D. Phillips, “Trap-related photoconductivity in ZnO epilayers,” *Journal of Electronic Materials*, vol. 35, pp. 543–549, 2006.

[252] I. Tashiro, T. Kimura, and E. Katsutoshi, “A study of the surface photovoltage of ZnO-resin layers,” *Applied Optics*, vol. 8, pp. 180–182, 1969.

[253] R. J. Collins and D. G. Thomas, “Photoconduction and surface effects with zinc oxide crystals,” *Journal of Luminescence*, vol. 112, pp. 388–395, 1958.

[254] L. Lagowski, E. S. Sproles, and H. C. Gatos, “Quantitative study of the charge transfer in chemisorption; oxygen chemisorption on ZnO,” *Journal of Applied Physics*, vol. 48, pp. 3566–3575, 1977.

[255] A. Rothschild, Y. Komem, and N. Ashkenasy, “Quantitative evaluation of chemisorption processes on semiconductors,” *Journal of Applied Physics*, vol. 92, pp. 7090–7097, 2002.

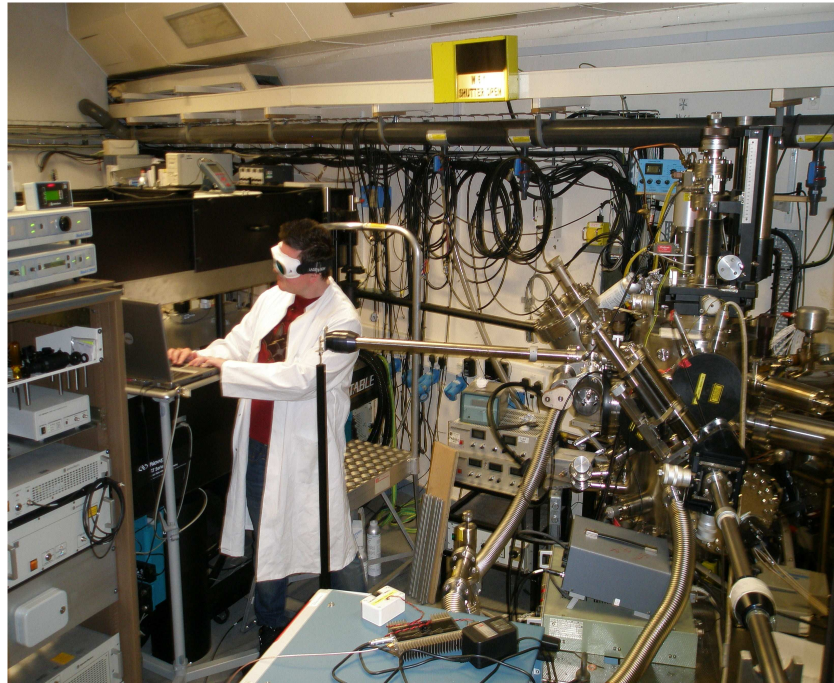

Figure 6.1: The Author.